



**TECHNISCHE
UNIVERSITÄT
WIEN**
Vienna University of Technology

MASTER THESIS

Experimental and numerical analysis of high speed multiphase flows

Thesis supervisors:

Univ.Prof. Dipl.-Ing. Dr.Dr.h.c. Anton FRIEDL
Ass.Prof. Dipl.-Ing. Dr. Michael HARASEK

and

Dipl.-Ing. Christian JORDAN
M.Sc Bahram HADDADI

E166-Institut für Verfahrenstechnik, Umwelttechnik und
Techn. Biowissenschaften
Forschungsbereich für Thermische Verfahrenstechnik und Simulation

By

Zsolt Harsfalvi
Matr.Nr.: 1029281

Vienna, October 7, 2015.

Kurzfassung

In dieser Arbeit wurden zwei komplexe Fälle von Hochgeschwindigkeits-Mehrphasenströmungen experimentell und mittels fluiddynamischer Simulation untersucht.

Im ersten Fall geht es um die Bestimmung der Tropfengrößenverteilung bei einem Zweistoff-Zerstäuber in einem Hochofen, wo Schweröl als Ersatzreduktionsmittel verwendet wird. Nachdem die Möglichkeiten für direkte Messungen im Hochofen wegen der extremen Umgebung stark begrenzt sind, wurde eine Dimensionsanalyse durchgeführt, um ein verkleinertes Modell zu konstruieren. Somit ist es möglich, die Zerstäubung näher zu betrachten und Messungen durchzuführen. Die Messungen wurden mithilfe einer Hochgeschwindigkeitskamera durchgeführt. Die Aufnahmen wurden mittels *Particle Image Velocimetry* ausgewertet, um die Tropfengrößenverteilung zu ermitteln.

Um den Vorgang zu analysieren, wurden Modellflüssigkeiten verwendet. Der Bereich der Flüssigkeitseigenschaften (Dichte, Viskosität, usw.) hat sich relativ zu den Vorarbeiten wegen den verwendeten Modellflüssigkeiten wie Ethanol, Wasser, Paraffinöl und verschiedene Wasser-Glycerin-Lösungen stark vergrößert. Nachdem die Messungen für alle Flüssigkeiten und Einstellungen durchgeführt wurden, konnten die verschiedenen Tropfengrößenverteilungen festgestellt und verglichen werden. Die Auswertung der Aufnahmen war nur teilweise erfolgreich, weil die Qualität der Bilder und somit die Genauigkeit der Messung bei Modellfluiden mit höherer Viskosität gesunken ist. Demzufolge hat war die günstigste Flüssigkeit gegenüber Paraffinöl reines Wasser und seine Lösungen mit Glycerin. Die Untersuchung hat gezeigt, dass dieses Verfahren effektiv funktionieren kann, aber um die Genauigkeit auch bei hohen Viskositätswerten zu erreichen, sind weitere Entwicklungen bei der Messung durchzuführen, wie zB.: Konstante und intensive Beleuchtung der Zerstäubung, höhere Auflösung und bei höheren Eindüsung-Geschwindigkeiten kürzere Verschlusszeit. Nachdem die Messungen bei niedrigeren Viskositätswerten und somit bei ungünstigen dimensionslosen Kennzahlen (welche den Umständen des tatsächlichen Hochofens nicht entsprechen) erfolgreich waren, ist es nötig, das Phänomen weiter zu überprüfen und die Messverfahren weiter zu entwickeln.

Im zweiten Fall wird eine mit Druckluft und Wasser betriebene Rakete untersucht. Mit dem Opensource Programm OpenFOAM® wurde eine CFD Berechnung durchgeführt, um die zweiphasige Hochgeschwindigkeitsausströmung bei einer Lavaldüse und einer einfachen Düse (mit größerem Innendurchmesser) zu verstehen und den Impuls beim Düsenaustritt zu berechnen. Die Ergebnisse der Berechnung dienen auch dazu, die innere Strömung in dem Raketenkörper zu analysieren. Weiteres Ziel war auch die Außenströmung bei der Rakete zu betrachten und den Widerstandskoeffizienten zu berechnen. Aus Validierungsgründen wurde eine vereinfachte analytische, numerische Berechnung für den gesamten Flug durchgeführt. Neben diese Berechnungen stehen auch Videoaufnahmen über den Abflug für die Validierung der CFD Berechnungen zur Verfügung.

Die gewonnenen Ergebnisse bzw. das Geschwindigkeitsfeld zeigt eine starke Analogie mit der Realität und paßt auch überwiegend mit den numerischen Berechnungen zusammen. Neben vielen neu gewonnenen Informationen und Erkenntnissen haben die Ergebnisse auch die Vorteile der Lavaldüse gezeigt. Die bessere Effizienz wurde jedoch mit den eingestellten Anfangsbedingungen gemäß der Simulationen von der einfachen Düse erreicht.

Die Ergebnisse der CFD Berechnungen haben es bestätigt, dass die zweiphasige Ausströmung ein sehr komplexes Phänomen ist. Die präsentierten Ziele wurden erfolgreich erfüllt, aber um den Vorgang besser zu verstehen und die optimale Düsenform zu finden sind weitere Simulationen und/oder Messungen nötig.

Abstract

In this thesis two cases of high-speed multiphase flows were analyzed using experimental measurements techniques and computational fluid dynamics simulations.

The first case considers the injection of fuel oil into the raceway of a blast furnace through a two-fluid lance. Because of the extreme ambient conditions direct measurements at the blast furnace are impossible, so a downscaled lab model is used for a high speed imaging analysis of the droplet break up. Data from the lab measurements are the basis for deriving a general correlation for the droplet size distribution.

To investigate the behavior of the process, variations of the atomization settings using different model fluids like ethanol, water, paraffin oil, and different solutions of water and glycerol were used. Due to the various model fluids the investigated interval of viscosity, and other fluid properties was larger than in any other previous measurements. After the image analysis the Sauter Mean Diameter (SMD) was calculated for each distribution function and also a comparison of the functions was achieved. The data processing of the high speed video recordings was only partly successful because of the unforeseen measurement difficulties especially in the high viscosity regions. Therefore the most favorable model fluid was pure water, followed by the solutions of water and glycerol due to the lower viscosity. The investigation proved that the image analysis is an effective way to find out the SMD and the distribution functions. But for more accurate measurements, also in case of lower or higher viscosities where the values of the dimensionless numbers are closer to the real blast furnace application, the modification and improvement of the measurement system is indispensable. The further understanding of the process is needed for the improvement of the atomization process in the real blast furnace.

The second case will deal with a pressurized air - water rocket. Using CFD simulation – with the open source program OpenFOAM® – a two phase high speed outflow for two different nozzle geometries was analyzed. The results of the simulations are serving for the understanding of the flow inside the rocket chamber and also to calculate the generated momentum at the nozzle exit.

In this way, the functioning of a Laval and a simple nozzle (with a larger inner diameter) can be analyzed and compared. The investigation includes a one phase stationer simulation to determine the rocket's drag coefficient. As validation the two phase outflow was calculated analytically and numerically in a simplified way. For further validation also video recordings were available to compare the behavior of the outflow.

According to the preparative numerical calculations and the video recordings the simulation results were positive because they showed a strong analogy with the reality. Besides of the large amount of new information the results showed the advantages of the Laval against the simple nozzle. Irrespectively of this result using the presented initial conditions the simple nozzle achieved a better efficiency because of the larger inner diameter. The results also helped to understand the behavior of the two phase flow inside the rocket chamber.

The simulation results showed the complexity of the multiphase outflow. The presented goals were successfully achieved but to better understand the impact of the different nozzles, initial conditions and to find the optimal nozzle shape further calculations or/and measurements are needed.

Content

Nomenclature	8
List of tables	11
List of figures.....	12
Acknowledgment	15
I. Introduction	16
II. Basics of multiphase flows - atomization.....	17
II. 1. Physical basics	17
II. 1.1. Spray types.....	17
II. 1.1.1. Monodisperse spray.....	17
II. 2.1.1. Polydisperse spray	17
II. 2.1. The atomization effected fluid properties.....	17
II. 1.1.1. Viscosity	17
II. 2.1.1. Density	18
II. 3.1.1. Surface and interfacial surface tension.....	19
II. 3.1. Dimensionless numbers.....	19
II. 1.1.1. Reynolds number	19
II. 2.1.1. Weber number	20
II. 3.1.1. Ohnesorge number	20
II. 4.1.1. Bond number	20
II. 2. Different atomization types	20
II. 1.1. Droplet formations through desintegration of the jet flow	20
II. 2.1. Atomization of the droplet (secondary atomization)	22
II. 1.1.1. Deformation and vibrational breakup	23
II. 2.1.1. Bag breakup	23
II. 3.1.1. Sheet-thinning breakup	23
II. 4.1.1. Multimode breakup	24
II. 5.1.1. Catastrophic breakup.....	24
II. 3.1. Different atomizer designs.....	25
II. 1.1.1. Single-fluid nozzle	25
II. 2.1.1. Two-fluid nozzle	26
II. 3.1.1. Mechanical atomizers	26
II. 4.1.1. Other atomizers	26
III. First example - atomization in a blast furnace.....	27
III. 1. Introduction of the blast furnace.....	27
III. 2. Presentation of the problem.....	28
III. 2.1. The goal of the investigation.....	28
III. 2.2. Dimensional analysis – brief summary –.....	29

III. 2.2.1. Buckingham Pi - Theorem	29
III. 2.3. From the technical data to the lab model	30
III. 2.4. Evaluating the atomization	34
III. 2.4.1. Calculation of the dimensionless numbers	37
III. 3. High speed camera measurements	39
III. 3.1. The buildup of the model and the measurement system	39
III. 3.2. Technical equipment.....	40
III. 3.3. Process of the measurement	41
III. 3.4. Calibration of the measurement.....	43
III. 3.5. Validation with different sugar classes	43
III. 3.5.1. Adjustment of the data processing.....	43
III. 3.5.2. Results with sugar used as reference.....	45
III. 3.6. Processing of the obtained data	47
III. 4. All the performed measurements.....	50
III. 4.1. Physical properties of the used fluids and solutions	50
III. 4.2. Table of measurements	54
III. 4.2.1. Atomization using paraffin.....	55
III. 4.2.2. Atomization using water	55
III. 4.2.3. Measurement with glycerol water solutions	56
III. 5. Results of the measurements and evaluations.....	57
III. 5.1. Results of the different model fluids	57
III. 5.1.1. Selected results for water	58
III. 5.1.2. Selected results for glycerol – water solutions.....	62
III. 5.1.3. Selected results for paraffin oil.....	66
III. 5.2. Problems and difficulties with the measurement and data processing	68
III. 6. Conclusions	69
III. 6.1. The evaluated interval	69
III. 6.2. Unsuccessful measurements	69
III. 6.3. Successful measurements.....	70
III. 6.4. Summary of the conclusions.....	71
III. 7. Future plans – Possible improvements of the measurement.....	72
IV. Second example - momentum of an air - water propellant rocket	74
IV. 1. Introduction of the rocket.....	74
IV. 2. Presentation of the problem - the goal of the investigation	74
IV. 3. The operation of the system.....	75
IV. 3.1. The rocket	75
IV. 3.2. The launch pad.....	76
IV. 3.3. The process of the flight	77
IV. 4. The selected CFD methods for the problem	78
IV. 4.1. Outer flow	78
IV. 4.2. Inner flow	81

IV. 5.	Determining the drag coefficient of the rocket - simulation of the outer flow.....	82
IV. 5.1.	Preparative simulations	82
IV. 5.2.	Simulation of the rocket outer flow.....	89
IV. 5.2.1.	The geometry and the properties of the generated mesh	89
IV. 5.2.2.	Results of the simulation.....	90
IV. 5.2.3.	Calculated drag coefficient with OpenRocket	91
IV. 5.2.4.	Evaluation and conclusion	93
IV. 6.	Calculating the generated momentum at the rocket nozzle - inner flow.....	95
IV. 6.1.	Preparative calculations and simulations	95
IV. 6.1.1.	Analytical, numerical calculation of the outflow	96
IV. 6.1.2.	Stepwise development of the simulation setup	108
IV. 6.2.	Simulation of the rocket inner flow	110
IV. 6.2.1.	The geometry and the properties of the generated mesh	110
IV. 6.2.2.	Results of the simulation.....	111
IV. 6.2.3.	Evaluation of the simulation results	121
IV. 6.2.4.	Conclusions	126
IV. 7.	Calculating the maximum altitude of the rocket, comparison of the nozzles	130
IV. 8.	Future plans	132
V	Summary	134
VI	Literature and sources	136
VII	Appendix A Recorded images with the HS camera.....	138
VIII	Appendix B The used boundary conditions	140
IX	Appendix C Further results of the simulations	142
X	Appendix D Further details of the rocket	144

Nomenclature

In this work, two different multiphase flow phenomena have been analyzed. Nomenclature has been used differently for both cases in accordance with conventions:

Blast furnace:

<i>Symbol</i>	<i>Unit</i>	<i>Definition</i>
A	$[m^2]$	<i>area</i>
Bo	[1]	<i>Bond number</i> $Bo = \frac{\rho g d_0^2}{\sigma}$
d	$[m]$	<i>diameter</i>
d_{32}	$[m]$	<i>sauter mean diameter</i>
D	$[m]$	<i>diameter</i>
F	$[N]$	<i>force</i>
g	$[m/s^2]$	<i>acceleration due gravity</i>
l	$[m]$	<i>length</i>
m	$[kg]$	<i>mass</i>
\dot{m}	$[kg/s]$	<i>mass flow</i>
Oh	[1]	<i>Ohnesorge number</i> $Oh = \frac{\eta}{\sqrt{d_0 \rho \sigma}}$
p	$[Pa]$	<i>pressure</i>
P	[%]	<i>relative power</i>
R	$[J/molK]$	<i>gas constant</i>
R_i	$[J/kgK]$	<i>specific gas constant</i>
Re	[1]	<i>Reynolds number</i> $Re = \frac{\rho v d_0}{\eta}$
T	$[K]$	<i>temperature</i>
v	$[m/s]$	<i>velocity</i>
\dot{V}	$[m^3/s]$	<i>volume flow</i>
V	$[m^3]$	<i>volume</i>
We	[1]	<i>Weber number</i> $We = \frac{\rho v^2 d_0}{\sigma}$
Z	[1]	<i>compressibility factor</i>
α	$[^\circ]$	<i>angle of insufflation relative to the gasflow</i>

β	[°]	<i>Angle of the primary beam of insufflation relative to the axis of the oil lance</i>
ν	[m ² /s]	<i>kinematic viscosity</i>
η	[Pa · s], [cP]	<i>dynamic viscosity</i>
ρ	[kg/m ³]	<i>density</i>
σ	[N/m], [Dyne/cm]	<i>surface tension</i>
τ	[N/m]	<i>shear stress</i>
ϕ	[1]	<i>impulse ratio</i>
Δ	[mm]	<i>relative span factor</i>

Rocket

<i>Symbol</i>	<i>Unit</i>	<i>Definition</i>
a	[m/s ²]	<i>acceleration of the rocket</i>
A	[m ²]	<i>area</i>
A_{cs}	[m ²]	<i>area of the largest cross section of the rocket normal to the flow direction</i>
c_D	[1]	<i>drag coefficient</i>
d	[m]	<i>diameter</i>
D	[N]	<i>drag force</i>
F	[N]	<i>force</i>
g	[m/s ²]	<i>gravitational acceleration</i>
h	[m]	<i>altitude of the rocket</i>
h	[J/kg]	<i>specific enthalpy</i>
H	[m]	<i>altitude of the rocket calculated numerically</i>
k	[m ² /s ²]	<i>turbulent kinetic energy</i>
L	[m]	<i>length</i>
m	[kg]	<i>mass</i>
\dot{m}	[kg/s]	$\dot{m} = u\rho A = K$ <i>Mass flow, constant case</i>
p	[Pa]	<i>pressure</i>
p_r	[Pa]	<i>pressure in the rocket chamber</i>

\dot{q}	[kg/s]	<i>mass flow, unsteady case</i>
R	[J/molK]	<i>gas constant</i>
Re	[1]	<i>reynolds number</i>
r	[m]	<i>radius</i>
s	[J/K]	<i>specific entropy</i>
t	[s]	<i>time</i>
T	[K]	<i>temperature</i>
T	[s]	<i>end time of the outflow</i>
u	[m/s]	<i>velocity</i>
V	[m ³]	<i>volume</i>
v_r	[m/s]	<i>velocity of the rocket</i>
v	[m/s]	<i>velocity</i>
y^+	[1]	<i>dimensionless wall distance</i>
γ	[°]	<i>angle of the launching direction of the rocket</i>
δ	[mm]	<i>thickness of the boundary layer</i>
ε	[m ² /s ³]	<i>turbulent dissipation</i>
κ	[1]	<i>adiabatic gas exponent</i>
ν_t	[m ² /s]	<i>turbulent viscosity</i>
ρ	[kg/m ³]	<i>density</i>
τ	[N/m ²]	<i>shear stress</i>
ω	[1/s]	<i>specific dissipation</i>

List of tables

Table 1: Weber number intervals [2]	22
Table 2: Operating parameters of the blast furnace [6].....	31
Table 3: Geometrical parameters of the nozzle [6].....	32
Table 4: Calculated operating parameters [6].....	32
Table 5: Calculated dimensionless parameters [6].....	32
Table 6: Operating parameters of the test rig [6]	33
Table 7: Comparison of the real and the model operating conditions [6].....	33
Table 8: Mean diameters and their applications, representative diameters of the droplet [7]	34
Table 9: Properties of the single hole nozzle and the supplied air [10]	37
Table 10: Characteristic lengths.....	38
Table 11: Technical equipments	40
Table 12: Validation using sugar	43
Table 13: Final adjustments for the data processing.....	47
Table 14: Temperature increase during the measurement	52
Table 15: Properties of the different fluids and solutions at 20 °C.....	54
Table 16: Measurement settings for paraffin.	55
Table 17: Measurement settings for water.....	55
Table 18: Measurement settings for water - glycerol solutions	56
Table 19: Properties of the atomization, water, Tuyere inlet vel. 0 m/s.....	58
Table 20: Properties of the atomization, water, Tuyere inlet vel. 33.6 m/s.....	59
Table 21: Properties of the atomization, water, Tuyere inlet vel. 53,4 m/s.....	60
Table 22: Properties of the atomization, water, Tuyere inlet vel. 53,4 m/s.....	61
Table 23: Properties of the atomization, glycerol - water, Tuyere inlet vel. 53,4 m/s	62
Table 24: Properties of the atomization, glycerol - water, pump power 20%.....	63
Table 25: Properties of the atomization, glyc. – water sol., pump power 10%, T. inlet vel. 70,6 m/s.....	64
Table 26: Properties of the atomization, glycerol – water solutions, pump power 10%.....	65
Table 27: Comparison of the num. dist. functions for oil, cover stream 80 l/min	66
Table 28: Summary of the measurements, comparison with the real system	67
Table 29: Nozzle geometries	76
Table 30: The used turbulent values for the inlet.....	84
Table 31: Results of the drag coefficient for different calculation methods.....	84
Table 32: Properties of the different sphere hexahedral meshes.....	84
Table 33: Results of the drag coefficient for different inlet velocities.....	90
Table 34: Settings of the computations.....	95
Table 35: Comparison of the measurement and simulation.....	133
Table 36: Boundary conditions for the preparative one phase simulations for estimating k, ε and ω	140
Table 37: Boundary conditions for determining the drag coefficient of the rocket.....	140
Table 38: Boundary conditions for the two phase simulation.....	141
Table 39: Settings in the controlDict file to calculate the drag coefficient.....	141

List of figures

Figure 1: Homogeneous liquid layer between two solid plates	18
Figure 2: Atomization mechanisms, Figure source: [4].....	21
Figure 3: Deformation and fragmentation of the droplet at different breakup types [2]	22
Figure 4: Deformation and vibrational breakup [2]	23
Figure 5: Schematic illustration of the bag breakup [2].....	23
Figure 6: Schematic illustration of the s-t breakup [2]	23
Figure 7: Schematic illustration of the cat. breakup [2].....	24
Figure 8: Classification of the different breakup mechanisms [5]	24
Figure 9: Schematic picture of plain orifice and the swirl nozzle [4].....	25
Figure 10: Schematic picture of internal- (left) and external- (right) mix nozzle [6]	26
Figure 11: Schematic view of rotary atomizers (a) disc, (b) cup [4]	26
Figure 12: Schematic picture of the blast furnace [8]	27
Figure 13: Diameter of the oil lance (left), Cover pipe and Tuyère (right) [10].....	28
Figure 14: Flow chart of the created model test rig parameters.....	31
Figure 15: Comparison of the various representative diameters on a drop size distribution function.....	35
Figure 16: Distribution functions	36
Figure 17: Schematic picture of the high speed measurement system.....	39
Figure 18: Model and the high speed measurement system Source: Zauner [10]	40
Figure 19: Setup of the reflectors A - A.....	41
Figure 20: Mounting positions of the HS camera (front view).....	42
Figure 21: Calibration plane [10].....	43
Figure 22: Distributions of the different sugar fractions (sieve analysis)	44
Figure 23: Comparisons of the different evaluations for normal crystal sugar.....	45
Figure 24: Comparisons of the different evaluations for fine crystal sugar.....	45
Figure 25: Comparisons of the different evaluations for castor sugar	46
Figure 26: Main steps of the data processing.....	47
Figure 27: The analyzed part (1024×1024 cropped to 400×400 - upper left).....	48
Figure 28: The basic steps of the analysis, results.	48
Figure 29: Disturbances and undesired results (examples).....	49
Figure 30: Main steps of the statistical evaluation in Microsoft Excel.....	50
Figure 31 Properties of the different fluids	51
Figure 32: Properties of the applied model fluids.....	51
Figure 33: Dynamic viscosity of the used fluids and solutions	52
Figure 34: Surface tension of the used fluids and solutions.....	53
Figure 35: Density of the used fluids and solutions.....	53
Figure 36: Comparison of the num. dist. functions for water, T. inlet vel. 0 m/s	58
Figure 37: Comparison of the vol. dist. functions for water, T. inlet vel. 0 m/s	58
Figure 38: Comparison of the num. dist. functions for water, T. inlet vel. $33,6 \text{ m/s}$	59
Figure 39: Comparison of the vol. dist. functions for water, T. inlet vel. $33,6 \text{ m/s}$	59
Figure 40: Comparison of the num. dist. functions for water, T. inlet vel. $53,4 \text{ m/s}$ Adjustment 2.....	60
Figure 41: Comparison of the num. vol. functions for water, T. inlet vel. $53,4 \text{ m/s}$ Adjustment 2	60

Figure 42: Comparison of the num. dist. functions for water, T. inlet v. $53,4 \text{ m/s}$	61
Figure 43: Comparison of the num. vol. functions for water, T. inlet vel. $53,4 \text{ m/s}$	61
Figure 44: Comparison of the num. dist. functions for glyc. - water solutions, T. inlet vel. $53,4 \text{ m/s}$	62
Figure 45: Comparison of the vol. dist. functions for glyc. - water solutions, T. inlet vel. $53,4 \text{ m/s}$	62
Figure 46: Comparison of the num. dist. functions for glycerol - water solutions, pump power 20%	63
Figure 47: Comparison of the vol. dist. functions for glycerol - water solutions, pump power 20%	63
Figure 48: Comparison: num. dist. f. glyc – water solutions, pump power 10% , T. inlet vel. $70,6 \text{ m/s}$	64
Figure 49: Comparison: vol. dist. f. glyc. – water solutions, pump power 10% , T. inlet vel. $70,6 \text{ m/s}$	64
Figure 50: Comparison of the num. dist. functions for glycerol - water solutions, pump power 10%	65
Figure 51: Comparison of the vol. dist. functions for glycerol - water solutions, pump power 10%	65
Figure 52: Comparison of the num. dist. functions for oil, cover stream 80 l/min	66
Figure 53: Comparison of the num. dist. functions for oil, cover stream 80 l/min	66
Figure 54: Trend of the SMD depending from the viscosity and the pump power	70
Figure 55: Buildup of the rocket (section view)	75
Figure 56: The CAD models of the exchangeable nozzles (left) Nozzle 2 fabricated (right)	75
Figure 57: The launching pad. Constructed (left), CAD model (right)	76
Figure 58: Section view of the launching pad	77
Figure 59: $u(x,y,z,t)$ in stationary and unsteady case [15]	78
Figure 60: Velocity distribution in the boundary layer. Source: [15]	80
Figure 61: Cross section of the cylinder domain.	83
Figure 62: Drag coefficient curve for a sphere and the equation from Morrison [24]	83
Figure 63: The value of y^+ and the field of k, ε in the symmetry cut plain of the sphere, $u_{inlet} = 50 \text{ m/s}$	85
Figure 64: The velocity field u_y in the symmetry plain of the sphere (full domain) $u_{inlet} = 50 \text{ m/s}$	85
Figure 65: The velocity field of the rounded cylinder	86
Figure 66: Boundary layer on the rounded cylinder $x = 400 \text{ mm}$	87
Figure 67: Values of the drag coefficient between $10^4 < Re < 10^6$	88
Figure 68: Drag coefficient of spheres as a function of the Re number (based on measurements) [19]	88
Figure 69: The import ready SolidWorks geometry	89
Figure 70: The structure of the domain, side view and overview	90
Figure 71: The velocity field u_y in the whole domain (cross section) at $u_{y,inlet} = 10 \text{ m/s}$	90
Figure 72: Part of the domain (cross section) at $u_{y,inlet} = 10 \text{ m/s}$	91
Figure 73: The modeled rocket in OpenRocket	92
Figure 74: The drag coefficient by OpenRocket	92
Figure 75: The growth of the boundary layer thickness in flow direction	93
Figure 76: Velocity field of the rocket cut at six different locations	94
Figure 77: Sketch of the rocket	96
Figure 78: Velocity and expansion in the Laval nozzle, ideal case, according to [26] and [27]	101
Figure 79: Optimal exit area of the nozzle at different pressure ratios	102
Figure 80: Flight of the rocket. Function of the acceleration, velocity and altitude in time	105
Figure 81: The function of the total mass and the pressure difference in the rocket during the flight	105
Figure 82: The function of the drag force during the flight, calculated with $c_D = 0,48$	106
Figure 83: Theoretical optimum of the water amount	106
Figure 84: Case start-up	108
Figure 85: The simplified case in 2D	108

Figure 86: Pressure and velocity field after the nozzle, $2D$ case	109
Figure 87: Geometry of the chambers.....	110
Figure 88: Mesh around the nozzle, cut from the domain	111
Figure 89: Behavior of the two phases at two initial water levels, at nozzle 3	113
Figure 90: Velocity field in the first chamber for two initial water levels at nozzle 3	113
Figure 91: Behavior of the two phases and the velocity field at few time steps for nozzle 3, $3l$	114
Figure 92: Total accelerating force at the nozzle exit, nozzle 3, $3l$	115
Figure 93: Mass flow at the nozzle exit, nozzle 3, $3l$	115
Figure 94: Velocity field at the nozzle; (left) Under-expanded, (right) Optimal; at nozzle 3, $3l$	116
Figure 95: The force at the nozzle exit as a result of the pressure difference at nozzle 3, $3l$	116
Figure 96: Total mass of the rocket during the outflow at nozzle 3, $3l$	117
Figure 97: The behavior of the two phases and the velocity field at few time steps for nozzle 4	118
Figure 98: The resulting total accelerating force, at nozzle 4	119
Figure 99: Mass flow during the outflow at nozzle 4	119
Figure 100: Force at the nozzle exit as a result of the pressure difference at nozzle 4	120
Figure 101: Total mass of the rocket during the outflow at nozzle 4	120
Figure 102: Comparison of the acceleration functions for the simulation results and numerical calc.	121
Figure 103: Comparison of the flight of the rocket for the simulation results and the numerical calc.....	122
Figure 104: Velocity profile at the exit of nozzle 4, at the very beginning of the water outflow	122
Figure 105: Velocity field in the whole domain at $t = 0,547 s$, using logarithmic scale	123
Figure 106: Pressure and velocity values in the rocket, along the symmetry axis; for nozzle 4.....	123
Figure 107: Pressure and velocity values in the rocket, along the symmetry axis; for nozzle 3, $3l$	124
Figure 108: Jet shapes at other rocket models with different nozzle and chamber geometries,	125
Figure 109: Exploding of the water jet, starting of the two phase outflow nozzle 4	125
Figure 110: Exploding of the water jet, starting of the two phase outflow at nozzle 3, $3l$	126
Figure 111: Backflow in the first chamber at nozzle 3, $t = 0,84 s$	127
Figure 112: Comparison of the calculated total momentum at nozzle 4 and nozzle 3	128
Figure 113: Comparison of the mass flow at nozzle 3 and nozzle 4.....	129
Figure 114: Flying of the rocket using nozzle 3, $3l$	131
Figure 115: Flying of the rocket using nozzle 4	131
Figure 116: Comparison of the flights for nozzle 3, nozzle 4 and the numerical results.....	132
Figure 117: Air-water rocket (previous model)	132
Figure 118: Atomization of ethanol (low viscosity) at the nozzle outlet.....	138
Figure 119: Water droplets after the atomization	138
Figure 120: Atomization of paraffin oil at the nozzle.....	138
Figure 121: Atomization of a single paraffin oil droplet	139
Figure 122: Atomization of pure glycerol (high viscosity) into filaments at the nozzle	139
Figure 123: Stream lines around the rocket, steady state single phase simulation, $u_{y,inlet} = 10 m/s$	142
Figure 124: Water amount in the bottle, nozzle 3, $3l$ at $t = 0,55 s$	142
Figure 125: Pressure field around the rocket, steady state single phase simulation, $u_{y,inlet} = 10 m/s$	143
Figure 126: Shock cell structure and the resulting velocity field after the nozzle after the nozzle 3, $3l$.	144
Figure 127: Details of the rocket geometry	144

Acknowledgment

Immeasurable appreciation and deepest gratitude for the help and support are extended to the team of the Process Engineering Institute of Vienna University of Technology, especially to **Michael Harasek** and **Anton Friedl**. The received assistance, trust and patience at the Institute gave me even more motivation to prepare the thesis.

In case of any occurred technical problems I could count on the help of **Christian Jordan**, whether measurement difficulties or server problems. The only thing better as his support was his reaction time.

Without the help and assistance of **Bahram Haddadi**, the acquirement of OpenFOAM and the success of my CFD computations would have been unimaginable. His support and calmness even at the hardest, futureless parts of the thesis charged me with additional motivation and confidence.

My gratefulness concerns also the Institute of Production Engineering, especially **Michael Heger**, who supported me at the production of the rocket opening mechanism and also the production of the rocket nozzles and the nose cone. The future rocket measurements could not be accomplished with this higher professionalism without his help.

Beyond that I am thankful for my boss, **Martin Putschek** at Swimsol GmbH who supported me at the writing of the thesis with the high flexibility of my working hours and with the allowing of long intermissions of my work at the company.

Last but not least I could not come this far without of the support of my **family**. The motivation and maintenance I received from them and from my girlfriend **Dora**, made my path much easier.

Circumstances like these will make it easy to assume further challenges!

Thank You All!

I. Introduction

There are a lot of examples for multiphase flows in the manufacturing, energy related technologies and also in our environment where the physical or/and chemical processes are executed in more than one phase. Such processes are for example: Steam production for turbines, atomization of fuel in engines, cavitation, climate systems (like clouds), cryogenics, bubbles, fountains etc.

There are different purposes of the atomization in the industry, for example achieve a better heat exchange. The accretion of these effects in the industry ministered to a high level of investigation of these multiphase processes. With the aid of these investigations processes can be defined more precisely and they can be monitored with more attention to the details hereby the system can be improved and optimized. For example we can optimize the system to reach a higher efficiency and so a lower energy consumption. Furthermore the happening of adventitious unwanted by-processes can be avoided.

If it is possible at all, the rating of the quality of sprays in the industry is highly complicated because of its complexity. It could be just done with considerable technical and financial expense. The goal of this thesis is to investigate two examples where the two - phase flow – atomization – occurs.

Both discussed examples are multiphase flows, where the two - phase system is effectuated by atomization through a nozzle. The difference between the two examples is the nozzle type and the purpose of the atomization.

The first example illustrates the injection of fuel into the raceway of a blast furnace where the efficiency of the process principally depends from the quality of the atomization. The investigation of the first case will be achieved with measurements and in the second case by CFD computation. The measurement will be performed by image analysis using a high speed camera to gain the different droplet size distributions and the Sauter mean diameters for the individual settings at a model test rig. The lab scale model is the part of a blast furnace – on a small scale – where the fuel injection respectively the atomization can be analyzed. For this process a method should be created whereby the prediction of the atomization at the real process can be achieved.

The goal of the second example is to accomplish a preparative analytical and numerical calculation followed by a CFD simulation for a pressurized air - water rocket to understand the details of the two phase outflow behavior at a Laval nozzle, where the outflow becomes partly supersonic. With the detailed investigation the resulting momentum of the rocket respectively the accelerating force could be improved to reach higher altitudes. The calculation of the process for every little time step would make it possible to see and understand the interaction of the fluid in the rocket chamber.

Considering the two investigations, the purpose is the better understanding of the processes and hereby the improvement of the performance.

II. Basics of multiphase flows - atomization

II. 1. Physical basics

The physical definition of atomization is the production of many single droplets from a contiguous liquid volume or mass flow. The product of the atomization process is a droplet pack which is called spray.

II. 2.3. Spray types

Depending on the diameters of the droplets two different spray types can be differentiated, the mono- and the polydisperse spray.

II. 1.3.2. Monodisperse spray

If all the droplets in the spray have the same droplet diameter, then the spray is called monodisperse. This means, that the properties of the spray can be expressed with just one value, which describes the diameter of the drops. This characteristic is in most of the cases untrue.

II. 2.3.2. Polydisperse spray

A spray with different droplet diameters is called a polydisperse spray. Mainly it characterizes most of the atomization.

II. 2.3. The atomization effected fluid properties

II. 1.3.2. Viscosity

The inner friction of a fluid or so called the viscosity is a fluid parameter, which describes the degree of the inner resistance against the shear stresses. The viscosity plays an important role in the atomization, because it highly influences the capability of fragmentation of droplets, therefore the needed amount of energy for the atomization process. Temperature and pressure have a high influence on the viscosity of a fluid. The value of the viscosity can be so high, that the fluid acts like a solid material.

There are two types of the viscosity, dynamic and kinematic viscosity. The connection between the two values can be expressed with the following correlation:

$$\nu = \frac{\eta}{\rho} \left[\frac{m^2}{s} \right] \quad (1.)$$

To further investigate the dynamic viscosity we can easily imagine an amount of fluid closed between two solid plates as in *Figure 1*. The fluid between the two plates is homogeneous and has a constant temperature. Pulling the upper plate with constant velocity, while holding the bottom plate still, a linear velocity profile will take shape in the fluid. For the constant velocity at the upper plate a constant force is needed.

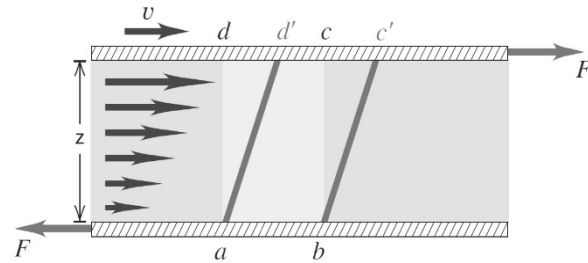


Figure 1: Homogeneous liquid layer between two solid plates

$$F = \tau A = \eta A \frac{v}{z} [N] \quad (2.)$$

A more detailed description of the correlations can be found under [1]

In this case the liquid has a linear stress versus strain relation, which is called Newtonian fluid. A Newtonian liquid has an approximately linear stress versus strain relation. This assumption is in most of the cases true. Some examples: water, alcohol, most hydrocarbon fuels. The other non-Newtonian liquids are rated in three different classes.

- ◆ Nonlinear pure viscous liquids
- ◆ Linear viscoelastic liquids
- ◆ Nonlinear viscoelastic liquids

II. 2.3.2. Density

The volumetric mass density of a substance is its mass divided by its volume.

$$\rho = \frac{m}{V} \left[\frac{kg}{m^3} \right] \quad (3.)$$

The leading influential factor of the density is the temperature. Another influential factor is the pressure. It strongly depends if the substance we investigate is a gas or liquid, because in case of liquids the influence of the pressure is near negligible (except very high pressures), that's why the liquids are called incompressible. The previous conception is not the same for gases, because with growing pressure the density of the gas changes firmly (compressible). An estimation of the density can be done by using the thermal equation of state for ideal gases. [1]

$$\rho = \frac{p}{Z R_i T} \left[\frac{kg}{m^3} \right] \quad (4.)$$

II. 3.3.2. Surface and interfacial surface tension

In liquids, the parameter surface tension grants resistance ability against external forces. The value of the surface tension is relatively low and this value will sink even more with growing temperature and impurity of the liquid. The effect of the surface tension can be shown clearly if we consider a thin, elastic membrane. In reality this membrane is composed of a single atom or molecule layer. For instance at air-liquid interfaces the surface tension derives from the difference of the attraction between water - water (greater), water - air molecules. A consequence of the surface tension is, that droplets have a relatively stable sphere form, which is caused by the inner pressure of the droplet. This effect is acting against the further fragmentation of the droplet, thus the greater the surface tension the more energy will be needed for the atomization. The value of the surface tension has a high influence on the droplet fragmentation.

$$\sigma = \frac{\text{Force}}{\text{Length}} \left[\frac{N}{m} \right] \quad (5.)$$

The tension at the connection surface of two different liquid layers covering each other (which are not mixable) is called the interfacial surface tension.

II. 2.3. Dimensionless numbers

Dimensionless numbers are parameters which can be used for describing physical problems in case of models. Through proper combination of physical variables - which are describing the model - it is possible to effectuate a dimensionless system with the advantage of less (but dimensionless) equations and properties. This method is called dimensional analysis. Some of the most important dimensionless numbers in the multiphase flows are for instance the Reynolds, Ohnesorge, Weber and Bond number which are presented below. A more detailed description of the dimensional analysis can be found under [1] or also in [2], in chapter 6.

II. 1.3.2. Reynolds number

The ratio of the force of inertia and viscosity results in the dimensionless Reynolds number. The use of the Reynolds number is that the turbulent behavior of the system, at geometrically similar bodies will be identical if this dimensionless value is the same. Therefore it can be well used for constructing scale models in fluidics. The Reynolds number also demarcate the different art of flows with its value Re_{crit} . This value is the border between laminar and turbulent flow. Near to this value the flow becomes transitional.

$$Re = \frac{\text{inertial forces}}{\text{viscous forces}} = \frac{\rho v d_0}{\eta} \quad (6.)$$

II. 2.3.2. Weber number

The two most important forces governing the breakup of drops are the disruptive aerodynamic force and the restorative surface tension force. Their ratio results in the non-dimensional Weber number:

$$We = \frac{\text{force of inertia}}{\text{surface tension}} = \frac{\rho v^2 d_0}{\sigma} \quad (7.)$$

The greater this ratio, the higher the tendency will be to breakup. Therefore the value of the Weber number can be used to characterize the mechanism of the breakup.

II. 3.3.2. Ohnesorge number

Another dimensionless number is the Ohnesorge number, which representing the ratio of drop viscous forces to surface tension forces. It describes the influence of viscosity in the system, which prevents the fluid from disintegration. If the value of the Ohnesorge number is lower than 0.1 , than the process of the breakup is assumed to be independent of Oh .

$$Oh = \frac{\text{friction force}}{\sqrt{\text{force of inertia} \cdot \text{surface tension}}} = \frac{\eta}{\sqrt{d_0 \rho \sigma}} = \frac{\sqrt{We}}{Re} \quad (8.)$$

II. 4.3.2. Bond number

The Bond number or Eötvös number represents the ratio of gravitational force to the surface tension force. It is used to investigate the behavior of drops and bubbles. For instance - according to Richter [1] - at a capillary outlet, the outflow of the liquid will occur if $Bo > 28$.

$$Bo = \frac{\text{gravitational force}}{\text{surface tension}} = \frac{\rho g d_0^2}{\sigma} \quad (9.)$$

II. 2. Different atomization types

II. 2.1. Droplet formations through desintegration of the jet flow

A liquid jet emanating from a nozzle into an ambient gas may break up into small drops when it is exposed to even minute disturbances. The disturbances can derive on the one hand from the supply system or on the other hand from the jet surface. Such disturbances are for instance pressure, velocity, temperature or surface tension fluctuations. All these actions transmit energy into the jet flow which causes the breakup. Basically the transmitted energy generates waves on the jet flow, which first falls apart into filaments and then into smaller droplets.

The starting point of the atomization, the resulted droplet shapes and droplet diameter distributions depend on plurality of parameters. *Figure 2* represents the mechanism of the different desintegrations with increasing pressure difference in the system. (a) Rayleigh breakup. Drop diameters larger than the jet diameter. Breakup occurs many nozzle diameters downstream of nozzle. (b) First wind-induced regime. Drops with diameters of the order of jet diameter. Breakup occurs many nozzle diameters downstream of nozzle. (c) Second wind induced regime. Drop sizes smaller than the jet diameter. Breakup starts some distance downstream of nozzle. (d) Atomization regime. Drop sizes much smaller than the jet diameter. Breakup starts right at the nozzle exit, according to [3].

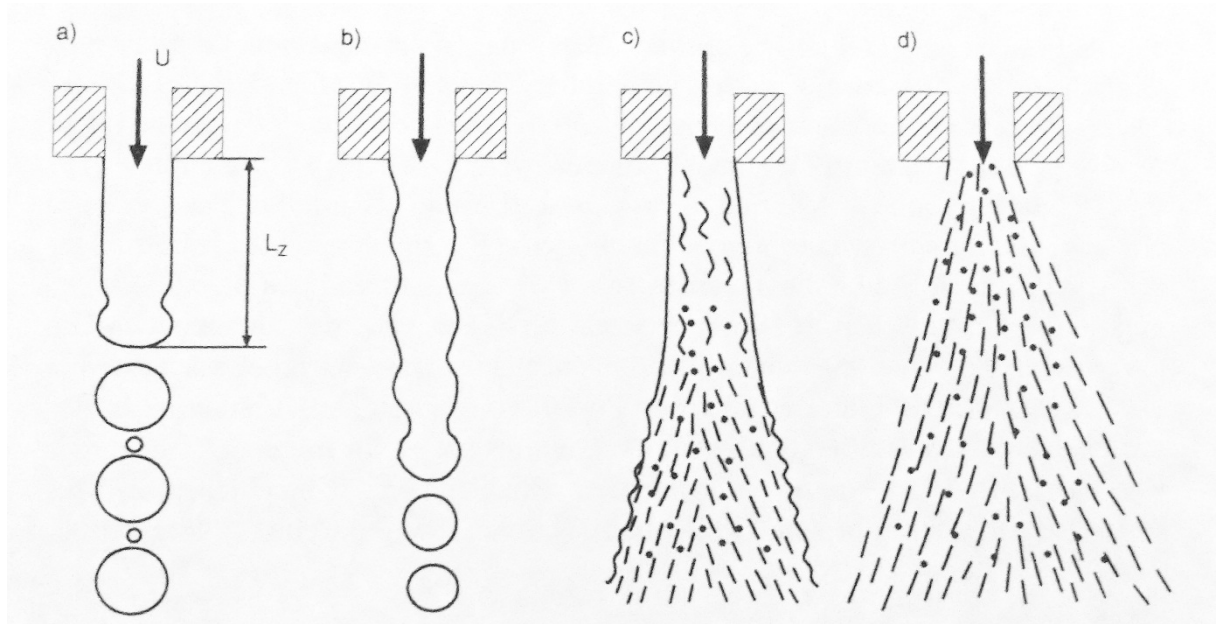


Figure 2: Atomization mechanisms, Figure source: [4]

Other mechanisms for droplet formations are for instance drip off, disintegration of liquid layers or secondary atomization. A comprehensive description about these mechanisms can be found under [4].

II. 2.2. Atomization of the droplet (secondary atomization)

The value of the Weber number as presented before (*Chapter I.1.3.2.*) has a high influence on the droplet breakup as presented in [2] chapter 6. As seen in *Table 1* and some examples of them in *Figure 3*. it is possible to group the different types of atomization with the help of the Weber number. The mentioned cases are just valid for Newtonian fluids with $Oh < 0,1$. At the outflow in a capillaries the critical value $We = 8$ of the Weber number, marks where the drip off transforms into a beam.

Vibrational (no breakup) ²	$0 < We < \sim 11$
Bag	$\sim 11 < We < \sim 35$
Multimode	$\sim 35 < We < \sim 80$
Sheet thinning	$\sim 80 < We < \sim 350$
Catastrophic	$\sim 350 < We$

Table 1: Weber number intervals [2]

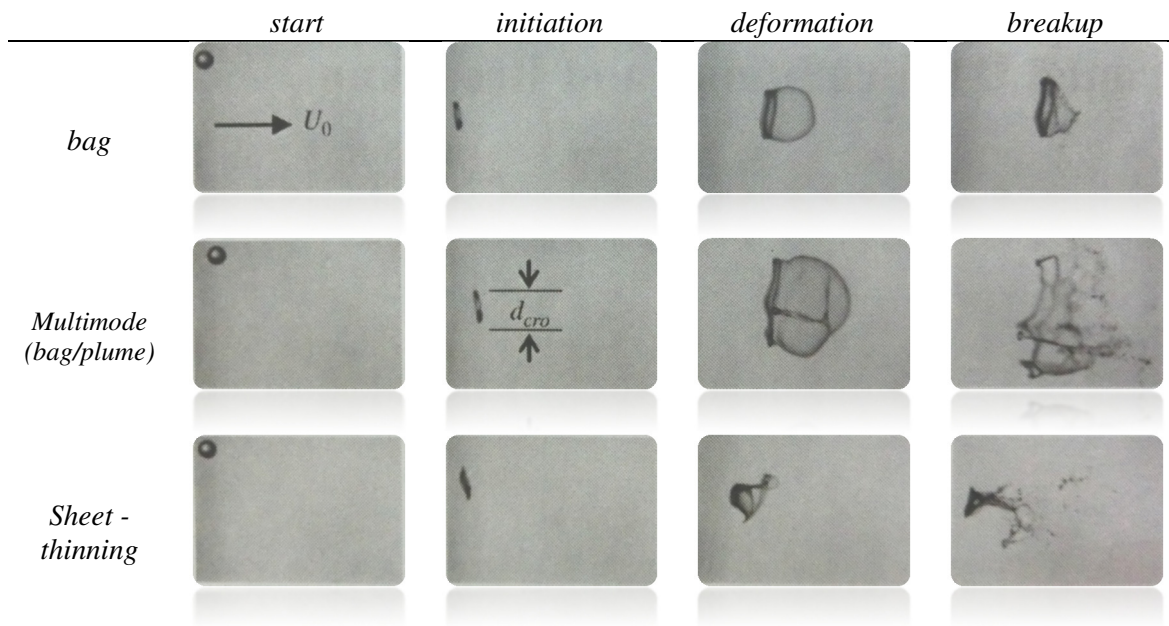


Figure 3: Deformation and fragmentation of the droplet at different breakup types [2]

II. 2.2.1. Deformation and vibrational breakup

If a spherical drop enters into a gas flow, aerodynamical forces will act on it, and try to fragmentize the droplet. First the forces lead to deformations, because the gas flow causes an unequal pressure distribution on the sphere shape. If the deformation reaches a certain level (the drag force will be greater than the surface tension force), fragmentation will occur. Against the aerodynamical forces and deformations the acting contra force is the surface tension, thus if the We number is low, the surface tension force will be able to restore the shape to a certain degree. The effect of these forces acting on the surface of the droplet against each other leads to the oscillation of the droplet. At times this oscillation can cause fragmentation. This phenomena is called the vibrational breakup. This breakup will not lead to the final small fragment sizes. The following figures, *Figure 5 – 7* were taken from [2] chapter 9.

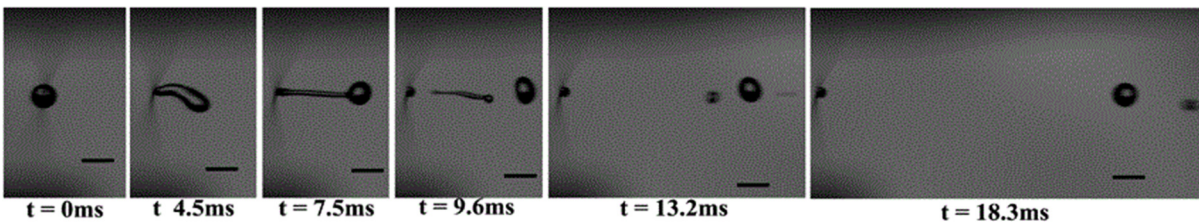


Figure 4: Deformation and vibrational breakup [2]

II. 2.2.2. Bag breakup

Bag breakup occurs at low We. It is the most favorable atomization because of the low specific energy demand. In this case the aerodynamic force causes a dominant positive pressure difference between the front and the back sides of the droplet. This is the reason, why the center of the droplet will be blown up to form a bag and the outer edge forms a toroidal ring which is attached to the bag.



Figure 5: Schematic illustration of the bag breakup [2]

After the breakup the ring fragmentizes in few larger pieces, not like the bag part, which is forming lots of small droplets. *Figure 5* represents the breakup process.

II. 2.2.3. Sheet-thinning breakup

Sheet-thinning breakup occurs at higher relative velocities (higher We) than bag breakup, and happens firmly different. After the initial deformation instead of a bag, a sheet shape will be formed. The sheet evolves into ligaments, which break up into smaller fragments. The process continues until the drop is completely fragmented,



Figure 6: Schematic illustration of the s-t breakup [2]

or until it has accelerated to the point at which aerodynamic forces are negligible. *Figure 6* also illustrates the breakup

II. 2.2.4. Multimode breakup

Multimode breakup is a combination of the sheet-thinning and bag breakup and occurs between the *We* values of the mentioned atomizing processes.

II. 2.2.5. Catastrophic breakup

In case of catastrophic breakup – *Figure 7* – the value of the Weber number is extremely high. The droplet atomizes into multitude of fine fragments because in this case unstable surface waves will appear on the deformed drop and develop, hereby causing the breakup. Practical applications of this breakup are limited because of the high velocities and energy demand.

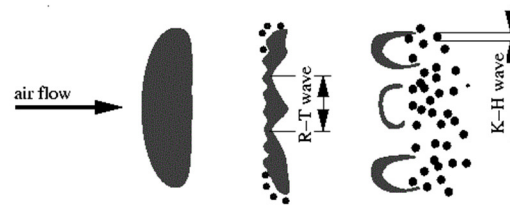


Figure 7: Schematic illustration of the cat. breakup [2]

Rayleigh – Taylor (R-T) and Kelwin – Helmholtz (K-H) instabilities are common models for the atomization. A comprehensive presentation about the models can be found in [2] chapter 9.

The classification – showed in *Figure 8* – can be more complex and it is possible to define more classes as introduced before. A more detailed mechanism of the breakup of the droplet can be found under [5] where the disintegration of a free falling droplet is investigated.

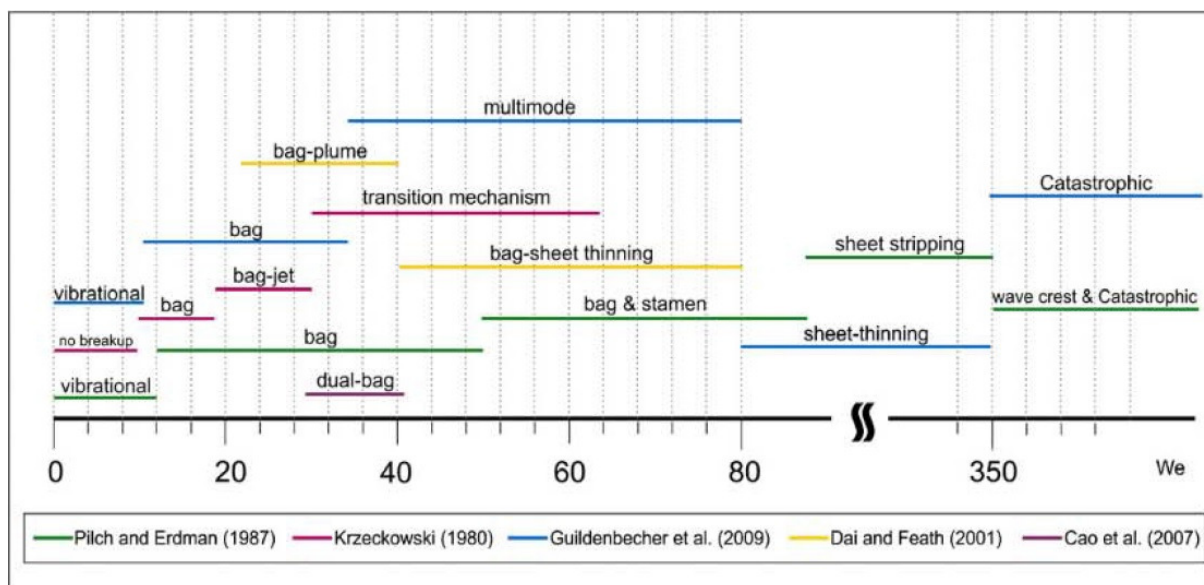


Figure 8: Classification of the different breakup mechanisms [5]

II. 2.3. Different atomizer designs

To obtain a spray from a contiguous liquid volume, energy is consumed. Depending on the process, different atomizers and nozzles are serving to deliver the necessary amount of it. The following and further atomizers are presented particularly by Wozniak in [4].

II. 2.3.1. Single-fluid nozzle

The most simple atomizer is the single-fluid nozzle, where the kinetic energy is transported with the fluid itself. These atomizers are also called pressure atomizers, because the mentioned kinetic energy, thus the high velocity of the fluid derives from the pressure applied to the fluid. Such atomizers are for instance the plain orifice nozzle and the swirl nozzle.

In the most common case of the plain orifice nozzle the set-up is a cylindrical part where the end of the nozzle outlet is structured like in the case of a capillar. The higher the pressure in the fluid, the closer the disintegration will start to the nozzle orifice.

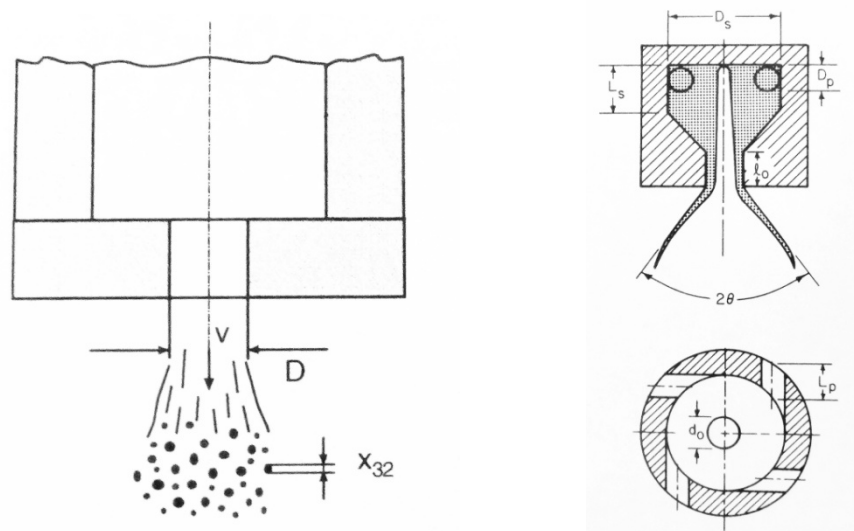


Figure 9: Schematic picture of plain orifice and the swirl nozzle [4]

In the case of the swirl nozzle as seen in *Figure 9* - which is also cylindrical - supply pipes are built in the prechamber where the fluid is inserted in tangential direction into the system, so it comes to high angular velocities which lead to an even fluid film on the inner surface of the cylinder. Also here the cylindrical form shrinks, and so the fluid accelerates. At the throat the fluid film becomes smaller until it leaves the nozzle and desintegrates. In the center of the cylindrical shape a gas channel is formed, which is useful for preventing possible choking in the system.

II. 2.3.2. Two-fluid nozzle

The energy for the atomization in two-fluid nozzles, as in *Figure 10* is transported by a secondary mass flow, in most of the cases a gas flow. The mixture of the two different flows can be realized internally or externally, thus after leaving the nozzle. In the case of an internal-mix nozzle the mixing of the fluids starts already in the so called prechamber or mixchamber, so the outflow at the nozzle outlet is yet a two-phase flow.

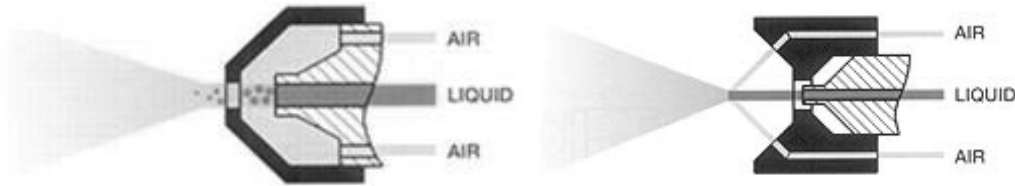


Figure 10: Schematic picture of internal- (left) and external- (right) mix nozzle [6]

II. 2.3.3. Mechanical atomizers

Rotary atomizers showed in *Figure 11* are atomizers where the energy is transmitted mechanically. This also has advantages and disadvantages, because the system – thanks to greater fluid profiles – withstands choking and it can work under low pressure, but therefore through permanent rotating, the mechanical load is high because of the centrifugal forces which may lead to erosion.

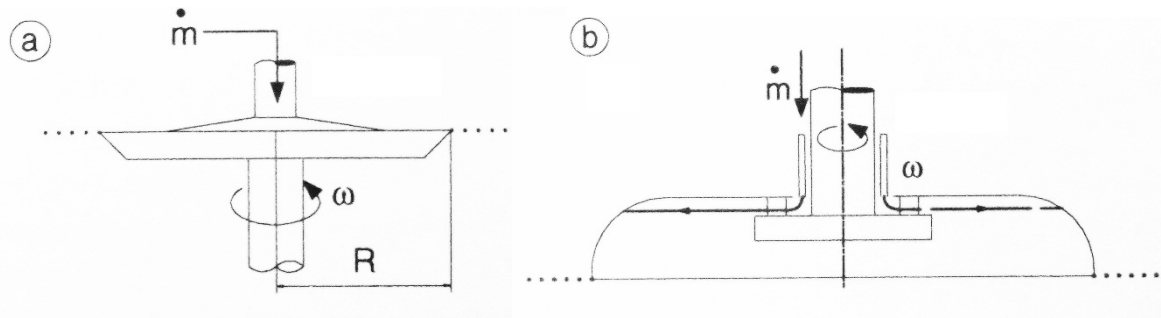


Figure 11: Schematic view of rotary atomizers (a) disc, (b) cup [4]

II. 2.3.4. Other atomizers

There are of course atomizers, where the functioning is based on other physical effects. Such atomizers are for instance ultrasonic or electrostatic nozzles. These and the described atomizers with single – fluid, two – fluid nozzles and the mechanical atomizer systems can be found under [7] and [4].

III. First example - atomization in a blast furnace

III. 1. Introduction of the blast furnace

A blast furnace illustrated in *Figure 12* is a type of metallurgical furnace which is used to produce different industrial metals by working the different ores off. Through smelting in the furnace, base metals are extracted from their ores by reducing the metal oxide content in the ore over chemical processes and melting the resulting metal, which trickles down and collects at the bottom. Such metals are for example iron, silver, copper, etc.

The used reductant is mainly coke, but there are also other alternatives, like fuel oil or natural gas. Because of the high price of the coke and the environmental restrictions which are becoming more restrictive from time to time, further optimizations and development is needed.

In our case we investigate the iron making blast furnace „A” from the company voestalpine Stahl GmbH. Here the smelting process takes place by using auxiliary reducing agents injected into the raceways in the coke bed. The oil flows in a pipe – so called oil lance – until it reaches the pipe outlet where it gets into the center of a larger tube, the Tuyere, shown in *Figure 13*, where it meets with the high velocity gas, the hot blast. At this point due to the high air velocities the atomization of the oil can start immediately. Because of the extreme ambient conditions (pressure, high temperature) the oil lance must be shielded which is achieved by an additional coaxial cover stream. It means, that the oil lance is covered with an additional surrounding coaxial pipe which carries superheated steam in the resulting ring gap. This concurrent flow has two functions, first it has a preheating effect to keep the oil viscosity low in the cold section of the lance and second it has a role in the cooling of the streaming oil so it prevents the baking of the oil in the lance.

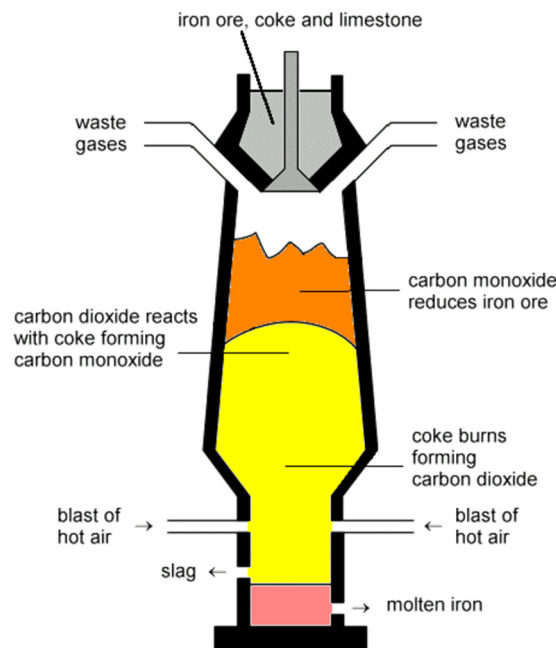


Figure 12: Schematic picture of the blast furnace [8]

III. 2. Presentation of the problem

III. 2.1. The goal of the investigation

One of the most important things of the smelting is the proper reaction of the reducing agents to supply energy and reducing species. In our investigated case heat and carbon monoxide are partially generated by burning the fed atomized heavy oil – air mixture as well as the coke surrounding the raceway. The circumstances of the feeding process are extreme. The ambient temperature is about $1200\text{ }^{\circ}\text{C}$ and the velocity of the multiphase flow is near 200 m/s . This part of the process is analyzed with the aim of reaching the ideal utilization of the two phase mixtures.

Resulting from the air injection in the ore – coke – mix, a cavity, so called raceway will be formed. In the sense of ideal oil usage, the proper atomized droplet size must be defined in such a way, that until the reaching of the end of the raceway, the reaction takes entirely effect. If the reaction is not totally accomplished, additional substances, like soot will appear in the system, which can easily lead to difficulties. This raises the most important questions:

- What is the optimal droplet size?
- How is it possible to obtain it?
- How is the droplet size influenced by the different parameters and settings?

To start with our exploration first we need to know how the process (feed, atomization, reaction) happens. In this thesis we will mainly concentrate on the investigation of the atomization with different atomization settings. It is not possible to accomplish any measurement under operating conditions at the nozzle, so a cold model test rig was constructed [9], [10]. Here the investigation of the atomization becomes feasible, because the ambient conditions are much better to achieve these measurements. Another advantage is that it will be possible to take a much closer look on the atomization effects itself because the test rig is built of plexiglas.

Similar measurements were already performed in the test rig by Zauner [10] and Kirchbacher [9]. An additional goal was to use different model fluids instead of paraffin oil like ethanol, water, glycerol - water mixtures to understand the atomization process in a larger viscosity interval.

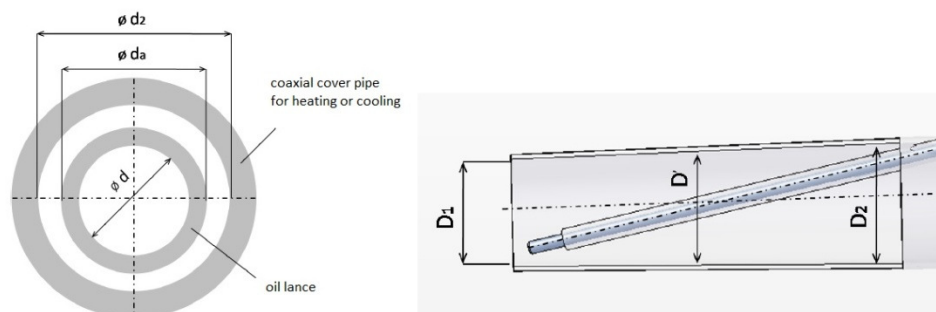


Figure 13: Diameter of the oil lance (left), Cover pipe and Tuyère (right) [10]

III. 2.2. Dimensional analysis – brief summary –

As it was mentioned before direct measurements at the nozzle exit respectively in the raceway is not possible so a scale down model test rig was constructed to investigate the sauter mean diameter (*SMD*). To find the proper operation settings for the model construction to accomplish the measurement, the dimensionless parameters of the system had to be calculated. For this reason, first dimensional analysis had to be applied. The analysis was carried out by Zauner and the details of the derivation can be found under [10]

The *SMD* or d_{32} is influenced by various factors. 13 parameters of influence were suggested by [10].

$$d_{32} = d_{32}(v_G, \rho_G, \eta_G, v_{oil}, \rho_{oil}, \eta_{oil}, v_C, \rho_C, \eta_C, \sigma, l, \alpha, \beta) \quad (10.)$$

Three properties (velocity, density and dynamic viscosity) are relevant in the case of the heated gas "G", which delivers the most energy for the atomization. They play a standard role also in the case of the atomized oil "Oil" and the axial cover streaming marked with "C". Other specifying parameters are the surface tension and the geometrical properties.

III. 2.2.1. Buckingham Pi - Theorem

With the help of the relevant parameters a correlation can be created for the investigated *SMD*. This correlation can be simplified with the help of the Buckingham Pi - Theorem. *Equation 10* can be written also:

$$f(d_{32}, v_G, \rho_G, \eta_G, v_{oil}, \rho_{oil}, \eta_{oil}, v_C, \rho_C, \eta_C, \sigma, l, \alpha, \beta) = 0 \quad (11.)$$

This can be also expressed as using the help of the dimensionless variables π_i :

$$F(\pi_1, \pi_2, \pi_3, \pi_4, \pi_5, \pi_6, \pi_7, \pi_8, \pi_9, \pi_{10}, \pi_{11}) = 0, \text{ or} \quad (12.)$$

In [10] the variables π_i have been identified like the following:

$$F\left(\alpha, \beta, \frac{d_{32}}{l}, Re_G, Re_C, \phi, Oh, \frac{v_G}{v_{oil}}, \frac{\rho_{oil}}{\rho_G}, \frac{\rho_{oil}}{\rho_C}, \frac{\eta_{oil}}{\eta_C}\right) = 0 \quad (13.)$$

As written by Herwig [11], the correlation, *Equation 11* – with n variables e_i , with the number of m basic physical dimensions, where e_l is the wanted variable –

$$f(e_1, e_2, \dots, e_n) = 0 \quad (14.)$$

can be represented in the form:

$$F(\pi_1, \pi_2, \dots, \pi_{n-m}) = 0 \quad (15.)$$

if:

- the variables e_i are linearly independent
- the equation $f(e_i)$ is valid independent from the units, wherein the variables e_i are specified.

It means that all the physical correlations between n variables can be simplified to a correlation with $n-m$ independent dimensionless variables. As in our case $n = 14$ and $m = 3$, the number of the independent dimensionless variables is 11 . So it can be used to search for the number of the relevant variables in the system, but what exactly the *Equation 11* looks like is another question and needs to be solved with other, for instance experimental, solutions. The detailed deduction about the dimensional analysis and the dimensionless parameters can be found in the thesis of Zauner [10].

III. 2.3. From the technical data to the lab model

Typical data about blast furnace voestalpine Stahl were provided by the blast furnace operate for the year 2009 from documents of the development team “Institute of Chemical Engineering – Research area Thermal Process Engineering and Simulation”. In the blast furnace both the nozzles single hole and multi hole were used for the atomization process, but in this thesis the measurements were based just on the atomization with the single hole nozzle.

After the dimensional analysis the defined dimensionless numbers and their correlations were known. The values of the dimensionless numbers of the blast furnace can be calculated by knowing the typical operating properties and geometrical data. This will deliver the operating conditions of the model test rig. The precise values of the dimensionless numbers could not be always realized at the model test rig, therefore the calculation involves restrictions and modifications. A brief overview about the model creation can be seen in *Figure 14*.

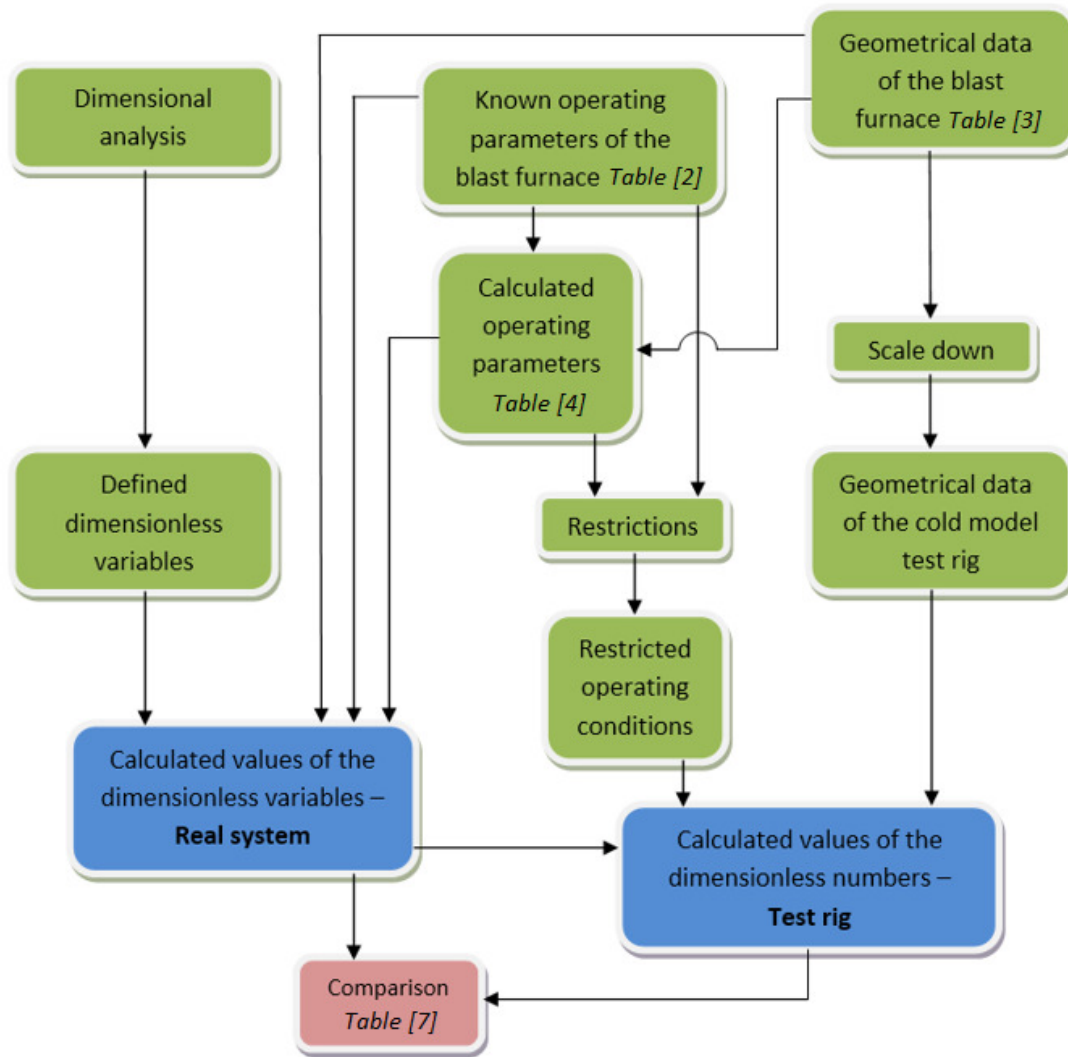


Figure 14: Flow chart of the created model test rig parameters

Operating parameters of the blast furnace (BFA, Voestalpine, Linz):

Gas velocity heated airflow	$v_{G,Tech} = 200 \text{ m/s}$
Absolute pressure heated airflow	$p_{G,Tech} = 5,1 \text{ bar}$
Temperature heated airflow	$T_{G,Tech} = 1220^\circ\text{C}$
Mass flow heavy oil	$\dot{m}_{oil,Techn} = 1200 \text{ kg/h}$
Viscosity heavy oil	$\eta_{oil,Techn} = 0,5 \text{ Pa} \cdot \text{s}$
Density heavy oil	$\rho_{oil,Techn} = 980 \text{ kg/m}^3$
Surface tension heavy oil	$\sigma_{Techn} = 0,035 \text{ N/m}$
Massflow superheated steam (coaxial cover stream)	$\dot{m}_{M,T} = 0,016 \text{ kg/s}$
Temperature superheated steam	$T_{C,Tech} = 170^\circ\text{C}$
Absolute pressure superheated steam	$p_{M,Tech} = 5,1 \text{ bar}$

Table 2: Operating parameters of the blast furnace [6]

Geometrical parameters of the nozzle (BFA, Voestalpine, Linz):

Angle of the nozzle axis	$\alpha_{Techn} = 12^\circ$
Angle of the jet outflow (relative to nozzle axis)	$\beta_{Techn} = 0^\circ$
Diameter of the outflow heavy oil	$d_{Techn} = 0,0126m$
Outer diameter of the oil lance	$d_{Techn}^a = 0,0172m$
Inner diameter of the cover pipe	$d_{2,Techn} = 0,0217m$
Tuyère inlet diameter	$D_{2,Techn} = 0,16m$
Tuyère outlet diameter	$D_{1,Techn} = 0,14m$

Table 3: Geometrical parameters of the nozzle [6]

Calculated operating parameters:

Velocity of the oil at the nozzle outlet	$v_{Oil,Techn} = 2,73 m/s$
Viscosity heated airflow	$\eta_{G,Techn} = 53,70 \cdot 10^{-6} Pa \cdot s$
Density heated airflow	$\rho_{G,Techn} = 1,19 kg/m^3$
Density superheated steam (coaxial cover stream)	$\rho_{C,Techn} = 2,6 kg/m^3$
Velocity superheated steam	$v_{C,Techn} = 45 m/s$
Viscosity superheated steam	$\eta_{C,Techn} = 14,8 \cdot 10^{-6} Pa \cdot s$
Middle diameter Tuyere	$D'_{Techn} = 0,15m$
Size of the ring gap	$s_{Techn} = 2,25 \cdot 10^{-3}m$

Table 4: Calculated operating parameters [6]

Calculated dimensionless parameters:

π_1	α	12
π_2	β	0
π_3	d_{32}/l	d/d_{32}
π_4	Re_G	664,804
π_5	Re_C	35,574
π_6	ϕ	$4,0 \cdot 10^{-4}$
π_7	Oh	0,076
π_8	v_G/v_{oil}	73,3
π_9	ρ_{oil}/ρ_G	823,5
π_{10}	ρ_{oil}/ρ_C	376,9
π_{11}	η_{oil}/η_C	12

Table 5: Calculated dimensionless parameters [6]

Calculated (restricted) operating parameters of the model test rig:

α	12°
β	0°
$v_{Oil,Mod}$	1,36 m/s
$\rho_{Oil,Mod}$	980 kg/m ³
$\rho_{C,Mod}$	2,6 kg/m ³
D'_{Mod}	0,077m
\dot{V}	0,466 m ³ /s
M	1:2
$v_{C,Mod}$	23,39 m/s
$\eta_{C,Mod}$	4 · 10 ⁻⁶ Pa · s
$\eta_{Oil,Mod}$	0,0135 Pa · s
σ_{Mod}	5,4 · 10 ⁻³ N/m

Table 6: Operating parameters of the test rig [6]

Comparison of the systems:

Variables	Real system	Model	Ratio
α	12	12	1
β	0	0	-
Re_G	664.804	500.000	1,33
Re_C	35.574	5362	6,63
ϕ	4,0 · 10 ⁻⁴	3,8 · 10 ⁻⁴	1,05
Oh	0,076	0,37	0,21
$\frac{v_G}{v_{Oil}}$	73,3	73,5	1
$\frac{\rho_{Oil}}{\rho_G}$	823,5	728	1,13
$\frac{\rho_{Oil}}{\rho_M}$	376,9	728	0,52
$\frac{\eta_{Oil}}{\eta_G}$	3378	8516	0,4

Table 7: Comparison of the real and the model operating conditions [6]

In the case of the ideal model, the value of all the ratios should be I . Because of the performed limitations on the model, some of the calculated values could not be realized, so the built model has some deviations from the ideal values. The applicability of the model can be verified on experimental ways. The values of the different variables were taken from Zauner [10]. The detailed calculations and the performed limitations, modifications on the model can be found also in [10].

III. 2.4. Evaluating the atomization

In most of the engineering applications at least two parameters are needed to describe the drop size distribution. In case of this polydisperse spray the goal is with each individual measurement to create a comprehensive evaluation as possible. This allows to compare the retrieved functions. The most common method is to represent the volumetric and numeric droplet size distributions, for the droplet size and there featuring parameters (mean diameter, representative diameters). The mentioned mean diameters, their applications and the representative diameters are listed in *Table 8*. To perform a comparison of the distributions, it is feasible to work only with mean or average diameters instead of the complete drop size distribution as written by Lefebvre [7]. The author also additionally compared the different distribution functions retrieved from the measurements, therefore the distributions are represented in percentage as in *Figure 16*.

a	b	Symbol	Name of mean diameter	Expression	Application
1	0	D_{10}	Length	$\frac{\sum N_i D_i}{\sum N_i}$	Comparisons
2	0	D_{20}	Surface area	$\sqrt{\frac{\sum N_i D_i^2}{\sum N_i}}$	Surface area controlling
3	0	D_{30}	Volume	$\sqrt[3]{\frac{\sum N_i D_i^3}{\sum N_i}}$	Volume controlling
3	2	D_{32}	Sauter (SMD)	$\frac{\sum N_i D_i^3}{\sum N_i D_i^2}$	Mass transfer, reactions

$D_{0.1}$ = drop diameter such that 10% of total liquid volume is in drops of smaller diameter

$D_{0.5}$ = drop diameter such that 50% of total liquid volume is in drops of smaller diameter

$D_{0.9}$ = drop diameter such that 90% of total liquid volume is in drops of smaller diameter

D_{peak} = value of D corresponding to peak of drop size frequency distribution curve.

Table 8: Mean diameters and their applications, representative diameters of the droplet [7]

The listed diameters are represented also in *Figure 15*. One of the parameters calculated from the representative diameters is the relative span factor which is:

$$\Delta = \frac{D_{0.9} - D_{0.1}}{D_{0.5}} \quad (16.)$$

It defines a direct indication of the range of drop sizes relative to the mass median diameter (MMD).

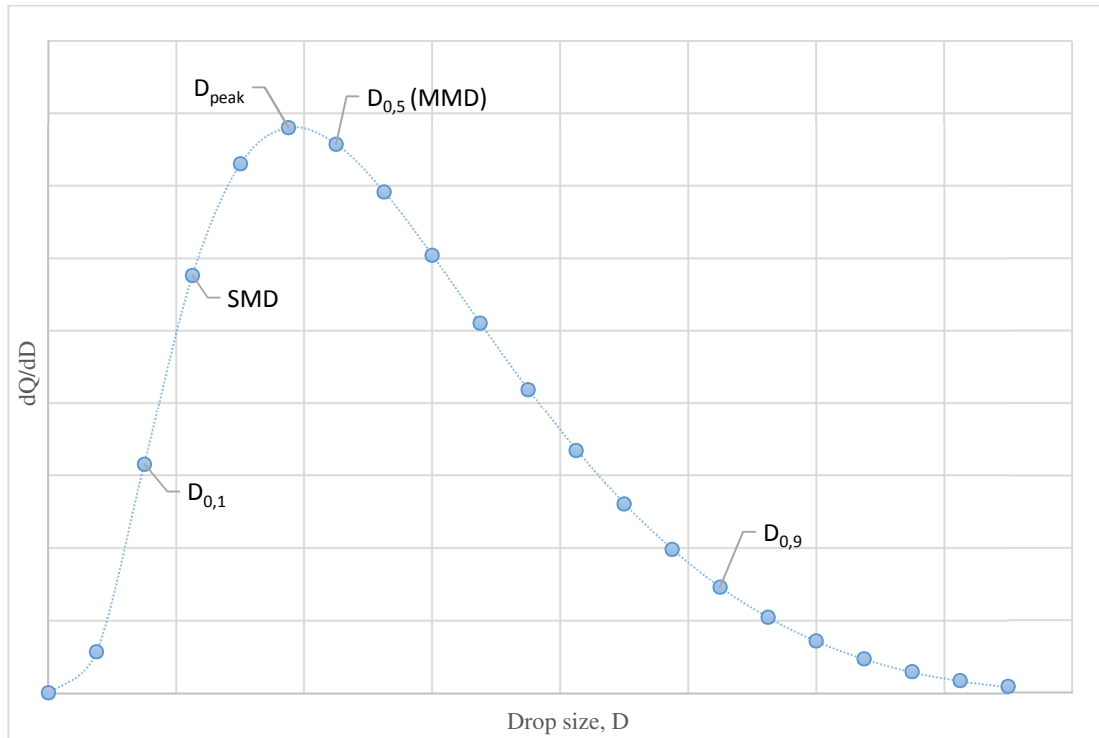


Figure 15: Comparison of the various representative diameters on a drop size distribution function

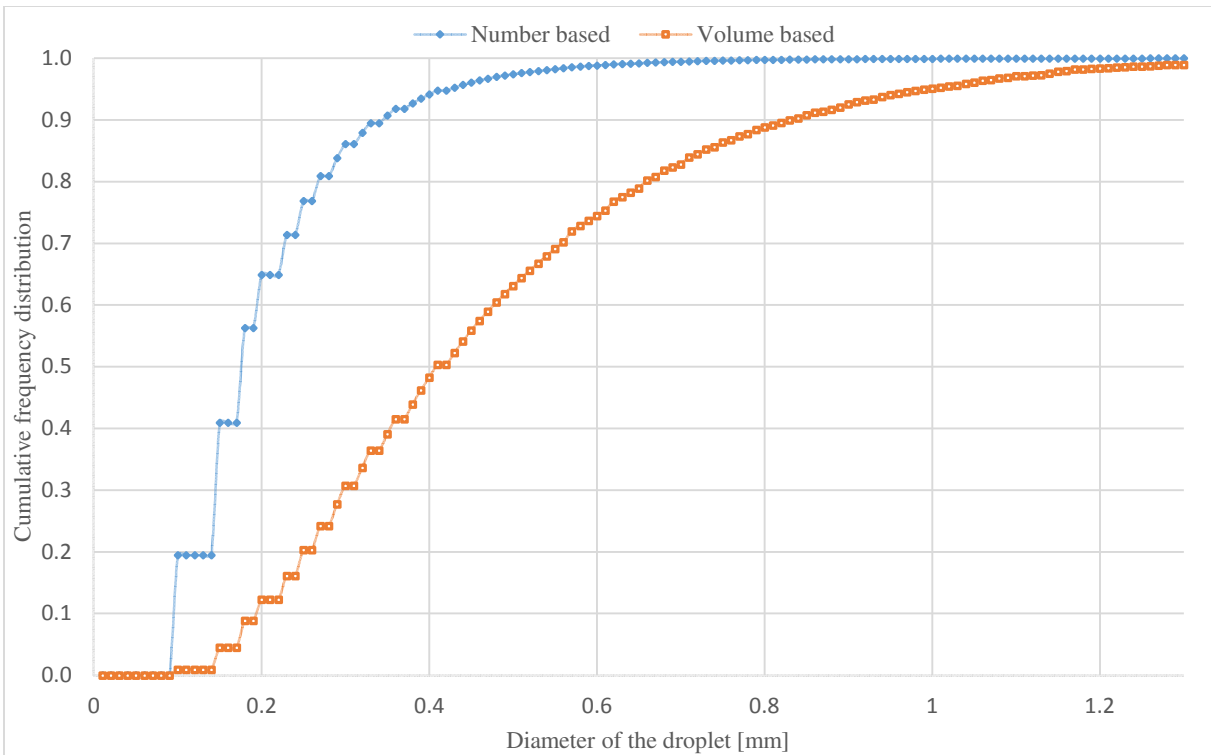
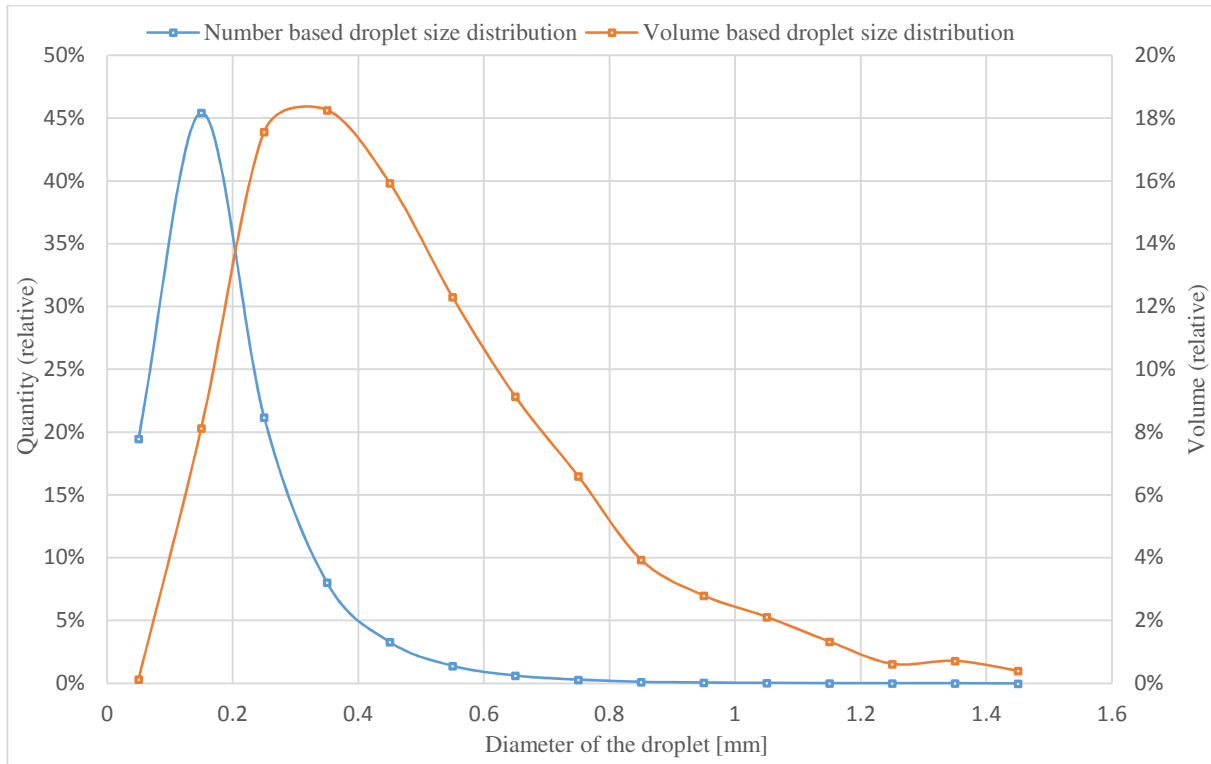


Figure 16: Distribution functions
 Volumetric and numeric drop size distribution in percentage (first), Cumulative frequency (second) (example)

III. 2.4.1. Calculation of the dimensionless numbers

In this part all the necessary dimensionless numbers were calculated for the measured operating conditions and these results were compared with the dimensionless values of the real operating conditions of the blast furnace.

In the first step all the physical and geometrical data were collected to accomplish the calculation as seen in *Table 20*.

<i>Marking</i>	<i>Appellation</i>	<i>Value</i>	<i>Unit</i>
d_{pr}	diameter of the Prandtl tube	0,082	m
d_m	medium diameter of the velocity profile in the air inlet tube	0,077	m
d_2	inner diameter of the cover stream supply tube	0,01	m
d_a	outer diameter of the nozzle	0,008	m
$d_h = d_2 - d_a$	diameter difference between the coaxial tubes	0,002	m
d_D	inner diameter of the nozzle	0,006	m
ρ_{Air}	density of the supplied air	1,205	[kg/m ³]
η_{Air}	dynamic viscosity of the supplied air	$1,82 \cdot 10^{-5}$	[Pas]

Table 9: Properties of the single hole nozzle and the supplied air [10]

The only missing information to calculate the dimensionless numbers is the mass flow and the velocity of the used fluid. This can be easily calculated from the characteristic curve of the pump, which is according to [9]:

$$\dot{V} = \frac{0,0192 \cdot P_p^2 + 0,4163 \cdot P_p + 3,1515}{10^6} \quad (17.)$$

With the mass flow of the oil also the oil inlet velocity can be calculated:

$$v_{Fluid} = \frac{\dot{V}_{Fluid}}{d_D^2 \cdot \frac{\pi}{4}} \quad (18.)$$

The incoming air velocity will be defined with the pressure difference measured with the Prandtl tube in the inlet. Regarding the velocity profile the formula will be extended and so the average air velocity $v_{G,a}$ can be calculated:

$$v_{G,a} = \frac{v_G \cdot d_{Pr}^2 \cdot \frac{\pi}{4}}{d_m^2 \cdot \frac{\pi}{4}} = \frac{\sqrt{\frac{2 \cdot \Delta p_{Pr}}{\rho_G}} \cdot d_{Pr}^2 \cdot \frac{\pi}{4}}{d_m^2 \cdot \frac{\pi}{4}} \quad (19.)$$

With these values the dimensionless number as the Reynolds number at the inlet is:

$$Re_G = \frac{\rho_G \cdot v_{G,m} \cdot l_G}{\eta_G} \quad (20.)$$

Reynolds number at the covering coaxial stream:

$$Re_M = \frac{\rho_G \cdot \left(\frac{4\dot{V}_M}{(d_2 - d_a)\pi} \right) \cdot l_M}{\eta_G} = \frac{\rho_G \cdot \left(\frac{\dot{V}_M}{A} \right) \cdot l_M}{\eta_G} = \frac{\rho_G \cdot v_M \cdot l_M}{\eta_G} \quad (21.)$$

The Ohnesorge number:

$$Oh = \frac{\eta_{Fluid}}{\sqrt{\rho_{Fluid} \cdot \sigma_{Fluid} \cdot l_{Pump}}} \quad (22.)$$

And finally the Weber number:

$$We = \frac{\rho_{Fluid} \cdot v_{Fluid}^2 \cdot l_{Pump}}{\sigma_{Fluid}} \quad (23.)$$

For calculating the dimensionless values characteristic length listed in *Table 10* were chosen:

Re_G	l_G	d_m
Re_M	l_M	d_h
Oh, We	l_{Pump}	d_D

Table 10: Characteristic lengths

III. 3. High speed camera measurements

To record the atomization process a Photron Fastcam SA 3 high speed camera was used. The retrieved images from the measurement were evaluated with the freeware ImageJ [12].

Basically the illuminated cross sections of the atomized droplets were recorded for one second and with the help of the software, the surface and the amount of each different surface sizes could be calculated. From the calculated surfaces the diameters of the nearly round droplets could be computed. With the obtained information the searched distributions for each individual measurement could be created.

III. 3.1. The buildup of the model and the measurement system

With the information retrieved from the dimensional analysis (showed in *Chapter III.2.3.*) the test rig respectively the measurement system – *Figure 17, 18* – looks the following:

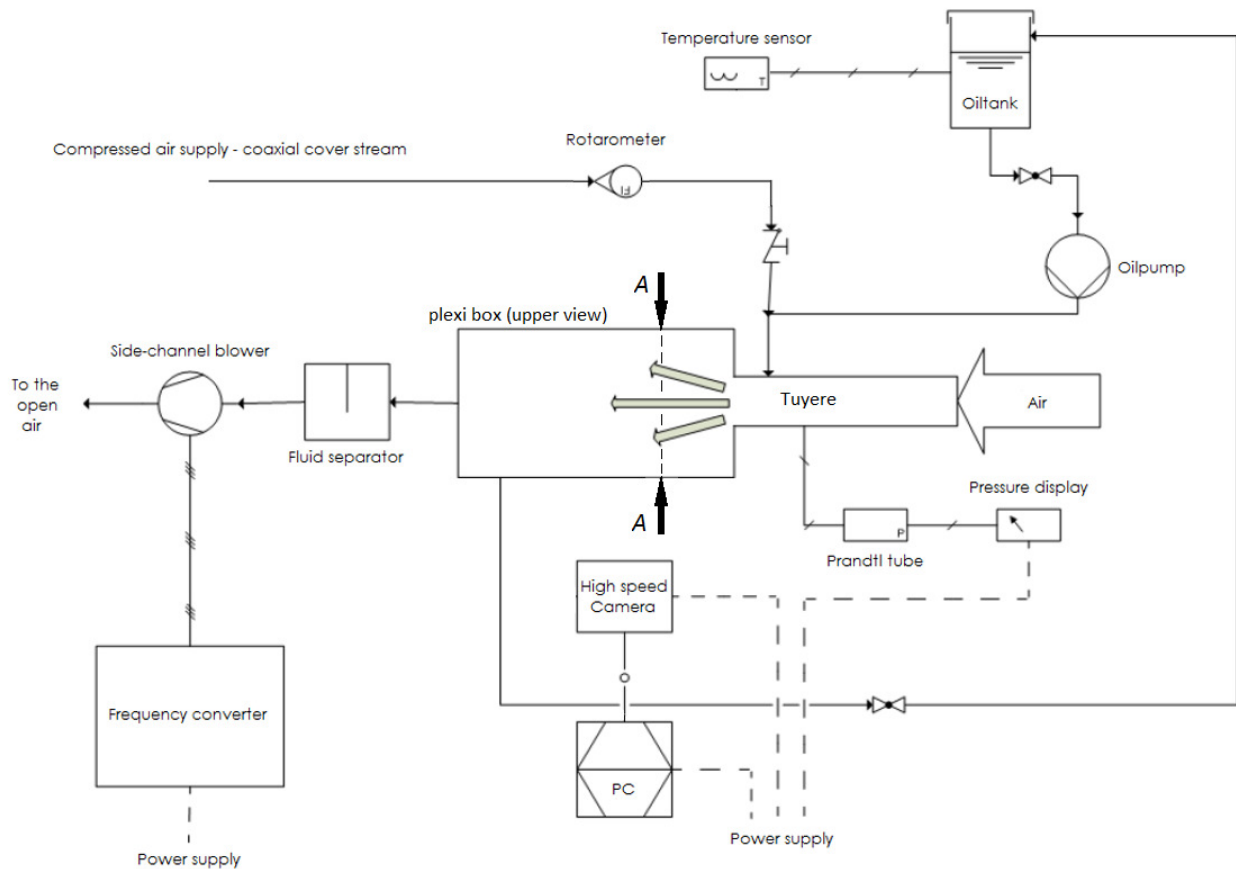


Figure 17: Schematic picture of the high speed measurement system

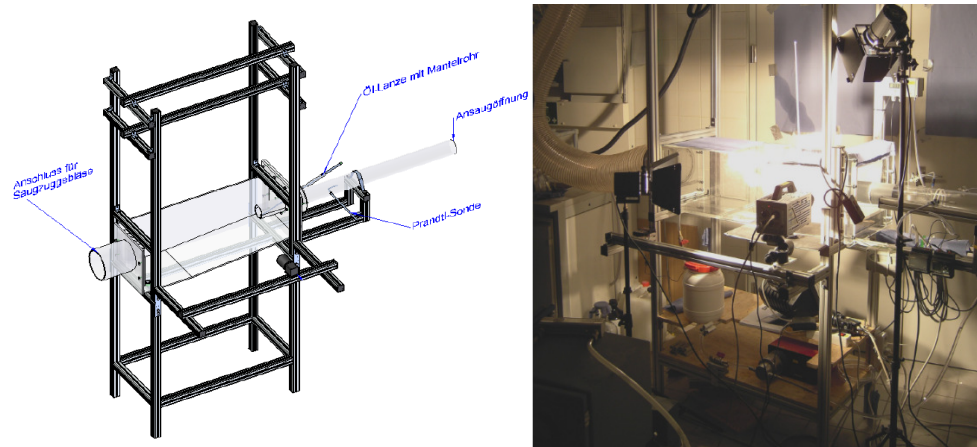


Figure 18: Model and the high speed measurement system Source: Zauner [10]

III. 3.2. Technical equipment

The measurements were achieved with the equipment listed in *Table 11*. The Redlake MotionPro HS cam listed in the table was not sufficient enough to create the required image quality so the camera was replaced.

<i>Side channel blower:</i>	Creative Blower Austria, Model FJET 1K11 DS/22/2
<i>Frequency converter</i>	Danfoss, VLT HVAC Drive FC100
<i>Filter bin</i>	Air-Fresh-Service Industriefilter GmbH, FMN-V12
<i>Fluid pump</i>	Verder, Model 2035
<i>Hightspeed Camera</i>	1. Redlake Motion Pro 2. Photron, Fastcam SA-3, Model 120 K-M11
<i>Other measurement equipments</i>	<ul style="list-style-type: none"> · Temperature sensor · Digital barometer · Dynamic pressure sensor · Rotameter (air)
<i>Illumination</i>	<ul style="list-style-type: none"> · Halogen reflector lamps 1000 W (2x)

Table 11: Technical equipments

III. 3.3. Process of the measurement

After proper cleaning of the rig, checking the measurement devices and setting the appropriate adjustments, the measurement system was ready to start.

First the blower was started to generate the required air velocity in the induction pipe – Tuyere – which could be adjusted with the frequency converter at the channel blower motor and controlled with the differential pressure sensor in the induction pipe. After starting the blower and setting the needed pressure difference – respectively the velocity – the reflectors were turned on. Because of the high frame rate and even higher shutter speed the necessary light intensity rises strongly. Two reflectors (each with 1000 W power) were used to satisfy this demand. It is important to use the reflectors for the shortest time possible, because the produced heat could melt and deform the walls of the model rig and also warm up the circulated, atomized fluid. The change of the temperature will affect the viscosity and the surface tension, respectively the atomization. In this case as in the section view (image section A – A taken from the schematic picture of the system in Figure 17) showed on *Figure 19* both of the reflectors were installed next to each other right above the upper plexiglas in a way that most of the light is concentrated in the recorded spot.

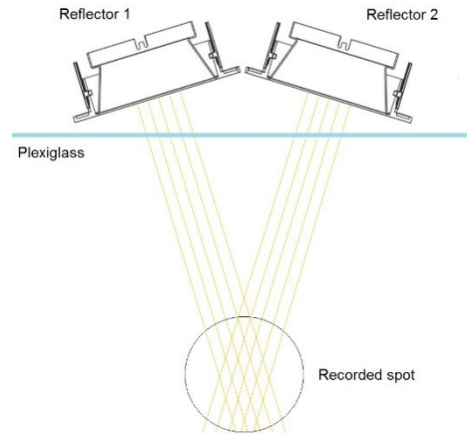


Figure 19: Setup of the reflectors A - A

In the next step the pump will be turned on to deliver the fluid to the nozzle and start the atomization. Right after the turning on the recording starts and last for few seconds.

After finishing the recording, everything – starting with the reflectors – will be shut down. During the recording atomized fluid will appear also on the side plexiglas walls, strongly reducing the recorded image quality, so the next step is to pick out the most usable part of the recorded video and save it. Because of the mentioned droplets appearing on the plexiglas walls a wiper was built in to the box to clean the walls between the measurements.

If the pause between the measurements is short, the atomized fluid can accumulate at the bottom of the rig, because it has no time to run off. The measurement should stop until the rig is completely empty. Because of the strong suction and the imperfect fluid separator - mostly in the case of high velocities - the tube of the side channel blower carried some of the atomized fluid along, which stuck in the system and lowered the efficiency of the blower. That is why the same (re)adjusted frequency on the frequency converter does not result in the same pressure difference as later in *Table 16, 17, 18*.

After the measurement all the following parameters were registered:

- Ambient temperature
- Temperature of the atomized fluid
- Set point of the frequency converter
- Pressure difference at the inlet – Tuyere – to calculate inlet velocity
- Velocity at the induction pipe as reference for lower velocities
- Power of the fluid pump
- Volumetric flow of the cover stream (air)
- Settings of the high speed camera
- Possible changes

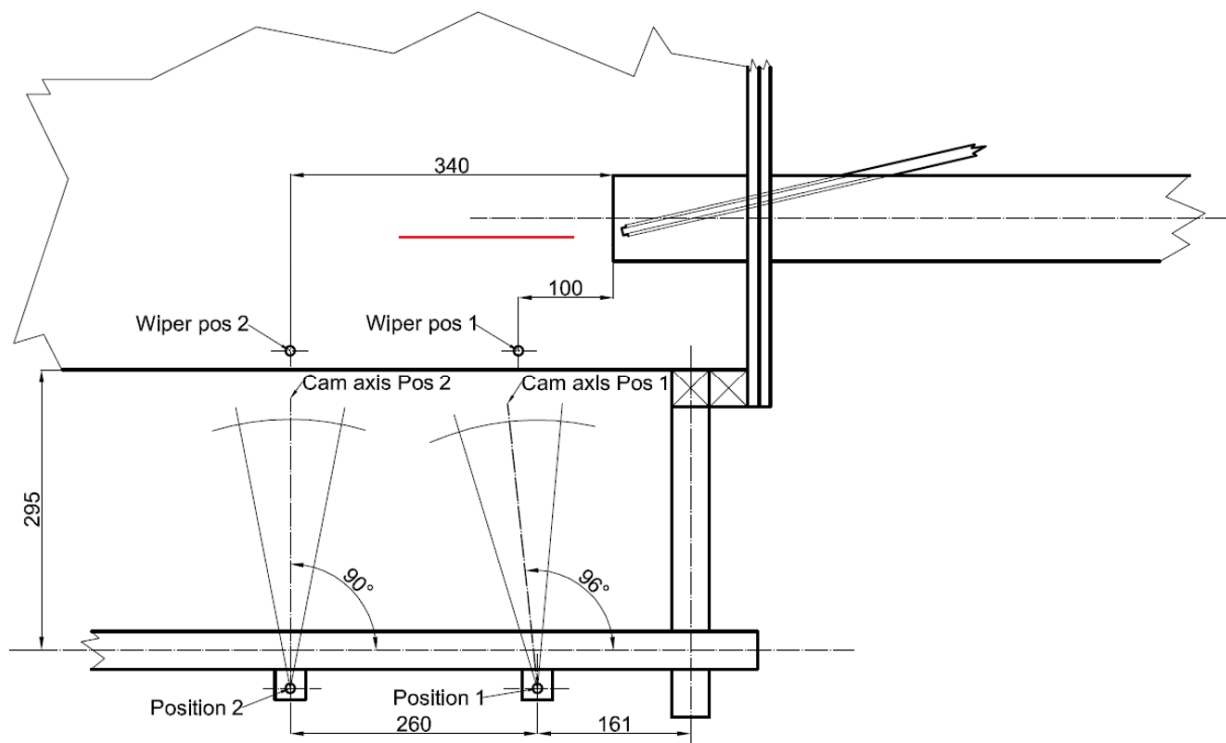


Figure 20: Mounting positions of the HS camera (front view)

Except very few cases – which are marked – all the videos were recorded with the settings listed below. In *Figure 20* also the exact position of the L profile is described where the camera fastening system, respectively the HS camera was mounted. The figure represents a part of the top-view of the arrangement.

- Frame rate: *1000 fps*
- Resolution: *1024x1024 pixel*
- Shutter speed: *100 kHz*
- Aperture: maximal closed
- Lens settings: *5,6*

- Position: Position 1
- Focus plane: $\sim 6^\circ$ angle with the calibration plate (*Chapter III.3.4.*) for Position 1

III. 3.4. Calibration of the measurement

For the pixel calibration of the high speed camera millimeter paper was used as showed in *Figure 21*. The paper attached to a quadratic plexiglas plate was positioned into the symmetry plane of the Tuyere with the help of a metal stick. After the adjusting the lens settings for this focus plane the correct size of the recorded surface will be known. With the settings used the resolution of the recorded image is 1024×1024 pixel on the focused 90×90 mm surface. This means, that on the recorded image the size of one pixel is $0,088$ mm and the resolution of one millimeter is $11,38$ pixel. With other words one pixel is equal to a surface of $0,00772$ mm². The approximate position of the calibration plate is showed in *Figure 20* by a red line.

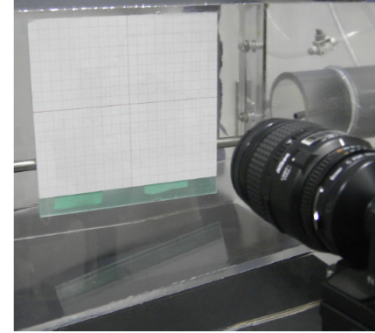


Figure 21: Calibration plane [10]

III. 3.5. Validation with different sugar classes

Before carrying out all measurement also a calibration was achieved by blowing sugar particles into the system, simulating the droplets. The idea behind this procedure is that the size distribution of the sugar particles was already known –measured through a sieve analysis – and it could be compared with the measured size distribution.

<i>Sugar classes</i>	<i>Pressure difference [mbar]</i>	<i>Frequency [Hz]</i>	<i>Quality</i>
crystal sugar (normal)	17	30,6	good*
crystal sugar (fine)	17	30,6	sufficient*
castor sugar	17	30,6	poor*
sieved sugar 0,8	17	30,6	good*
sieved sugar 0,5	17	30,6	poor*

Table 12: Validation using sugar

III. 3.5.1. Adjustment of the data processing

For the proper data processing first the values of the different settings in ImageJ (circularity, size, etc...) are needed. To find these optimized settings the measurement should be accomplished in a way that the distribution function of the particles blow into the model raceway is already known. Using this procedure we can adjust the settings of ImageJ until we get close to a known the original distribution function of the used particles.

For this reason sugar particles were used. The distribution function of the sugar particles were measured before the measurement in a different way, by applying a sieve analysis.

With the help of this analysis the search for the most favorable settings in the data processing can start until the result of the processing becomes the ideally same, or at least gets close to the actual distribution measured by the sieve analysis. For this validation the Author used five different sugar fractions listed in *Table 12*. The results of the sieve analysis are shown in *Figure 22*.

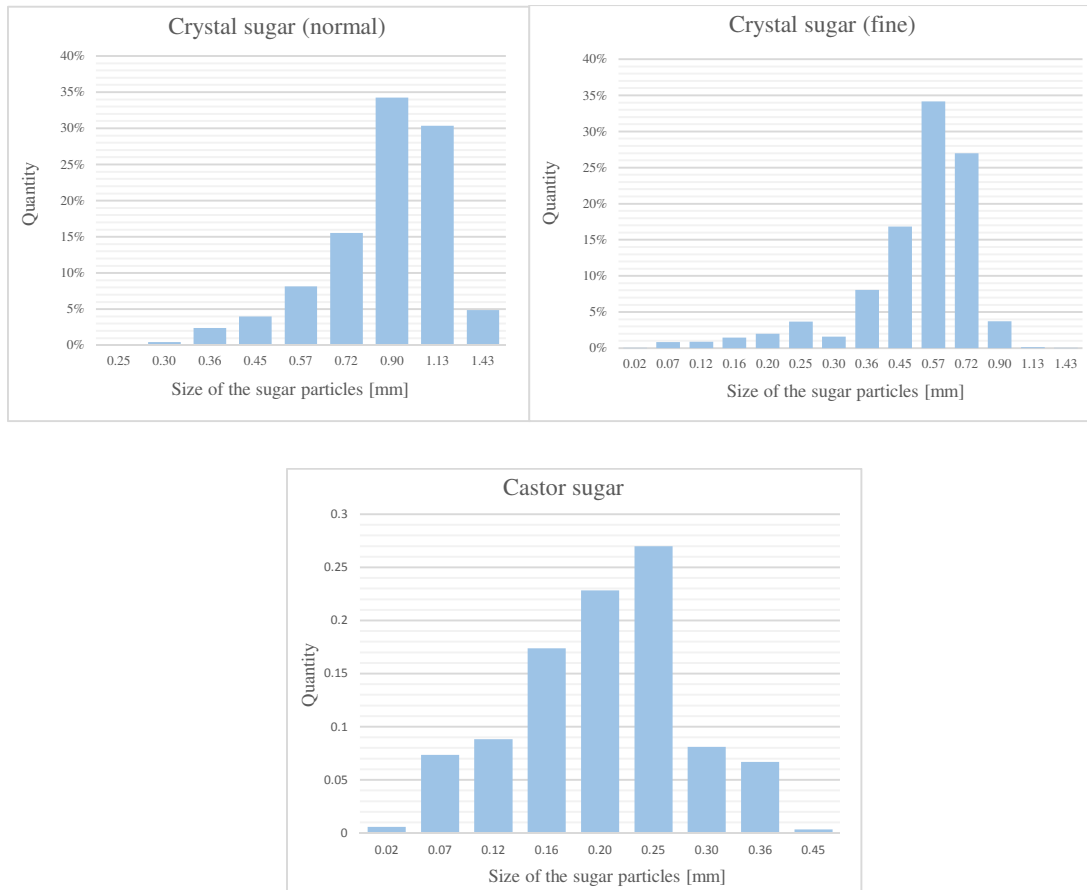


Figure 22: Distributions of the different sugar fractions (sieve analysis)

III. 3.5.2. Results with sugar used as reference

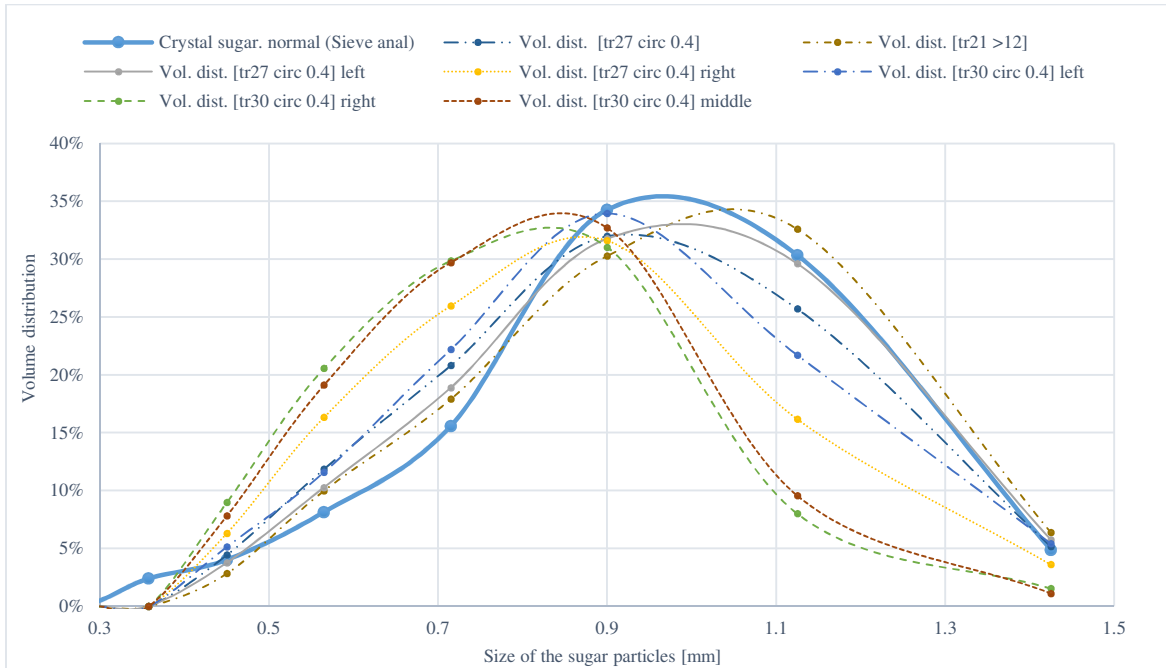


Figure 23: Comparisons of the different evaluations for normal crystal sugar

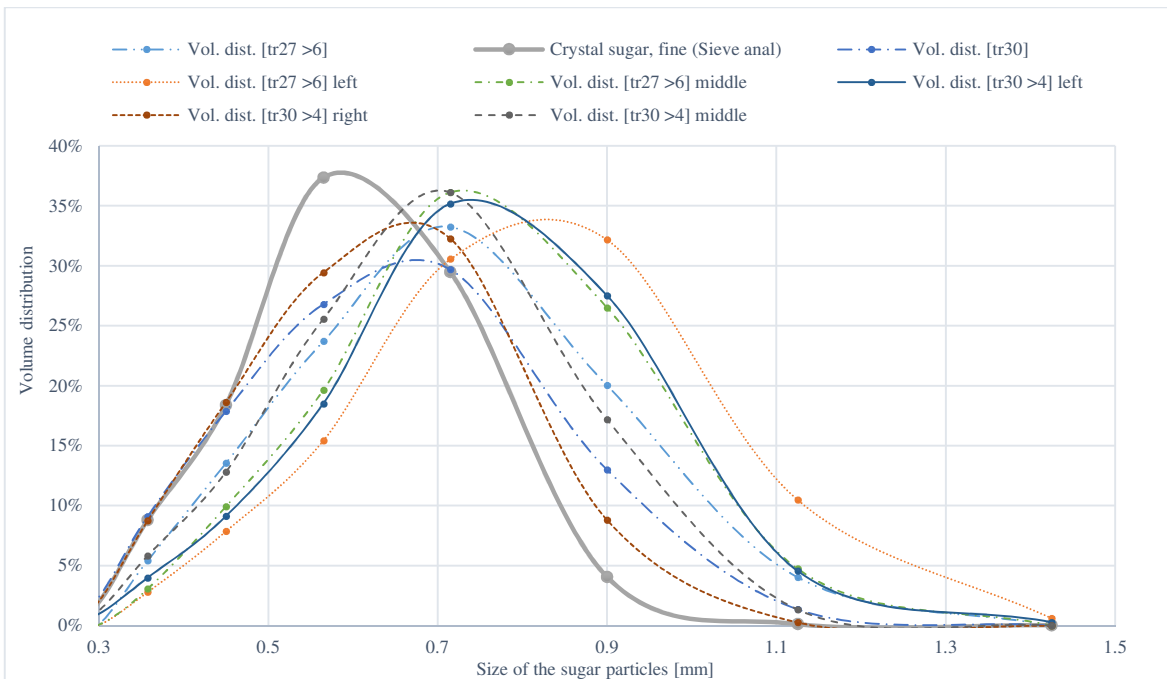


Figure 24: Comparisons of the different evaluations for fine crystal sugar

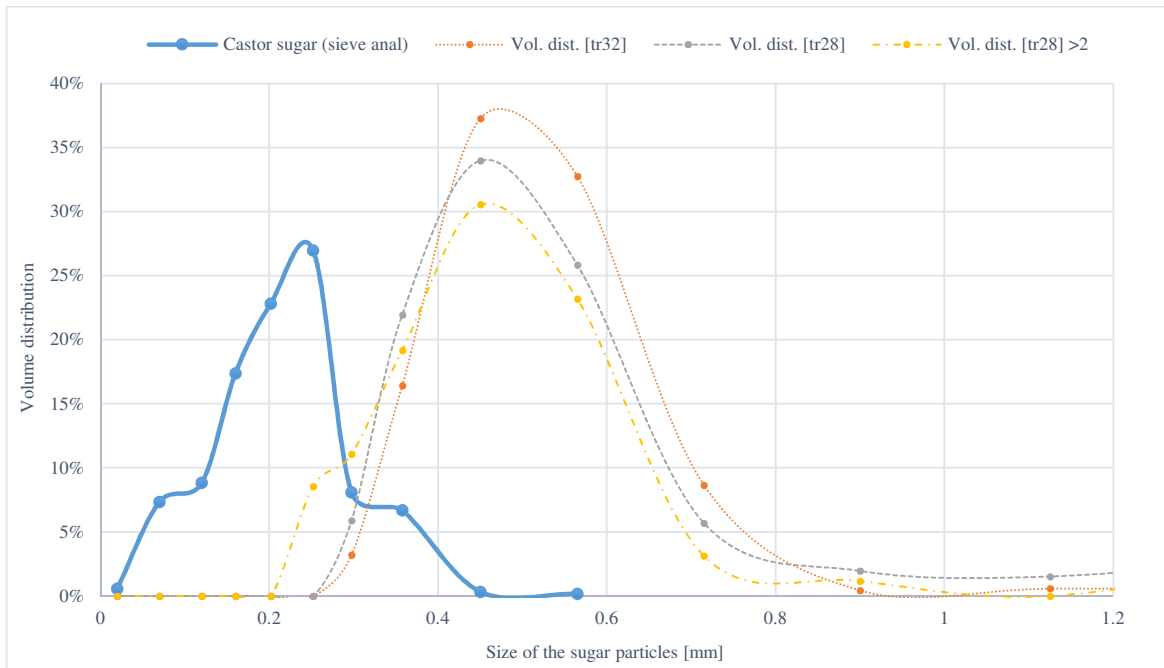


Figure 25: Comparisons of the different evaluations for castor sugar

The result shows in *Figure 23, 24, 25* that the evaluation becomes more inaccurate and difficult if the size of the sugar particle size decreases. In the case of the normal sugar, the data processing provides almost the same distribution function with the right settings, but in the case of the castor sugar where the sugar particles are very small, the two differently obtained functions are far from each other. As shown in *Figure 25* the measured value of the SMD is almost the double of the real value, but the characteristic of the function is nearly the same, especially in the case of $[tr28] > 2$.

In the data processing there are four important settings (also marked in the diagrams):

- Threshold level – „ [tr32] ”
- Position of investigated/cut area – „ left ”
- Circularity – „ [circ 0.4] ”
- Size filtering – „ >2 ”

These settings have advantages and also disadvantages in the case of different particle size intervals, but to create comparable results we need to find only one setting, a compromise for all the measurements which is working acceptable in the small and also in the large particle range.

Most of the times for the position of the investigated area the top left corner worked as the best. The lighting of the image was weakly depending on the amount of the atomized fluid, so the size of the top left corner was moving between 400×400 and 700×700 pixel.

After the different evaluations two adjustments were chosen:

	<i>Adjustment 1</i>	<i>Adjustment 2</i>
<i>Investigated area</i>	Top left corner	Top left corner
<i>Threshold level (ImageJ)</i>	26	26
<i>Circularity (ImageJ)</i>	0,5	0,5
<i>From the evaluation excluded particles „size”</i>	particles under 4 pixel	nothing was excluded

Table 13: Final adjustments for the data processing

III. 3.6. Processing of the obtained data

To get to the final distributions, the videos respectively the individual images for every measurement must be evaluated. For the processing of the pictures first the open source program ImageJ [12] (Image processing and analysis in Java) then Microsoft Excel was used for statistical evaluation.

To analyze the drops on the recorded image, first it must be edited. The picture package for one measurement becomes manageable after creating a stack, because the edition will have an effect on all the pictures included in the stack. In order to analysis the picture effectively, the most advantageous zone has to be taken into consideration. This part will be cut out [Image/Adjust/Canvas Size] and depending from its position respectively its brightness level the proper threshold level will be adjusted [Image/Adjust/Threshold Level/B&W]. The steps are illustrated also in *Figure 27, 28*.



Figure 26: Main steps of the data processing

After the edition the particle analysis can start [Analyze/Analyze Particles]. With the settings „size” and „circularity” the unwished particles (strongly deformed particles, non-atomized filaments, to large particles or other disturbances in *Figure 29*) can be removed from the evaluation.

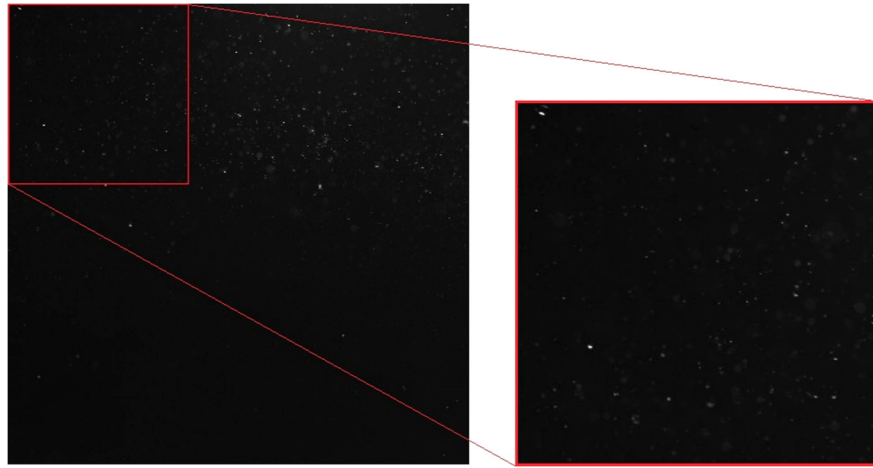


Figure 27: The analyzed part (1024x1024 cropped to 400x400 - upper left)

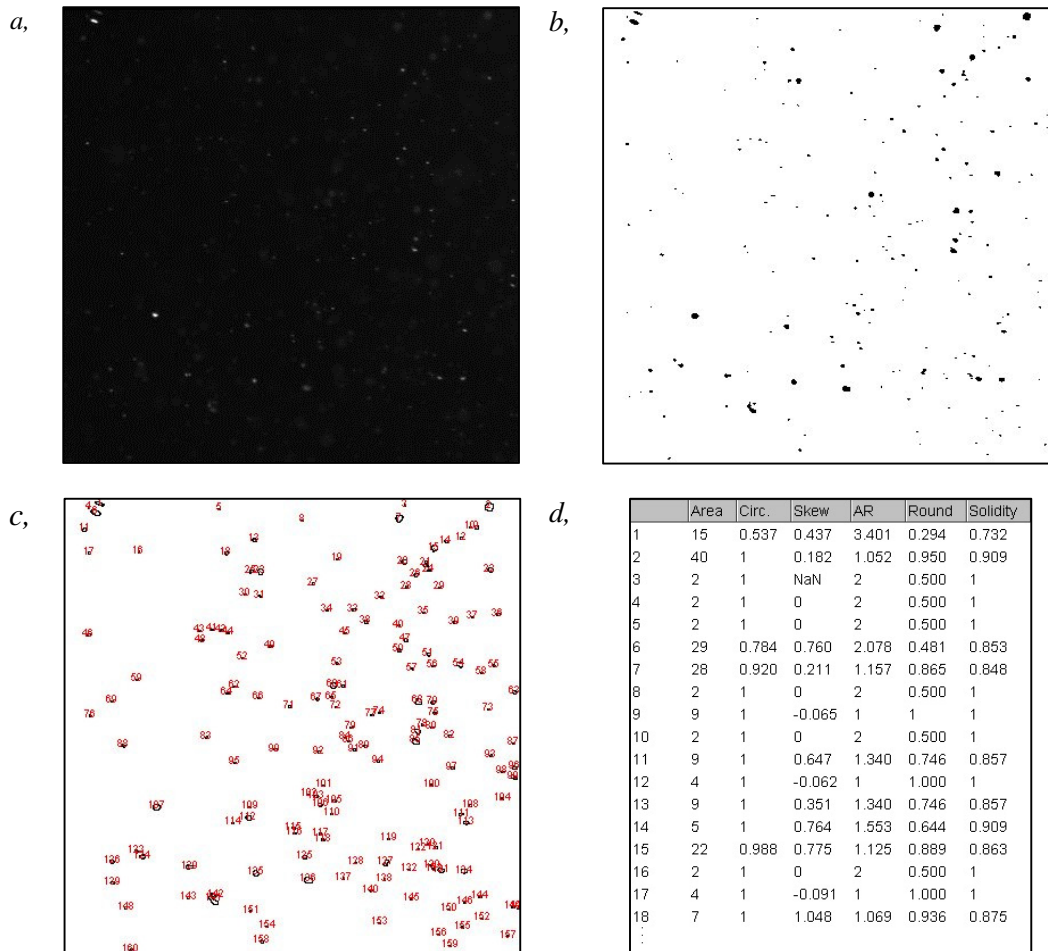


Figure 28: The basic steps of the analysis; results.

a, Cropped picture b, Adjusted threshold level c, Counted droplet surfaces d, Listed results

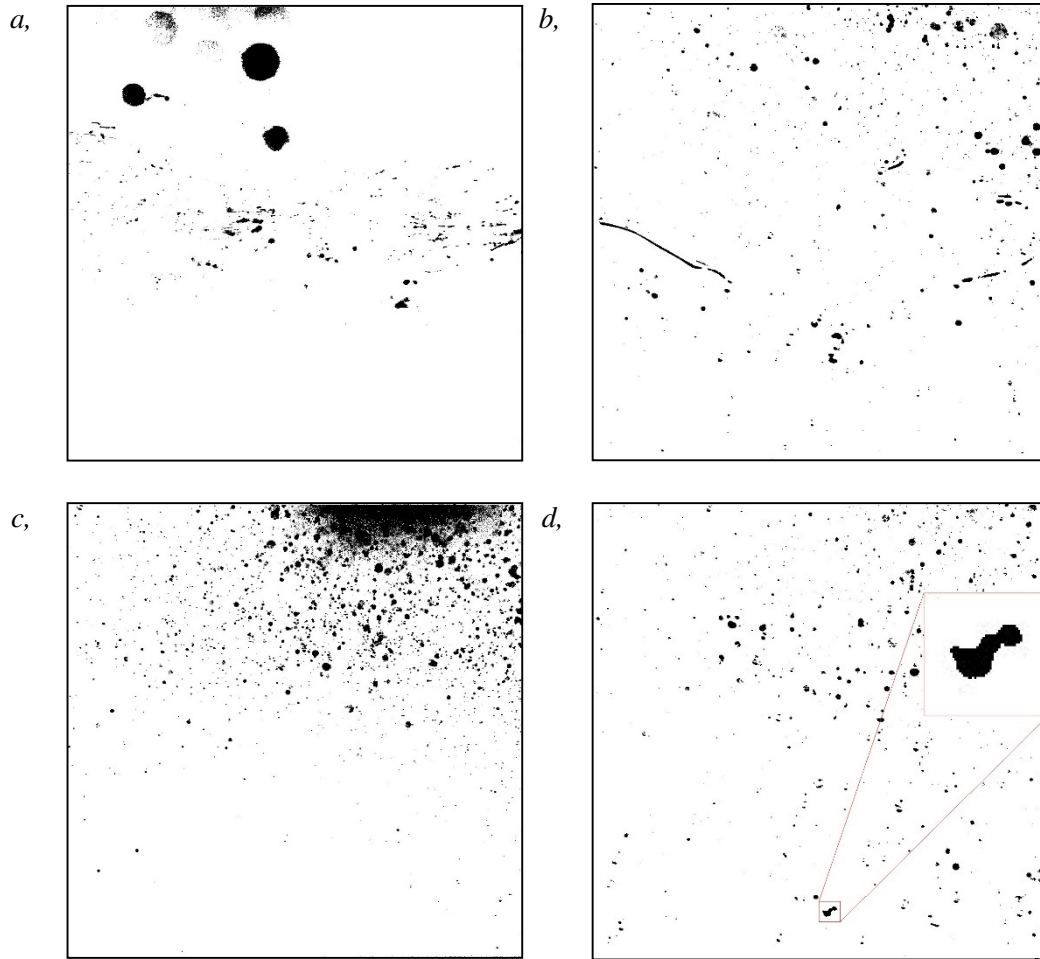


Figure 29: Disturbances and undesired results (examples).
 a, drops on the plexiglas b, filaments because of the high viscosity
 c, small left over particles from low threshold level d, deformed or combined particles

In the last step the obtained table of results can be easily inserted into a prepared Microsoft Excel table which creates all the necessary distribution functions and calculates the wanted values using just the source „Area”. The Area column in *Figure 28d* shows the amount of pixels contained by one recorded droplet. This is the main information for the statistical evaluation in Microsoft Excel. The mentioned Excel was used to evaluate using the correlations presented in *Chapter III.2.4*. The distribution functions are calculated for five different bin size resolutions, $d = 150\mu$, 100μ , 75μ , 50μ , 25μ . In the thesis the results are presented only with the $d = 100\mu$ bin size resolution, because this way the functions fitted well. The table with all details and all the distribution and probability functions can be found in the electronic appendix with all the used resolutions. The most important steps of the table are presented in *Figure 30*.

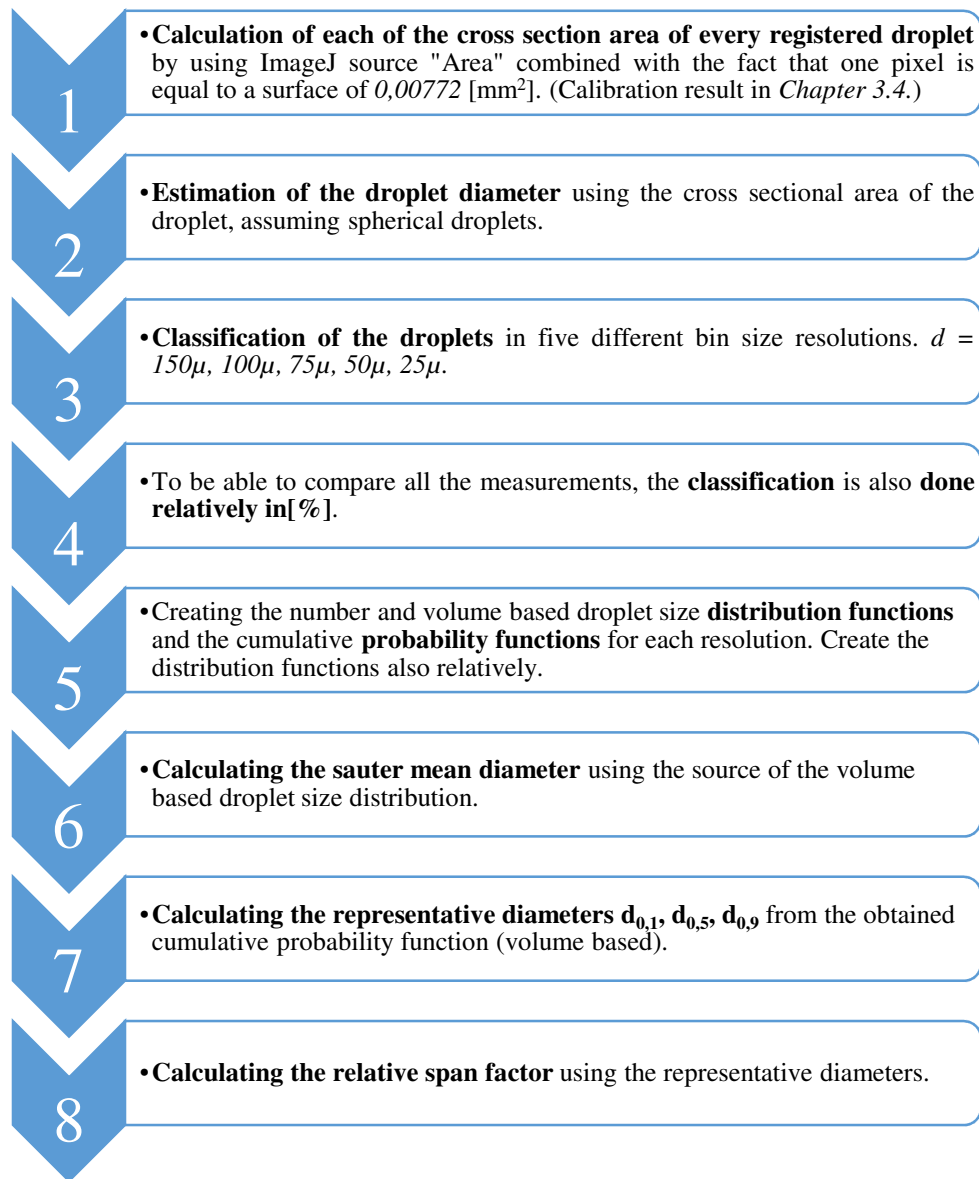


Figure 30: Main steps of the statistical evaluation in Microsoft Excel

III. 4. All the performed measurements

III. 4.1. Physical properties of the used fluids and solutions

As mentioned before in *Chapter 1.1.2.* the fluid properties have a high effect on the atomization. The most important variables are the viscosity, surface tension and the density.

The circumstances during the measurement are not uniform. For example the temperature of the fluid increases because of the higher ambient temperature and the strong lighting during the atomization process. The variables are mostly depending from the temperature of the fluid, but in all cases the fluid temperature changes during the measurements are low, around 1 °C – listed

in Table 14 – which results in a small viscosity, surface tension or density difference as shown in Figure 32.

The increase of the interval of the fluid properties will be achieved with the use of different model fluids instead of using the impact of the temperature. The chosen model fluids are ethanol, water, solutions of water and glycerol, paraffin oil.

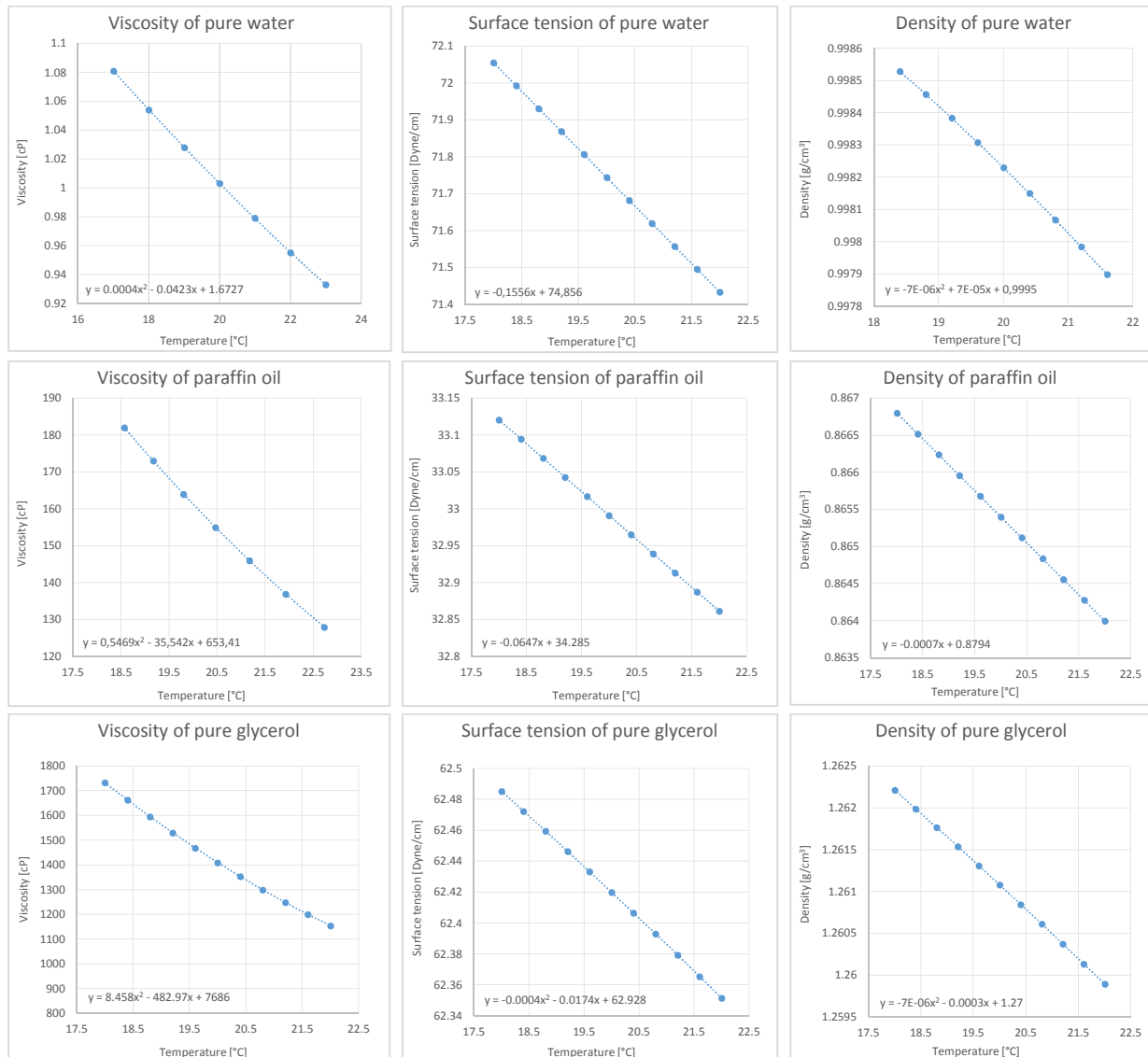


Figure 32: Properties of the applied model fluids

Fluid properties of water, paraffin oil and glycerol in function of the temperature. The fluid properties were taken from Kirchbacher [9], [13] and [14]. (The functions of the trend lines are just for this temperature interval valid.)

<i>Temperature [°C]</i>	<i>Pure water</i>	<i>Paraffin oil</i>	<i>Glyc. water sol.</i>
<i>T lowest</i>	17	19,6	19,1
<i>T highest</i>	18,5	20,2	19,9
<i>Difference¹</i>	1,5	0,6	0,8
<i>Ambient temperature</i>	21,2	19,7	21,2

Table 14: Temperature increase during the measurement

The change of the fluid properties because of the influence of the temperature – *Figure 32* – is almost negligible especially in the case of the density and the surface tension. With the solution of water and glycerol the available intervals of the fluid properties are becoming larger and theoretically they could be set to a wished value. During the measurement, the used glycerol was diluted with water in more steps to investigate the mechanism of the atomization of different viscosities, densities and surface tensions. The following diagrams *Figure 33, 34, 35* and *Table 15* are representing all the important parameters of the used fluids.

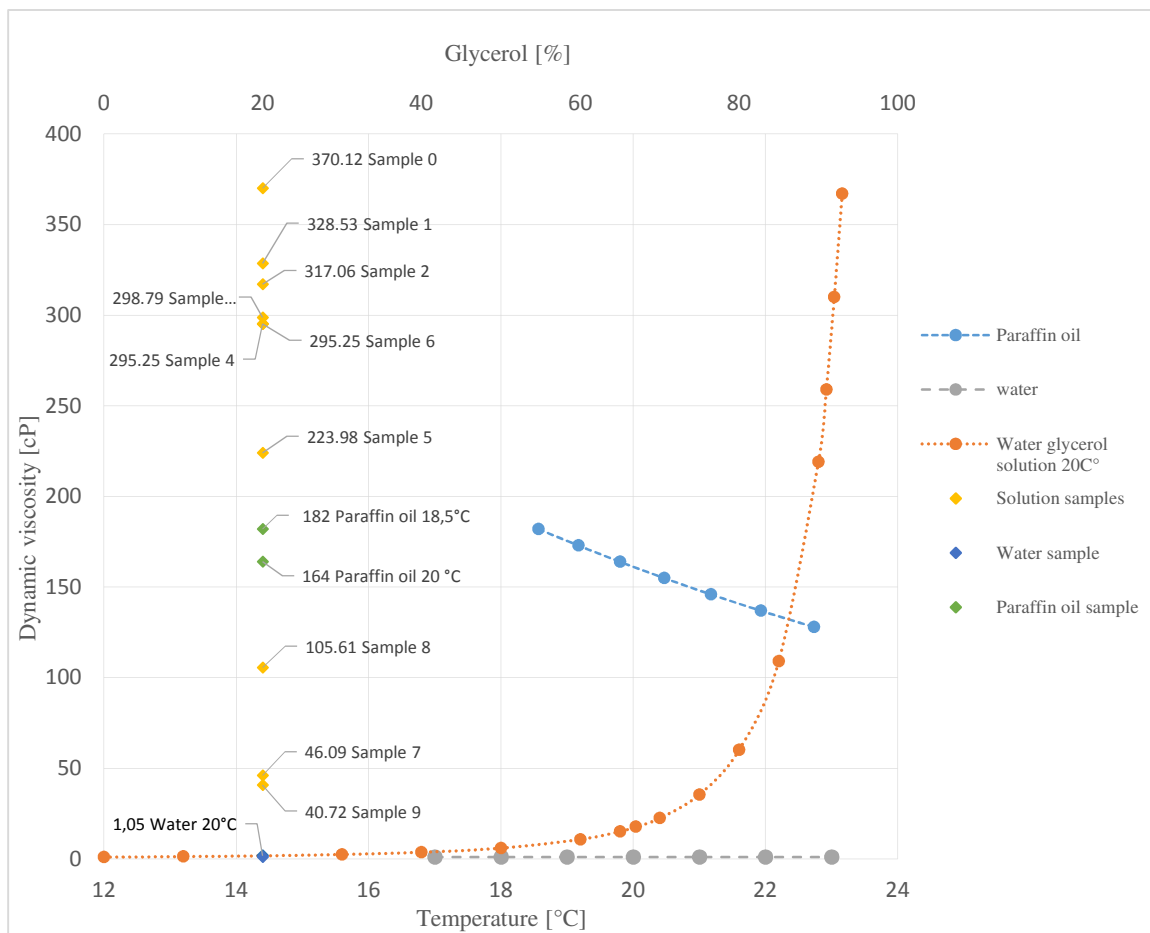


Figure 33: Dynamic viscosity of the used fluids and solutions

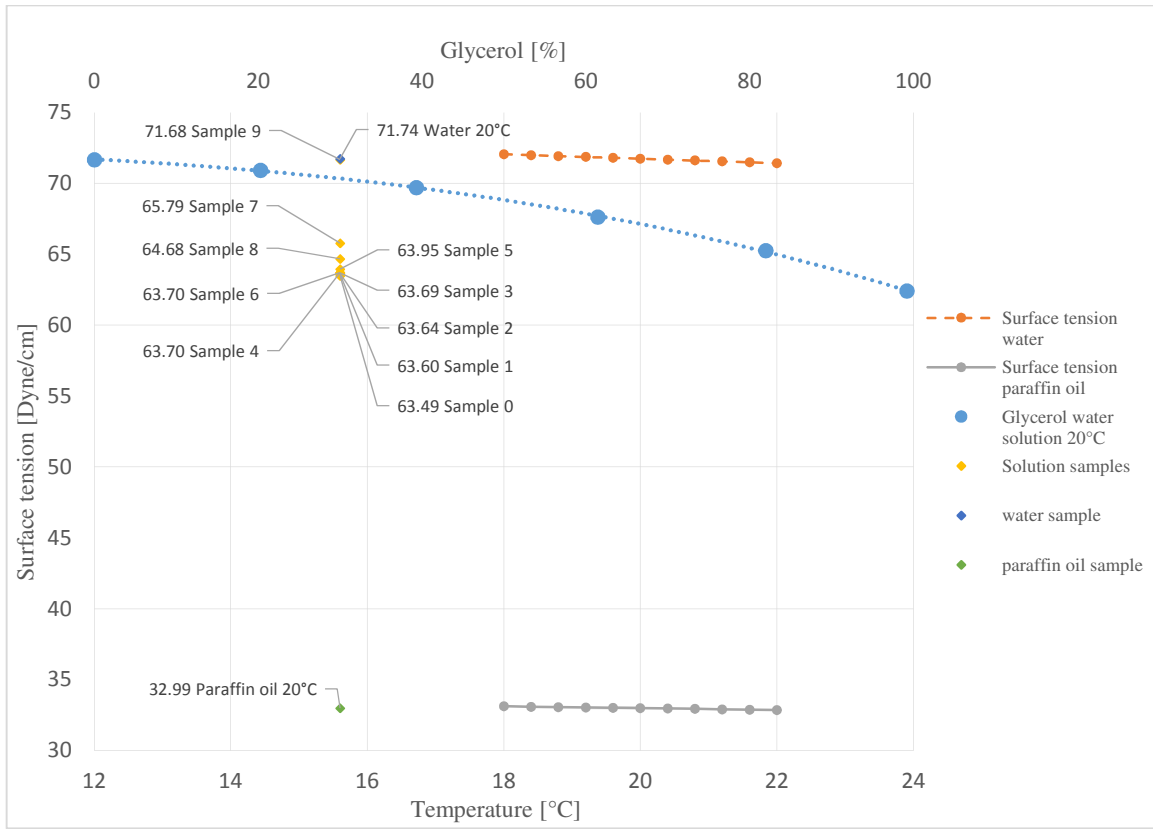


Figure 34: Surface tension of the used fluids and solutions

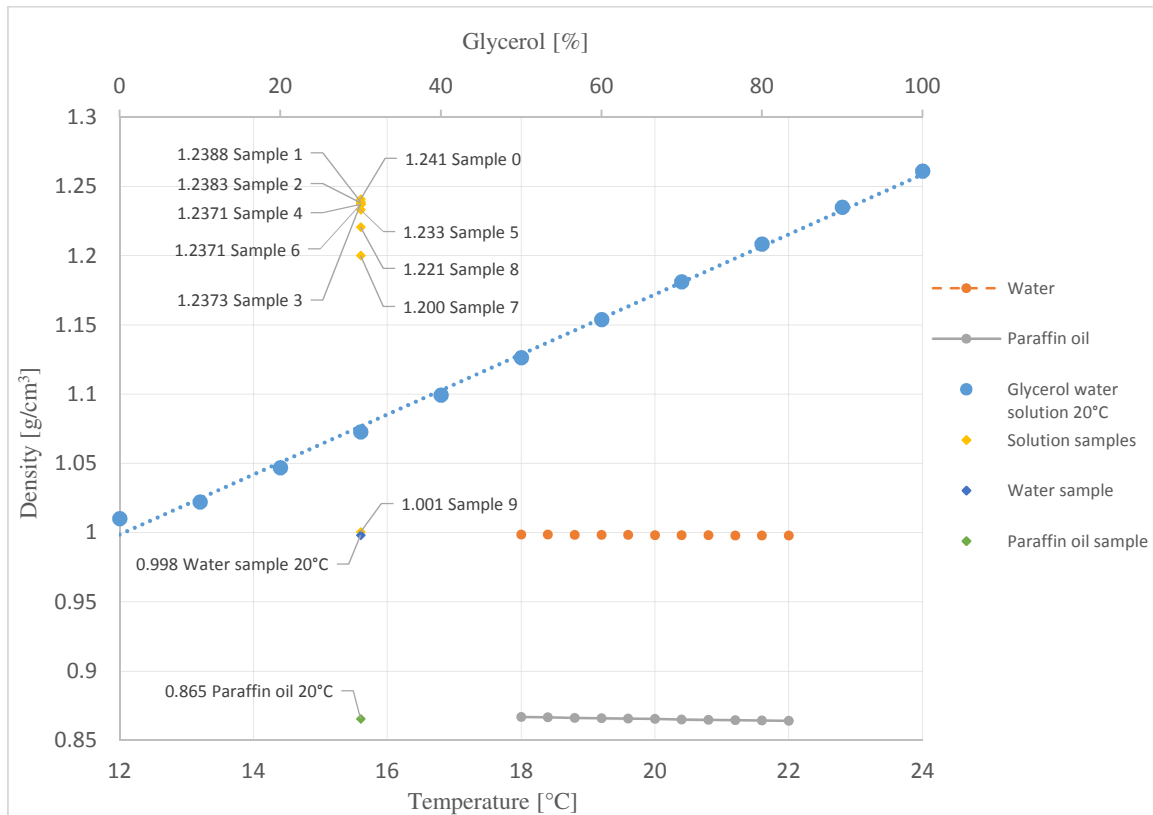


Figure 35: Density of the used fluids and solutions

<i>unit</i>	<i>Viscosity</i> [cP]	<i>Surface tension</i> [Dyne/cm]	<i>Density</i> [g/cm ³]	<i>Glycerol %</i> weight [%]
<i>Pure water</i>	1,003	71,744	0,99823	-
<i>Paraffin oil</i>	160	32,991	0,8654	-
<i>G-W sample 0</i>	370,12	63,486	1,24066	93,06
<i>G-W sample 1</i>	328,53	63,6013	1,23881	92,35
<i>G-W sample 2</i>	317,06	63,6357	1,23826	92,14
<i>G-W sample 3</i>	298,79	63,6928	1,23733	91,78
<i>G-W sample 4</i>	295,25	63,7042	1,23715	91,71
<i>G-W sample 5</i>	223,98	63,9525	1,23308	90,15
<i>G-W sample 6</i>	295,25	63,7042	1,23715	91,71
<i>G-W sample 7</i>	46,09	65,7918	1,20016	77,49
<i>G-W sample 8</i>	105,61	64,6797	1,22069	85,38
<i>G-W sample 9</i>	40,72	71,6755	1,00052	76,28

Table 15: Properties of the different fluids and solutions at 20 °C

III. 4.2. Table of measurements

As mentioned before not just paraffin oil but also other fluids were used for the measurements. In some extreme cases (high velocity, low or high viscosity) the concept of the measurement was not working as well as planned. For example in the case of ethanol the viscosity was so low that the desintegration happened quickly and intently. The size of the atomized droplets were too small and not appropriate for the evaluation. For this reason the measurements were executed only with paraffin oil, water and different water - glycerol mixtures, as listed in *Table 16, 17, 18*.

III. 4.2.1. Atomization using paraffin

Nr.	Frequency [Hz]	Pressure difference [mbar]	Power of pump [%]	Volumetric flow [l/min]	Nr.	Frequency [Hz]	Pressure difference [mbar]	Power of pump [%]	Volumetric flow [l/min]	
o1	0	0	15	80	o9 ¹	30,6	17,2	25	0	Position 1
o2	0	0	25	80	o10 ¹	30,6	17,2	25	0	
o3	18,9	6,7	15	0	o11 ¹	30,6	17,2	40	0	
o4	18,9	6,7	15	30	o12 ¹	30,6	17,2	40	80	
o5	18,9	6,7	15	80	o13	30,6	16,7	15	80	
o6	18,9	6,7	15	80	o14	30,6	16,9	15	30	
o7	18,9	6,8	15	0	o15	30,6	17,1	15	0	
o8	18,9	6,8	15	30	o16	30,6	17,4	25	0	
o17	41,6	29,5	15	0	o20	41,6	29,5	25	0	
o18	41,6	29,5	15	30	o21	41,6	29,5	25	30	
o19	41,6	29,5	15	80	o22	41,6	29,5	25	80	
o23	0	0	30	80	o30	35	20	30	0	
o24	19	6	30	0	o31	35	20	30	30	
o25	19	6	30	30	o32	35	20	30	80	
o26	19	6	30	80	o33	35	20	23	80	
o27	25	10,5	30	0	o32 ²	41,6	25	25	0	
o28	25	10,5	30	30	o35	41,6	25	25	0	
o29	25	10,5	30	80	o36	41,6	25	25	80	
o34	41,6	25	40	30	o37	41,6	25	25	30	
										Position 2

Table 16: Measurement settings for paraffin.

¹Lens settings: 2,8; ² For the lighting LED lamps were used

III. 4.2.2. Atomization using water

Nr.	Frequency [Hz]	Pressure difference [mbar]	Power of pump [%]	Volumetric flow [l/min]	Nr.	Frequency [Hz]	Pressure difference [mbar]	Power of pump [%]	Volumetric flow [l/min]
w1	0	0	16	50	w14	30,6	16,9	12,5	80
w2	0	0	16	80	w15	30,6	17,0	12,5	30
w3	0	0	25	80	w16	30,6	17,2	12,5	0
w4	0	0	50	80	w17	30,6	17,2	25	30
w5	18,9	6,8	15	0	w18	30,6	17,2	25	80
w6	18,9	6,8	15	30	w19	30,6	17,4	25	0
w7	18,9	6,8	15	80	w20	30,6	17,0	50	30
w8	18,9	6,6	25	30	w21	30,6	17,0	50	80
w9	18,9	6,6	25	80	w22	30,6	17,2	50	0
w10	18,9	6,8	25	0	w26	41,6	29,9	12,5	30
w11	18,9	6,6	50	80	w27	41,6	29,7	25	30
w12	18,9	6,7	50	30	w28	41,6	29,7	25	80
w13	18,9	6,8	50	0	w29	41,6	29,9	25	0
w23	41,6	29,6	12,5	80	w30	41,6	29,9	50	0
w24	41,6	29,8	12,5	30	w31	41,6	29,9	50	30
w25	41,6	29,9	12,5	0	w32	41,6	29,9	50	80

Table 17: Measurement settings for water

III. 4.2.3. Measurement with glycerol water solutions

Nr.	Frequency [Hz]	Pressure difference [mbar]	Power of pump [%]	Volumetric flow [l/min]	Sample ID	Glycerol weight [%]	Nr.	Frequency [Hz]	Pressure difference [mbar]	Power of pump [%]	Volumetric flow [l/min]	Sample ID	Glycerol weight [%]
s1 ⁰	30,6	17,4	25	0	0	93,06	s32 ⁶	18,9	6,6	10	80	6	91,71
s2 ¹	30,6	17,4	25	0	1	92,35	s33 ⁶	18,9	6,7	10	0		
s3 ²	0	0	10	85	2	92,14	s34 ⁶	18,9	6,7	20	80	7	77,49
s4 ²	30,6	17,4	15	0									
s5 ²	30,6	17,4	15	0									
s6 ²	30,6	17,4	25	0									
s7 ²	30,6	17,4	15	30									
s8 ²	30,6	17,4	15	85									
s9 ²	30,6	17,5	10	0									
s10 ³	0	0	15	85									
s11 ³	30,6	17,5	10	30	3	97,78	s35 ⁷	18,9	6,7	10	0		
s12 ³	30,6	17,5	10	30									
s13 ³	30,6	17,5	10	85									
s14 ³	30,6	17,5	10	85									
s15 ⁴	0	0	20	85	4	91,71	s36 ⁷	18,9	6,7	10	30		
s16 ⁴	30,6	17,2	15	85									
s17 ⁴	30,6	17,4	15	30									
s18 ⁴	30,6	17,4	15	0									
s19 ⁴	30,6	17,4	20	85									
s20 ⁴	30,6	17,4	20	30									
s21 ⁴	30,6	17,4	20	0									
s22 ⁵	18,9	6,7	20	0	5	90,15	s37 ⁷	18,9	6,7	10	80		
s23 ⁵	18,9	6,7	20	30									
s24 ⁵	41,6	30,2	10	0									
s25 ⁵	41,6	30,2	10	30									
s26 ⁵	41,6	30,4	10	30									
s27 ⁵	41,6	30,8	20	0									
s28 ⁵	41,6	30,8	20	30									
s29 ⁵	41,6	30,8	10	80									
s30 ⁵	41,6	30,8	20	80									
s31 ⁶	18,9	6,6	10	30			6	91,71	s38 ⁷	30,6	16,8	10	30
									s39 ⁷	30,6	16,8	10	80
							s40 ⁷	30,6	17,1	10	0		
							s41 ⁷	41,6	29,9	10	0		
							s42 ⁷	41,6	29,9	10	30		
							s43 ⁷	41,6	29,9	10	80		
							s44 ⁸	18,9	6,6	20	80	8	85,73
							s45 ⁸	18,9	6,7	20	30		
							s46 ⁸	18,9	6,8	20	0		
							s47 ⁸	30,6	16,8	20	80		
							s48 ⁸	30,6	17,1	20	0		
							s49 ⁸	30,6	17,1	20	30		
							s50 ⁸	41,6	29,9	20	0		
							s51 ⁸	41,6	29,9	20	30		
							s52 ⁸	41,6	29,9	20	80		
							s53 ⁹	18,9	6,8	40	0		
							s54 ⁹	18,9	6,8	40	30		
							s55 ⁹	18,9	6,8	40	80		
							s56 ⁹	30,6	16,8	40	80		
							s57 ⁹	30,6	17,2	40	30		
							s58 ⁹	30,6	17,2	40	0		
							s59 ⁹	41,6	29,4	40	80		
							s60 ⁹	41,6	29,8	40	0		
							s61 ⁹	41,6	29,8	40	30		

Table 18: Measurement settings for water - glycerol solutions
The different exponent marks the sample of the water glycerol solution

III. 5. Results of the measurements and evaluations

III. 5.1. Results of the different model fluids

With these represented settings and all the calculated dimensionless numbers the final results for the searched distribution functions for the model fluid water, paraffin oil and for the different solutions for glycerol and water can be created. Because of the amount of the measured and evaluated points just the most important and successfully measured points of the distribution functions were illustrated in the thesis.

The distribution functions can be found under *Figure 36 – 53* and under *Table 19 – 27*. Also a summary of these results are obtainable in *Table 28* where the dimensionless numbers of the actual measurement are compared with the real system. If the value is equal 1 or at least is close to 1, then the property is the same as in the real furnace. For the perfect correspondence all the properties should be equal to 1, which is impossible from the start because of the initial restrictions in the model according to *Table 7*. The results of all the measured points can be found in the electronic appendix.

III. 5.1.1. Selected results for water

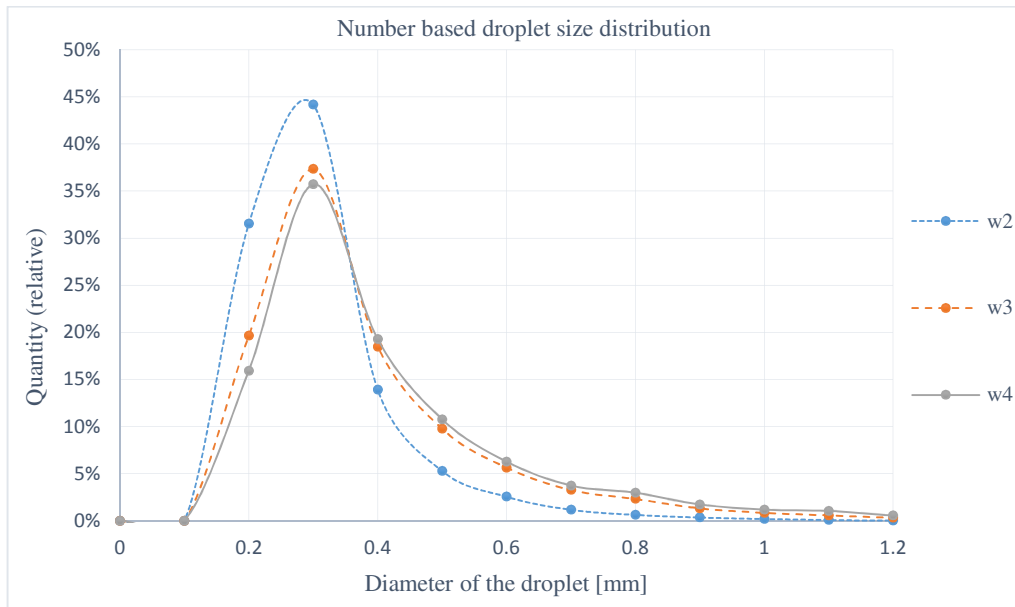


Figure 36: Comparison of the num. dist. functions for water, T. inlet vel. 0 m/s

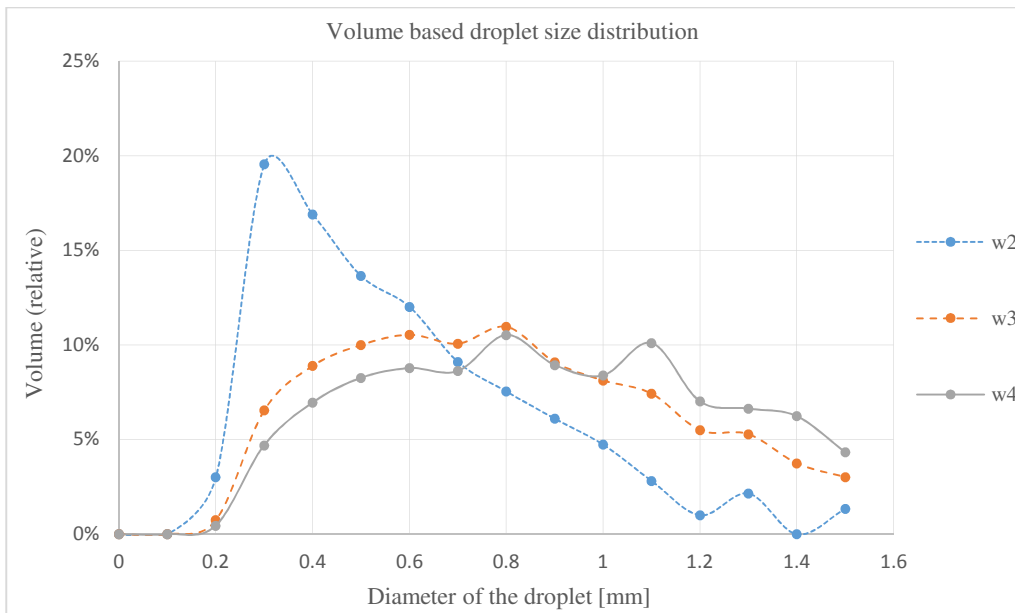


Figure 37: Comparison of the vol. dist. functions for water, T. inlet vel. 0 m/s

	<i>Adjustment</i>	<i>We</i>	<i>Oh</i>	<i>Re_M</i>	<i>Re_G</i>	<i>SMD [mm]</i>	<i>Δ [mm]</i>
w2	1	22,6				0,41	2,3
w3	1	68,2	0,00153	6244	0	0,59	1,62
w4	1	540,7				0,66	1,38

Table 19: Properties of the atomization, water, Tuyere inlet vel. 0 m/s

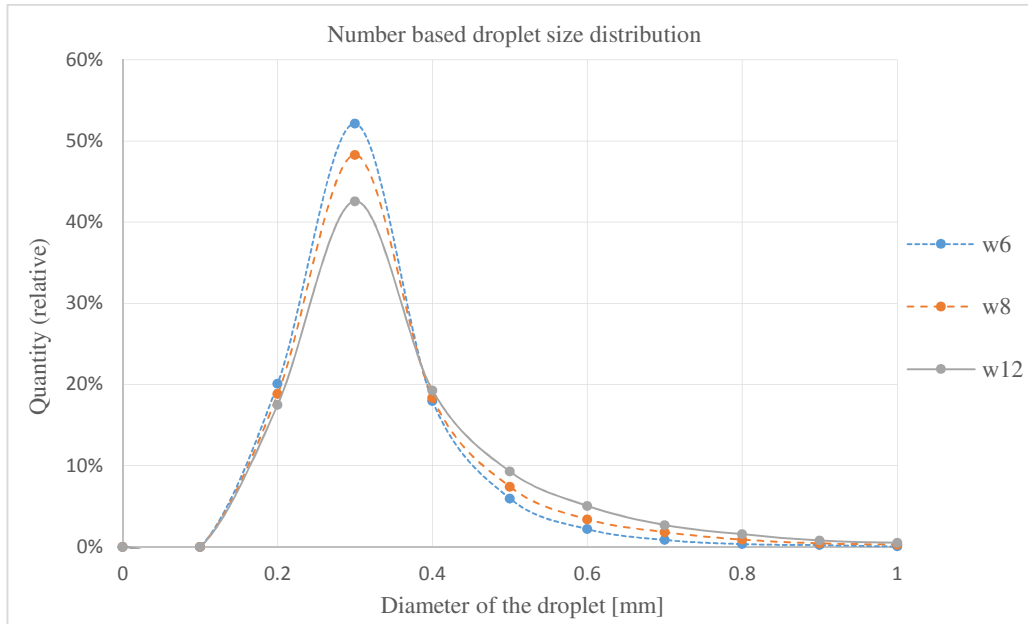


Figure 38: Comparison of the num. dist. functions for water, T. inlet vel. 33,6 m/s

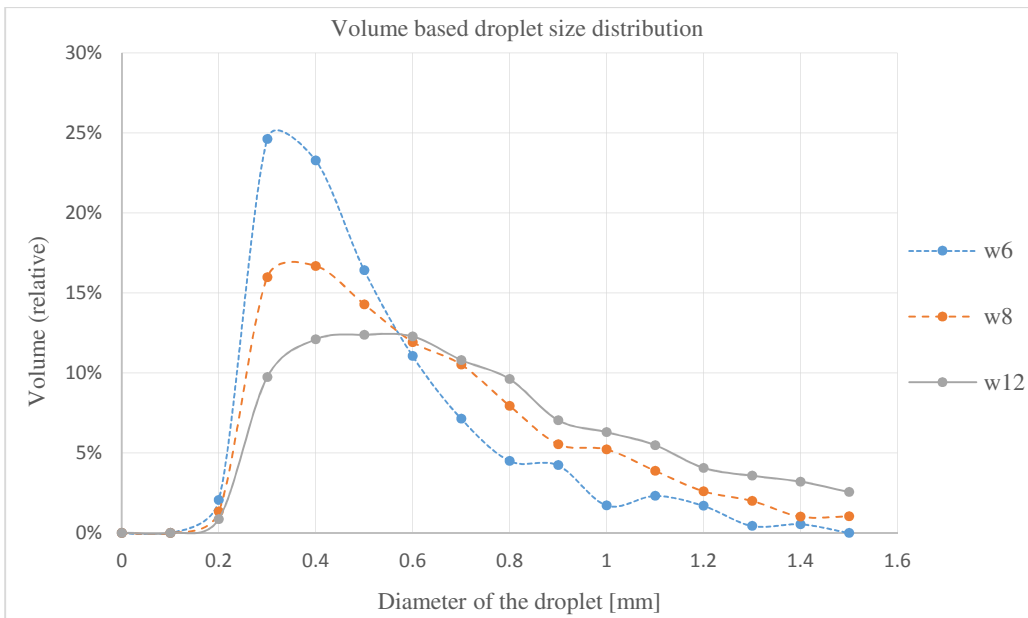


Figure 39: Comparison of the vol. dist. functions for water, T. inlet vel. 33,6 m/s

	<i>Adjustment</i>	<i>We</i>	<i>Oh</i>	<i>Re_M</i>	<i>Re_G</i>	<i>SMD [mm]</i>	<i>Δ [mm]</i>
w6	1	19,6	0,00153	2342	194235	0,377	1,809
w8	1	68,2				0,448	2
w12	1	540,7				0,526	2,054

Table 20: Properties of the atomization, water, Tuyere inlet vel. 33.6 m/s

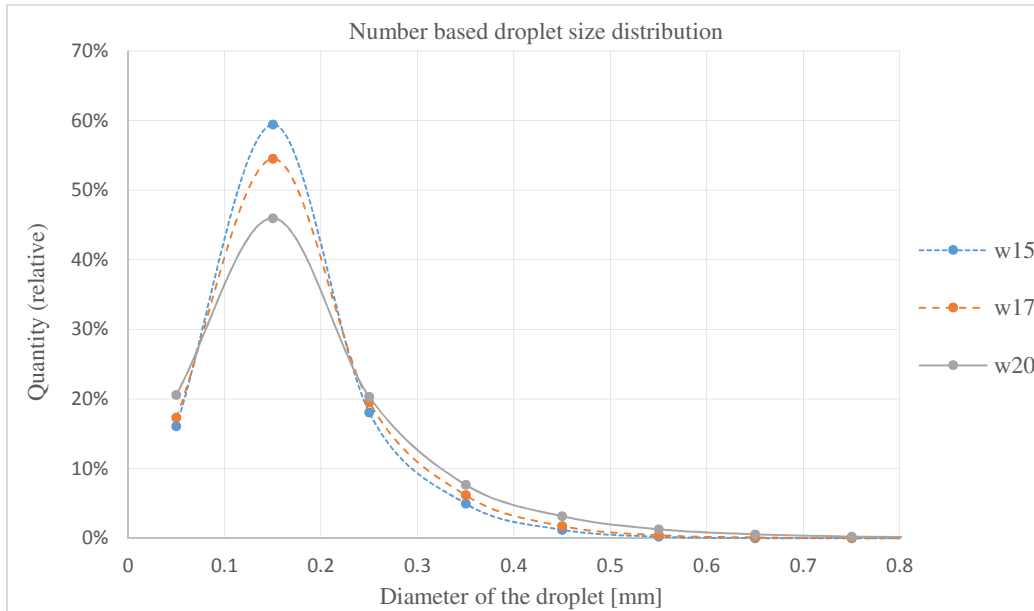


Figure 40: Comparison of the num. dist. functions for water, T. inlet vel. 53,4 m/s Adjustment 2

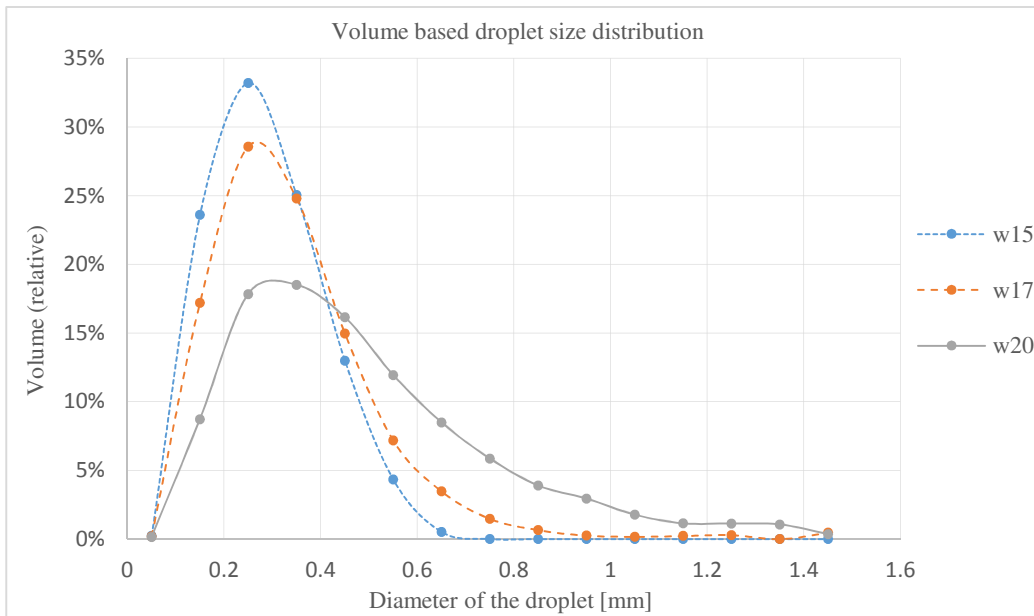


Figure 41: Comparison of the num. vol. functions for water, T. inlet vel. 53,4 m/s Adjustment 2

	<i>Adjustment</i>	<i>We</i>	<i>Oh</i>	<i>Re_M</i>	<i>Re_G</i>	<i>SMD [mm]</i>	<i>Δ [mm]</i>
<i>w15</i>	2	13,5				0,246	1,073
<i>w17</i>	2	540,7	0,00153	2342	308915	0,274	1,278
<i>w20</i>	2	68,2				0,358	2,378

Table 21: Properties of the atomization, water, Tuyere inlet vel. 53,4 m/s

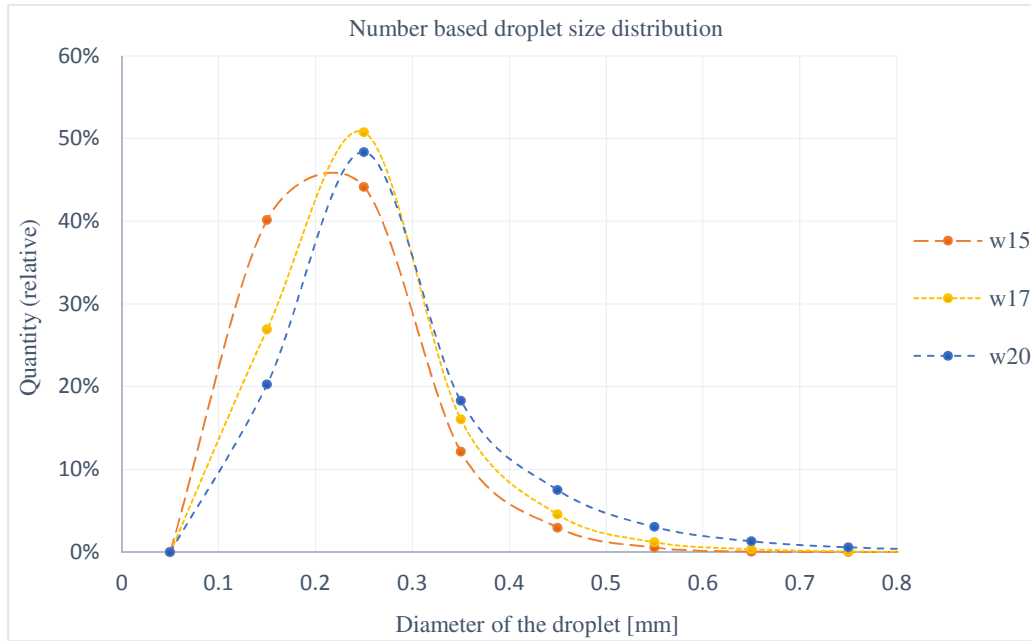


Figure 42: Comparison of the num. dist. functions for water, T. inlet v. 53,4 m/s

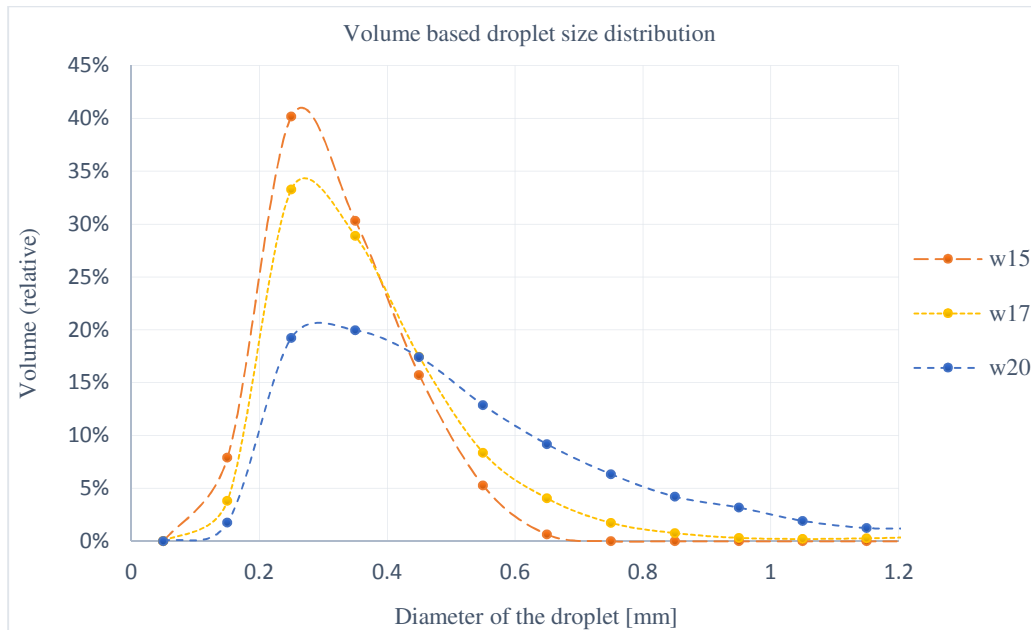


Figure 43: Comparison of the num. vol. functions for water, T. inlet vel. 53,4 m/s

	<i>Adjustment</i>	<i>We</i>	<i>Oh</i>	<i>Re_M</i>	<i>Re_G</i>	<i>SMD [mm]</i>	<i>Δ [mm]</i>
w15	1	13,5				0,278	1
w17	1	540,7	0,00153	2342	308915	0,323	1,071
w20	1	68,2				0,408	1,83

Table 22: Properties of the atomization, water, Tuyere inlet vel. 53,4 m/s

III. 5.1.2. Selected results for glycerol – water solutions

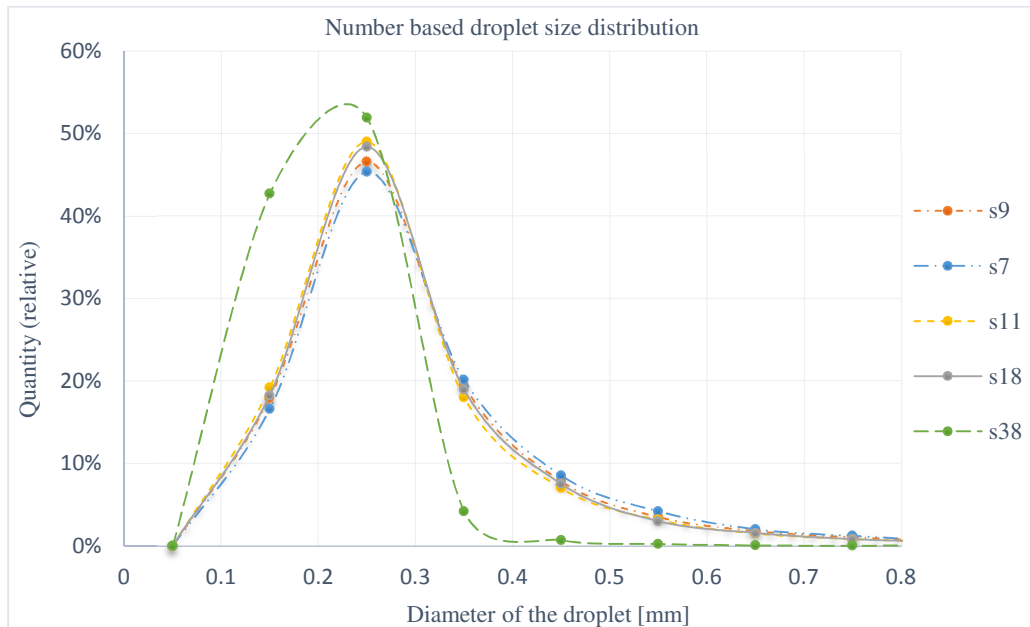


Figure 44: Comparison of the num. dist. functions for glyc. - water solutions, T. inlet vel. 53,4 m/s

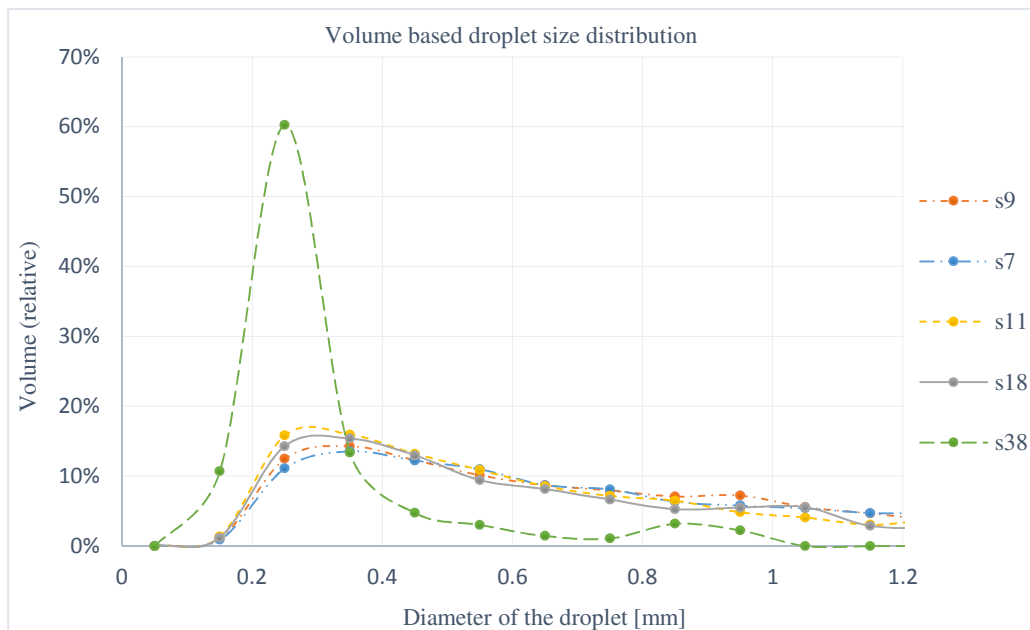


Figure 45: Comparison of the vol. dist. functions for glyc. - water solutions, T. inlet vel. 53,4 m/s

	<i>Adjustment</i>	<i>We</i>	<i>Oh</i>	<i>Re_M</i>	<i>Re_G</i>	<i>SMD [mm]</i>	<i>Δ [mm]</i>
<i>s9</i>	1	12,4	0,461	0	308975	0,499	2,226
<i>s7</i>	1	27,4	0,461	2342		0,518	2,291
<i>s11</i>	1	12,4	0,434	2342		0,438	2,345
<i>s18</i>	1	27,4	0,429	0		0,484	2,784
<i>s38</i>	1	11,7	0,067	2342		0,262	1,316

Table 23: Properties of the atomization, glycerol - water, Tuyere inlet vel. 53,4 m/s

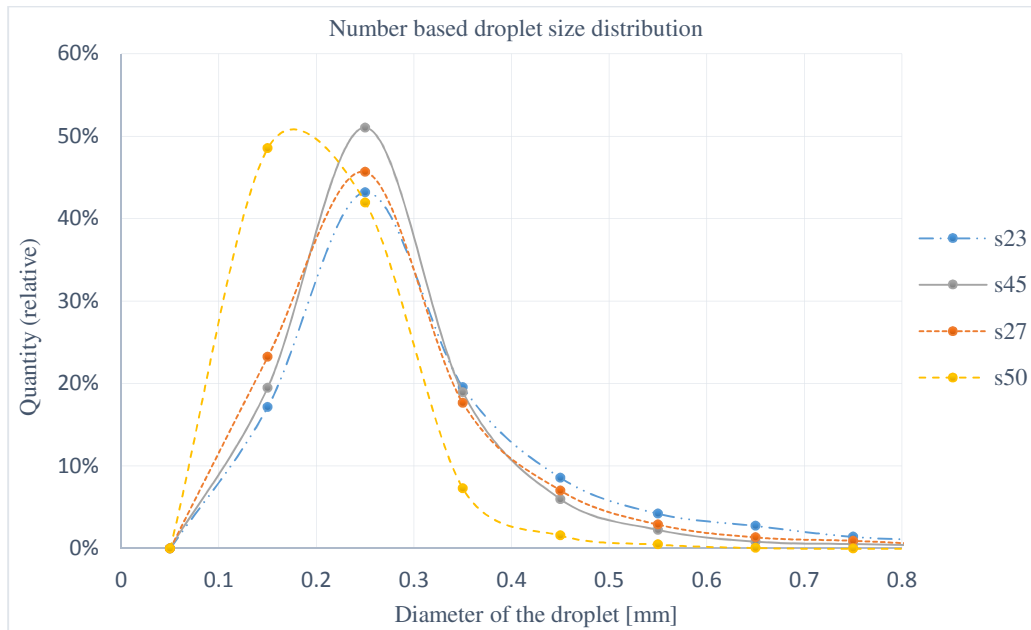


Figure 46: Comparison of the num. dist. functions for glycerol - water solutions, pump power 20 %

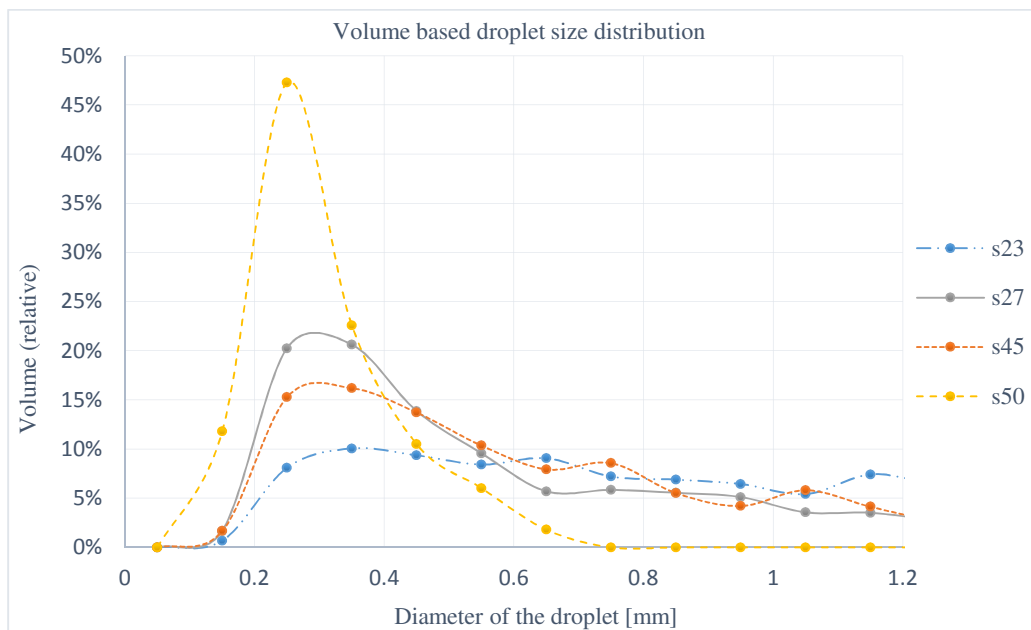


Figure 47: Comparison of the vol. dist. functions for glycerol - water solutions, pump power 20 %

	<i>Adjustment</i>	<i>We</i>	<i>Oh</i>	<i>Re_M</i>	<i>Re_G</i>	<i>SMD [mm]</i>	<i>Δ [mm]</i>
<i>s23</i>	1	53,1	0,3256	2342	194235	0,595	2
<i>s27</i>	1	53,1	0,1534	0	407976	0,458	2,275
<i>s45</i>	1	52	0,3256	2342	194235	0,418	2,511
<i>s50</i>	1	52	0,1534	0	407976	0,265	1

Table 24: Properties of the atomization, glycerol - water, pump power 20%

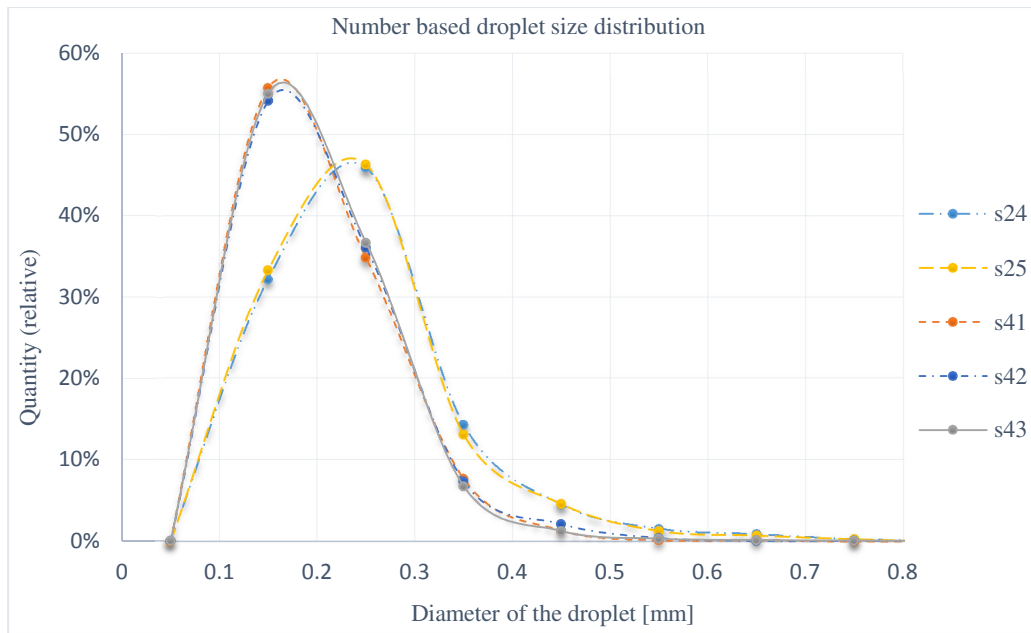


Figure 48: Comparison: num. dist. f. glyc – water solutions, pump power 10 %, T. inlet vel. 70,6 m/s

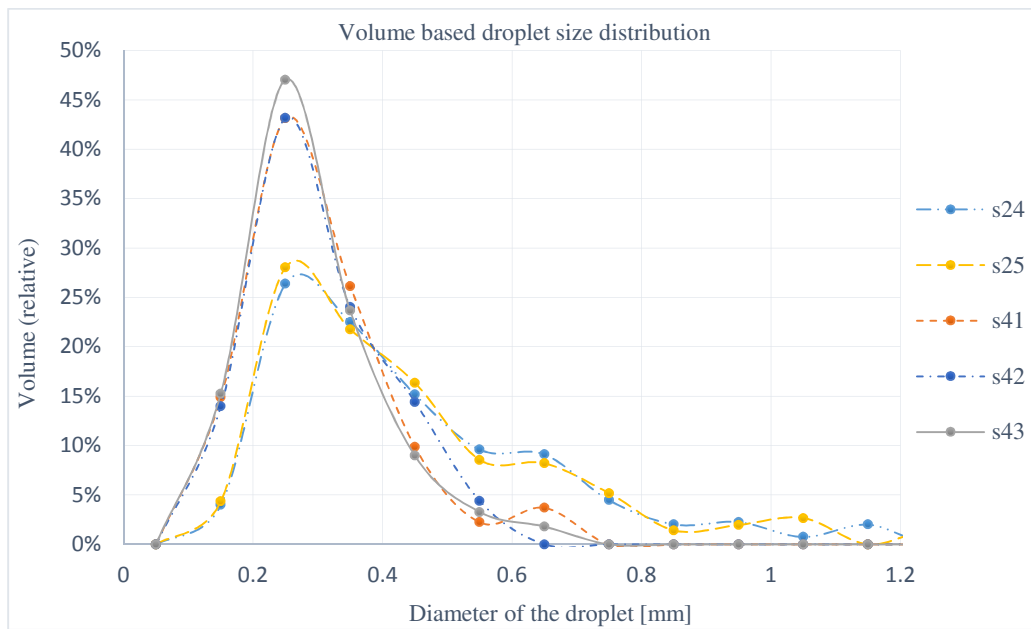


Figure 49: Comparison: vol. dist. f. glyc. – water solutions, pump power 10 %, T. inlet vel. 70,6 m/s

	<i>Adjustment</i>	<i>We</i>	<i>Oh</i>	<i>Re_M</i>	<i>Re_G</i>	<i>SMD [mm]</i>	<i>Δ [mm]</i>
<i>s24</i>	1	12,34	0,3256	0	407976	0,356	1,6
<i>s25</i>	1			2344		0,35	1,786
<i>s41</i>	1	0	0,258	0,882			
<i>s42</i>	1	11,68	0,067	2342		0,261	0,974
<i>s43</i>	1		6244	0,253		0,816	

Table 25: Properties of the atomization, glyc. – water sol., pump power 10%, T. inlet vel. 70,6 m/s

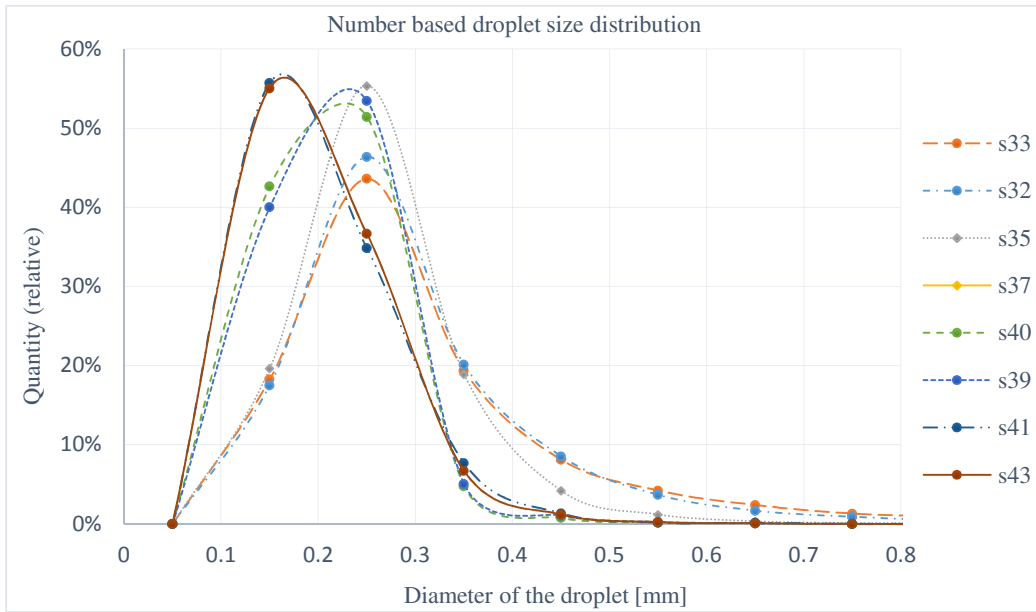


Figure 50: Comparison of the num. dist. functions for glycerol - water solutions, pump power 10 %

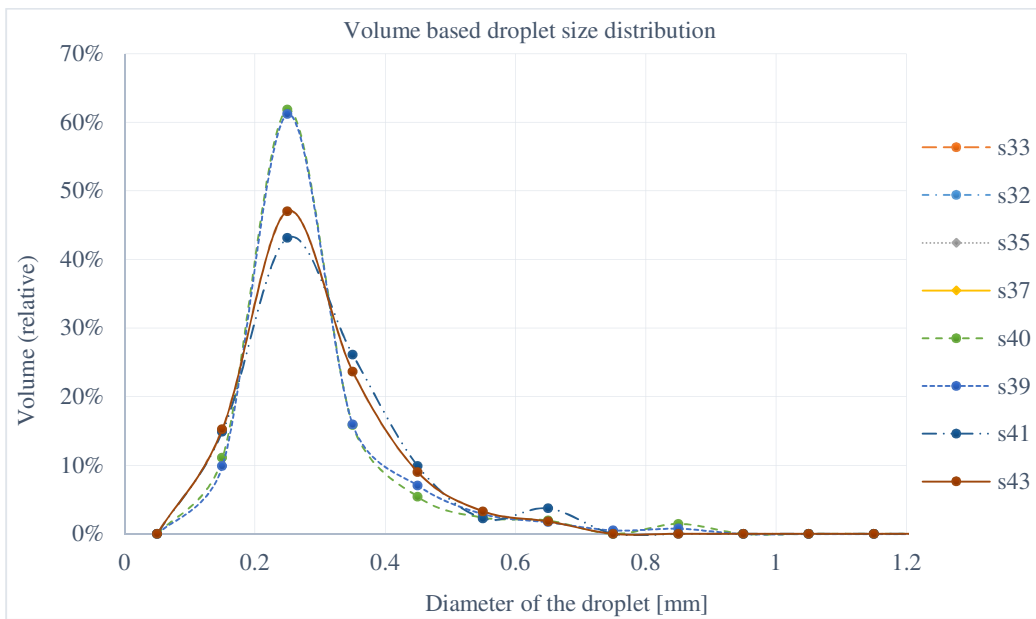


Figure 51: Comparison of the vol. dist. functions for glycerol - water solutions, pump power 10 %

	Adjustment	We	Oh	Re _M	Re _G	SMD [mm]	Δ [mm]
s33	1	12,43	0,4294	0	194235	0,557	2,107
s32	1		0,4294	6244		0,462	2,314
s35	1			0		0,334	1,261
s37	1	11,68	0,067	6244	308915	0,308	1
s40	1			0		0,253	0,906
s39	1			6244		0,257	0,816
s41	1			0		407976	0,258
s43	1			6244		0,253	0,816

Table 26: Properties of the atomization, glycerol – water solutions, pump power 10%

III. 5.1.3. Selected results for paraffin oil

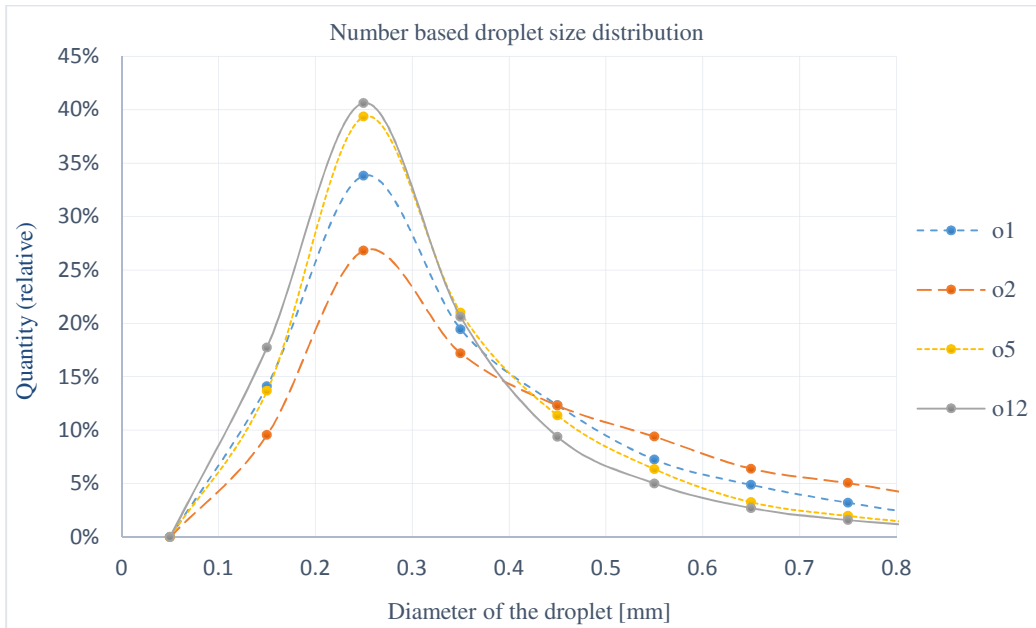


Figure 52: Comparison of the num. dist. functions for oil, cover stream 80 l/min

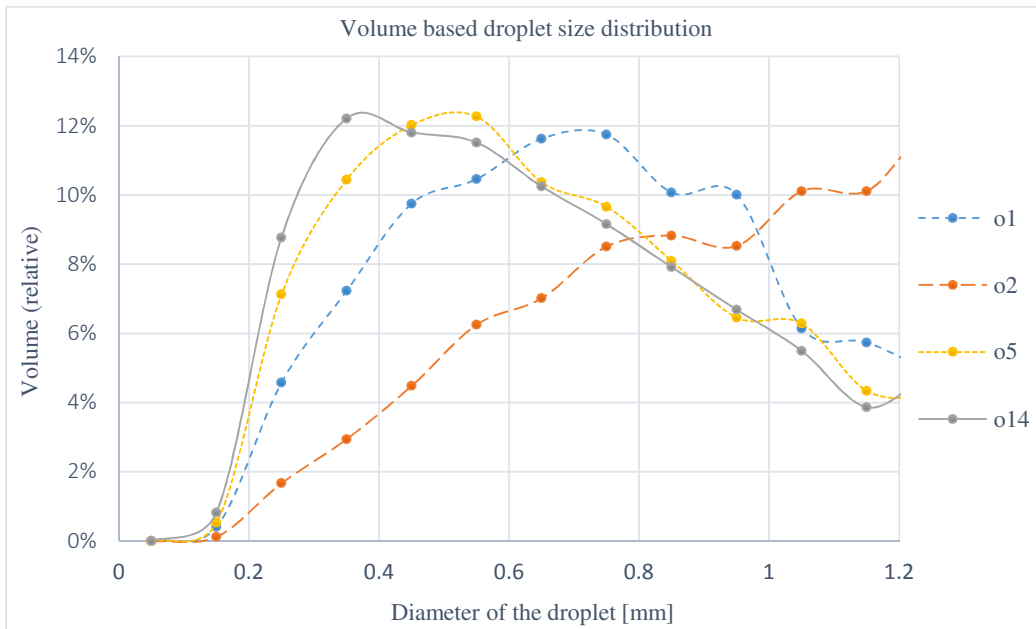


Figure 53: Comparison of the num. dist. functions for oil, cover stream 80 l/min

	Adjustment	We	Oh	Re _M	Re _G	SMD [mm]	Δ [mm]
o1	1	540,7	0,386	6244	0	0,629	1,366
o2	1	128,6				0,828	0,79
o5	1	37			0,569	1,887	
o12	1	502,5			0,55	1,705	

Table 27: Comparison of the num. dist. functions for oil, cover stream 80 l/min

<u>The measured and evaluated points</u>					<u>Reality/operating conditions</u>			
<i>Nr.</i>	<i>Sample</i>	v_G	v_{Fluid}	v_M	Re_M	Re_G	Oh	v_G/v_{Oil}
<i>[-]</i>	<i>[-]</i>	<i>[m/s]</i>	<i>[m/s]</i>	<i>[m/s]</i>	<i>[-]</i>	<i>[-]</i>	<i>[-]</i>	<i>[-]</i>
w2	water	0	0,52	47,16	5,7	-	49,66	-
w3	water	0	0,9	47,16	5,7	-	49,66	-
w4	water	0	2,54	47,16	5,7	-	49,66	-
w6	water	38,1	0,48	17,68	15,19	3,42	49,66	0,94
w8	water	38,1	0,9	17,68	15,19	3,42	49,66	1,74
w12	water	38,1	2,54	17,68	15,19	3,42	49,66	4,91
w15	water	60,59	0,40	17,68	15,19	2,15	49,66	0,49
w17	water	60,59	2,54	17,68	15,19	2,15	49,66	1,1
w20	water	60,59	0,9	17,68	15,19	2,15	49,66	3,09
o1	oil	0	0,48	47,16	5,7	-	0,2	-
o2	oil	0	0,90	47,16	5,7	-	0,2	-
o5	oil	38,1	0,48	47,16	5,7	3,42	0,2	0,94
o12	oil	60,59	1,78	47,16	5,7	2,15	0,2	2,17
s9	2	60,59	0,32	0	-	2,15	0,16	0,4
s7	2	60,59	0,48	17,68	15,19	2,15	0,16	0,59
s11	3	60,59	0,32	17,68	15,19	2,15	0,17	0,4
s18	4	60,59	0,48	0	-	2,15	0,18	0,59
s38	7	60,59	0,32	17,68	15,19	2,15	1,13	0,4
s23	5	38,1	0,67	17,68	15,19	3,42	0,23	0,23
s27	5	80,03	0,67	0	-	1,63	0,23	0,62
s45	8	38,1	0,67	17,68	15,19	3,42	0,5	1,31
s50	8	80,03	0,67	0	-	1,63	0,5	0,62
s24	5	80,03	0,32	0	-	1,63	0,23	0,3
s25	5	80,03	0,32	17,68	15,19	1,63	0,23	0,3
s41	7	80,03	0,32	0	-	1,63	1,13	0,3
s42	7	80,03	0,32	17,68	15,19	1,63	1,13	0,3
s43	7	80,03	0,32	47,16	5,7	1,63	1,13	0,3
s33	6	38,1	0,32	0	-	3,42	0,18	0,63
s32	6	38,1	0,32	47,16	5,7	3,42	0,18	0,63
s35	7	38,1	0,32	0	-	3,42	1,13	0,63
s37	7	38,1	0,32	47,16	5,7	3,42	1,13	0,63
s40	7	60,59	0,32	0	-	2,15	1,13	0,4
s39	7	60,59	0,32	47,16	5,7	2,15	1,13	0,4

Table 28: Summary of the measurements, comparison with the real system

III. 5.2. Problems and difficulties with the measurement and data processing

The biggest challenge in the data processing was to find the proper settings in ImageJ for the evaluated area. This problem was due to a gradient of lighting seen in *Figure 29c*. The intensity of the lighting depended also on the atomized fluid amount. If the atomized fluid amount was increasing, the brightness of the recorded image reduced. In this non-constant case the use of a threshold level could be difficult, because the preset threshold level is valid for the whole image. This means that if the threshold level is low then the dark regions will be bright as desired, but the bright regions will become brighter than necessary. This leads to the shrinkage of the analyzed droplets due to lower contrast, which is disturbing the evaluation. The current solution for the problem was to reduce the analyzed area to the most constant lighting, which leads to the loss of droplets as a side effect.

In case of a higher viscosity the atomization befalls not completely. A lot of filaments and larger droplets are disturbing the data processing. Secondary atomization is observable. To be able to evaluate the real Sauter mean diameter the distance from the nozzle should be increased.

The camera is focused on a plane in the middle of the atomization, but the desintegration of the fluid happens in space, also behind and in front of this plane. Non-focused blurry droplets will appear and disturb the data processing, because blurry droplets are usually larger than the real ones. If we move in this case to higher velocities and high pump powers than the atomized droplets can form a cloud in front of the focus plane making the whole image blurry.

In lot of the cases droplets can be partly cover each other which leads on the 2D image to an even bigger also not real droplet as presented before in *Figure 29d*. A similar basic problem of the evaluation is that the droplet diameters are estimated using the cross section area of the droplet, assuming spherical droplet shape. This assumption brings additional inaccuracy in the evaluation.

In case of lower viscosity or higher gas velocities the atomized droplets will become so small, that the used resolution or/and shutter speed will be improper for the measurement making the data processing even more difficult or impossible.

III. 6. Conclusions

III. 6.1. The evaluated interval

The aimed measured interval was large regarding the viscosity, the velocity and other physical properties. The high number of combinations of these physical values in this large interval led to high amount of measured points. Hereby these measurements included also some points which deviate from the actual analyzed atomization process.

Even so the interval and so the quantity of the measured points were reduced due to uncertainties (mentioned in *Chapter III.5.2.*) in the evaluation. These difficulties appeared in most cases at important zones near to the advantageous dimensionless numbers, where the high velocity or/and the high viscosity decreases the quality of the recording until the point where it is not sufficient enough.

In some cases it was already perceivable during the measurement that the evaluation will not produce a qualitative result. These evaluations had low precision and led to a false result.

III. 6.2. Unsuccessful measurements

During the evaluation of the measurements it could be noticed that the precision is actually decreasing with the rising of the velocity or/and the viscosity. In these cases the imperfection was unambiguous, because for example considering two measured points where the only difference between the atomization settings is the v_G velocity, then it is evident that the smaller SMD will appear with higher v_G , because the more energy is transmitted to the fluid the smaller the SMD will be. In these difficult cases the results delivered not every time this behavior. A measured higher SMD through a higher velocity inlet v_G is not possible. That means that in the high viscosity regions the imprecision of the measurement became so high, that the measurement lost its authenticity.

This behavior and the listed SMD for all the measured points can be obtained in the electronic appendix.

Few results of the evaluated paraffin oil measurements are illustrated in *Figure 52, 53*. The evaluation of the paraffin oil droplets was challenging because the mentioned disturbing effects. On the recorded images appeared filaments, blurry droplets which lowered the precision of the measurement dramatically. The atomization of the oil was not complete and therefore the recording spot was moved further away from the nozzle as illustrated in *Figure 20*. This solution was an improvement but still not good enough.

The evaluation of the recorded images functioned only with low inlet gas velocities where the size of the desintegrated droplets was large as seen in the *SMD* values in *Table 27* These recordings delivered sharp, for the data processing useable images. Higher velocities delivered blurry images, making the processing impossible. To make the recording sharper at higher inlet velocities we tried to use higher shutter speed. Higher shutter speed requires a higher light

intensity. For this reason two reflectors were changed to LED lamps to fulfill this demand. These changings improved the performance but still not enough to obtain image sequences which can be evaluated accurately. The availability of the high speed camera was limited, therefore the measurements ended at this point.

III. 6.3. Successful measurements

At lower viscosities, especially in the case of water – *Figure 36 - 43* – the measurements delivered reasonable results. The atomization with higher v_G velocity led also to lower SMD and at lower v_G velocities the size of the desintegrated particles became larger. It can be also noticed on the results – *Figure 38 and 39* – that with the same v_G hence with the same energy input the droplet size will change if the mass flow of the atomized fluid is higher or lower. The effect is similar. The same energy input at lower mass flow (Apv_{Fluid}) leads to smaller SMD and in case of higher mass flow to higher SMD. This ratio, v_G/v_{Fluid} is actually one of the defined dimensionless numbers, the specific energy input ratio.

In the case of these low viscosity measurements the accuracy is also proven by the small effect of the coaxial cover stream v_M , which was noticeable in the results in *Table 26* at the groups (*s32 s33*), (*s41 s43*) (*s35 s37*) and in *Table 25* at (*s24 s25*) - and in various other measurements with low viscosity - in the difference of the SMD. With rising viscosity first the impact of the coaxial cover stream was disappearing from the results and by using model fluids with even higher viscosity values the measurement become completely inaccurate.

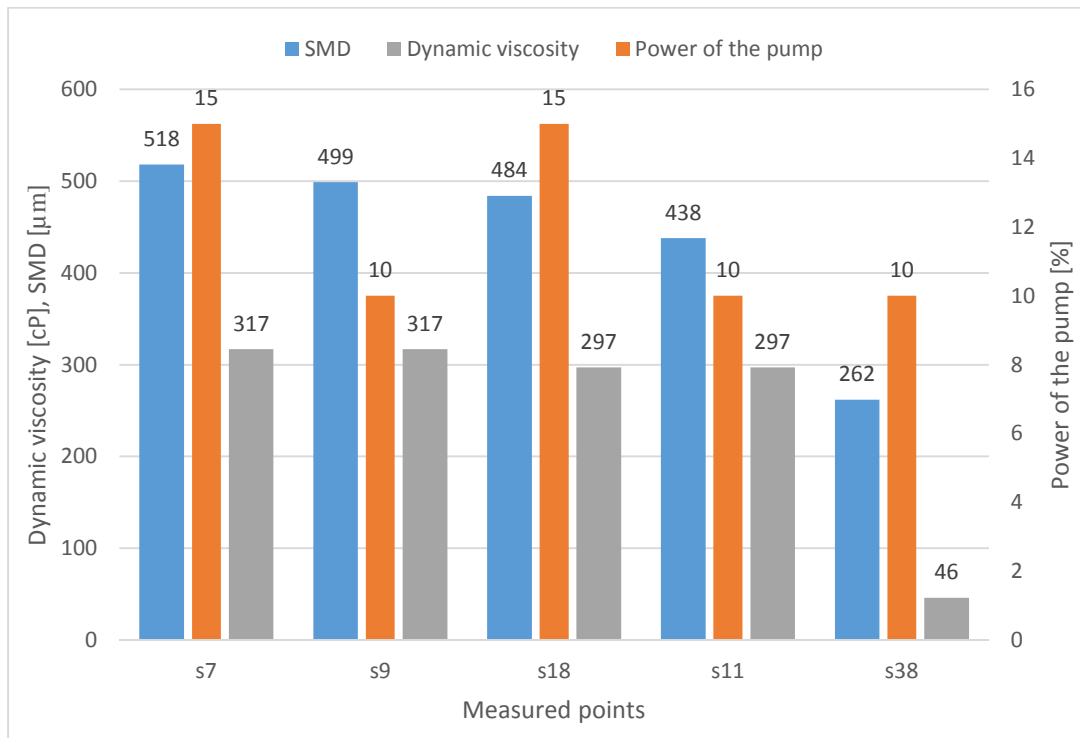


Figure 54: Trend of the SMD depending from the viscosity and the pump power

Let us take a closer look on *Figure 44, 45* and *Table 23* where the effect of the viscosity difference can be well noticed. The five presented distributions are picked from four different water - glycerol solutions, but the solutions of measurement *s11* and *s18* are standing close enough to each other that the difference is negligible as seen in *Figure 33*. The measurement with the highest viscosity ($v = 317 \text{ cP}$) is group (*s9, s7*) followed by group (*s11, s18*) with the viscosity ($v = 297 \text{ cP}$) and finally *s38* the distribution with the lowest value ($v = 46 \text{ cP}$). In the case of *s7* and *s18* the pump is functioning with a power of $P = 15 \%$ and in all other cases only with $P = 10 \%$. The high and also the low viscosity difference can be well noticed with the additional impact of the power of the pump. *s38* stands closest to pure water hence has the lowest viscosity and for this reason prominently the lowest *SMD*. This is followed by the group with a higher viscosity value, where from *s11* will have the second lowest *SMD* value because of the 5% power difference in the pump. The higher power of the pump means a higher mass flow for the same atomization energy, which leads to higher *SMD*. The distributions and the *SMD* of the other measured point in this diagram are following this rule. The same effect is presented in *Figure 46, 47* and *Table 23*.

To see also the impact of the adjustment during the data processing let us compare the measurements evaluated differently in *Figure 40 – 43* and in *Table 21, 22*. The settings of these adjustments can be obtained in *Table 13*. By excluding particles under 4 pixels will make roughly 10 -15 % difference in the final result in the *SMD*. Any other settings like the threshold level or the circularity has an effect as already proven at the calibration in *Chapter III.3.5.1*. Therefore it is important to know the most advantageous settings at the data processing, which is hard to say.

III. 6.4. Summary of the conclusions

Summarizing these conclusions we can say that the measurement process is working and it is possible to measure the *SMD* with this procedure, but using this setup, not all operating points of the test rig can be measured with sufficient accuracy. In *Table 28* we can see the summarized dimensionless values for the presented measurements and as conclusion we can say that the approach of the dimensionless numbers of the real furnace was just in few cases, but even than just partly successful. For improving the approach further measurements need to be accomplished. For the measurement of the higher viscosities and/or velocities some improvements of the measuring process and some changes has to be done. In *Appendix A* some recorded images are showed for the different atomized model fluids.

III. 7. Future plans – Possible improvements of the measurement

As listed before there are some difficulties with the measurement and for further investigation of the atomization they should be fixed especially in the case of higher velocities and higher viscosities.

In the case of higher viscosity a better solution could be to move farther on from the nozzle, because the desintegration of the fluid needs more „time“. Instead of the searched droplets just filaments can be found close to the nozzle so the camera has to be moved to another, far position. This effect can be noticed on *Figure 118* in *Appendix A*.

In the case of higher velocities the shutter speed could be the right solution. It is not sure that we need to record the whole atomization in *1000 fps*. It could be possible that a camera with less frame rate but better shutter speed and maybe also a better quality then *1024x1024 pixel* would perform better. Actually the camera we used could perform a better shutter speed, but for this the amount of light should be increased. In case of a camera with lower frame rate the same measurement has to be repeated because the plexiglas wall will be quickly blurry due to the droplets appearing on the wall.

A sufficient evaluation needs as many images as possible to approach the actual distribution of the atomized droplets. The recorded amount of images with one measurement is around thousand, but at the beginning and at the end of the recorded sequence few hundred images had to be deleted because they improper contents. At the beginning of the recording the atomization is not developed completely and the image package can contain useless information regarding the data processing. At the end of the recording, because of the more and more droplets landing on the plexiglas wall the wall will become blurry, which will result also in unusable images. In the case of the Photron HS camera one measurement delivers few hundred clear images from the droplets with *1000 fps*. In the case of lower frame rate also the amount of the recorded clear images will be lower and that is why in this case the same measurement needs to be done multiple times to achieve the same amount of images. Another solution is to use the built in windscreen wiper more often during the recording to clean the plexiglas wall.

As mentioned before a higher resolution would be also an improvement to have an accurate measurement especially in the case of lower viscosity and higher velocity where the atomization eventuates small droplets.

To avoid the uncertainty of the evaluation because of the unwished gradient lighting, the lighting system should be developed. This would have additionally the advantage to apply better shutter speed. The future lighting in the measurement should be improved in a way that the gradient in the recorded images disappears totally. In this case the evaluated area will be much bigger and also the evaluation itself becomes much easier. In the case of a bigger evaluated image the number of the evaluated droplets on the image will be much higher and so the measurement itself will be more accurate.

The nozzle in the system points to the side wall of the model rig where from the measurements are recorded. If the recording would happen from the opposite direction of the test

rig, the recording time could be maybe longer and the plexiglas wall would not become blurry that quickly.

Regarding the measurement process in the future it would be advantageous to consider the measured pressure difference as a reference value instead of the preset frequency on the frequency converter. The built in fluid separator was not working perfectly and the side channel blower sucked every time a little amount of the used model fluid into the system by lowering the efficiency of the blower and hereby also the pressure difference measured in the Tuyere. This is the reason of the lower pressure differences at the same preset frequencies, which can be seen in *Table 16, 17, 18*.

Considering these possible improvements and changes the quality of the recording (not to mention the data processing) would have a better quality. This would allow to have an easier evaluation which would deliver more accurate, more detailed results. Using these results the comparisons between the model fluids would deliver more information.

IV. Second example - momentum of an air - water propellant rocket

The investigation deals with a rocket filled with certain amount of water and pressurized air. The operation of the rocket is based on Newton's third law. That means that the rocket's accelerating force is a consequence of the two phase outflow at the nozzle exit. The intense atomization of the water at the nozzle outlet is the results of the pressurized air which is cutting through the water level and accelerates over the transonic region. This high speed flow lends more than enough energy for the water to desintegrate after the nozzle.

In this case the atomization is just the consequence of the high speed two phase outflow and the investigation brings rather the generated momentum into focus as the emerging drop size distribution.

IV. 1. Introduction of the rocket

The rocket itself is a thin walled chambered plastic construction, which can be filled with the wished amount of water and pressurized air. After the filling, the vertically aligned rocket can be started by opening the nozzle outlet. The pressurized air is pushing the water through the nozzle providing a high momentum and acceleration. After the outflow of the water the pressurized air also escapes at the nozzle outlet by delivering additional momentum until the inner pressure will be equal with the pressure of the atmosphere. At this moment the rocket will begin it's slow down until it reaches the highest altitude. At this point the velocity of the rocket is zero and it begins its free fall after opening the built in parachute.

The rocket was built for hobby purposes and was developed step by step with the goals to create a lighter construction, use better nozzles, higher pressures, achieve better aerodynamics, create a reliable parachute opening and to create a reliable launch pad for starting. To summarize the actual goal is to reach higher altitudes and be safe. The final model is also equipped with an accelero- and altimeter to measure the flight of the rocket.

IV. 2. Presentation of the problem - the goal of the investigation

The outflow of the water and air from the rocket is a very quick process and it is invisible to the naked eye. Depending from the amount of the water and air filling the exhaustion will happen somewhere between one and two seconds. The outflow of the water which is the most interesting will happen just in few tenth of seconds. How exactly the water is leaving the nozzle exit is not unambiguous. The goal is to understand the outflow of the water at two different water levels and two different nozzles. For this reason the rocket geometry will be created and meshed to prepare it for a transient CFD simulation using the volume of fluid method (VOF) in OpenFOAM. With the results of the simulation the outflow of the water at the nozzle will be more understandable. The results can also be used to calculate the created momentum, which will tell the advantages or disadvantages of the two compared nozzles. Additional goal is to calculate the drag coefficient of the rocket to know the value of the air resistance and so the drag force. The solution for this task is also the computational fluid dynamics but now in steady state.

Another challenge is to simplify the flying process, create a simplified model and calculate it analytically, numerically for validation reasons and also to prepare for the actual simulation.

IV. 3. The operation of the system

IV. 3.1. The rocket

The rocket – showed on *Figure 55* – is composed of three cylindrical chambers which are connected to each other. The diameter of the connection is much smaller than the diameter of the chambers. That is because of the shapes of the used plastic bottles and because of the required space in the rocket for the carried equipment like parachute, accelerometer, camera, battery and similar devices. The chambers are glued and reinforced PET bottles and they are connected with carbon fiber composite tubes and the bottles are reinforced from the outside additionally with another carbon texture layer with the fiber directions $+45^\circ/-45^\circ$. The last chamber is covered with the nose cone to provide better aerodynamics. The rocket has three thin fins in 120° pattern to increase the stability. The length of the rocket is 2200 mm and the diameter of the chambers is 104 mm . It has a dry mass of 1650 g . The maximal operating pressure is 22 bar . Further drawings are obtainable in *Appendix C*.

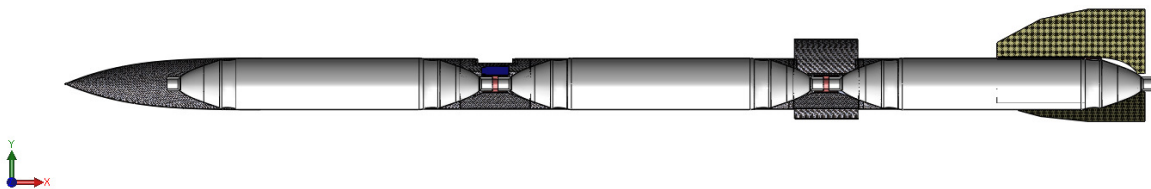


Figure 55: Buildup of the rocket (section view)

At the bottom of the rocket the nozzle can be found which is exchangeable. For the rocket four different nozzles are created, one simple nozzle and three different Laval nozzles to improve the efficiency of the air outflow. The nozzles – showed in *Figure 56* – have the same length $43,6\text{ mm}$ and the diffusor side of the Laval nozzle has a beavel-angle of 15° as listed in *Table 29*. In the thesis the simple nozzle (*nozzle 4*) and one of the Laval nozzles (*nozzle 3*) are compared to investigate the evolvement of the momentum at takeoff.

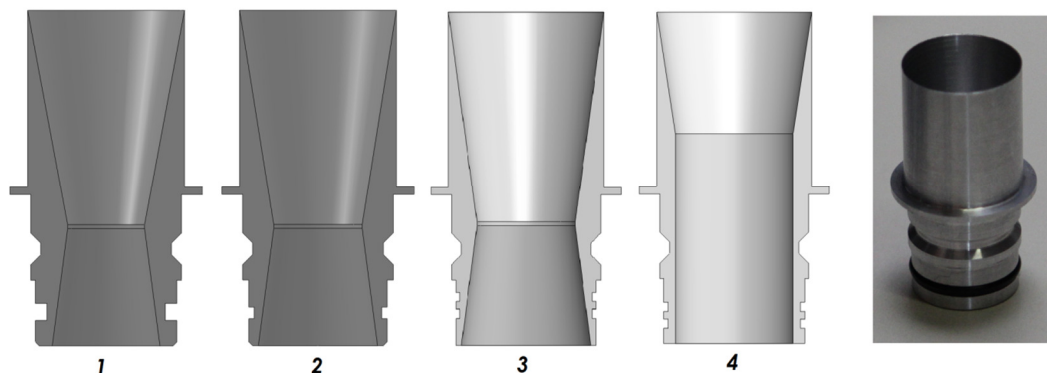


Figure 56: The CAD models of the exchangeable nozzles (left) Nozzle 2 fabricated (right)

	d_{small} [mm]	d_{large} [mm]	bevel-angle [°]
Nozzle 1	10	14	15
Nozzle 2	11,5	15,5	15
Nozzle 3	12,9	17	15
Nozzle 4	15,5	15,5	0

Table 29: Nozzle geometries

IV. 3.2. The launch pad

The launch pad, showed in *Figure 57* is a construction where the rocket is prepared for the start and later on launched. For the start the opening mechanism is responsible which holds the rocket in upright position until it is pressurized and opens as soon the rocket is ready for lift off. The pad has also a depressurizing system in case of any failure. The launching pad can be controlled with a radio remote controller to be on the safe side.

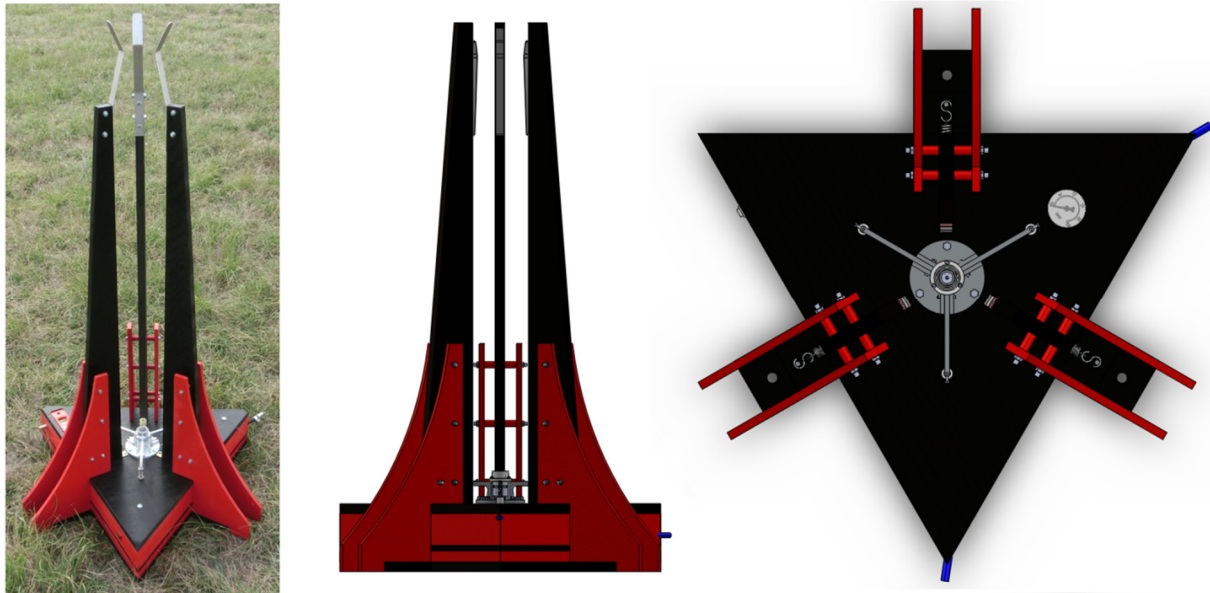


Figure 57: The launching pad. Constructed (left), CAD model (right)

IV. 3.3. The process of the flight

After positioning the launch pad it is ready to place the rocket into it. After the rocket is in the pad and the nozzle is also sitting in the right position all the electronic devices - most important is the parachute opening system - will be prepared for the flight. After this point the rocket is going to be filled with the proper amount of water. The next step is the pressurizing. As pressurized air source serves a diving cylinder with a capacity of 6 l and 300 bar pressure. Through a pressure reductor the selected air pressure can be set in the rocket. If the rocket is filled until the desired pressure, than it is

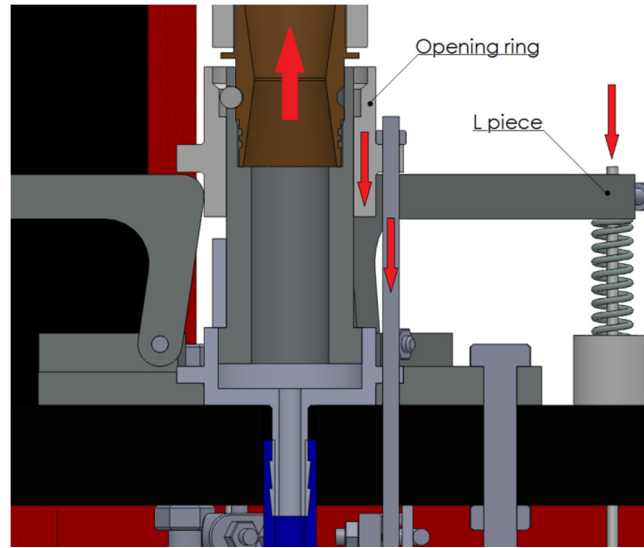


Figure 58: Section view of the launching pad

ready for the launch. The launching will be initiated with the opening mechanism. The L piece of the mechanism will be pulled down with the help of a servo, as showed in *Figure 53*. After this moment the opening ring can move freely and will be pulled down by a spring force. If the ring reaches its lowest position the ball will be pushed out by the rocket nozzle because of the pressure difference. In this moment the rocket will be free and it is able to lift off.

After the launch the lift goes on for 5-6 seconds and it can be split into three phases. In phase one all the water is pushed out from the chamber and the rocket will be accelerated. In phase two the chamber will be depressurized until it will be equal to the atmospheric pressure. At this phase the outflow velocity of the air can reach 2 Mach, hereby the rocket will be further accelerated. Phase one and phase two can also overlap for some time if the high pressure is cutting through the water level. After the propellant runs out the rocket will begin with its free fly until it slows down to zero velocity and reaches the maximum altitude. In the next step the rocket will start to fall back. The parachute will open and the rocket will land safely.

IV. 4. The selected CFD methods for the problem

Computational fluid dynamics or CFD is the procedure where the generated field of flow, or domain will be calculated by using the conservational laws of physics. CFD is applied not only in fluid flow but also in many other fields like for instance systems with heat transfer, chemical reactions, etc. The calculation itself can be quite complex and the computational need can easily explode by increasing the resolution in space and also in time. CFD has a lot of methods and models for the various challenges and by using the right model, the computation can become faster by reducing its complexity. The disadvantage of the reductions in these models is the higher imprecision, but with a well prepared mesh and simulation, chosen with the right parameters, we can reach a reasonable compromise between accuracy and computation time. In this section the author will present the models and solvers applied for the calculation.

For the simulation the open source program OpenFOAM was used. The simulation of the rocket will be split in two parts. The outer flow and the inner flow. The subject of the calculation of the outer flow is to obtain the drag coefficient. In this manner the drag force during the flight can be calculated. The computation of the inner flow is primarily responsible for the calculation of the momentum at the nozzle outflow and secondary important for understanding the two phase flow, the interaction of water and air in the first chamber of the rocket.

IV. 4.1. Outer flow

The determining of the outer flow for calculating the drag coefficient is rather a stationary problem for a simple phase turbulent flow. For this problem there are many models available. The chosen ones are the RANS based standard k- ϵ and the SST k- ω two equation, linear eddy viscosity models. RANS stands for Reynolds-averaged Navier-Stokes equations where the complexity of the turbulence is simplified by breaking up the physical variables of the flow into a mean value and into a value which is fluctuating around this mean value as written by Willinger [15]. The method – illustrated in *Figure 54* – has the advantage, that the value of the fluctuating component will be zero. The breaking up looks like in the case of the velocity:

$$u(x, y, z, t) = \bar{u}(x, y, z, t) + u'(x, y, z, t) \quad (24.)$$

Using this procedure in a stationary case the conservation equations – as written in [15], [16] – will transform to:

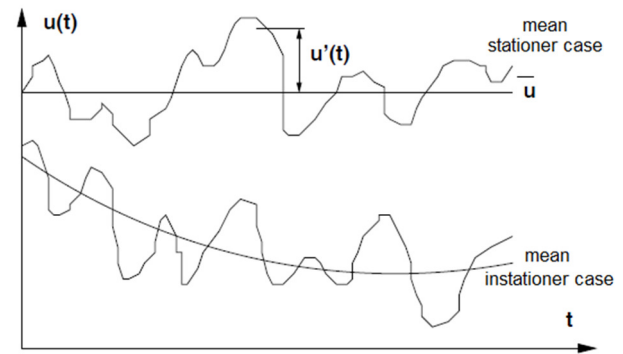


Figure 59: $u(x, y, z, t)$ in stationary and unsteady case [15]

Average conservation of mass:

$$\nabla \cdot (\rho \mathbf{U}) = 0 \quad (25.)$$

Average conservation of momentum:

$$\nabla \cdot (\rho U_i \mathbf{U}) = -\frac{\partial P}{\partial x_i} + \nabla \cdot (\mu U_i) - \left(\frac{\partial(\rho \overline{u'u'})}{\partial x} + \frac{\partial(\rho \overline{v'u'})}{\partial y} + \frac{\partial(\rho \overline{w'u'})}{\partial z} \right) + S_{Mi} \quad (26.)$$

Average conservation of passive scalars (\tilde{e}):

$$\nabla \cdot (\rho E U) = \nabla \cdot (k \nabla T) - \left(\frac{\partial(\rho \overline{u'e'})}{\partial x} + \frac{\partial(\rho \overline{v'e'})}{\partial y} + \frac{\partial(\rho \overline{w'e'})}{\partial z} \right) + S_e \quad (27.)$$

After the transformation new unknowns, turbulent stresses ($\rho \overline{u'u'}$, $\rho \overline{v'u'}$, ...) and turbulent fluxes show up. To solve the presented system of equations additional equations are needed which are arising from the chosen turbulent model. The mentioned turbulent stresses will be calculated with the help of the Boussinesq hypothesis where these stresses can be described as:

$$\tau_{ij,turb} = -\rho \overline{u'_i u'_j} = \nu_t \left(\frac{\partial U_i}{\partial x_j} + \frac{\partial U_j}{\partial x_i} \right) - \frac{2}{3} k \delta_{ij} \quad (28.)$$

where ν_t is the so called turbulent viscosity. The turbulent viscosity is modeled differently in the used models as showed in [15]. For $k - \varepsilon$ model the viscosity is modeled:

$$\nu_t = C_\mu \frac{k^2}{\varepsilon} \quad (28.a)$$

Introducing in the case of $k - \varepsilon$ model, the variables turbulent kinetic energy k , and the dissipation rate ε , the system of equation ends up with two additional self-dependent transport equations. In the case of the SST $k-\omega$, the viscosity, hence the turbulence is modeled differently and the two transport equations are governed by k and ω , where ω is called as the specific dissipation rate. A detailed description of the derivation and the transport equations can be found under [15].

For solving these equations the OpenFOAM standard solvers were used. The only addition in the simulation was the calculation of the drag coefficient. For this reason following additional information had to be used:

- The direction of the flow
- The absolute magnitude of the flow
- Density of the flowing fluid
- The area of the largest cross section of the rocket, normal to the flow direction
- Defining all the surfaces which have an impact on the drag coefficient

The used settings in the OpenFOAM file „controlDict” can be found in *Appendix B*

Another important thing at the calculation of the drag coefficient is the impact of y^+ . At turbulent flows and higher Reynolds numbers the resolution of the laminar region of the boundary layer can be difficult and end up in very high computation needs. For this reason the first cell layer on the surface is calculated with the help of wall functions. The velocity distribution in the boundary layer looks like *Figure 60*.

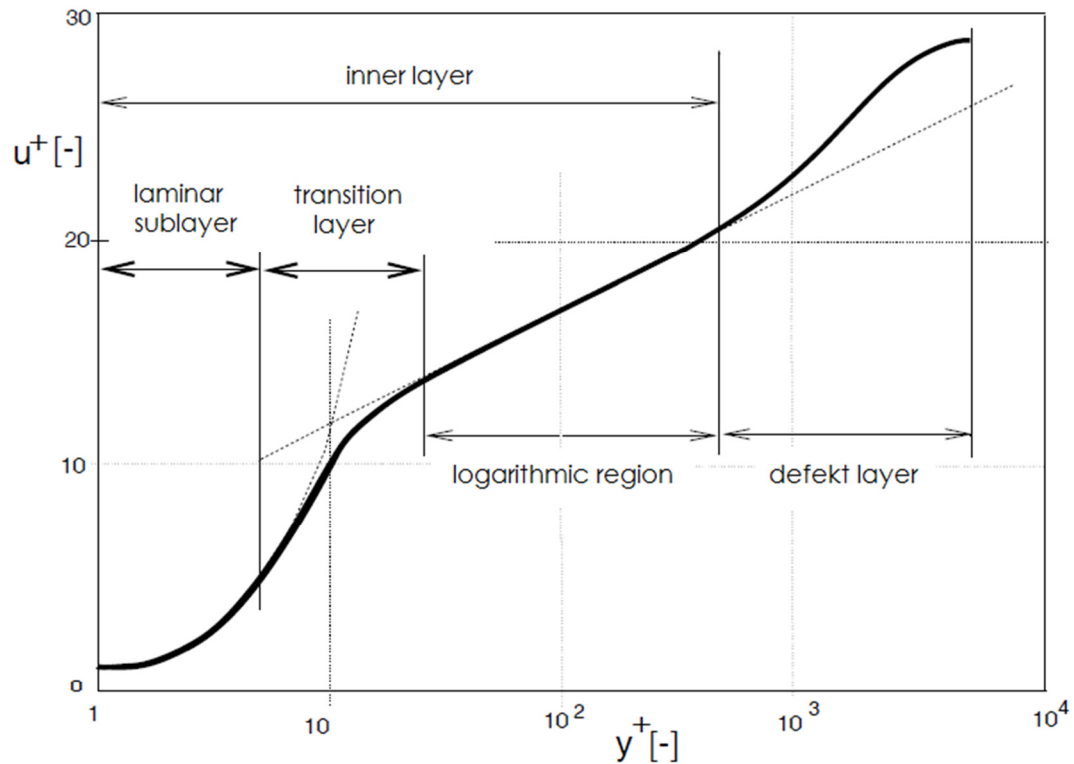


Figure 60: Velocity distribution in the boundary layer. Source: [15]

It can be seen that the change of velocity at high Reynolds numbers is be high in the laminar sublayer. That is the reason why in the case of using no wall function the number of cells and so the calculation need would diverge.

This universal velocity distribution combines multiple laws. In the laminar sublayer for instance applies the rule $u^+ = y^+$ until $y^+ < 5$. From this point until $y^+ = 30$ the function transforms into the logarithmic law. This is the most important region regarding the simulation. At high Reynolds numbers as our case the first cell will be calculated with the help of wall functions. In this case at the mesh creation it is important to hold y^+ between the values 30 and 300. $y^+ = 300$ is the upper limit and with respect to the accuracy it is advantageous to be near to $y^+ = 30$ as possible. At bodies with different velocities near to the surface the creation of a constant y^+ can be challenging. That is why y^+ is not constant all over the surface and can be described in the created mesh rather with an average value or by an interval like $a < y^+ < b$.

IV. 4.2. Inner flow

The inner flow is a much more complex computation, because it is a multiphase, transient flow including turbulence. The velocities at the nozzle region are in the supersonic region. Despite the complexity the process can be computed also with a standard OpenFOAM solver, compressibleInterFoam. The solver is intended for two compressible, isothermal immiscible fluids using a volume of fluid approach, as explained in [17]. In our case the two fluids are water and air without the need of the air dissolving in the water, hence the solver seems to be right for the job.

For the modeling of the turbulence, Large Eddy Simulation (LES) was applied. LES has the advantage that the ratio of the resolving and modeling at the computation is better than in the case of any RANS model and it delivers more accurate results if sufficiently fine grid resolution is used. The assumption that the large eddies of the flow are dependent on the geometry allows to explicitly solve for the large eddies in a calculation. The smaller eddies will be calculated implicitly, usually by employing the Boussinesq hypothesis. Therefore it needs a better mesh quality and longer computation time. For the modeling of the turbulence in this case in OpenFOAM the model „oneEqEddy” LES k equation eddy-viscosity model was applied. [17], page U-105

„The solution for the multiphase flow will be the VoF method which is already delivered by the solver compressibleInterFoam. „The volume of fluid method is based on the idea of so called fraction function C . It is defined as the integral of fluid's characteristic function in the control volume (namely volume of a computational grid cell). Basically, when the cell is empty (there is no traced fluid inside) value of C is zero, if cell is full, we have $C = 1$, and when the interphasal interface cuts the cell, then $0 < C < 1$. C is a discontinuous function, its value jumps from 0 to 1 when the argument moves into interior of traced phase.”

„The nature of the VOF method means that an interface between the species is not explicitly computed, but rather emerges as a property of the phase fraction field. Since the phase fraction can have any value between 0 and 1, the interface is never sharply defined, but occupies a volume around the region where a sharp interface should exist.” Source: [17] page U-56

The described fraction function C is a scalar function and will be solved separately from the LES equations.

IV. 5. Determining the drag coefficient of the rocket - simulation of the outer flow

IV. 5.1. Preparative simulations

After choosing the RANS two equation models, the next step was to prepare the solver with the proper boundary conditions and turbulent values, k , ϵ and ω . For this reason the first preparative simulation was a long empty air cylinder with the equal diameter as the final outer domain planned for the rocket. At the top of the air cylinder - *Figure 61* - is the velocity inlet with the value of $44,5 \text{ m/s}$ which is around of the maximal flying speed of the rocket. In this stationary simulation we make it possible for the turbulent flow to develop until the bottom of the cylinder. The result shows, that the deviation of the turbulent values is high between the inlet and outlet, especially at lower velocities as presented later in *Table 30*. With this procedure the turbulent values can be obtained. These calculated values at the outlet of the cylinder will be used as inlet turbulent values at the actual simulation at the rocket and also in all preparative simulations. Using this procedure the values of the turbulent properties will be closer to the reality as the initially used standard values in OpenFOAM. The same simulation was carried out also for $k - \omega$, to be able to apply the RANS SST $k - \omega$ model by using 165000 cells in the air cylinder domain.

Before we move to the actual challenge, first simpler cases will be computed for validation reasons. We will start with the computation of the drag coefficient of a simple sphere and this will be followed by a long cylinder with a half sphere as a head. These simulations have the advantage that they are simpler than the actual case, the number of cells is much lower and the mesh generation is quicker and simpler. These simple cases can be calculated quick even with using just few cores, unlike the final simulation. Therefore more different cases were computed until the boundary layer, the velocity field and so the drag coefficient were satisfactory. The created mesh in all cases used hexahedral mesh only.

As validation the c_D function, created by Morrison [18] will be used. This curve represents the drag coefficient in function of the Reynolds number in the case of a smooth sphere and it is valid for uniform flows. The equation of the function is also given in explicit form in the drag coefficient. The described function by Morrison corresponds well with the function, created via measurements in *Figure 68*, taken from [19]. It is not recommended to use the equation in case of higher Reynolds number as of 10^6 . The value of the Reynolds number in our case is not higher than $1,57 \cdot 10^5$, that means that the function is appropriate for our task.

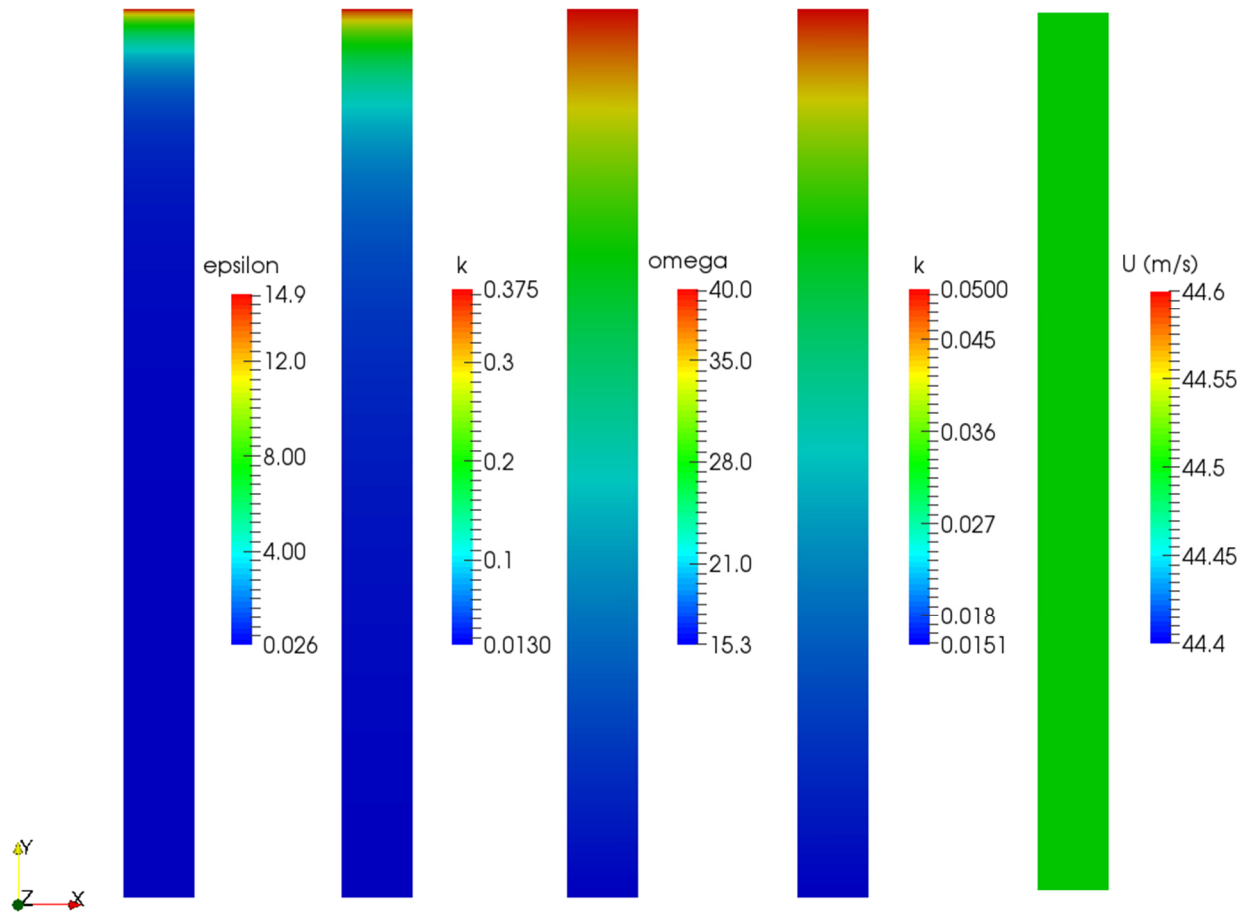


Figure 61: Cross section of the cylinder domain.

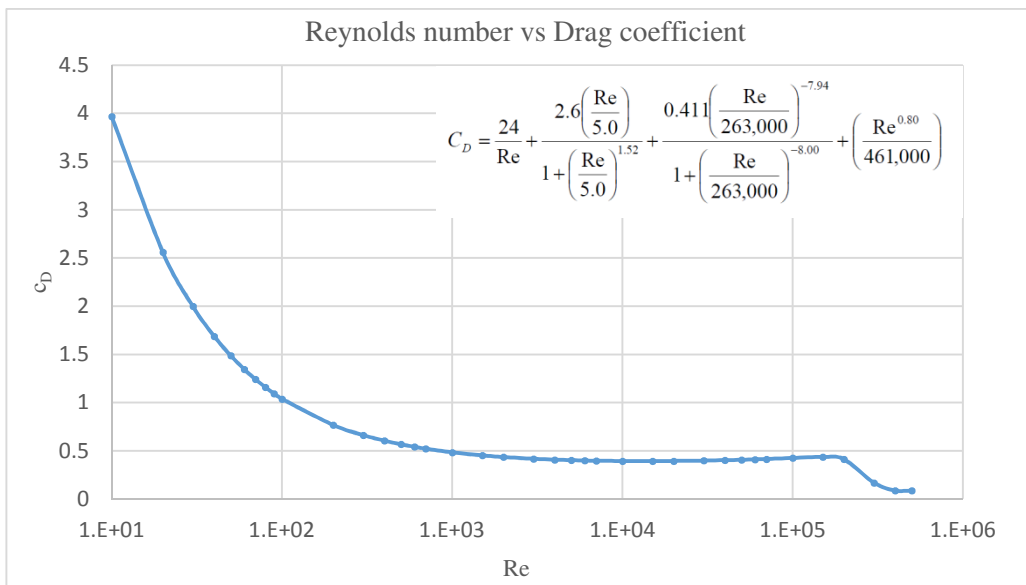


Figure 62: Drag coefficient curve for a sphere and the equation from Morrison [24]

The simulated sphere had a diameter of 40 mm and the domain had a cylindrical shape, with the measures showed in *Table 32*. The simulation was calculated for two turbulent cases with 40 and 50 m/s velocities with the OpenFOAM solvers "simpleFoam" and "rhoSimpleFoam". In the case of simpleFoam just the RANS standard $k - \varepsilon$ model was used, but using the solver rhoSimpleFoam both models RANS standard $k - \varepsilon$ and RANS SST $k - \omega$ were applied. To reduce the impact of the size of the domain, the diameter of the cylinder was increased in an additional case, showed in *Table 32*.

The results of these preparative simulations are listed below in *Table 31*. In the table the value obtained from the Morrison equation was chosen as reference. For all the simulated results the deviation is also represented below all the obtained drag coefficients using each model. The number of cells at the "normal" mesh where increased until the point where the impact of the rise had no more effect on c_D . It was perceivable that the impact on c_D derives much more from the first layers of the mesh - the setting of y^+ - as from the number of cells in the whole domain. In the case of the "extended" mesh, the diameter of the normal mesh was increased. The core of the extended mesh is the same as the normal. The results delivered that the further extension of the normal mesh has no impact on the calculation. A larger difference was registered in the different solvers which is also listed below.

Turbulent model			45 [m/s]	30 [m/s]	20 [m/s]	10 [m/s]
Standard $k - \varepsilon$	Turbulent kinetic energy	k	$1,3 \cdot 10^{-2}$	$8,6 \cdot 10^{-3}$	$5,7 \cdot 10^{-3}$	$2,6 \cdot 10^{-3}$
	Turbulent dissipation	ε	$2,6 \cdot 10^{-2}$	$1,2 \cdot 10^{-2}$	$6 \cdot 10^{-3}$	$1,5 \cdot 10^{-3}$
SST $k - \omega$	Turbulent kinetic energy	k	$1,5 \cdot 10^{-2}$	$1,1 \cdot 10^{-2}$	$7,6 \cdot 10^{-3}$	$3,8 \cdot 10^{-3}$
	Specific dissipation	ω	15	12	9	5

Table 30: The used turbulent values for the inlet

u [m/s]	Re [-]	$c_D(Re)$ Morrison	y^+	Mesh class	simpleFoam RANS $k-\varepsilon$	rhoSimpleFoam RANS $k-\varepsilon$	rhoSimpleFoam RANS $k-\omega$
40	$1,05 \cdot 10^5$	0,426	$y_{avg}^+ = 55,4$	Normal	0,403 (5,7%)	0,428 (0,5%)	0,407 (4,5%)
				Extended	0,4 (6,1%)	0,43 (0,9%)	-
50	$1,31 \cdot 10^5$	0,433	$y_{avg}^+ = 62,2$	Normal	0,4 (8,3%)	0,427 (1,4%)	0,407 (6%)
				Extended	0,396 (8,5%)	0,428 (1,2%)	-

Table 31: Results of the drag coefficient for different calculation methods

	Length [mm]	Diameter [mm]	Number of cells	Position of the sphere [mm]
Normal mesh	800	300	170.000	200 from the inlet
Extended mesh	800	640	240.000	200 from the inlet

Table 32: Properties of the different sphere hexahedral meshes

The further results of the simulation for the normal mesh with 50 m/s set as inlet velocity as shown in *Figure 63, 64*. The value of the drag coefficient - compared to the function presented by Morrison - and the velocity field look good enough to move to the next step. The difference between the calculated models was not strongly noticeable and they delivered nearly the same drag coefficient.

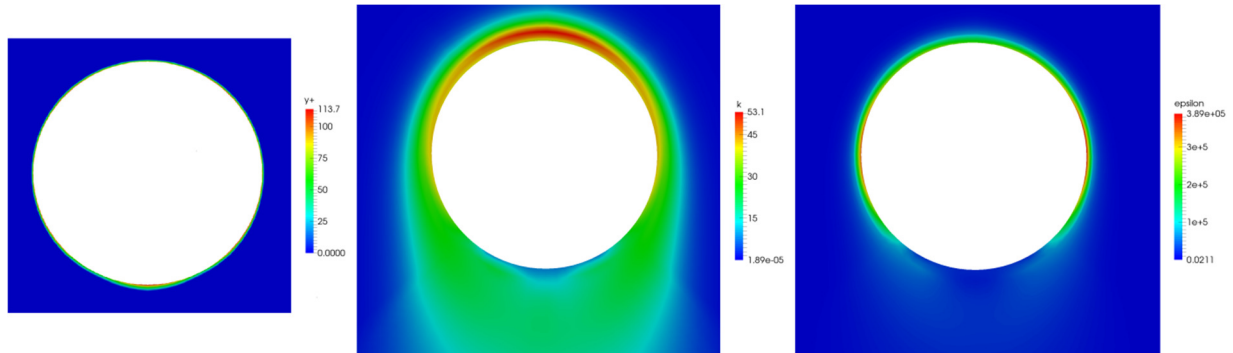


Figure 63: The value of y^+ and the field of k, ϵ in the symmetry cut plain of the sphere, $u_{inlet} = 50 \text{ m/s}$

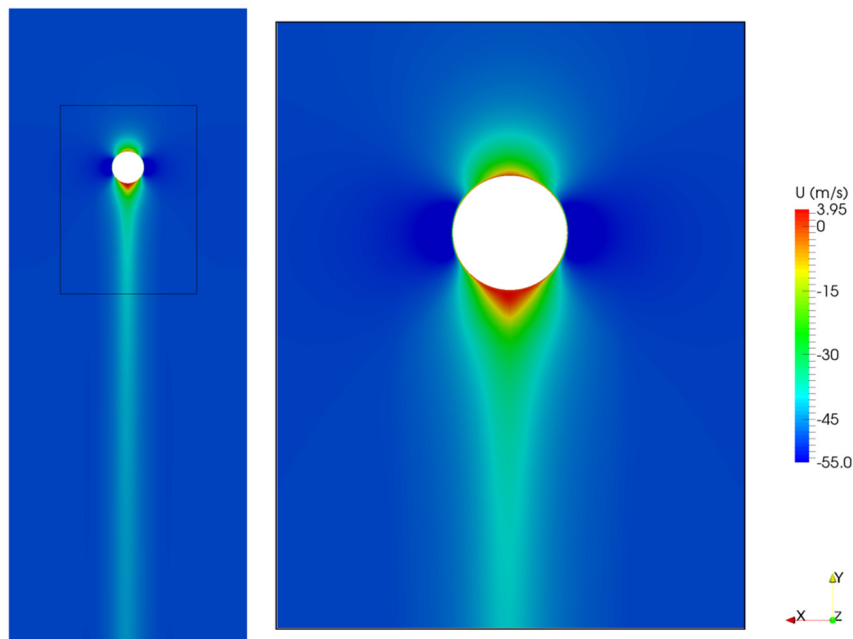


Figure 64: The velocity field u_y in the symmetry plain of the sphere (full domain) $u_{inlet} = 50 \text{ m/s}$

For safety reasons in the next step also a shape closer to the rocket was simulated with both turbulent models $k - \epsilon$ and $k - \omega$. The shape is a long cylinder ($L - r = 480 \text{ mm}$) with a half sphere head ($r = 20 \text{ mm}$). This simulation was run to check the behavior of the boundary as a in the function of the length of the cylinder. The number of cells was higher, around one million.

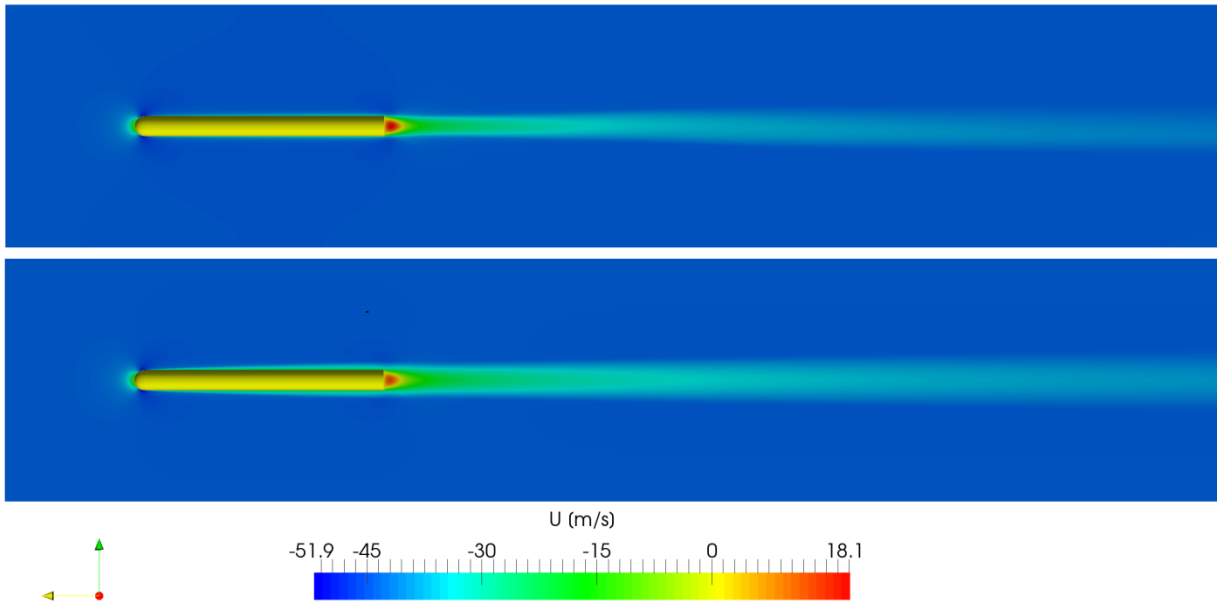


Figure 65: The velocity field of the rounded cylinder
 1. standard $k - \varepsilon$, 2. SST $k - \omega$, $u_{inlet} = 44,5 \text{ m/s}$

All the turbulent models delivered nearly accurate and similar drag coefficients until now. In the case of the SST $k - \omega$ model the size of the boundary layer was higher as it should be and also the drag coefficient was the double of the standard $k - \varepsilon$ model. This difference was only true for objects with high L/d ratio like this shape.

Simple equations for velocity distribution and shearing stress based on a very thorough experimental investigation - for velocity profiles and for the law of friction in smooth pipes - by J Nikuradse [19] were applied. As estimation respectively as validation *Equation 29a* describes the velocity profile in a smooth pipe and it is also related to Blasius's law of friction.

In the presented relation the exponent n varies slightly with the Reynolds number. As the value of the exponent $n = 7$ will be chosen which corresponds the most with Reynolds numbers around $Re = 10^5$. The approximations can be used also for flat plates because of the similarity of the velocity profiles. Applying also *Equation 29.c* for shearing stress at the wall and calculating the displacement thickness using *Equation 29.b* we will get the function of the boundary layer thickness, presented in *Equation 29.d*.

$$\frac{u}{u_{\infty}} = \left(\frac{y}{R}\right)^{\frac{1}{n=7}} \rightarrow \frac{u}{u_{\infty}} = \left(\frac{y}{\delta}\right)^{\frac{1}{n=7}} \quad (29.a), (29.b)$$

$$\frac{\tau_0}{\rho u_{\infty}^2} = 0,0225 \left(\frac{\nu}{u_{\infty} \delta}\right)^{\frac{1}{4}} = \frac{7}{72} \frac{d\delta}{dx} \quad (29.c)$$

$$\delta(x) = 0,37x \left(\frac{xu_{\infty}}{\nu}\right)^{-\frac{1}{5}} = 0,37 \frac{x}{Re^{1/5}} \quad (29.d)$$

x is the distance in the direction of the flow started from the edge of the plate. The further details of these assumption and the derivation of the presented equations can be obtained in [19].

If we assume the further similarity around the cylinder for the velocity profile as in the case of the flat plate than the presented estimation can be used least as rough estimation. The result of the estimation was $\delta_{x=400mm} = 9,4 \text{ mm}$ and the simulation with $k - \omega$ delivered $\delta_{x=400mm} \approx 19 \text{ mm}$, which is a high deviation. The $k - \varepsilon$ model delivered almost correct theoretical layer size, $\delta_{x=400mm} \approx 11 \text{ mm}$ and also an acceptable behavior of the function, as showed in *Figure 61*. The growing of the boundary layer in the function of the length of the cylinder was likewise correct. The difference between the two simulations was also noticeable in the value of the drag coefficient. The $k - \varepsilon$ model delivered a value $c_D=0,51$ and the $k - \omega$ model a result with $c_D=0,98$, which is clearly too high. This statement is based on *Figure 62*. In the right diagram the drag coefficient is represented in the function of L/d . The rounded cylinder is somewhere between the two illustrated shapes. Not even with low L/d ratio the value for this shape is that high but as seen on the diagram, a higher L/d ratio means first a much lower c_D and with further rise of this ratio the c_D increases much finer and the impact of L/d becomes lower. The diagram is valid roughly for $10^4 < Re < 10^6$ that means that it is employable for our case.

The simulations were run with the same mesh and the same boundary conditions. The boundary layer mesh had a $y_{avg}^+ = 47,8$ value. The reason of the high difference in the results was not further investigated and for the final simulation the well functioning RANS two equation standard $k - \varepsilon$ model was chosen with the solver rhoSimpleFoam.

We obtained from the preparative simulations that the highest impact derives from the created boundary layer mesh quality. Second important thing is to set at least the proper order of magnitude for the turbulent values for the inlet. If we set the inlet farther away from the simulated body, the impact of k , ε or ω will be lower because the stream can develop until it reaches the simulated object. This will cost more cells and additional calculation time. The impact of the size of the domain and the mesh quality in the far field is low.

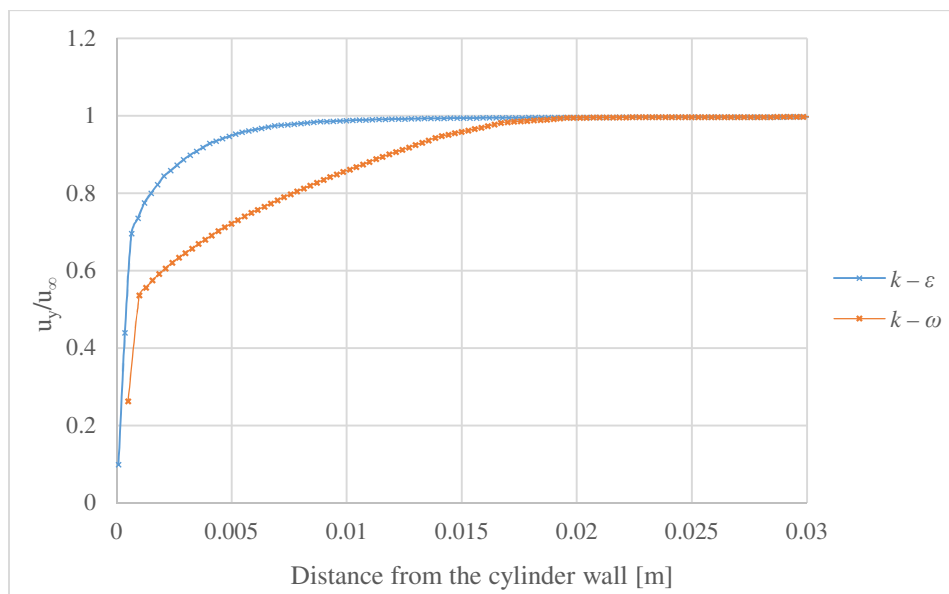


Figure 66: Boundary layer on the rounded cylinder $x = 400 \text{ mm}$

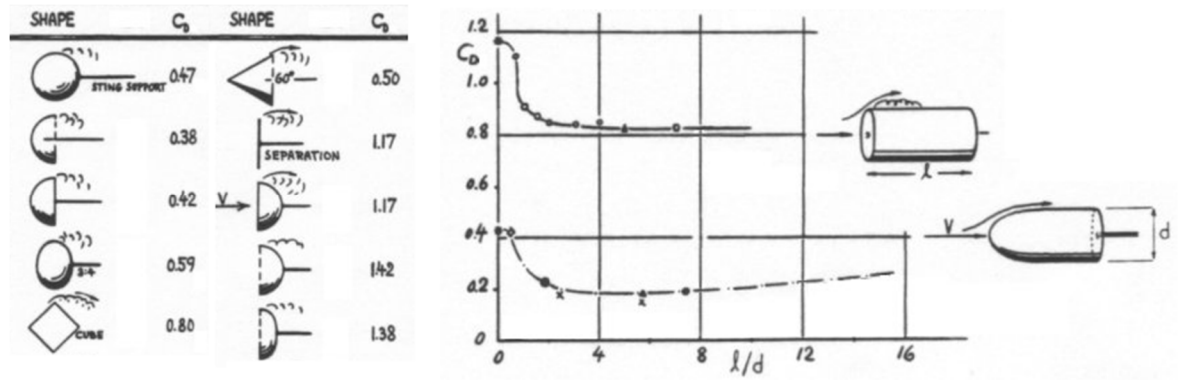


Figure 67: Values of the drag coefficient between $10^4 < Re < 10^6$
 Typical values of c_D (left) Behavior of c_D (right), Source: [20]

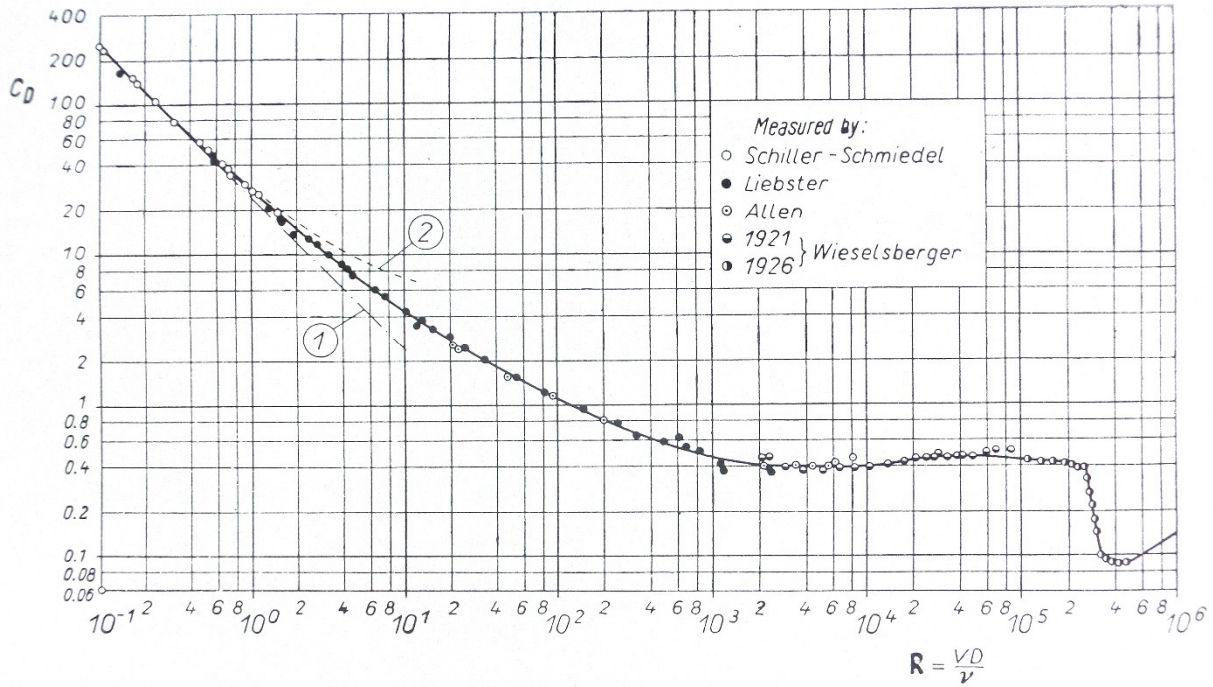


Figure 68: Drag coefficient of spheres as a function of the Re number (based on measurements) [19]

IV. 5.2. Simulation of the rocket outer flow

After performing the preparative simulations and the finding of the proper settings just few steps were missing until the final computation. First the simplified geometry was constructed with the 3D CAD design program SolidWorks [21], showed in *Figure 64*. Afterwards the geometry was imported into the meshing software Gambit [22] to create the domain, the mesh and set the patches. The created mesh was imported into OpenFOAM and after setting the boundary conditions the simulation was ready to start.

IV. 5.2.1. The geometry and the properties of the generated mesh

The geometry of the rocket was simplified a little to create friendlier meshing conditions. The small overhanging parts of the rocket like the camera – which can be removed anyway – or any roughness, small radius were ignored on the rocket surface. The final geometry of the rocket which was imported into Gambit can be seen below in *Figure 69*. As comparison the real geometry of the rocket is obtainable in *Appendix C*.

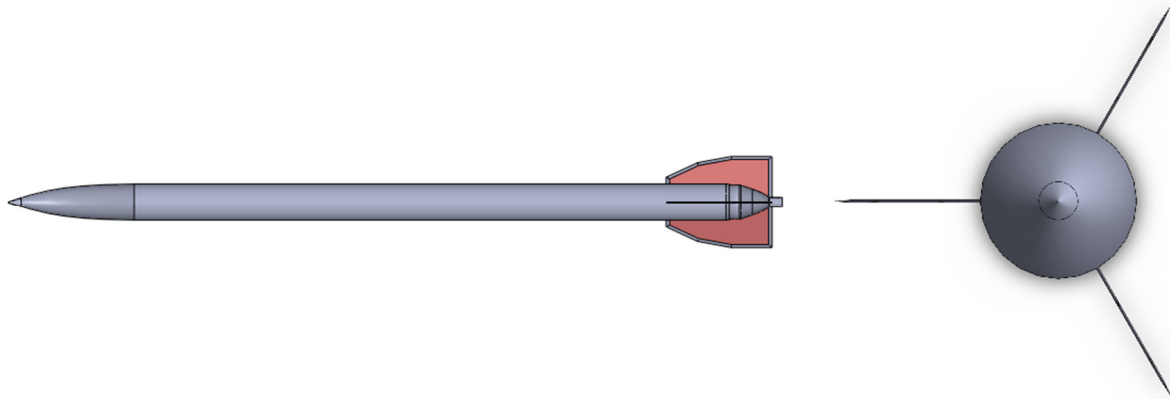


Figure 69: The import ready SolidWorks geometry

After the import into Gambit the domain and the mesh was created. To be at the safe side the length and the diameter of the domain was made larger as initially planned, but the cell size in these additional volumes were large to minimize the additional computational need. With this extension the domain ended up with a diameter of 2660 mm and a total length of 11000 mm . The origin is at the nozzle of the rocket and it is 5000 mm away from the inlet. The size of the surface used for the computation is the maximal cross section of the rocket normal to the flow direction $A_{cs} = 8,93 \cdot 10^{-3} \text{ m}^2$ which is the sum of the projection surface of the body and the three wing cross sections in axial direction.

The created mesh is hexahedral. The mesh generation was most complicated at the wing and at the nose cone area. At the generation principally the first layer mesh and the follow-up cells required the most attention for creating the proper size and density. As the created mesh was hexahedral, the dens (dens in 3D) mesh close to the surface had an effect on the far field mesh (dens only in 1D). As a consequence the generation of the far field cells required also additional attention to avoid the under-determined, flat cells. Finally the meshing was successful. The

domain was split up into 156 volumes and the number of cells in the domain reached almost ten million. The quality of the cells from the aspect of the skewness was well; the value of the maximal skewness is 0,49. The structure of the domain can be seen in *Figure 70*.

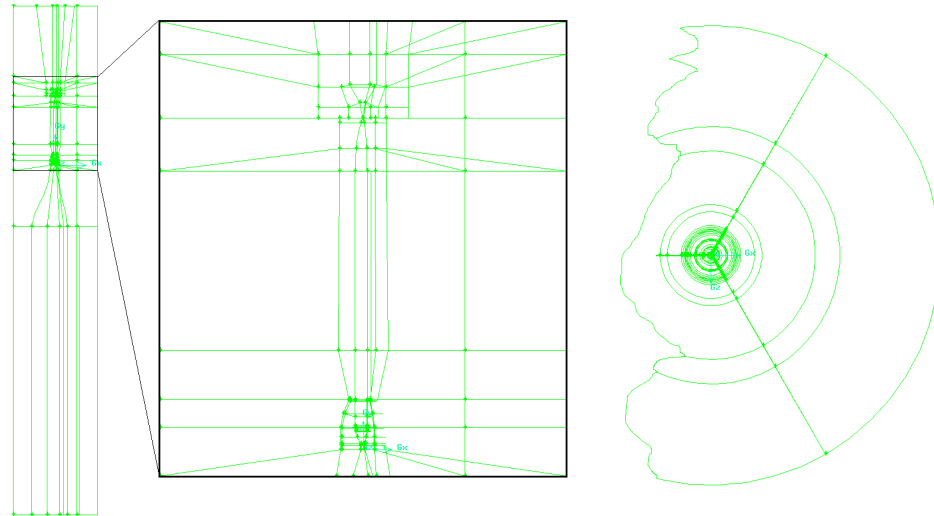


Figure 70: The structure of the domain, side view and overview

IV. 5.2.2. Results of the simulation

The simulation was computed with OpenFOAM, version 2.3. with the solver rhoSimpleFoam. For turbulent model the RANS two equation standard $k - \epsilon$ model was applied. The mesh was decomposed and calculated on 24 cores. The calculation time with these settings was about 16 hours and converged after ~ 1000 timesteps. The simulation was computed for four different velocities, see *Table 33*. The postprocessing was accomplished with the help of the open source program Paraview [23]. The results can be seen in the following *Figures 71, 72*; also in *Appendix C* and in *Table 36*. The setted boundary conditions are obtainable in *Appendix B*.

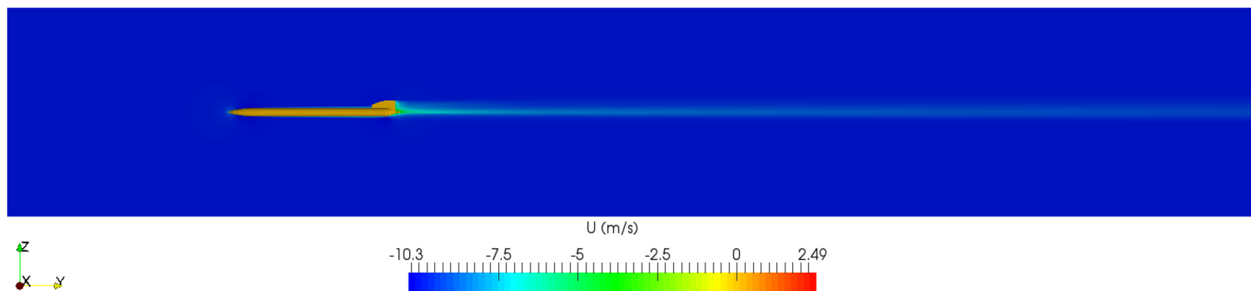
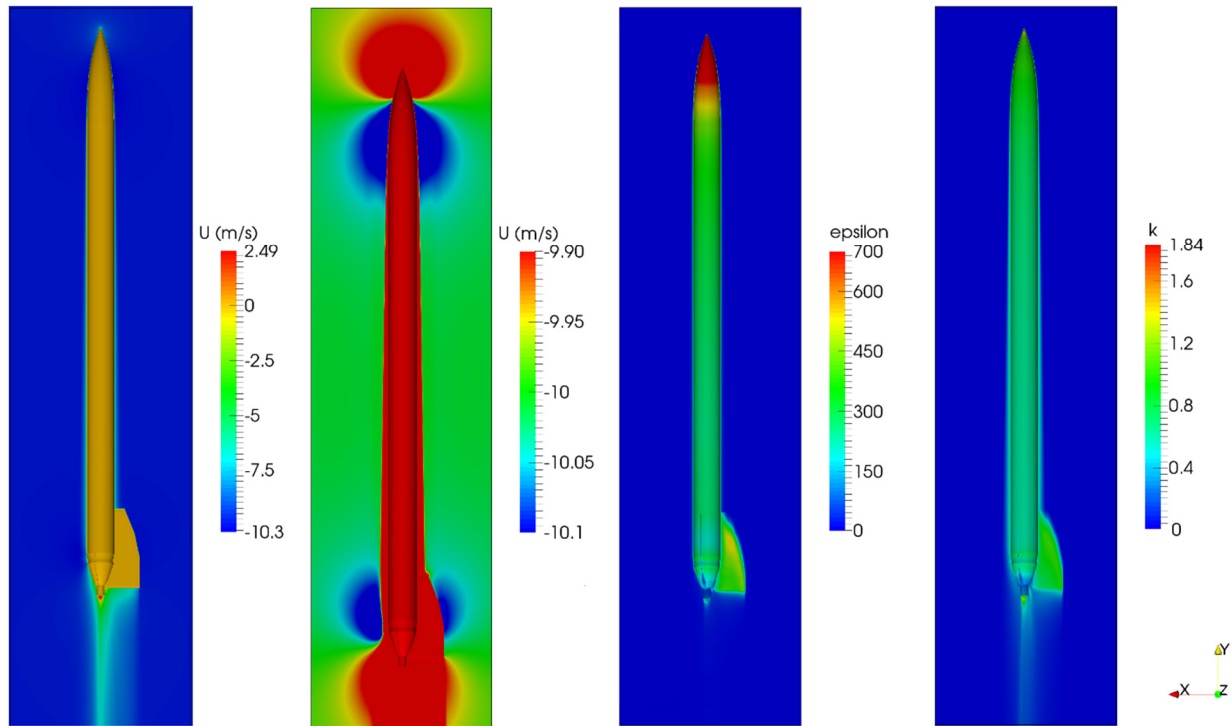


Figure 71: The velocity field u_y in the whole domain (cross section) at $u_{y,inlet} = 10 \text{ m/s}$

$u_{y, inlet} \text{ [m/s]}$	10	20	30	44,5
c_D	0,48	0,43	0,4	0,36
γ_{avg}^+	40,83	56,5	80,77	114,6

Table 33: Results of the drag coefficient for different inlet velocities

Figure 72: Part of the domain (cross section) at $u_{y,inlet} = 10 \text{ m/s}$

1. Velocity field u_y 2. The boundary layer $-9.9 < u_y < -10$, 3. The turbulent dissipation ϵ , 4. The turbulent kinetic energy k

The results in *Table 33* can be explained again with the impact of y^+ . With higher y^+ the behavior of the boundary layer and the value of the drag coefficient will change. In the interval $10 < u_{y, inlet} < 44,5$ the change of the drag coefficient should not be that high anyway. With higher velocities in the computed results the thickness of the boundary layer at the rocket surface reached an unphysical low thickness. For higher velocities the mesh has to be created again with a thinner boundary layer, to achieve reasonable results. The simulation with $u_{y, inlet} = 10 \text{ m/s}$ delivered a good boundary layer with a value of $\gamma_{avg}^+ = 40,83$, nearest to the desired $y^+ = 30$. Considering the fair results for $u_{y, inlet} = 10 \text{ m/s}$ and the fact that the change of the drag coefficient is negligible in this interval, the accepted drag coefficient for the rocket will be the value $c_D = 0,48$. The results will be further investigated under *Chapter IV.5.2.4*.

IV. 5.2.3. Calculated drag coefficient with OpenRocket

There exists another open source program called OpenRocket [24]. The program is well known and often used by hobby rocket modelers in the USA. It can be used to design and simulate model rockets with rocket motors available on the market. Therefore the program is not usable to simulate rockets with different propellants like the flying of a water - pressurized air rocket, like this. However it can be used to calculate the drag coefficient at different velocities. It is easy to use and model the existing rocket in the program. The program works quick, simple but it has also disadvantages in the calculation. For instance the program calculates with a “boundary layer” which has no laminar sublayer and is completely turbulent. The calculation of the equations in

OpenRocket happens in broad areas and volumes. These two facts are strong differences compared to CFD, but as a rough estimation and for comparison the program could be useful.

The investigated rocket was quickly modeled in the program with very little deviations. In the program also the turbulent properties, like turbulent intensity can be set, which is in our case for axial, uniform flows a low value, lower than 1 %. With the modeled rocket – *Figure 73* – and the even mentioned settings, the program delivered a function of the drag coefficient which can be seen in *Figure 74*. The program calculated not just the drag coefficient but also the components of it, base drag, friction drag and pressure drag coefficient. The base drag coefficient is a very low value with no impact on the final drag coefficient so it is not represented in the figure.



Figure 73: The modeled rocket in OpenRocket

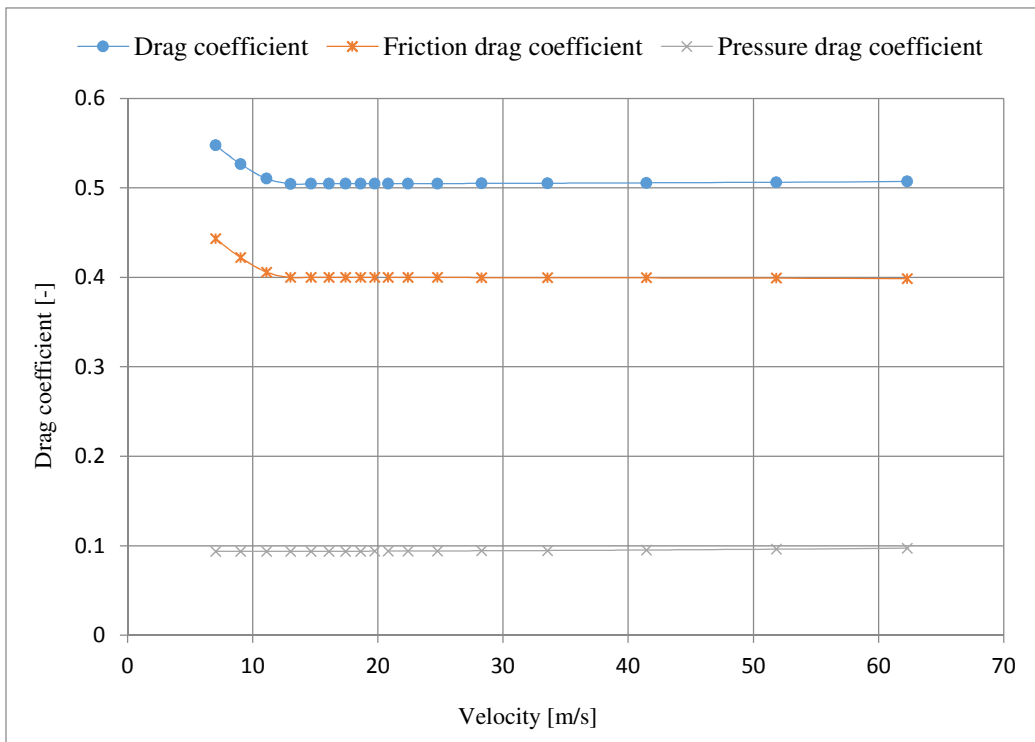


Figure 74: The drag coefficient by OpenRocket

The result for $u_y = 10 \text{ m/s}$ is $c_D = 0,52$ and after $u_y = 13 \text{ m/s}$ the drag coefficient in this interval has a constant value of $c_D = 0,505$. The pressure coefficient shows some raise but it is almost negligible. The calculated coefficient with OpenRocket is not that different, which is a positive observation.

IV. 5.2.4. Evaluation and conclusion

To inspect the velocity field a little closer and see the behavior of the boundary layer the velocity field was cut through at six different positions according to *Figure 76*. The functions of the boundary layer are looking independent and also together acceptable as showed in *Figure 75*. The thickness of the layer is at the beginning (*Slice 1*) very small, just 8 mm and this value becomes four times larger at the end (*Slice 3*) 32 mm. This behavior can be also recognized on the rocket fins at *Slice 5* and *Slice 6*. The growth of the boundary layer thickness along the rocket can be well seen also on *Figure 67/2* where the velocity legend was set to the limit 99 % of the inlet velocity, $u_y = 9,9 \text{ m/s}$. The differences in the pressure field – showed in *Appendix C* – was not significant because the rocket seemed to be a streamlined body and the effect of the pressure was low.

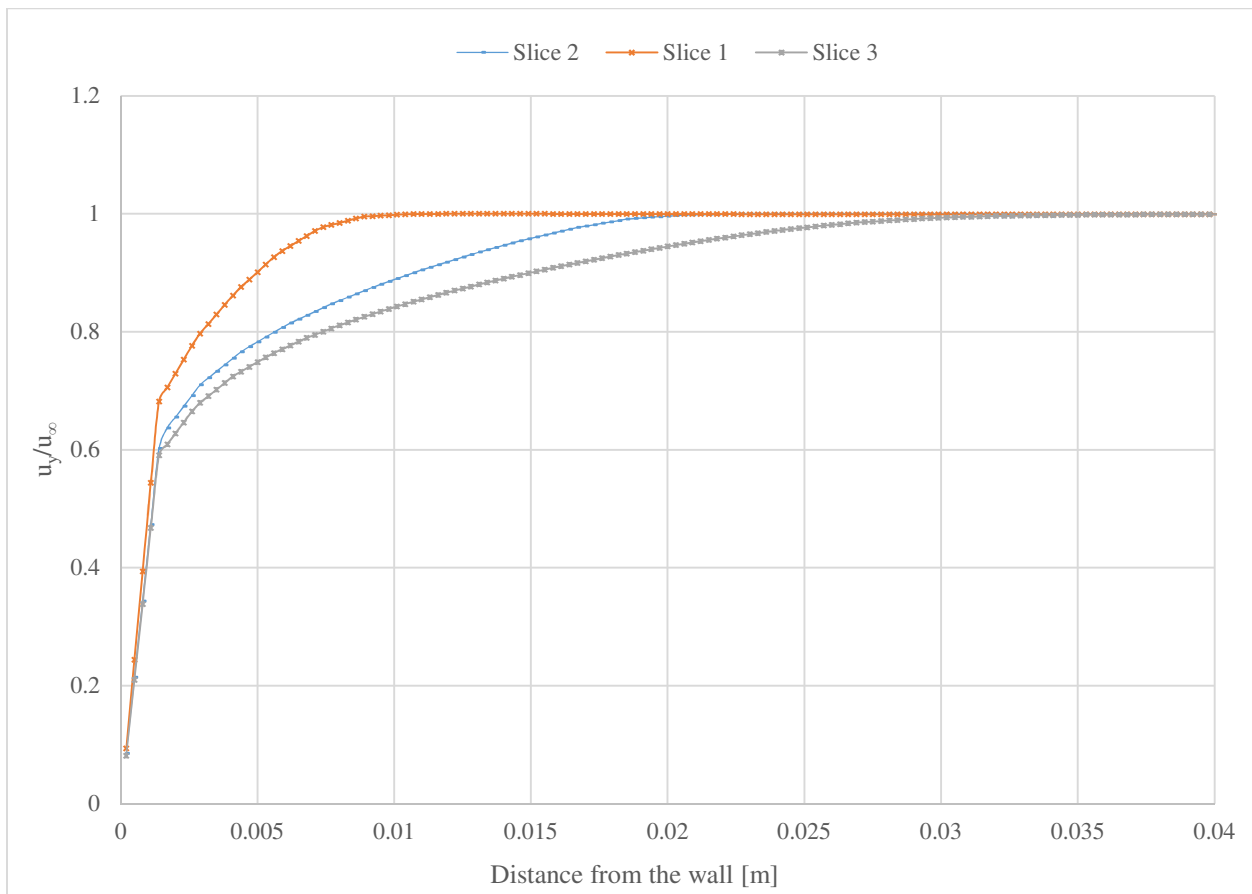


Figure 75: The growth of the boundary layer thickness in flow direction

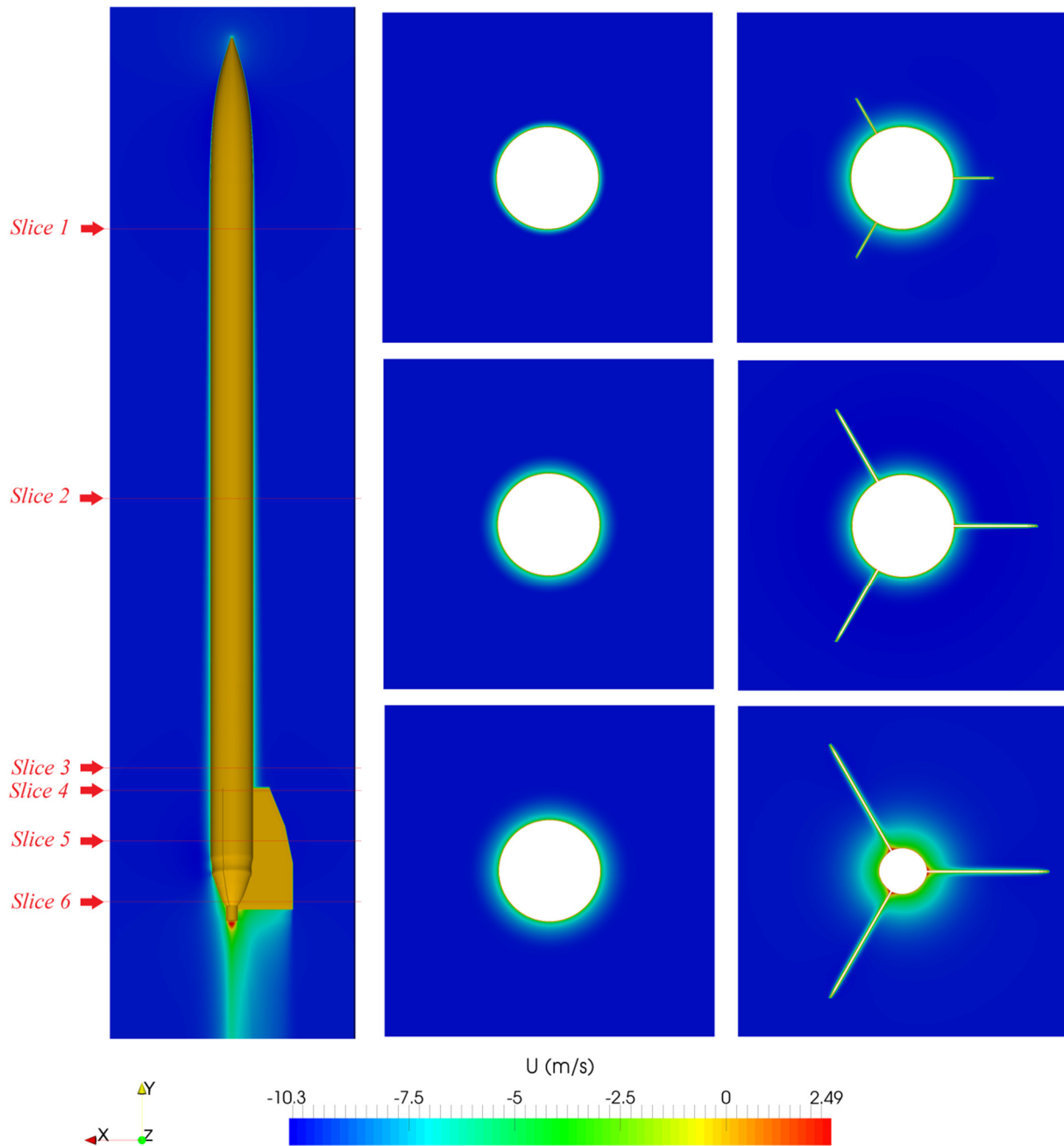


Figure 76: Velocity field of the rocket cut at six different locations

Summarising all the results we can say it with confidence that the calculated $c_D = 0,48$ is not far from the reality. The impact of the drag coefficient is more important at high speed. The value of this coefficient rises with decreasing velocity, but the effect of the coefficient is the drag force which is a quadratic function of the velocity. The value of c_D is maybe higher at lower speeds but here the impact of the drag force – at this rocket – is very low, as it can be seen later on in *Figure 76*. That is why the most important interval for the calculation is $10 < u_y < 60 \text{ m/s}$, where this coefficient is around the calculated value and does not change dramatically. This information will be enough to continue with the further steps. If there is a more accurate drag coefficient required, the problem has to be analyzed closer, with fewer simplifications and maybe also with

improved turbulence models and better boundary layer resolution. Another way to achieve an accurate drag coefficient is a wind tunnel measurement.

IV. 6. Calculating the generated momentum at the rocket nozzle - inner flow

The role of the simulation is to understand the depletion of the gas content and the liquid level inside the pressurized chambers of the rocket, especially in the case of the first chamber, which can be filled with water up to 3,5 l. A further challenge is to compute the momentum of the rocket, which is generated by the two phase outflow at the nozzle during the flight. The computation is achieved for a Laval nozzle, nozzle 3 and for a simple nozzle, nozzle 4. In these two cases the initial pressure of the rocket will be 17 bar and the water amount in the chamber will be 3 l. In an additional case, using nozzle 3 the behavior of the water in the chamber will be monitored also at a lower initial water level. By lowering the value of the surface tension it was taking into account that the used water is soapy, with the help of [25]. The initial conditions and other settings for the calculation are listed in Table 34.

	Unit	Nozzle 3	Nozzle 3	Nozzle 4	Nozzle 3
Type of calculation	[-]	CFD using OpenFOAM			Numerical calculation using Microsoft Excel
Initial pressure (absolute)	[bar]	17			
Initial water amount	l	3	2	3	3
Surface tension	[kg/s ²]	0,037, according to [25]			Not included in the calculation
Duration time of the calculation	[-]	Until depletion	Until depletion	Until the start of the two phase outflow	Until depletion

Table 34: Settings of the computations

IV. 6.1. Preparative calculations and simulations

Considering the complexity of the simulation proper preparation was indispensable. The set up of the simulation started from a basic problem and was extended step by step towards the final case setup. Parallel to this development also analytic calculations were accomplished to estimate the inlet boundary condition and also to help in the validation later on.

IV. 6.1.1. Analytical, numerical calculation of the outflow

IV. 6.1.1.1. Introducing the rocket equation, simple case

The flying of the rocket can be well described with Newton's second law respectively the momentum equation. With the help of the following *Figure 77* the equation can be constructed.

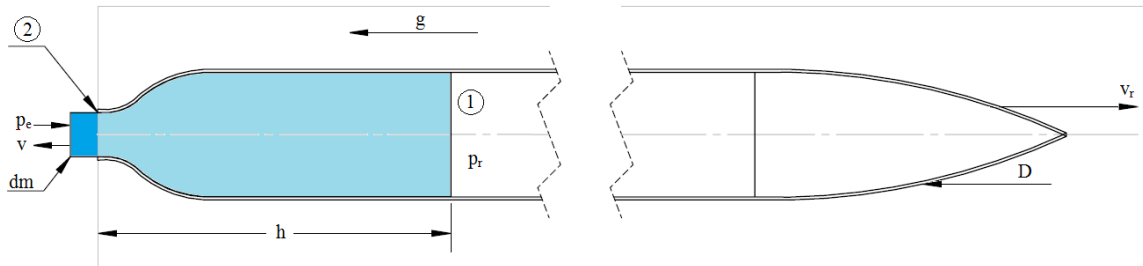


Figure 77: Sketch of the rocket

By considering a small mass, dm , which flows out from the rocket during a small time dt the change of the momentum can be described. Under the terms of conservation of momentum the change in this momentum will be equal with the momentum of the rocket. This can be also described with all the forces acting on the rocket multiplied with the time step dt .

Change in the momentum during dt :

$$m_k dv_r - u dm \quad (30.)$$

The acting forces:

$$\sum F = (p_e - p_0)A_2 - D - mg \cos \gamma \quad (31.)$$

Balance of the system:

$$m_r dv_r - u dm = [(p_e - p_0)A_2 - D - mg \cos \gamma] dt \quad (32.)$$

If we assume that

- $dm = \dot{m} dt = -\frac{dm(t)}{dt} dt$, and the mass flow is a constant value,
- the pressure of the propellant expands to the atmospheric pressure at the rocket nozzle,
- the rocket is flying straight up so $\gamma = 0$
- the drag force is negligible,

then we obtain the following simplified differential equation for the rocket:

$$m(t) \frac{dv_r}{dt} = -m(t)g + \dot{m}(t)u(t) \quad (33.)$$

$$m(t) \quad \text{total mass of the rocket} \quad (34.)$$

$$m(t) = m_f(t) + m_v \quad (35.)$$

$$m_k = m(t = 0) = m_f(t = 0) + m_v, \text{ where} \quad (36.)$$

m_k starting mass of the rocket

$m_f(t)$ mass of the propellant remaining in the rocket at t

$m_v = m(T)$ mass of the empty rocket

$$\dot{m}(t) = -\frac{dm(t)}{dt} = u\rho A_2 = K \quad \text{mass flow}$$

The solution of the equation gives the velocity of the rocket in time:

$$v_r(t) = -gt + u \ln \left(\frac{m_k}{m(t)} \right) \quad (37.)$$

The altitude of the rocket in time can be described as follows:

$$h(t) = -\frac{gt^2}{2} + u \left[\left(t - \frac{m_k}{K} \right) \ln \left(\frac{m_k}{m_k - Kt} \right) + t \right] \quad (38.)$$

The velocity of the rocket after the run out of the propellant:

$$v_r(T) = u \left[\frac{m_v}{m_k} + u \ln \left(\frac{m_k}{m_v} \right) - 1 \right] \quad (39.)$$

The altitude of the rocket after the run out of the propellant:

$$h(T) = \frac{u}{K} \left[\frac{m_k^2 - m_v^2}{2m_k} - m_v \ln \left(\frac{m_k}{m_v} \right) \right] \quad (40.)$$

The maximum altitude of the rocket:

$$h_{max} = h(T) + \frac{v_r^2(T)}{2g} \quad (41.)$$

IV. 6.1.1.2. Transforming the equation to the actual case

The *Equations 37 – 41* are describing the flight of the rocket well, thanks to the simplified circumstances. In the case of the pressurized air - water rocket these simplifications are not even nearly true. The mass flow is not constant over time anymore and not just the outflow velocity but also the density of the air is time dependent. Also the drag force of the rocket will be not negligible any more. The pressure difference at the nozzle exit is in the case of the clear outflow of water predictable. At the outflow of air this assumption at the nozzle exit is weak, but it will be handled the same as before. The fact that the rocket is flying straight up will be also handled the same way as at the simple case. At the calculation of the outflow we use the simplification that the velocity vector v is everywhere normal to the calculated cross-sectional area A_2 . Considering these conditions, the differential equation what needs to be solved looks like:

$$dv_r = \left[-g + \frac{\int_{A_2} \rho(t) u^2(t) dA}{m_k - \int_0^t \int_{A_2} \rho(t) u^2(t) dA dt} - \frac{\frac{1}{2} c_D A_r \rho_{air} v_r^2(t)}{m_k - \int_0^t \int_{A_2} \rho(t) u^2(t) dA dt} \right] dt \quad (42.)$$

If we assume that the water and air do not mix during the outflow, then the propulsion can be split in two phases, the outflow of pure water (until the time t_w) and the outflow of pure air (time interval from t_w to T). In this case the final solution for the maximum altitude would look like:

$$h_{max} = h(t_w) + h(T - t_w) + \frac{v_r^2(T)}{2g} \quad (43.)$$

This would allow to apply some simplifications for the calculation and it would make it possible to apply simple equations first for the pure water outflow and later for the transonic pure air outflow. This assumption would also make it possible to calculate with the very same nozzle geometry which would be not possible in the case of a two phase outflow. To model or approach the mixed outflow of water and air would make the calculation even harder and the approaching how the two phases mix and what kind of proportion they have at the nozzle exit is hard to forecast. It is sure that at the very beginning the outflow at the nozzle is pure water and it is also sure that at the end of the propulsion the outflow is nearly pure air. The key question is the duration of the overlap of the two stages, because the shorter it is, the more accurate is the approach. Therefore in the next step we calculate the introduced equation in the separated case numerically.

IV. 6.1.1.3. Solving the equation numerically

The numerical solution will be accomplished with more simplified equations solved for one time step. The results of t_n time step will be used as starting values for t_{n+1} . The first variable which will be calculated is the water outflow velocity in time step t_0 using the Bernoulli equation. The next stages for one time step are listed below starting with *Equation 44*. The steps and so the numerical simulation was imported and solved explicitly in Microsoft Excel with a time step size of $dt = 0,001$ s. The known variables are: $g, h, p_{r,0}, p_0, A_1, A_2, \rho_w, V_0, m_{w,0}, m_k$

1. For the outflow velocity in time step t_1 the Bernoulli and the continuity equation deliver:

$$v_{2,t} = \sqrt{\left(2(g + a_{r,t-1})h + \frac{2(p_{r,t-1} - p_0)}{\rho_w}\right) \cdot \left(\frac{(A_1 - A_2^2)}{A_1}\right)} \quad (44.)$$

where the influence of the term of the surfaces is very small, 0,0004 % therefore this term will be neglected. The influence of the force field compared to the pressure difference is also small, just 1 %. The velocity of the outflow is governed clearly by the high pressure difference as seen in *Equation 45* calculated for $t = 0,001$ s.

$$v_{2,t=0.001} = \sqrt{(65.4 + 3200) \cdot (0.99927)} = 57,123 \left[\frac{m}{s}\right] \quad (45.)$$

2. With the velocity, the theoretical mass flow and the expelled dm water mass will be calculated during dt time. With this information the dV increased air volume in the rocket and also the momentary mass will be known.

$$\dot{q}_{2,t} = v_{2,t} \rho_w A_2 \quad (46.)$$

$$dm_t = \dot{q}_{2,t} dt$$

$$m_t = m_{t-1} - dm_t$$

$$m_{water,t} = m_{water,t-1} - dm_t$$

$$dV_t = \frac{dm_t}{\rho_w}$$

3. Also the force acting on the rocket can be defined with the relative velocity.

$$F_{2,t} = (v_{2,t} - v_{r,t-1})^2 \rho A_2 - \frac{1}{2} c_D A_{cs} \rho_{air} v_{r,t-1}^2 \quad (47.)$$

4. From the calculated force the acceleration, the speed and the altitude of the rocket can be calculated easily using the following equations:

$$a_{r,t} = \frac{F_{2,t}}{m_t} \quad (48.)$$

$$v_{r,t} = a_{r,t} dt$$

$$h_{r,t} = v_{r,t} dt$$

5. The next step is to calculate the pressure decrease in the chamber after dm outflow of water:

$$V_t = V_{t-1} + dV_t \quad (49.)$$

$$p_{r,t} = \frac{p_{r,t-1} V_0}{V_t}$$

By calculating these steps we can start over with the next time step $t+1$ and continue until all the water volume m_{water} in the chamber is zero, which gives us time step $t = w$. At this point the computation for the outflow of water ends and release of the pressurized air begins.

At the outflow of water the Laval nozzle has no effect (constant density). The case is different for the air: At the outflow at a nozzle with decreasing diameter the propellant force at the nozzle exit is a sum of the force deriving from the velocity and a force deriving from the pressure difference. In this case the density, temperature, pressure and velocity are limited at the nozzle exit because the velocity of the gas can not be higher than the speed of sound and the pressure can expand only until a certain level as written in [26] page 595. This leads to high losses and to lower of the performance. This is the explanation of the first pressure term in Equation 31, because at the nozzle exit the expanded p_e pressure is still higher than the atmospheric pressure p_0 . This is only then true if the pressure ratio p_r/p_0 is higher than the critical value, presented in Equation 50 – 53. To be able to continue with the pressure expansion and the increasing of the velocity in the nozzle, an additional extension is needed. After the smallest cross section the diameter of the nozzle has to be increased progressively. These kind of nozzle is called the Laval nozzle as shown in Figure 78.

The rocket operates with way higher pressures than $p_r \approx 2 \text{ bar}$ and therefore the used nozzle is a Laval nozzle to increase the performance. Now in case of an ideal geometry the velocity can be further increased over the transonic region and there will be no pressure difference at the nozzle exit because the proper expansion. The presented calculation is valid for an isotropic, adiabatic case. The known variables are: $g, p_r, p_0, A_1, A_2=A_{throat}, A_{exit}, T_r, \kappa, a_{t=w}, v_{t=w}, h_{t=w}, R$.

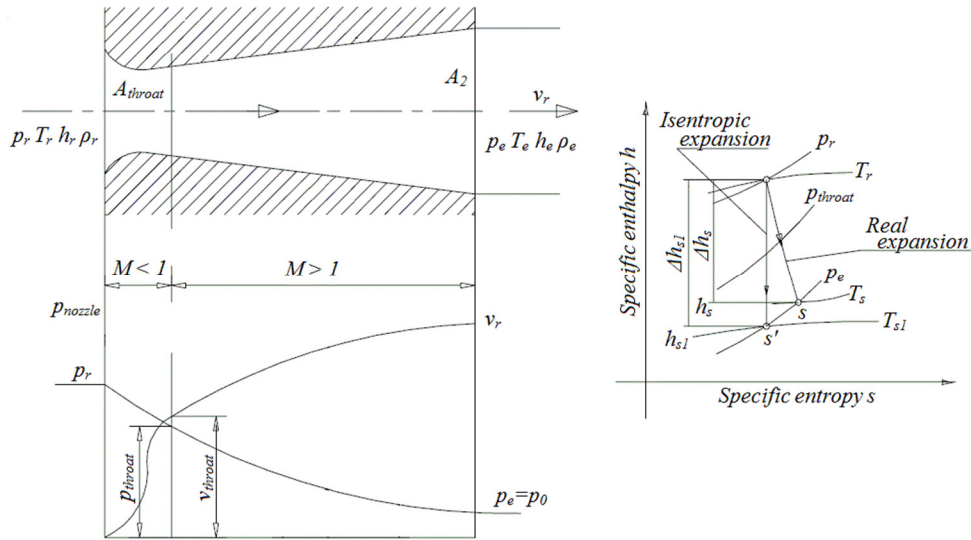


Figure 78: Velocity and expansion in the Laval nozzle, ideal case, according to [26] and [27]

With the help of the energy equation we can define the critical rates for the temperature, pressure, density and so the velocity. We obtain:

$$\frac{T_{throat}}{T_r} = \frac{2}{\kappa + 1} = 0,83 \quad (50.)$$

$$\frac{p_{throat}}{p_r} = \left(\frac{T_{throat}}{T_r}\right)^{\frac{\kappa}{\kappa-1}} = 0,53 \quad (51.)$$

$$\frac{\rho_{throat}}{\rho_r} = \left(\frac{T_{throat}}{T_r}\right)^{\frac{1}{\kappa-1}} = 0,63 \quad (52.)$$

$$v_{throat} = \sqrt{\kappa R T_{throat}} \quad (53.)$$

Now we can move from the throat to the nozzle exit by using the following (continuity) Equation 54 by assuming that the nozzle is working optimal, the expansion is isentropic and lasts until $p_e - p_0 = 0$.

$$0,63 \rho_t \sqrt{\kappa R 0,83 T_{throat}} A_2 = A_{exit} \rho_t \left(\frac{p_0}{p_r}\right)^{\frac{1}{\kappa}} \sqrt{\frac{2\kappa}{\kappa-1} R T_r \left[1 - \left(\frac{p_0}{p_r}\right)^{\frac{\kappa-1}{\kappa}}\right]} \quad (54.)$$

The theoretical mass flow during the outflow is not constant and so the velocity and the density are changing in time. That means that the optimal diameter of the nozzle exit should change during the flight to have the best performance and the assumption, that $p_e - p_0 = 0$ remains valid. Naturally the outflow diameter of the nozzle is not changing. That means that the

nozzle will perform the optimal performance just for a short time. First at the beginning of the nearly one phase air outflow the nozzle will be too short to realize the proper expansion. In this case, at too high pressure differences the nozzle will be under-expanded and the pressure difference at the nozzle exit will be a positive value, which leads to a thicker exhaust jet shape as the nozzle diameter. As the pressure in the rocket drops, the thickness of the jet will be smaller until reaching nearly the same diameter as the nozzle exit, which is the optimal case. After this point the pressure drops further by switching from an under-expanding case to the over-expanding air outflow. This has the consequence that the expansion continues over the optimum and the jet will shrink down to an even smaller diameter as the exit of the nozzle. This will result in negative pressure values at the nozzle exit due the unwished over expansion in the nozzle. This means that the optimal “location” of the expansion will change during the flight as showed in *Figure 79* and later also in *Figure 95*. The orange point marks the actual nozzle exit area for the used Laval nozzle. According to this calculation the nozzle operates for a longer time in the over-expanded condition.

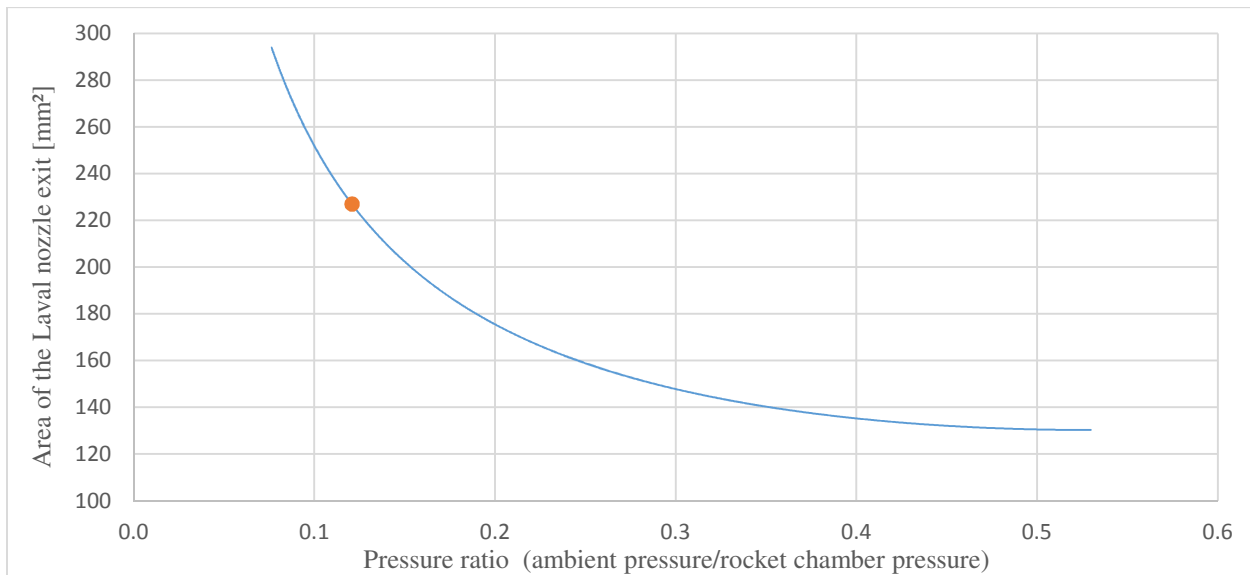


Figure 79: Optimal exit area of the nozzle at different pressure ratios

Because of the presented reason for every time step also the optimal nozzle exit diameter will be calculated and applied in the computation. If the calculated optimal diameter is smaller than the actual, than the calculated one will be used as showed in *Equation 58*. In the case of a greater optimal diameter as the existing nozzle outlet, the nozzle is with high probability under-expanded, the exit diameter of the nozzle will be applied in the calculation.

In comparison of nozzle performance for the outflow, the over-expanded nozzle is worse than the under-expanded nozzle because the nozzle's large exit area results in extra drag which derives from the negative pressure difference at the nozzle exit due to the unwished over expansion. In this numerical calculation the pressure difference will be neglected for simplification reasons.

1. First step is to calculate the nozzle outlet velocity

$$v_{2,w+n} = \sqrt{\frac{2\kappa}{\kappa-1} RT_r \left[1 - \left(\frac{p_0}{p_{r,w+n-1}} \right)^{\frac{\kappa-1}{\kappa}} \right]}, \text{ if } \frac{p_0}{p_{r,w+n-1}} > 0,53 \quad (55.)$$

$$\text{else: } v_{2,w+n} = \sqrt{\frac{2(p_{r,w+n-1} - p_0)}{\rho_{air}}} \left(\frac{A_2}{A_{exit}} \right)$$

2. Calculating the density at the exit

$$\rho_{2,w+n} = \rho_{r,w+n-1} \left(\frac{p_0}{p_{r,w+n-1}} \right)^{\frac{1}{\kappa}} \quad (56.)$$

3. The optimal cross section of the outflow

$$A_{exit_{opt,w+n}} = \frac{0,63 \rho_{r,w+n-1} \sqrt{\kappa R 0,83 T_r} A_{throat}}{\rho_{2,w+n} v_{2,w+n}} \quad (57.)$$

4. The velocity will be again used to calculate the mass flow

$$\dot{q}_{2,w+n} = v_{2,w+n} \rho_{2,w+n} A_{c,w+n} \quad (58.)$$

if $A_{exit_{opt,w+n}} > A_{exit}$, then $A_{c,w+n} = A_{exit}$, else $A_{c,w+n} = A_{exit_{opt,w+n}}$

5. The accelerating force

$$F_{2,w+n} = v_{2,w+n}^2 \rho_{2,w+n} A_{c,w+n} - \frac{1}{2} c_D A_{cs} \rho_{air} v_{r,w+n-1}^2 \quad (59.)$$

if $A_{exit_{opt,w+n}} > A_{exit}$, then $A_{c,w+n} = A_{exit}$, else $A_{c,w+n} = A_{exit_{opt,w+n}}$

6. The expelled dm and $dV_{air_{p_0}}$ during dt , calculation of the mass of the rocket. $dV_{air_{p_0}}$ is the air volume in the rocket calculated at atmospheric pressure.

$$dm_{w+n} = \dot{q}_{2,w+n} dt \quad (60.)$$

$$m_{air,w+n} = m_{air,w+n-1} - dm_{w+n}$$

$$m_{w+n} = m_{w+n-1} - dm_{w+n}$$

$$dV_{air_{p_0,w+n}} = \frac{dm_{w+n}}{\rho_{air}}$$

7. The acceleration, velocity and altitude of the rocket

$$a_{r,w+n} = \frac{F_{2,w+n}}{m_{w+n}} \quad (61.)$$

$$v_{r,w+n} = a_{r,w+n} dt$$

$$h_{r,w+n} = v_{r,w+n} dt$$

8. Finally the decrease of the pressure in the rocket

$$V_{air_{p_0},w+n} = V_{air_{p_0},w+n-1} - dV_{air_{p_0},w+n} \quad (62.)$$

$$p_{r,w+n} = \frac{V_{air_{p_0},w+n}}{V_{rocket}} p_0$$

We continue with the calculation until, $\frac{p_0}{p_{r,w+n-1}} = 0,53$. After this point the diffusor part of the nozzle does not accelerate the air anymore. Therefore the calculation changes again to the simpler equations starting with *Equation 55/2*. This is the last calculation phase until the point where p_r will be equal with p_0 , and the rocket runs out of propellant. The numerical calculation is more accurate with smaller time steps $dt \lim_{dt \rightarrow 0} H = h(t)$. The solutions of the numerical calculation with the initial settings $p_r = 17 \text{ bar}$ and $V_{water} = 3 \text{ l}$, using nozzle 3 can be seen on the following figures.

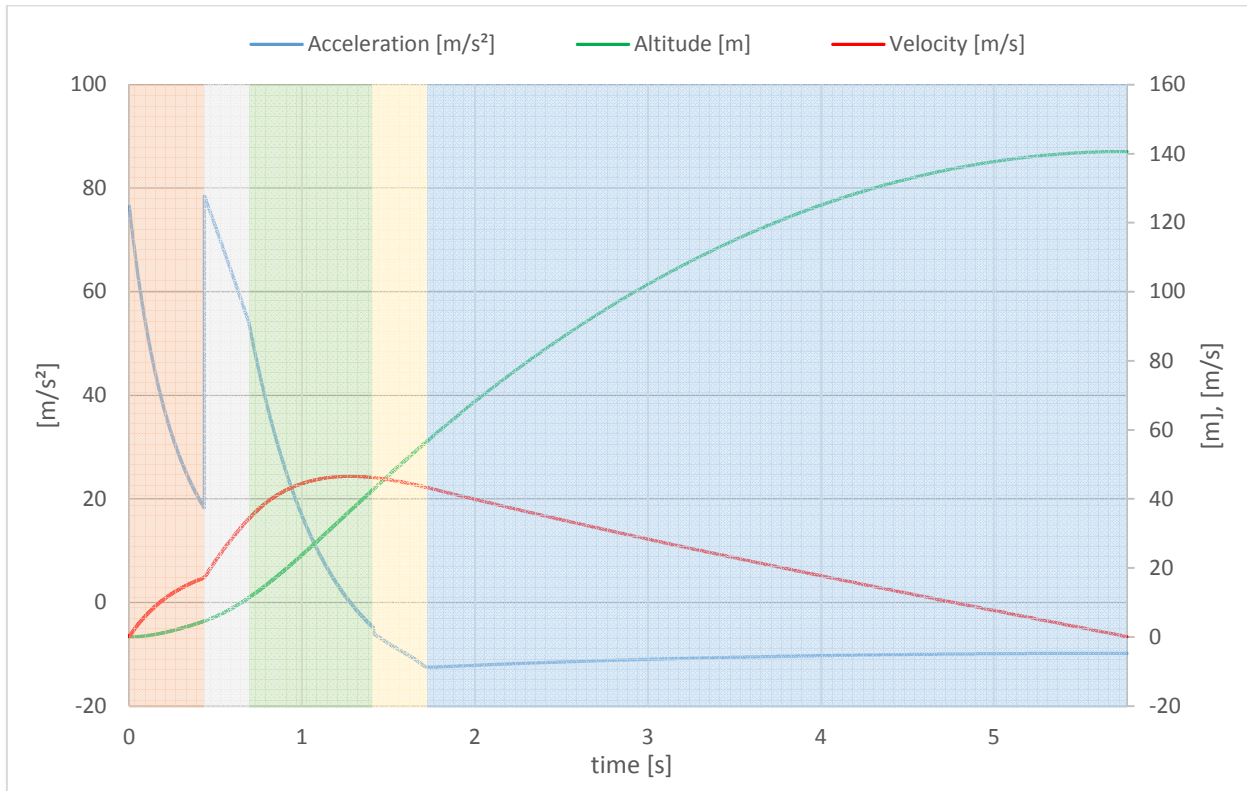


Figure 80: Flight of the rocket. Function of the acceleration, velocity and altitude in time

The two phases outflow of water and pressurized air can be recognized (separately) in the final functions, as in *Figure 80, 81, 82*. The outflow of water lasts approximately until $t = 0,5 s$ and this will be followed by the pressurized air propulsion. In reality a transition between the phases is to be expected, the border of these two phases is not that sharp.

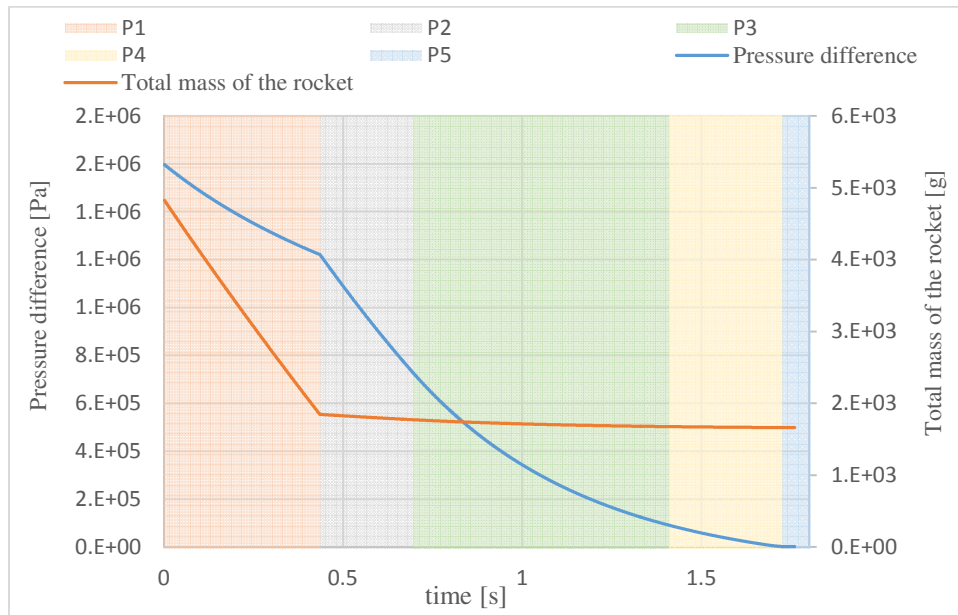


Figure 81: The function of the total mass and the pressure difference in the rocket during the flight

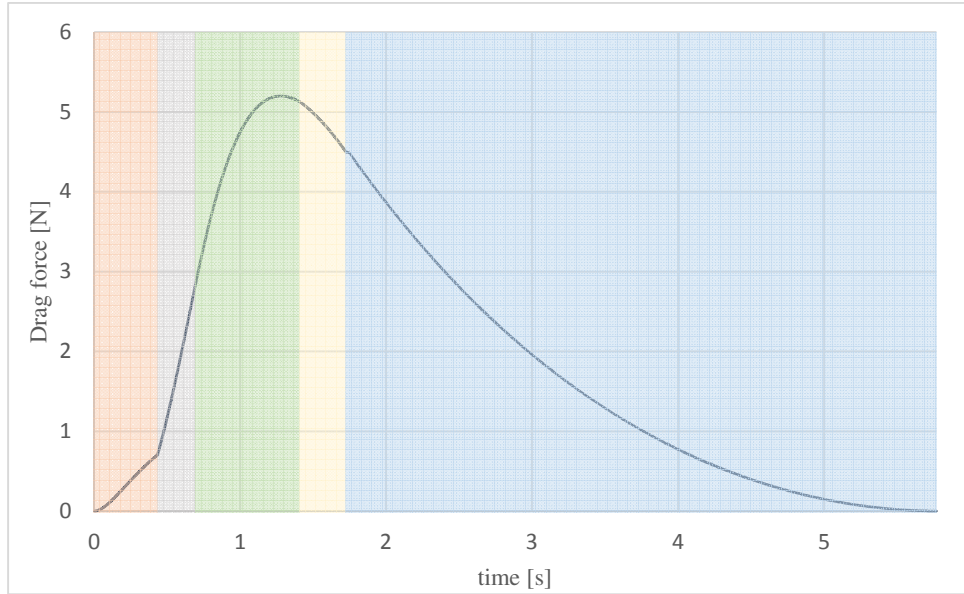


Figure 82: The function of the drag force during the flight, calculated with $c_D = 0,48$

By knowing the theoretical functions of the outflow based on the presented numerical calculation also the theoretical optimum of the water amount can be calculated, which can be seen on *Figure 83*. Naturally the rocket will reach a higher altitude with a lower dry mass. *N3_17bar** marks a function where the dry mass of the rocket is decreased by 15%. This weight loss of the rocket would lead to 30% higher altitude. Therefore it is advantageous to create lighter rocket bodies. Another option to increase the altitude is a higher operating pressure, which leads to the need for a stronger body, pressure chamber.

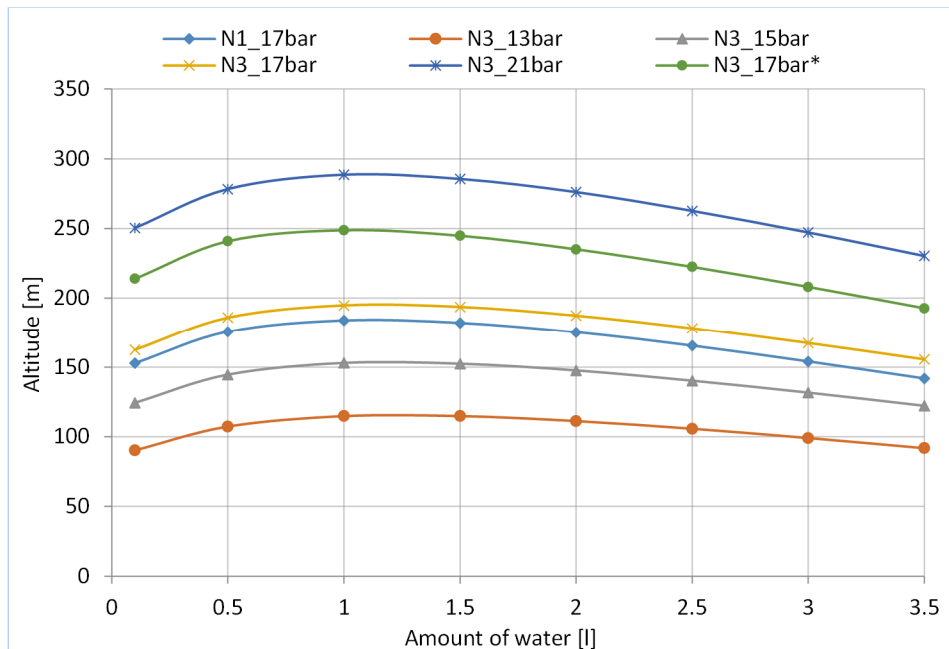


Figure 83: Theoretical optimum of the water amount

The result of the calculated drag force is presented in *Figure 82*. The relating equation of the calculation can be seen under the determination of the rocket forces, it is the second term of *Equation 47*, where the surface applied is the largest cross section of the rocket normal to the flow direction, $A_{cs} = 8,93 \cdot 10^{-3} m^2$. As seen in the figure, the impact of the drag force starts gaining weight around $t = 0,5 s$, where the speed of the rocket is around $v_r = 17 m/s$.

With these estimated information the evaluation of the simulation at the two phase outflow computed with OpenFOAM will be easier as presented later in *Chapter IV.6.2.3*. The most reliable outcome of the numerical calculation will be the results at the very beginning of the flight process. Because of the used simplifications, the deflection of the functions which are describing the flight, will be after each time step larger. Useful information are for instance the depleting time, the outflow velocity at the nozzle exit at the beginning of the water outflow, also for one phase water and air outflow for various pressure differences, etc. Using this numerical estimation we can also include at the two phase simulation a time depending velocity air inlet to simulate the rocket's rate of climb by the estimated flight speed function. By knowing these values we can move to the next step and begin with the two phase simulation for the outflow.

IV. 6.1.2. Stepwise development of the simulation setup

The actual problem was approached with small steps starting with the OpenFOAM tutorial written by Hemida [27] where the spilling of water from a capillary is simulated. This case is a simple simulation with low computational demands, calculated with the solver `interFoam` and it is a fair case to start from. The simulation was developed and expanded in every step until achieving a stable solver for the final case. The investigated case is complex and the expected computation time is high. The preparative simulations have to work stable and reliable to be able to move to the final case.

First the capillary showed in *Figure 84*, was modified to a bigger bottle with no inlet. Then the additional boundary conditions, patches were changed progressively. The domain walls were removed and the water was spilled into the free atmosphere instead of a vessel. As an additional modification the two top side boundaries were changed from atmosphere to a time depending velocity inlet to simulate the „liftoff” of the rocket. The time depending velocity inlet function was taken from the preceding analytic calculations shown in *Figure 80*.

First the case was simulated as laminar, then it was changed to the turbulent model standard $k - \varepsilon$, but finally the author decided to use an LES model. LES turbulent models need a finer mesh for the computation but considering that the VoF method alone necessitates this circumstance, the choice become easier. The next step was to switch from the solver `interFoam` to `compressibleInterFoam` to consider the compressibility of the flow, take also the Temperature into account. Afterwards the stability of the simulation was checked by moving to higher pressures and velocities. With this step also the proper function of the Laval nozzle could be checked. After the solver settings led to a convergence and to a stable result the actual case was computed first in *2D* to avoid any unexpected errors. Counting the final *2D* computation the initial case was modified in *16* steps until the final model, which is illustrated in *Figure 85*. These simulations were calculated in just few hours each, using *8 – 16* (last *2D* case *24*) cores depending on the mesh size. These preparative simulations where also important to investigate the required mesh density.

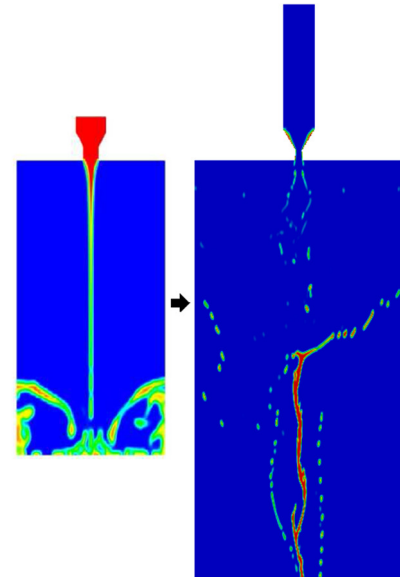


Figure 84: Case start-up

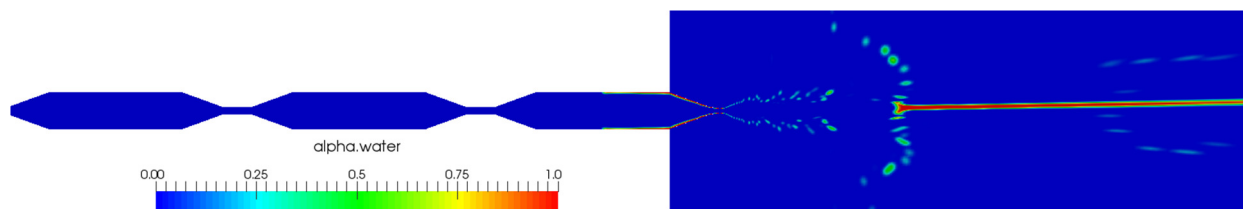


Figure 85: The simplified case in 2D

The solver in the $2D$ case functioned well in every phase of the simulation and delivered the desired results also at the Laval nozzle, even with the effect of shock waves, *Figure 86*. The fluid accelerates at the throat of the nozzle just until the speed of sound and the further behavior of the fluid in the nozzle is proper. Despite of the acceptable results, the outflow time, the behavior of the water and other properties can-not be taken completely seriously because the simulation was computed in $2D^1$. The final simulation settings and the boundary conditions can be found in *Appendix B*. Now with these promising settings we can move to the actual $3D$ case.

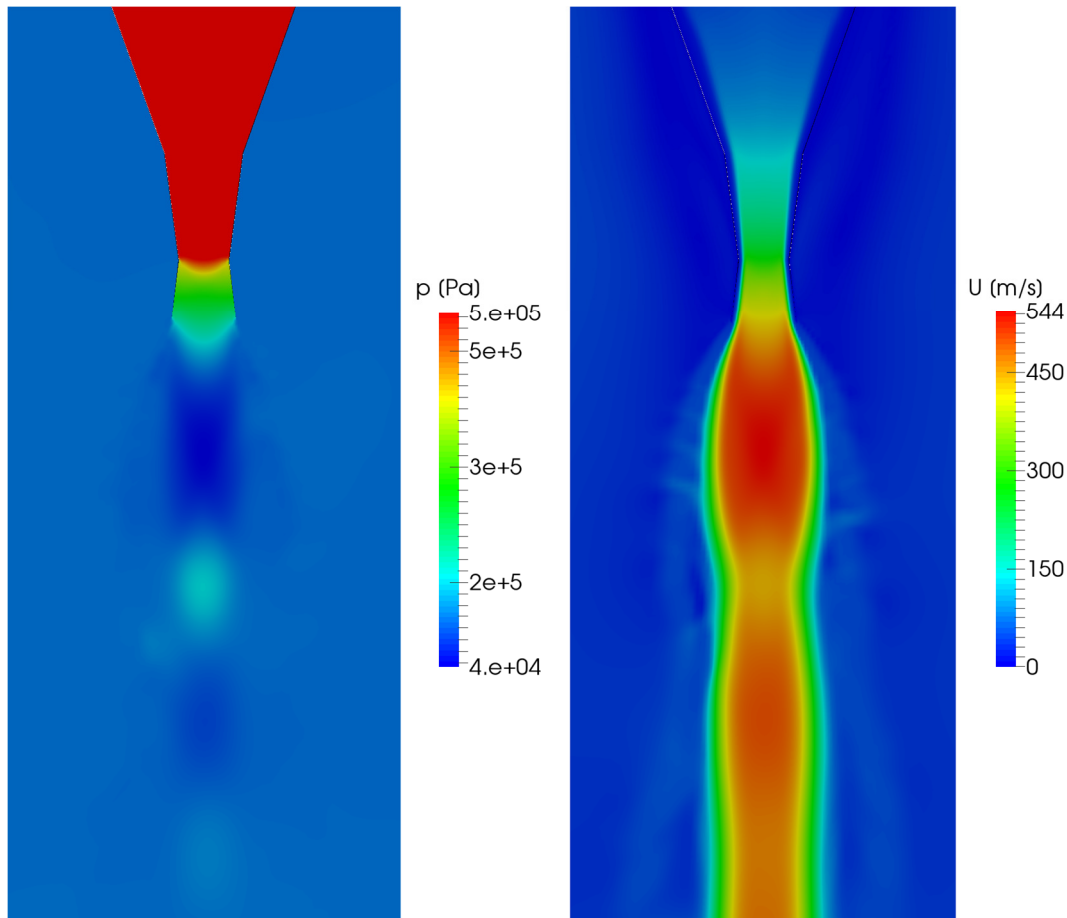


Figure 86: Pressure and velocity field after the nozzle, $2D$ case

¹LES turbulent models are invented for $3D$ cases. Nonetheless OpenFoam will allow to calculate it in a $2D$ cases. The results of these simulations were just partly important because the most significant object in these preparative simulations was to prepare the solver for a reliable usage as fast as possible. Preparing a well functioning solver with $3D$ cases would have been more time-consuming because of the calculation need, and meshing reasons.

IV. 6.2. Simulation of the rocket inner flow

IV. 6.2.1. The geometry and the properties of the generated mesh

In this case instead of the rockets outer geometry we will concentrate just on the inner buildup. The inside of the rocket is composed of three connected chambers with a nozzle at the end, as shown in *Figure 87*. The surrounding simulation volume will be extended downwards approximately with two chamber lengths. The domain will be also extended upwards to improve the effect of the time depending inlet. The created domain is cylindrical and in this case also completely axisymmetric. The diameter of the cylinder domain is five times larger as the chamber diameter.

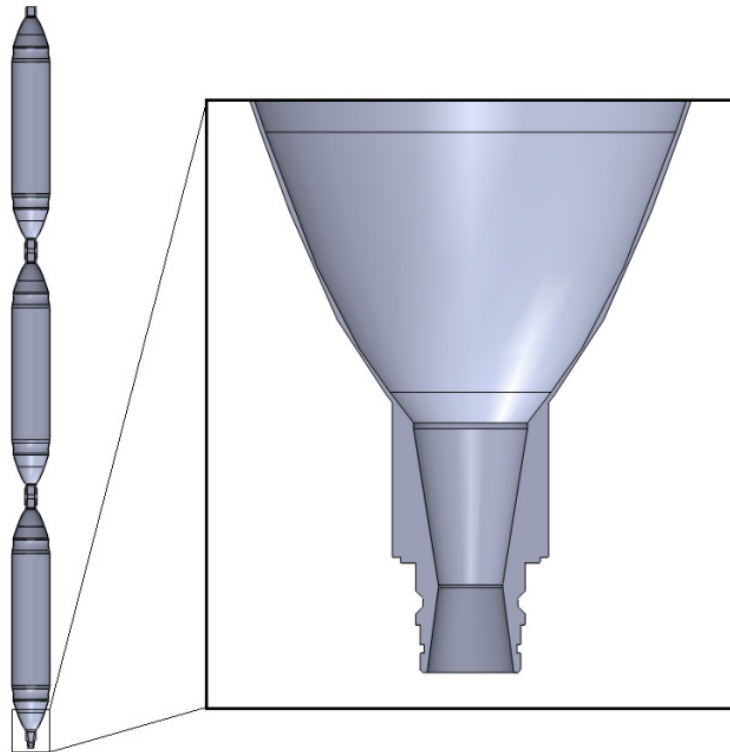


Figure 87: Geometry of the chambers

The most important part is the first chamber where the two phases, water and air, will interact. With high probability - after the *2D* simulations - we can safely say that the two other chambers will stay dry.

Another very important part of the geometry is the nozzle, where the fluid is going through drastic changes, like expansion, strong acceleration, cooling down. We have to calculate with the fact that these changes will not end at the nozzle exit. That means that these three zones will call for the most attention at the mesh generation. Therefore the most densely meshed area was the nozzle, followed by the zone after the nozzle exit and the first chamber. A detail of the mesh can be seen in *Figure 88*. The second and the third chamber were meshed with lower cell quantity.

In the geometry created the first chamber is double walled because the complexity of the flow differs strongly inside and outside of the chamber wall. This solution allows to generate different meshes at the two sides of the chamber wall. The density of the mesh decreases slowly downwards. The size of the cells is also growing in radial direction, but only in the case of the volumes outside the chambers.

Summarizing the geometry was split up into 53 volumes and it was meshed with a total of 2.920.000 cells. The mesh is hexahedral and the value of skewness at the worse cell is 0,51 according to Gambit. After specifying the boundary types and the continuum zones the mesh was imported into OpenFOAM for further analysis and settings. After a positive mesh check in OpenFoam the boundary conditions were set. These boundary conditions set for all the variables are listed in *Appendix B*. From this time forth the simulation was ready to start.

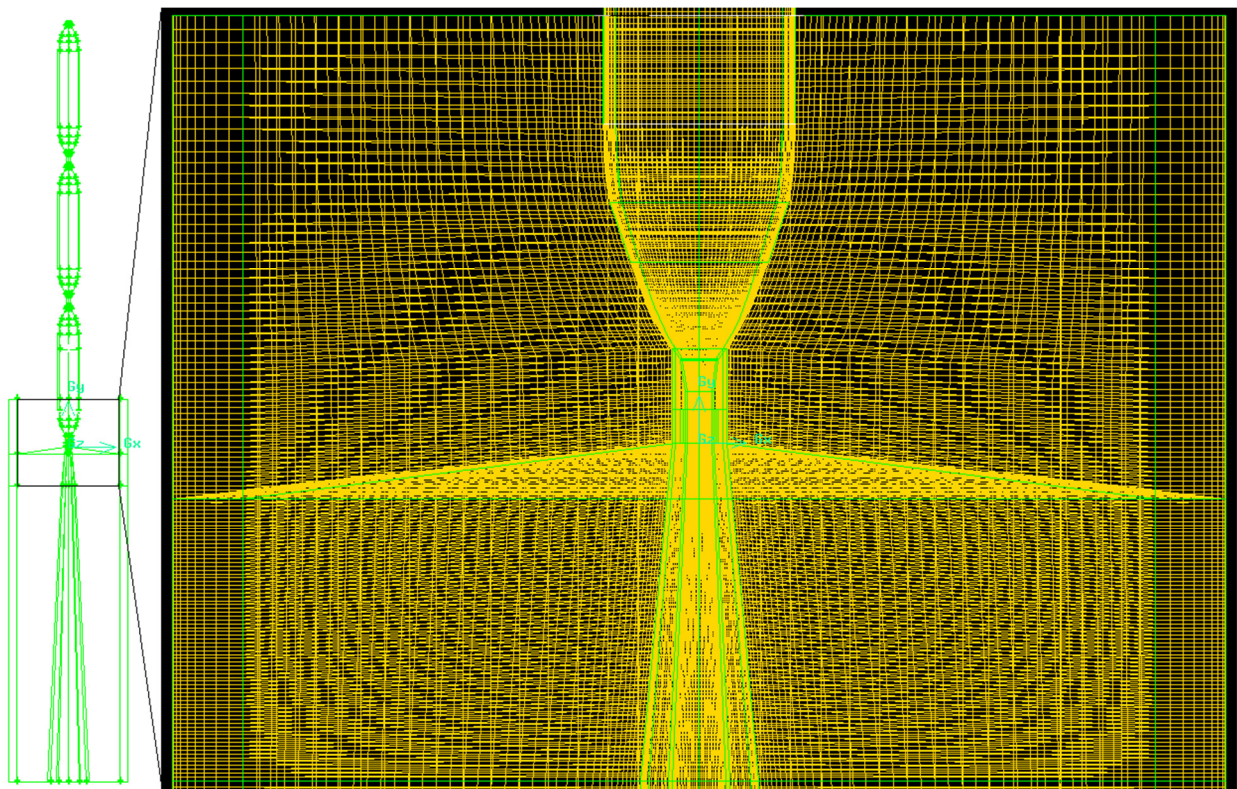


Figure 88: Mesh around the nozzle, cut from the domain

IV. 6.2.2. Results of the simulation

After running the “setFields” command to set the desired initial conditions, as the $p_r = 17 \text{ bar}$ chamber pressure, the water volume in the rocket, the simulation was started with the solver compressibleInterFoam. It was computed parallel on 40 cores and the calculation for one case required nearly six weeks.

The Courant number, C_Δ had a high effect on the stability of the simulation. The value of the number was always below 1 as required, but it was necessary to lower it in some cases until $C_\Delta = 0,2 - 0,3$, because of the appeared divergence. As it can be seen later in the results, for example in

Figure 92, the variables are fluctuating strongly. These circumstances led to divergence in case of higher Courant numbers. The solution of the problem delivered also other disadvantages. First the simulation required a higher supervision. Secondly during the calculation of the chaotic two phase outflow the time step decreased to a value of $\Delta t \cong 5 \cdot 10^{-7} s$ instead of the $\Delta t \cong 8 \cdot 10^{-6} s$, which was the typical value during the outflow of nearly single phase or at the moderate outflow of two phases. If the simulation reached a chaotic phase and it crashed, it was restarted with a lower Courant number from an earlier time. The simulation was controlled during the computation by checking the already calculated flow field using Paraview [23]. This helped to forecast the behavior of the outflow and by this, the rise or the lowering of the Courant number during the simulation. This made it possible to avoid the divergence and the crashing down. If the Courant number was not set low enough, the simulation crashed. It was hard to find the perfect value of the Courant number during the computation, because in case of low Courant number the time step will be also very low, which will make the computation stable, but slow. Using this solution the simulation was intermitted with a restart because of this reason 6 times.

The results were saved and evaluated for every milliseconds to create the determining functions of the whole process. The results are presented in the following sections.

IV. 6.2.2.1. Results of nozzle 3

The following *Figures 89* and *90* are demonstrating the outflow of water and the velocity field in the first chamber at a higher 3 l and a lower 2 l water level for six different time steps. The initial condition is the same except the water level. The pressure inside the rocket chamber is $p_r = 17 \text{ bar}$. After the comparison of the water levels all the results for the outflow at nozzle 3 are presented regarding the two phases and the velocity field in *Figure 85* and in *Figures 86 – 90* as well as all the important functions which are governing the flight of the rocket, as the accelerating force, the mass flow, the pressure difference at the nozzle exit and the mass of the rocket. The presented results will be discussed in *Chapter IV.6.2.3*.

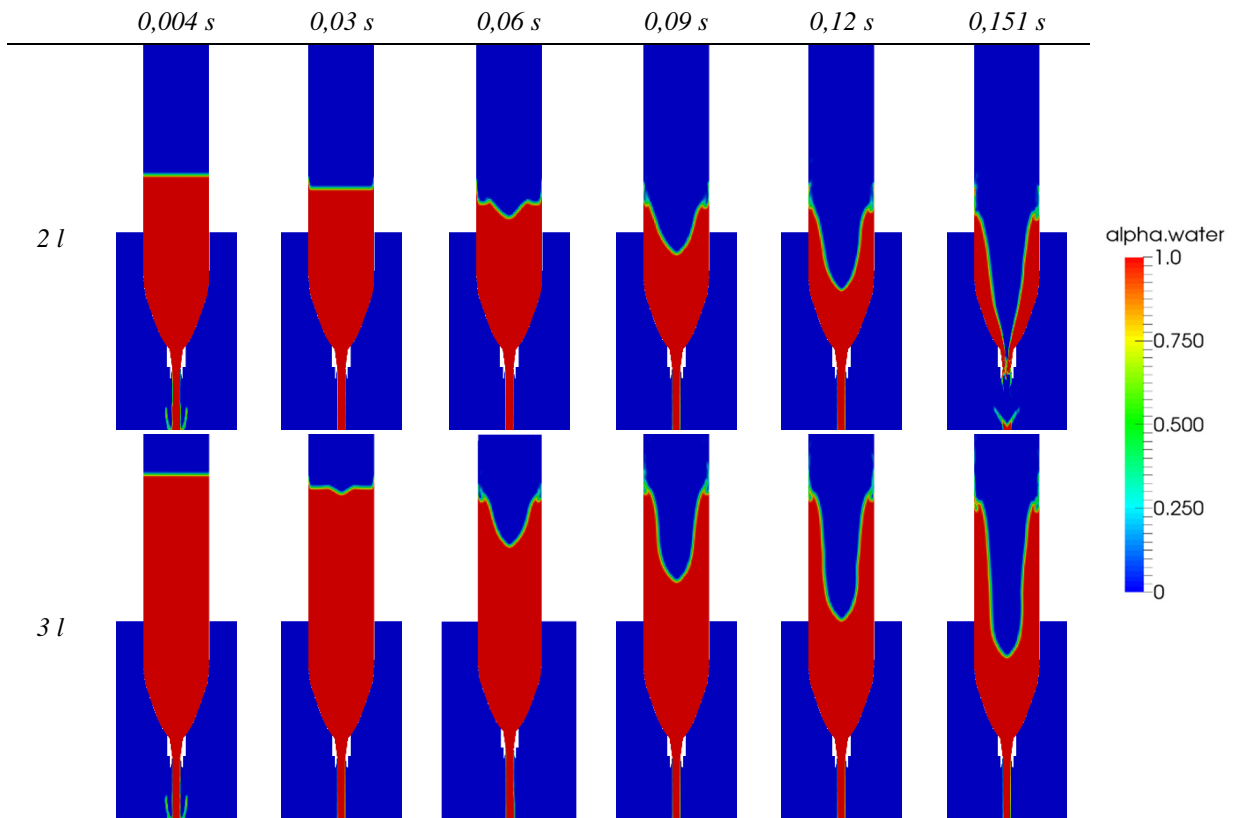


Figure 89: Behavior of the two phases at two initial water levels, at nozzle 3

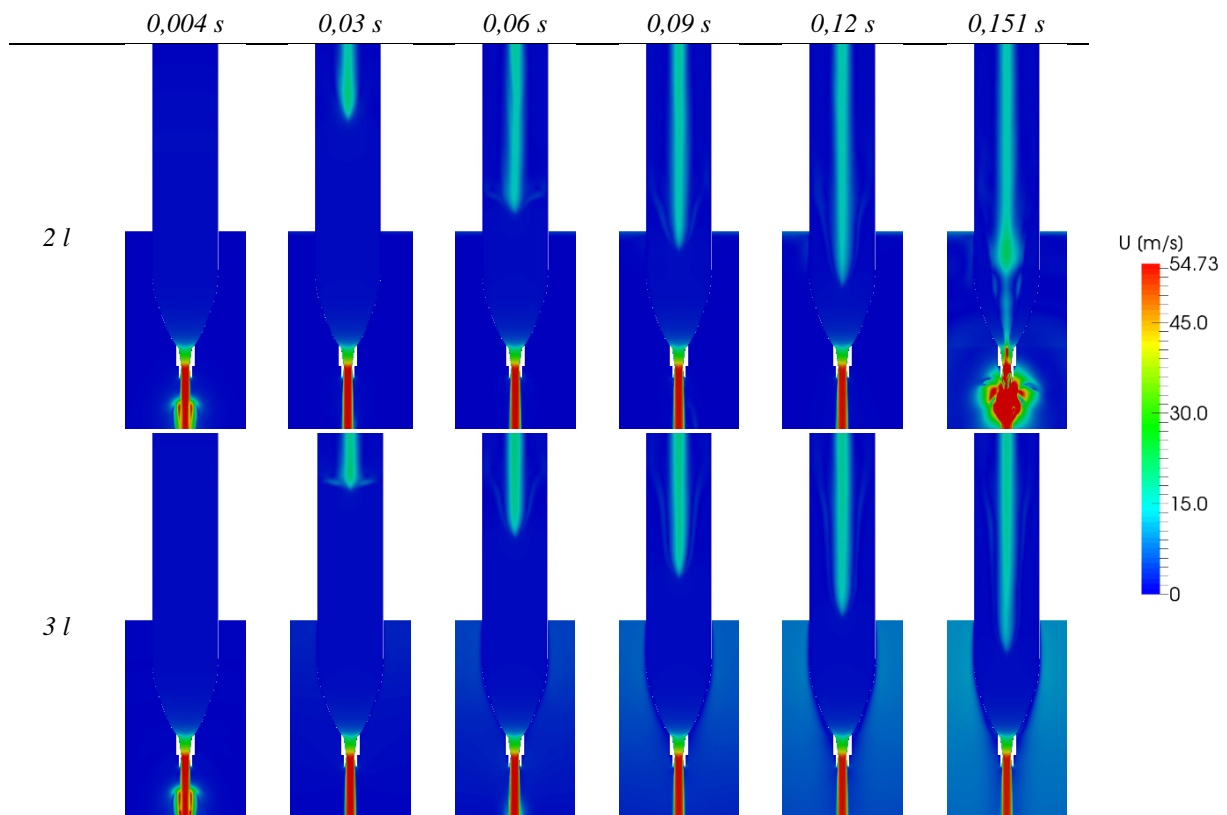


Figure 90: Velocity field in the first chamber for two initial water levels at nozzle 3

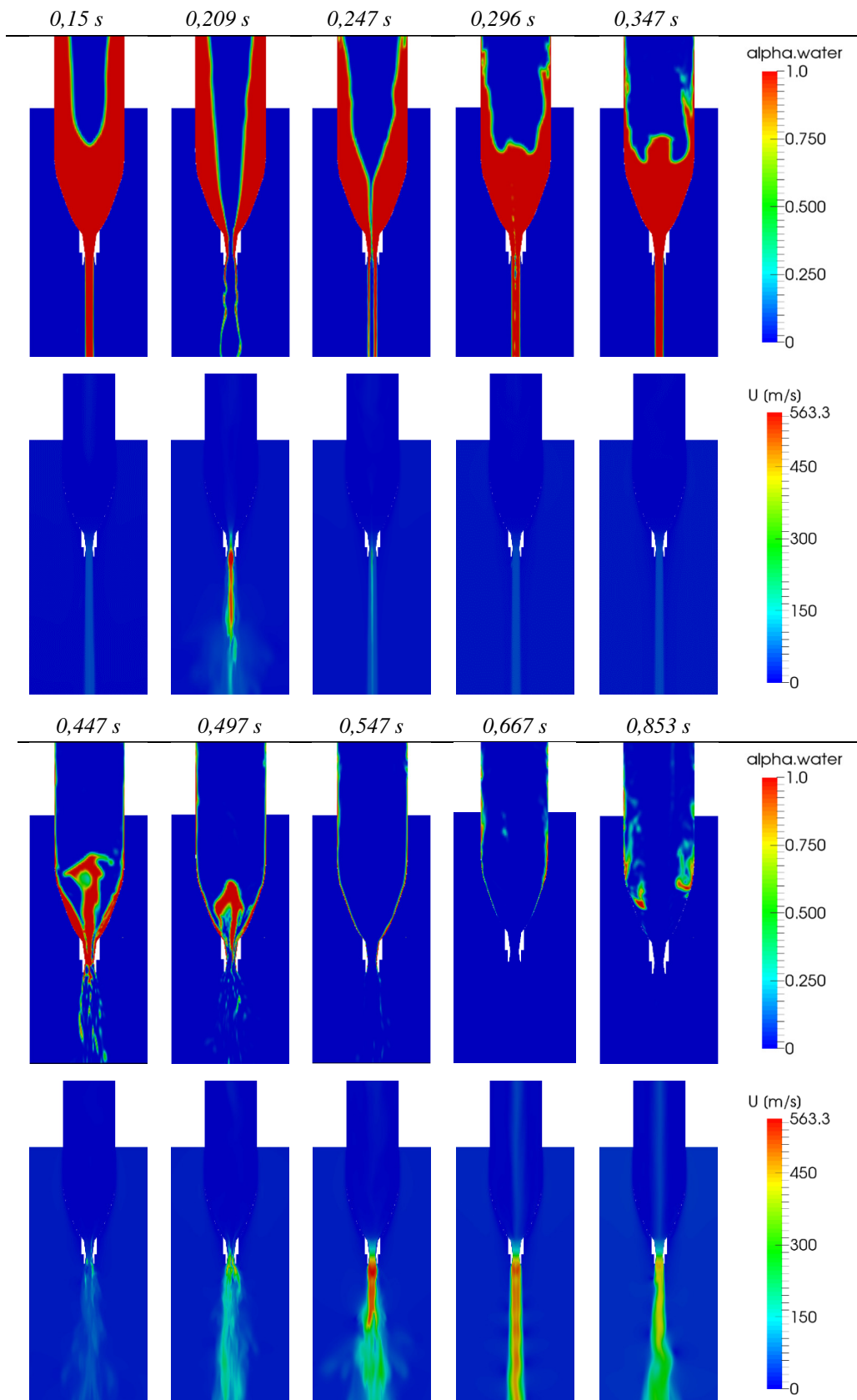


Figure 91: Behavior of the two phases and the velocity field at few time steps for nozzle 3, 3 l

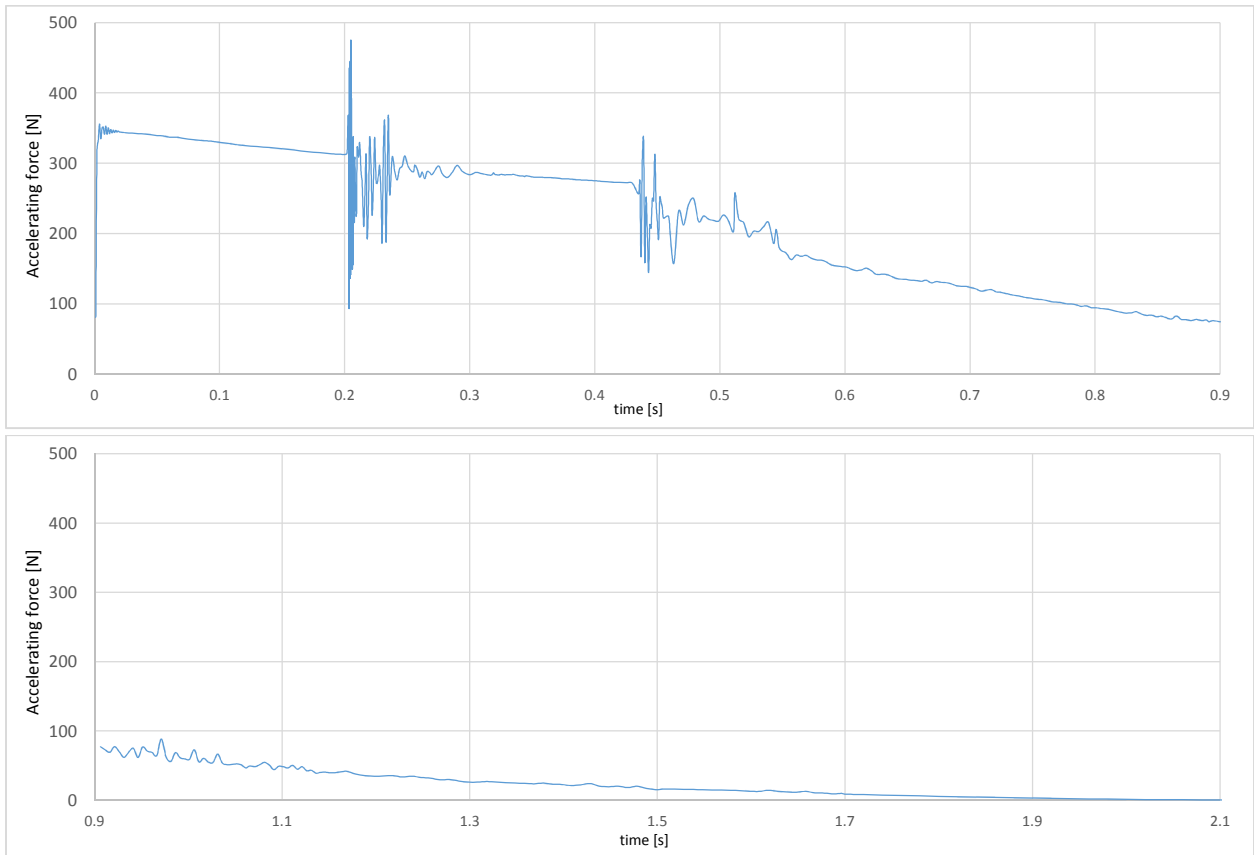


Figure 92: Total accelerating force at the nozzle exit, nozzle 3, 3 l

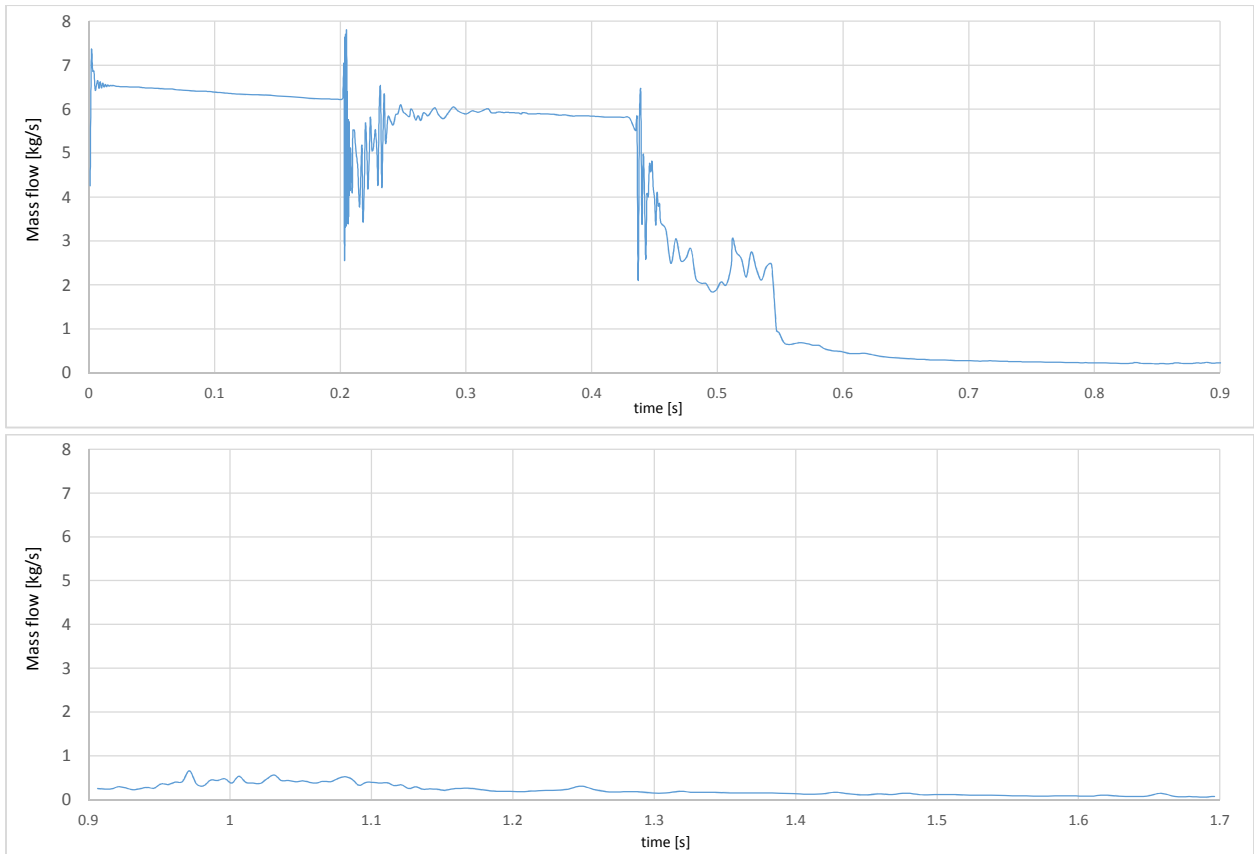


Figure 93: Mass flow at the nozzle exit, nozzle 3, 3 l

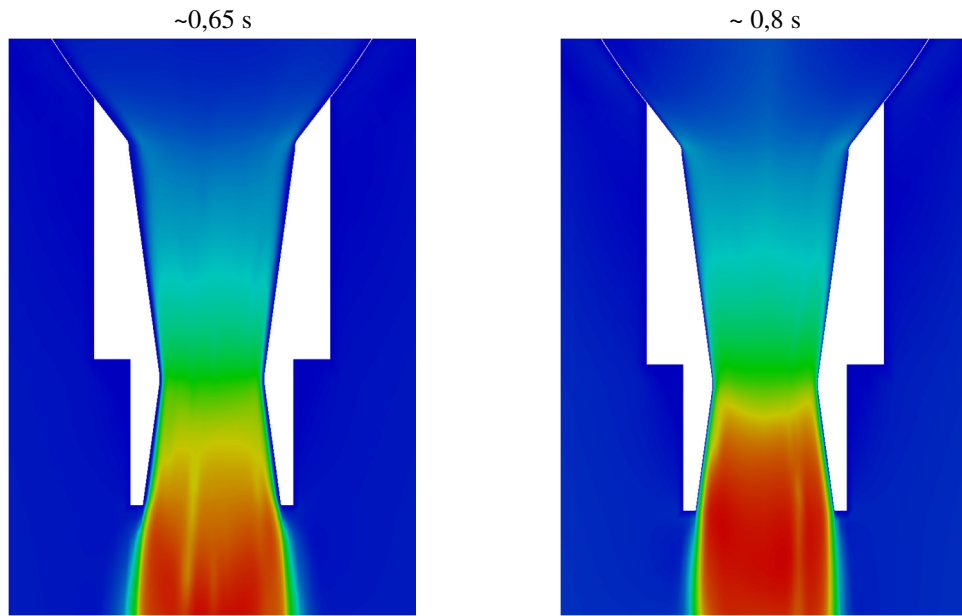


Figure 94: Velocity field at the nozzle; (left) Under-expanded, (right) Optimal; at nozzle 3, 3 l

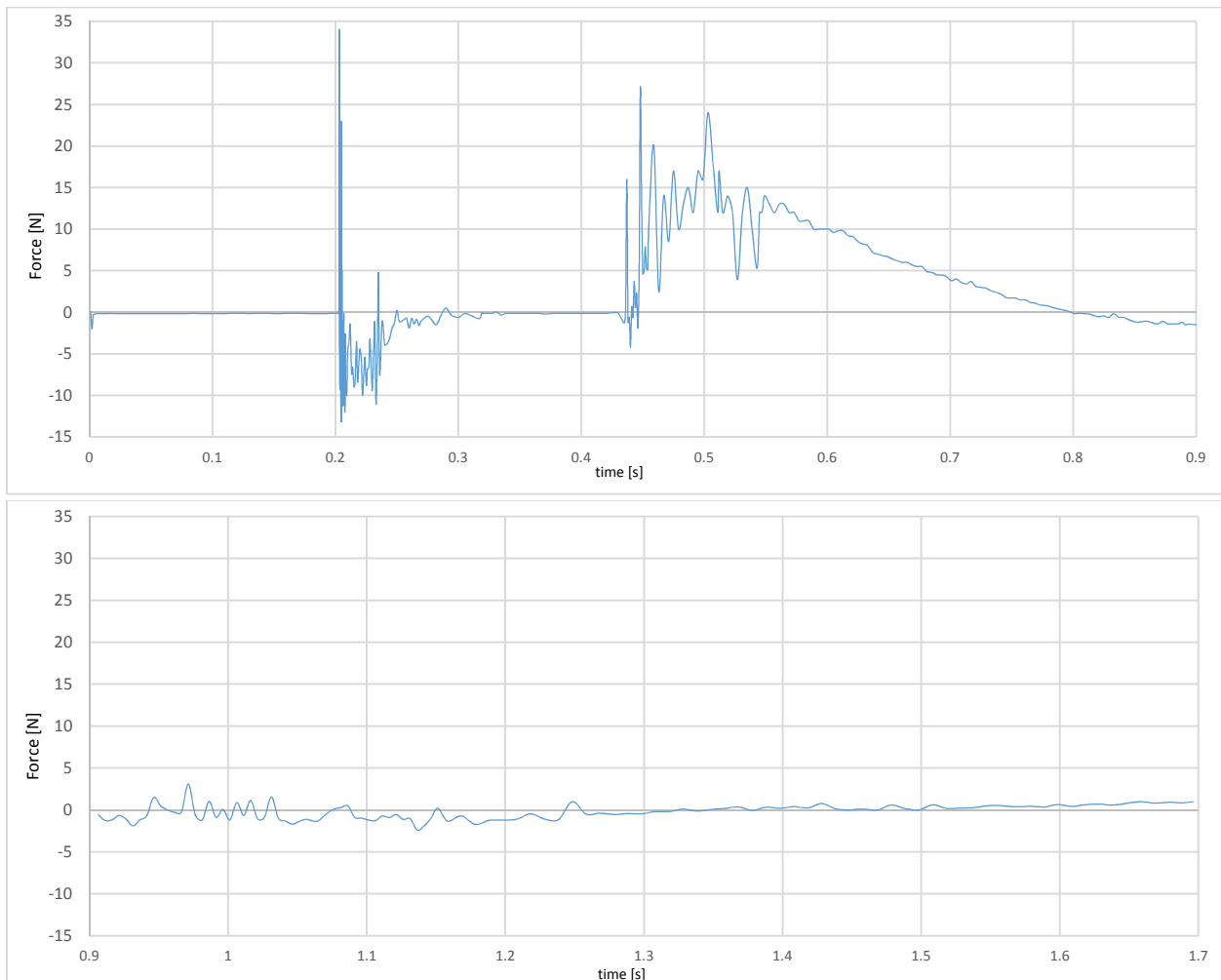


Figure 95: The force at the nozzle exit as a result of the pressure difference at nozzle 3, 3 l

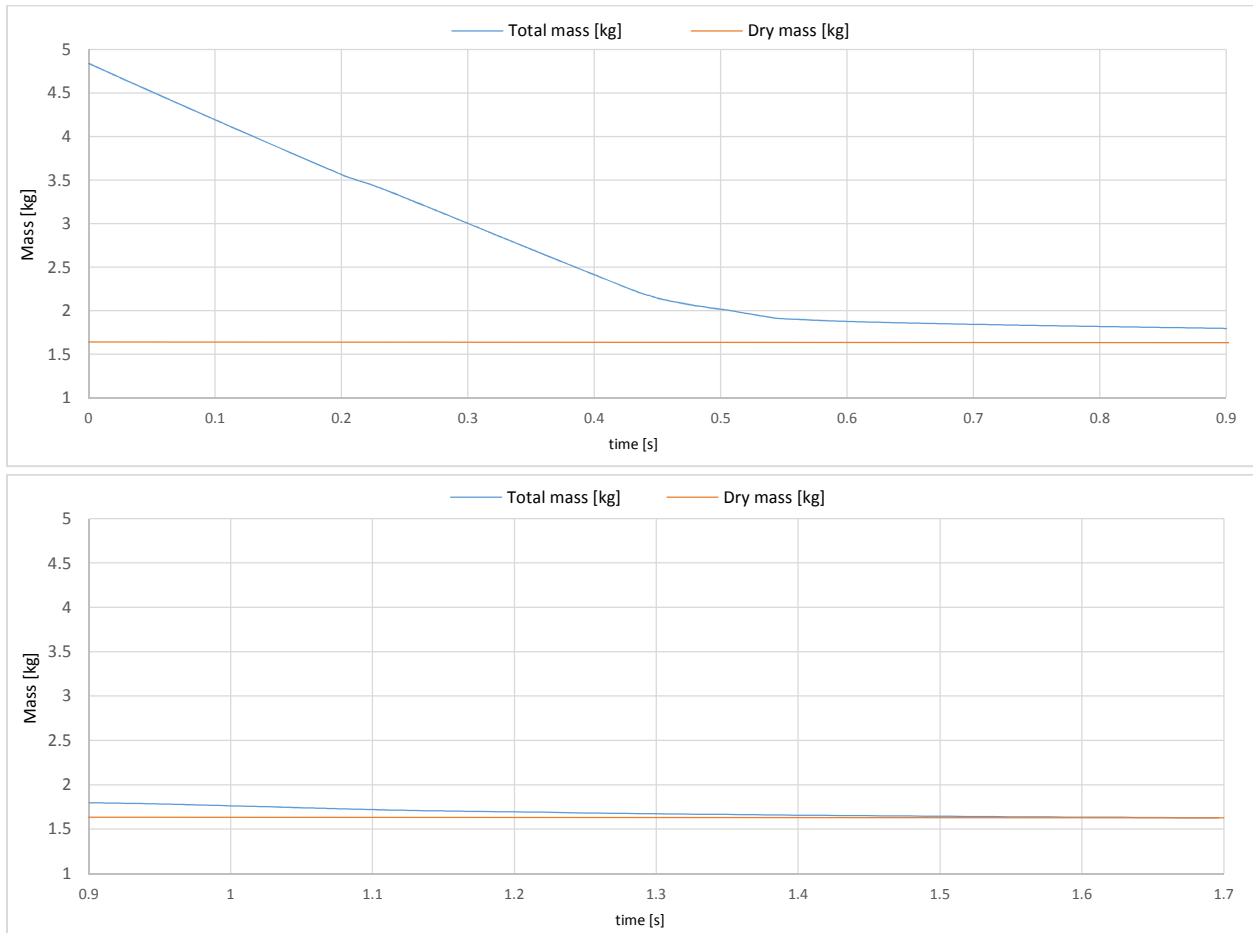


Figure 96: Total mass of the rocket during the outflow at nozzle 3, 3l

IV. 6.2.2.2. Results of nozzle 4

Figure 97 represents the two phase outflow and the velocity field for a few time steps at nozzle 4 with the same initial conditions as used at nozzle 3. Achieving the same evaluation as before, the most important functions of the outflow could be obtained. These functions are demonstrated in Figure 98, 99, 100 and 101. The presented results will be discussed in Chapter IV.6.2.3.

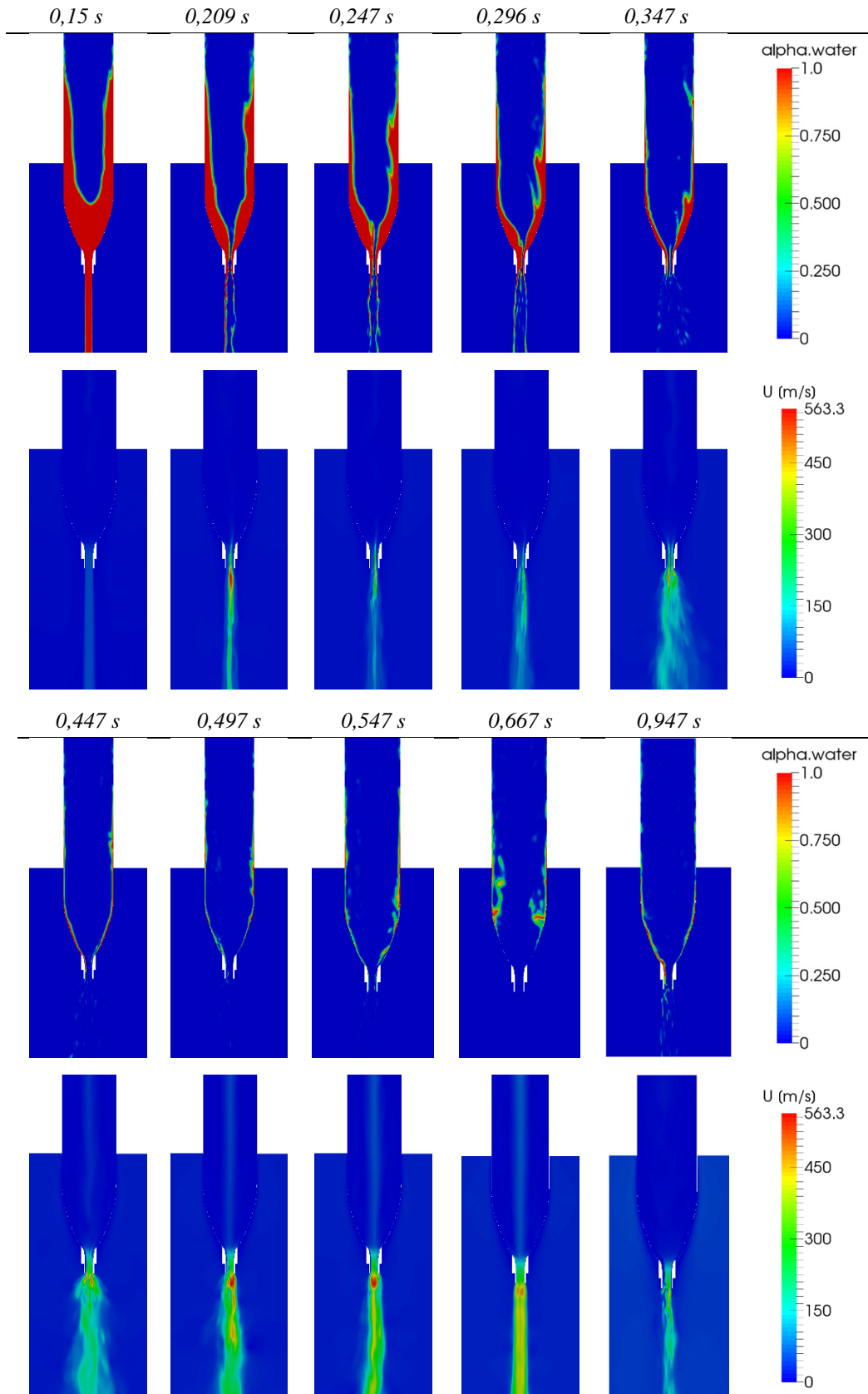


Figure 97: The behavior of the two phases and the velocity field at few time steps for nozzle 4

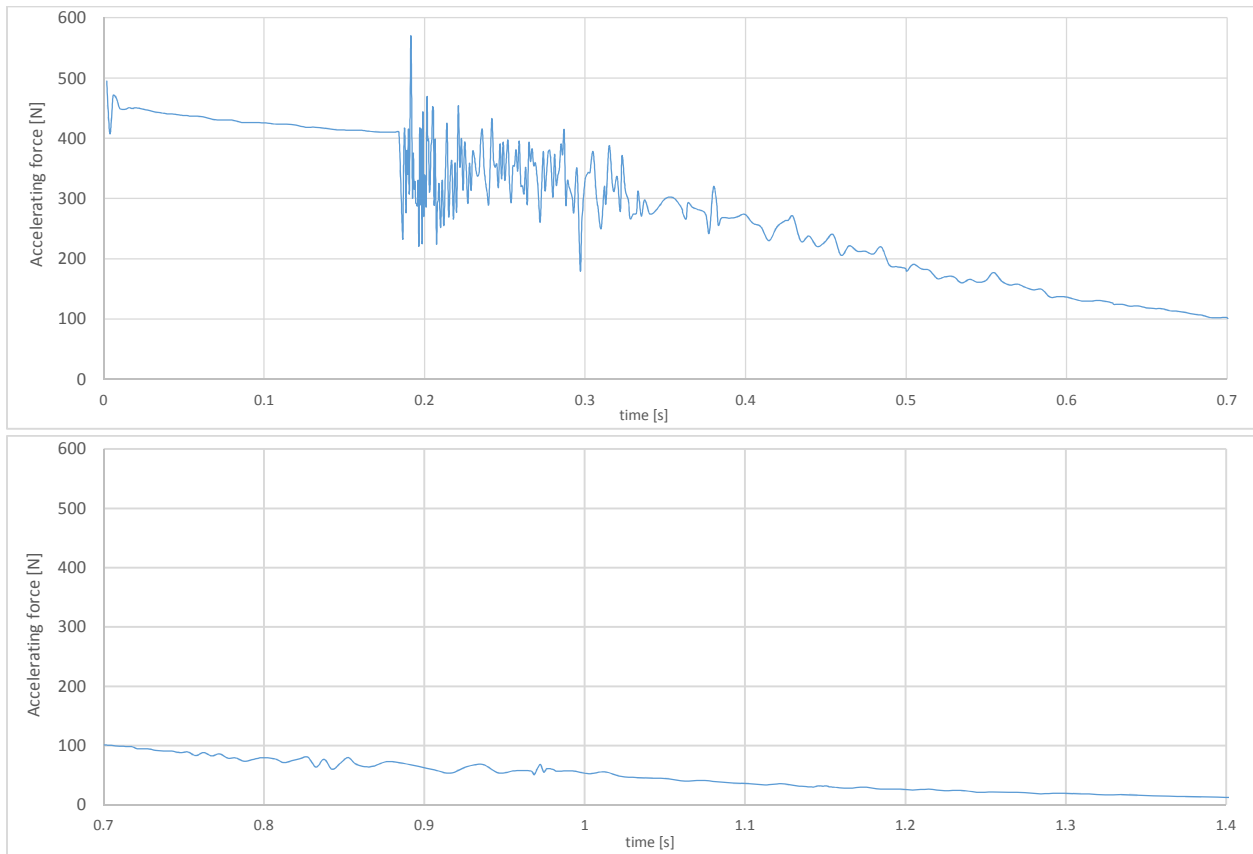


Figure 98: The resulting total accelerating force, at nozzle 4

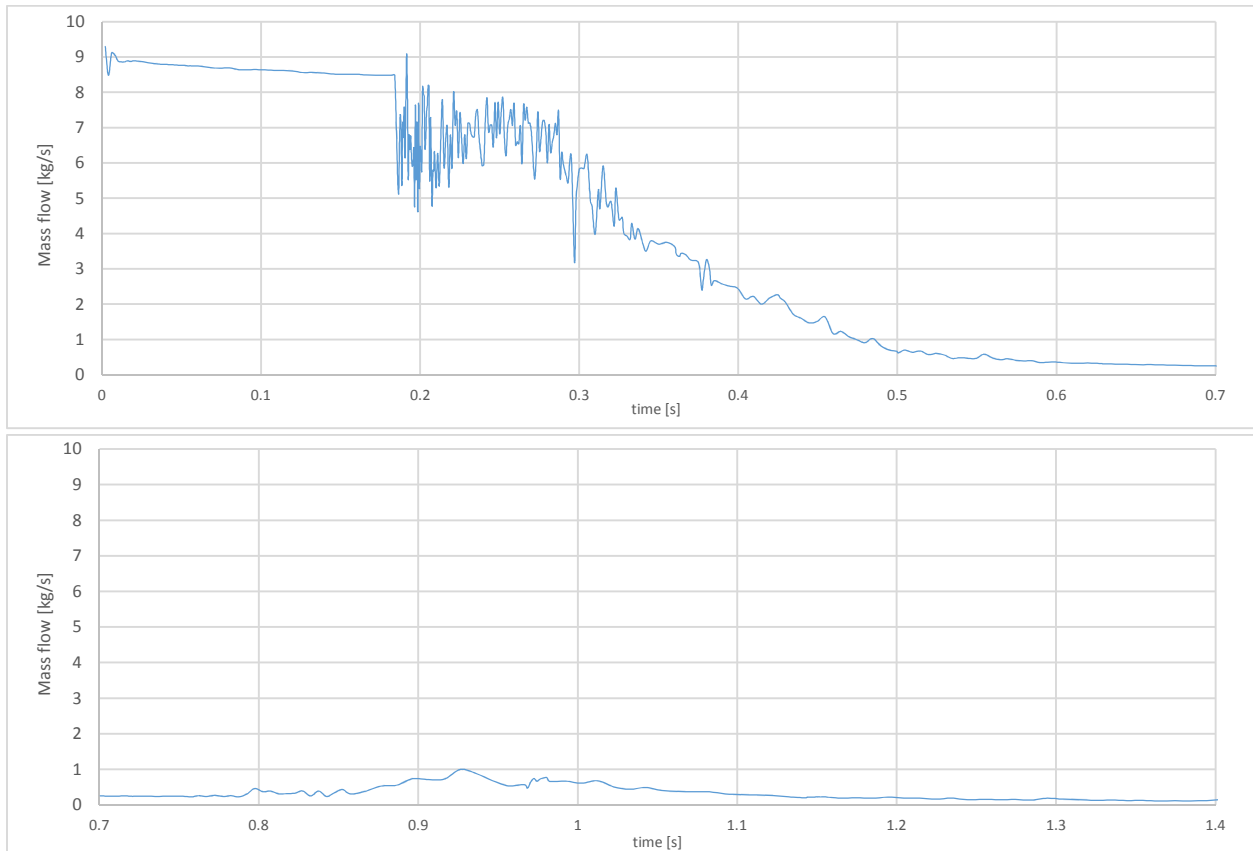


Figure 99: Mass flow during the outflow at nozzle 4

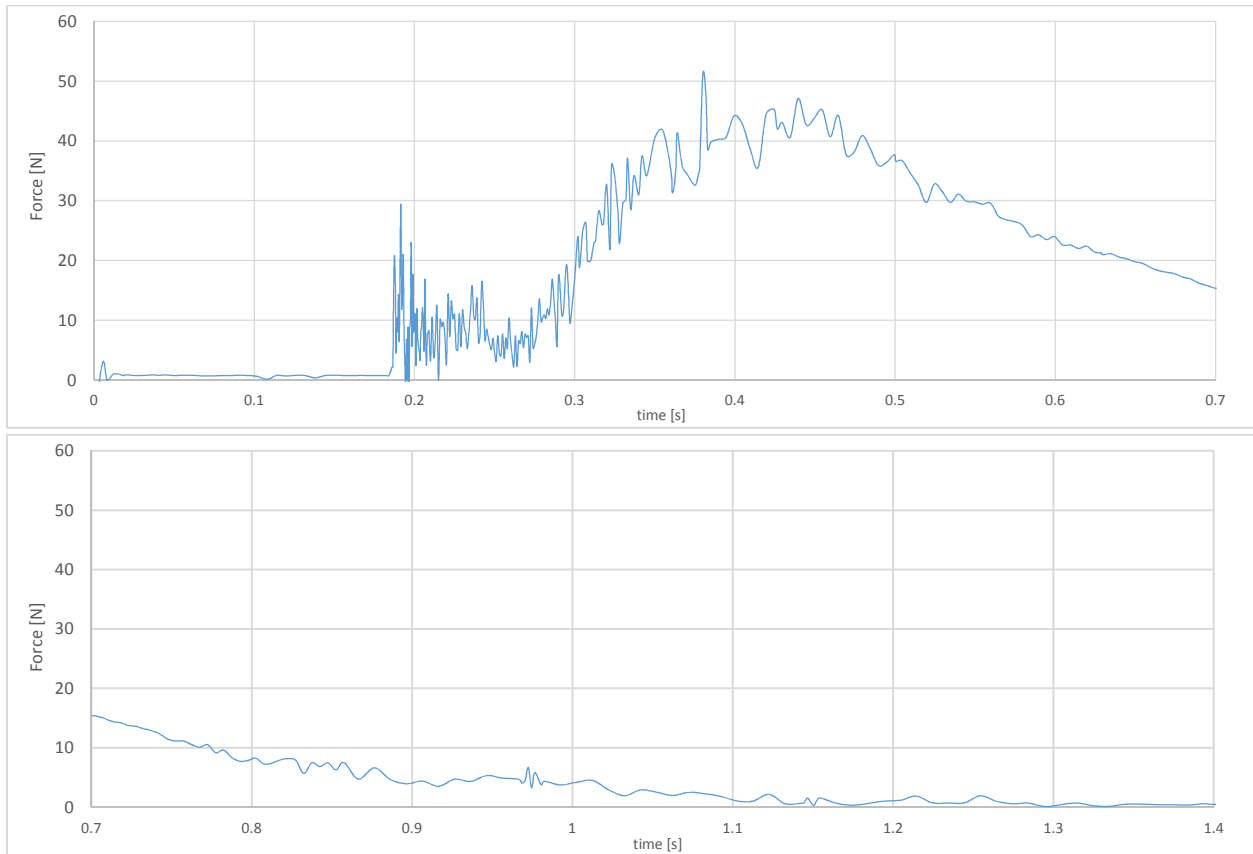


Figure 100: Force at the nozzle exit as a result of the pressure difference at nozzle 4

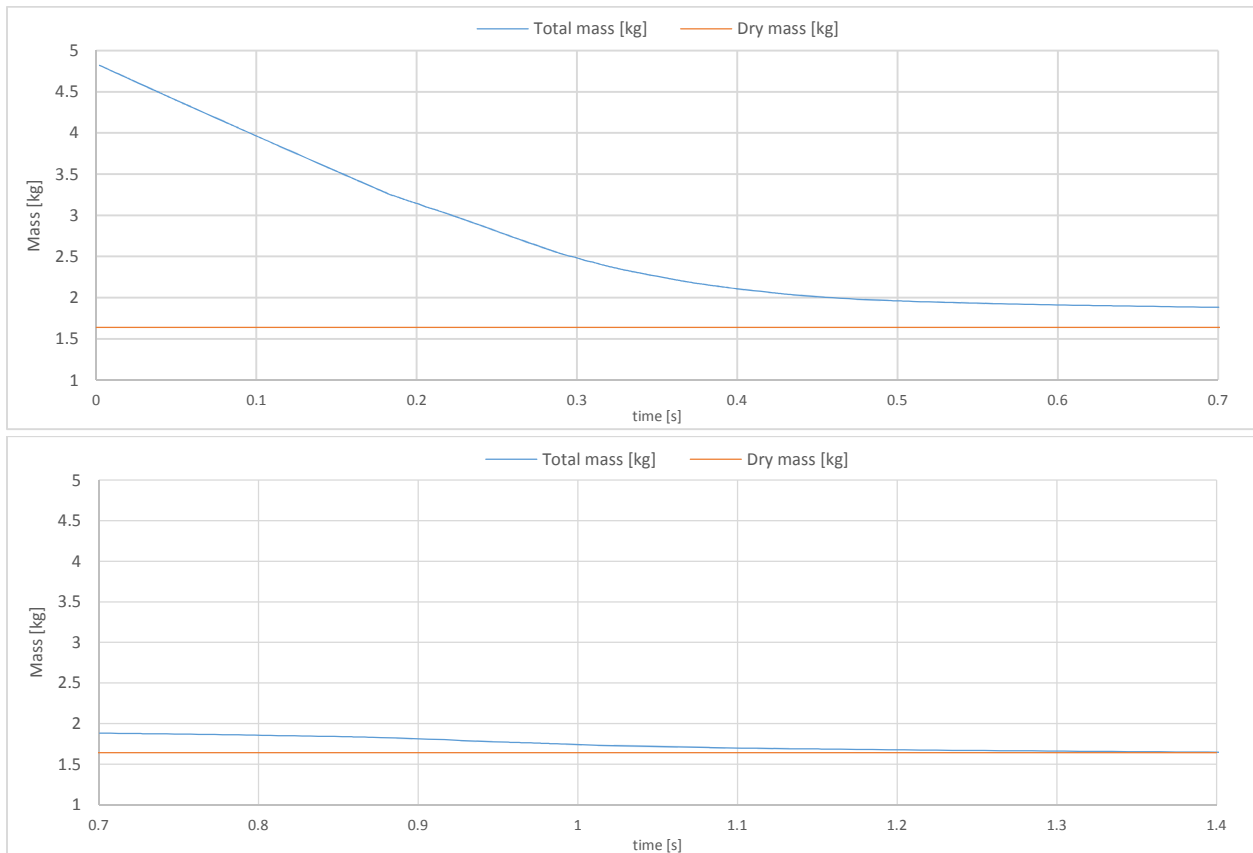


Figure 101: Total mass of the rocket during the outflow at nozzle 4

IV. 6.2.3. Evaluation of the simulation results

According to the simulation results the outflow process is very complex as predicted. The assumption that the outflow can be separated into three stages is not in every case true. In the case of nozzle 3 the result shows - *Chapter 6.2.1.1.* - that the synchronous outflow of water and air occurs mainly for two time intervals; in $[0,2 - 0,3]$ and in $[0,43 - 0,55]$ s. In all other times the outflow is nearly one phase. The results for nozzle 4 - *Section 6.2.1.2.* - indicate that the outflow can be separated indeed in the mentioned three stages but even so the numerical functions are weak assumptions because the presumed short overlap of the outflow of pure water and air. The difference is especially in the first phase, the clear water outflow notable as shown in *Figure 102*. The characteristic of the almost clear air outflow is quite similar. For this reason in the long run, presented in *Figure 103* the final functions do not differ strongly from each other and the difference in the final altitude is just 13 m, 9,2%. The functions retrieved by the simulation are showing that the overlap, the multiphase outflow is actually $\sim 0,28$ s long. This fact also influences the resulting functions and they will differ from the results of the numerical calculation.

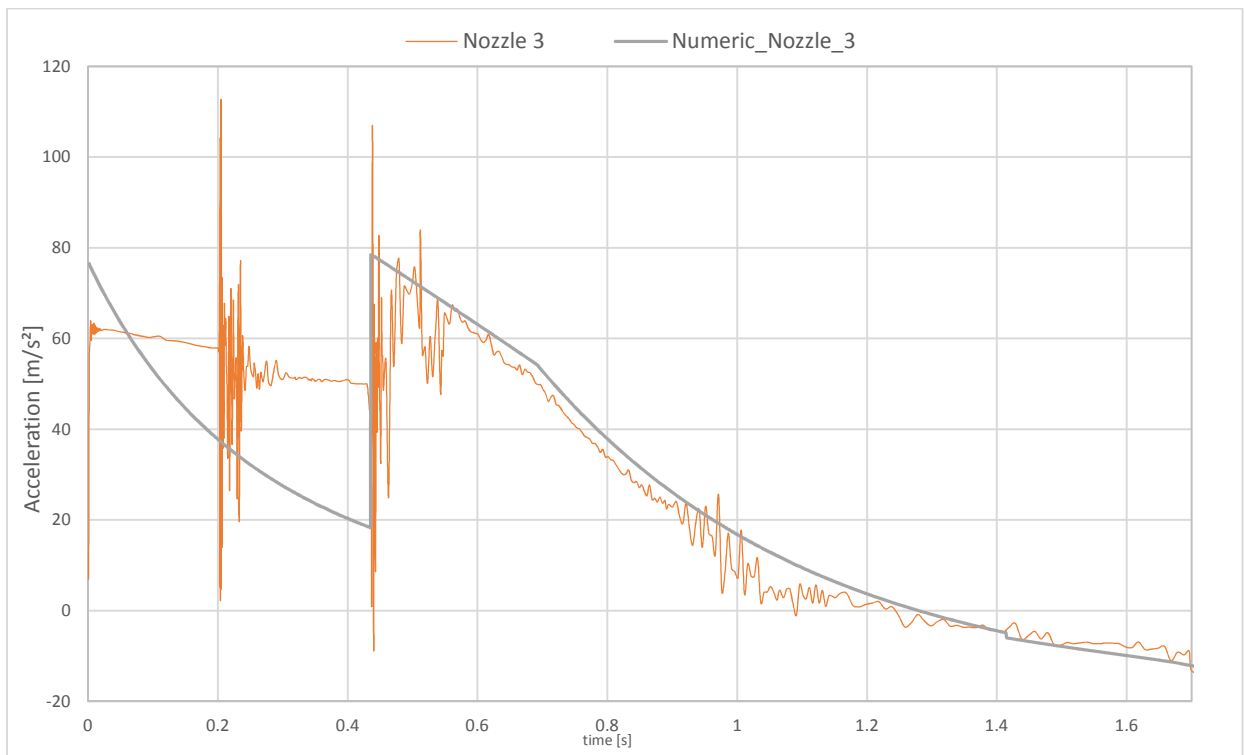


Figure 102: Comparison of the acceleration functions for the simulation results and numerical calculations

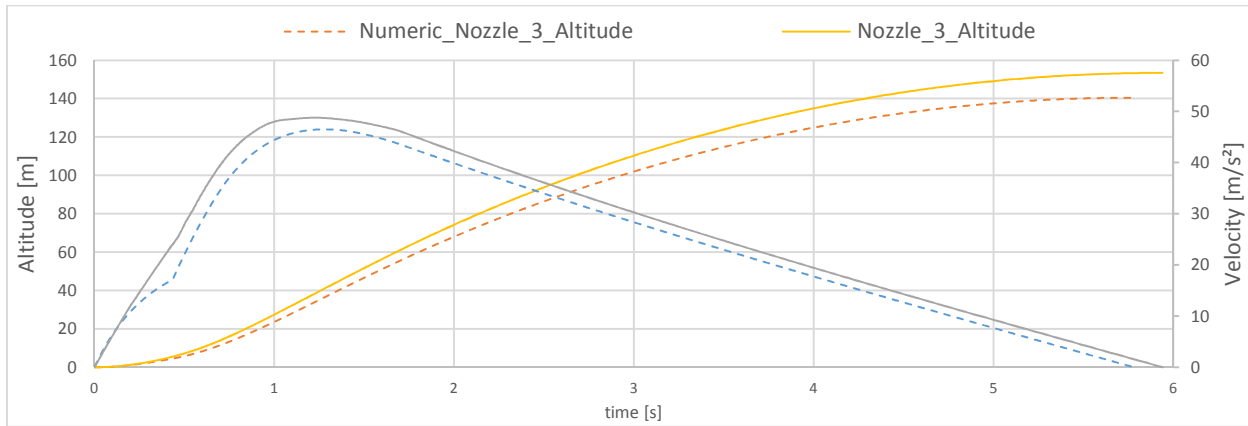


Figure 103: Comparison of the flight of the rocket for the simulation results and the numerical calculations

The numerical calculation is based on theoretical mass flows. That means that the outflow of water and air happens with a constant velocity in the whole nozzle cross section, which is in reality not true. The velocity profile at the very beginning of the water outflow in nozzle 4 is presented in *Figure 104*. It has the maximum outflow value $v_2 = 52,6 \text{ m/s}$ which nearly agrees the result of the numerical calculation $v_2 = 56,5 \text{ m/s}$. The difference of the maximal values is maybe low, which is a promising thing, but for instance the difference due the velocity profile in the function of mass flow will increase with time. This is also a fact which influences the numerical functions.

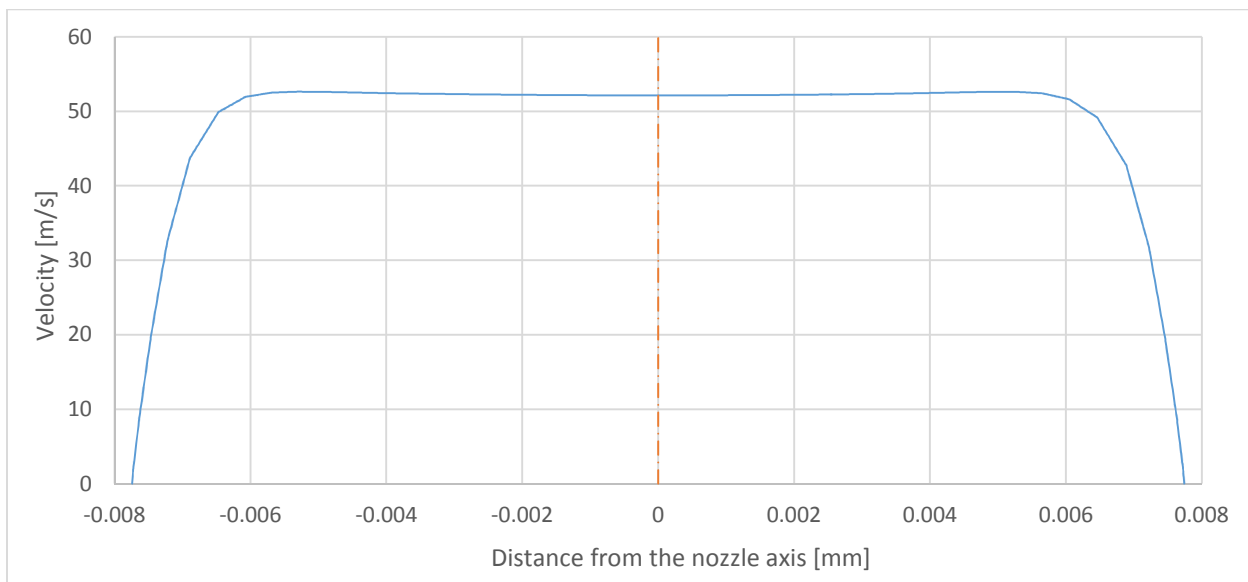


Figure 104: Velocity profile at the exit of nozzle 4, at the very beginning of the water outflow

To get a more detailed view of the pressure and velocity field in the three chambers, the following figures and functions were generated, demonstrated in *Figure 105*, *106*, *107*. To be able to present the wide interval of the velocity field, which derives from the large pressure difference in the domain, it was created using a logarithmic scale as shown in *Figure 105*. As further investigation for both nozzles the value of the velocity magnitude and the pressure was analyzed along the symmetry axis of the rocket for three time steps. Due the high pressure difference between the different time steps the pressure is represented using relative values. In the

functions shown in *Figure 106* and *107* the connection of the chambers, the narrow cross sections appeared unambiguously, especially in the case of the high speed outflow. Due the smaller diameters in the connections, the pressure distribution in the chambers will be nearly staggered and the velocity will rise in the connection tubes. Inside the three chambers the highest velocity will be at the first connection outlet, which has a high effect on the whole multiphase outflow process. If we compare the figures for both nozzles then we will see the greater differences at nozzle 4 because of greater mass flow at the outlet.

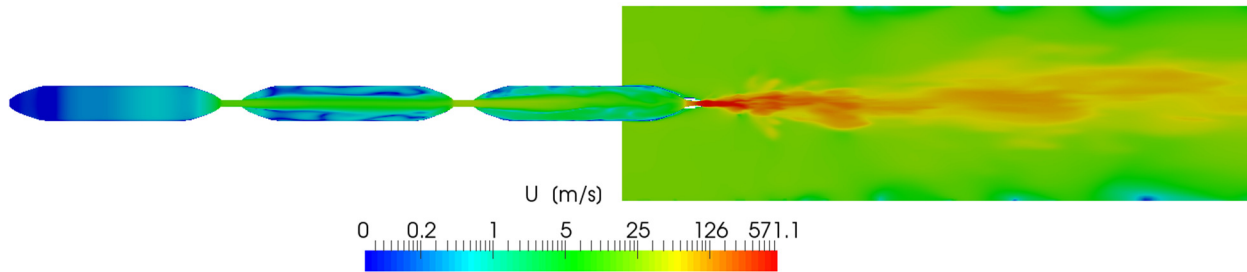


Figure 105: Velocity field in the whole domain at $t = 0,547$ s, using logarithmic scale

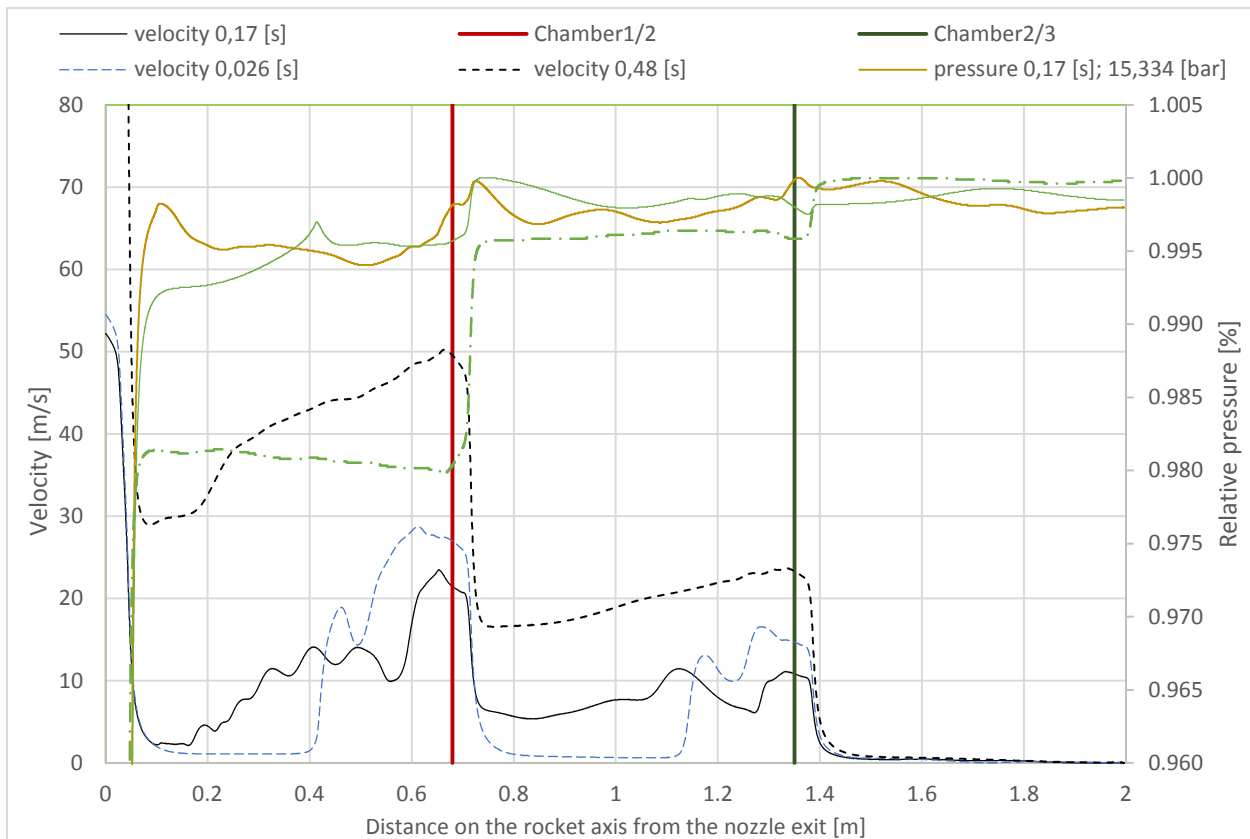


Figure 106: Pressure and velocity values in the rocket, along the symmetry axis; for nozzle 4

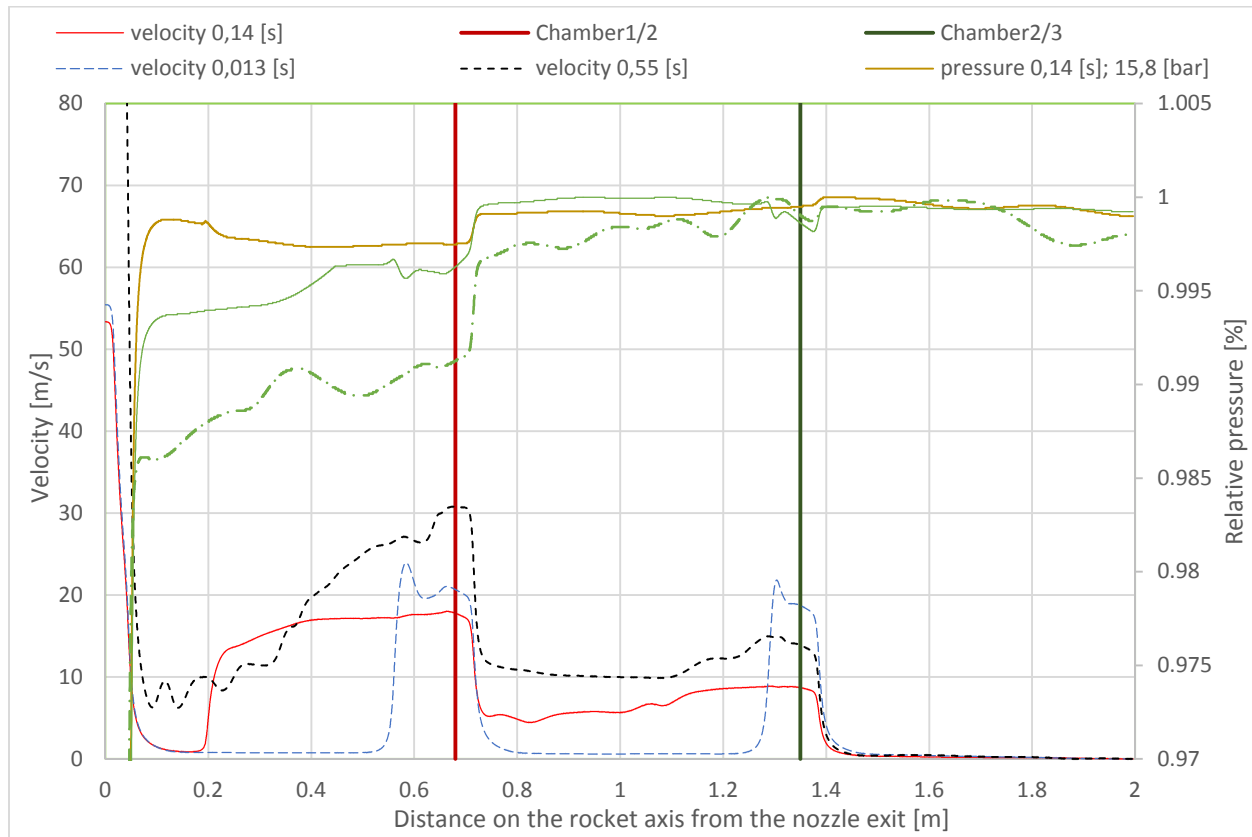


Figure 107: Pressure and velocity values in the rocket, along the symmetry axis; for nozzle 3, 3l

The next investigated phenomena will be the “explosion” of the water jet, the switch from single phase outflow to two phase outflow. The rocket model presented in the thesis with the four different nozzles is not the first one.

The model was developed from a much simpler construction using fewer, smaller chambers, smaller connecting tubes, different and simpler nozzles, etc. Some of the previous models during the flight are shown in *Figure 108*. The runoff of the outflow process is strongly influenced by the properties named before. For instance the overlapping of the outflow of water and air will be very short in a construction with one chamber - without any narrow connection shown on the (2) image of *Figure 108*, but using six smaller chambers with five even more narrow connection elements, showed on the (3) image, will lead to a very long two phase outflow with strong atomization. The reason of this effect, (as we know now according to the simulation) is the high velocity inside the rocket at the first chamber connection, especially at high water levels, which is true in the case of using more, smaller chambers. With no narrow elements in the rocket the air acts like a piston in the chamber, which can be clearly seen in *Figure 89* at the first two presented time steps for a lower 2 l water level.

To photograph the actual moment of the jet “explosion” is not easy especially when it happens in high altitudes. The small rocket with the single chamber does not reach high speeds and altitudes, therefore the phenomena could be photographed relatively easy. The Images shown in *Figure 108/2* are taken from a video recorded with 120 frames per seconds. The time difference between the frames is $\Delta t = 0,008$ s. As mentioned before, in the case of a single chamber the outflow of water and air are almost separated therefore it is not the best comparison, not to

mention the different nozzle type, but the effect can be recognized clearly as in the simulation results presented in *Figure 109* and *110*.

The most similar construction can be seen on *Figure 108/1*. The inner geometry except the Laval nozzle is the same. The pure simple phase water outflow is recognizable at the beginning of the flight as in the simulations.

Considering all these facts we can pronounce, that the simulation results are satisfying enough.

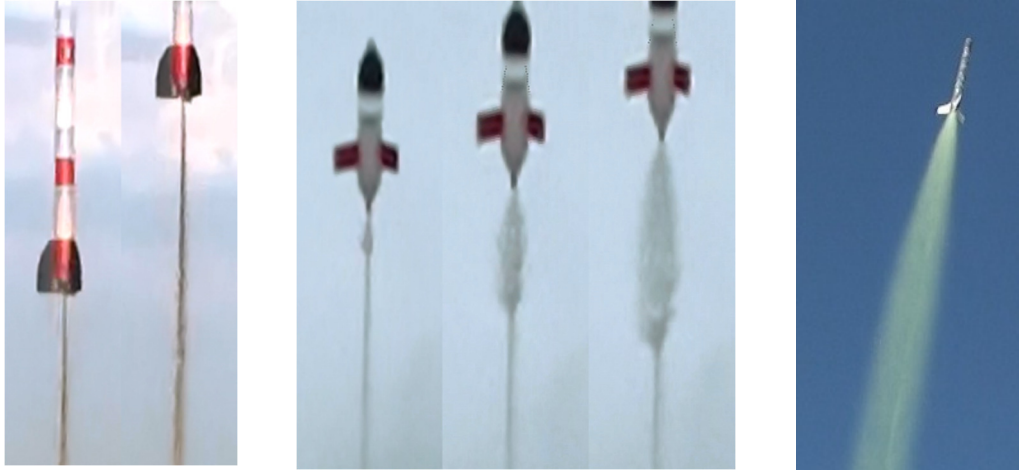


Figure 108: Jet shapes at other rocket models with different nozzle and chamber geometries, $p_r = 17 \text{ bar}$ (1) Beginning of the flight, using a Laval nozzle (2) The beginning of the air outflow at a simple nozzle (3) Rocket with more smaller chambers and a smaller simple nozzle $d_2 = 9 \text{ mm}$.

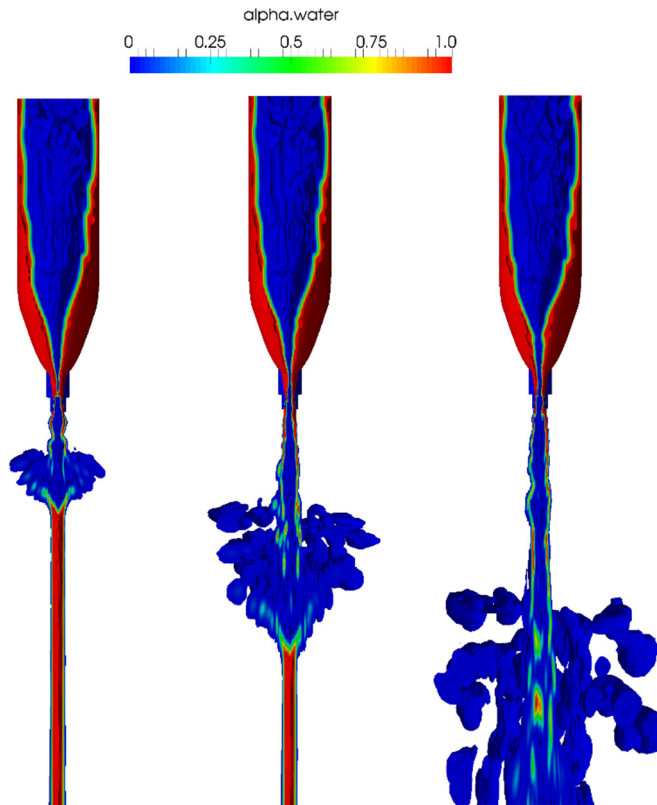


Figure 109: Exploding of the water jet, starting of the two phase outflow nozzle 4
 $t = 0.184 \text{ s}$

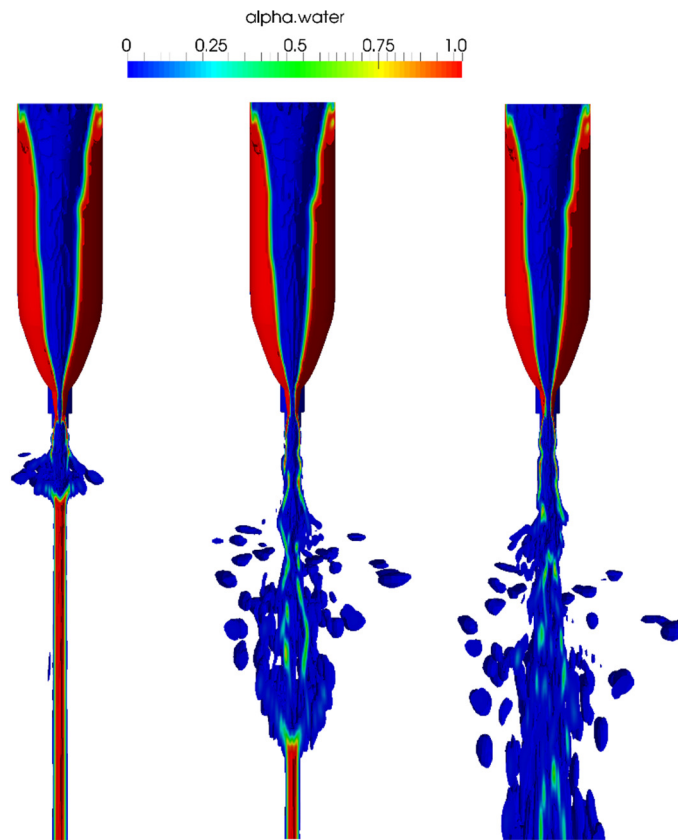


Figure 110: Exploding of the water jet, starting of the two phase outflow at nozzle 3, 3l
 $t = 0.202 \text{ s}$

IV. 6.2.4. Conclusions

The simulations delivered lot of new information about the outflow. First of all the most important thing is the behavior of the two phases in the first chamber. With the help of the results it can be clearly seen that in the thesis presented geometry as shown in *Figure 55* (or detailed in *Appendix C*) the synchronous outflow of water and air is longer than predicted and it depends strongly from the diameter of the chamber connection and the nozzle size as seen in *Figure 108*.

The accelerating air at the narrow cross section reaches the initially unharmed horizontal water level and generates a “cut” on the top of it. The cut will become deeper and deeper until the point where it reaches the nozzle exit. This phenomena can be recognized at both nozzles 3 and 4 as seen in *Figure 85* and in *91*. This is the point where the two phase outflow begins.

In the case of nozzle 3 the cut will close up due to the high water amount on the side of the chamber. The splashing water amount in the middle of the chamber will gain a momentum in the

opposite direction of the outflow. Therefore first the water ring on the side of the chamber will be pushed out due to the high pressure difference. That initiates a second simple phase outflow of pure water until the point where the air reaches the nozzle outlet again. After almost all the water is run out the simple phase outflow of air begins. The described phenomena can be also seen in the functions in *Figure 92, 93*. The two heavy disturbance in the function marks the beginning of the two-phase outflow for both times.

At nozzle 4 the process is simpler. It starts with the same cutting through effect but the velocity in the rocket and the mass flow is high enough in the nozzle to avoid the close up of this cut. Therefore the air pass way in the chamber is swirling around but it never closes up, generating a much longer two-phase outflow. Generally the multiphase outflow happened with the outflow of water in a ring cross section at the edge of the nozzle and the air was flowing out in the center of the described ring. This separation at the outflow can be well seen in *Figure 109, 110*. Due to the pulsations and the swirling of the air channel in the water, the mass flow and other functions become chaotic in these regions.

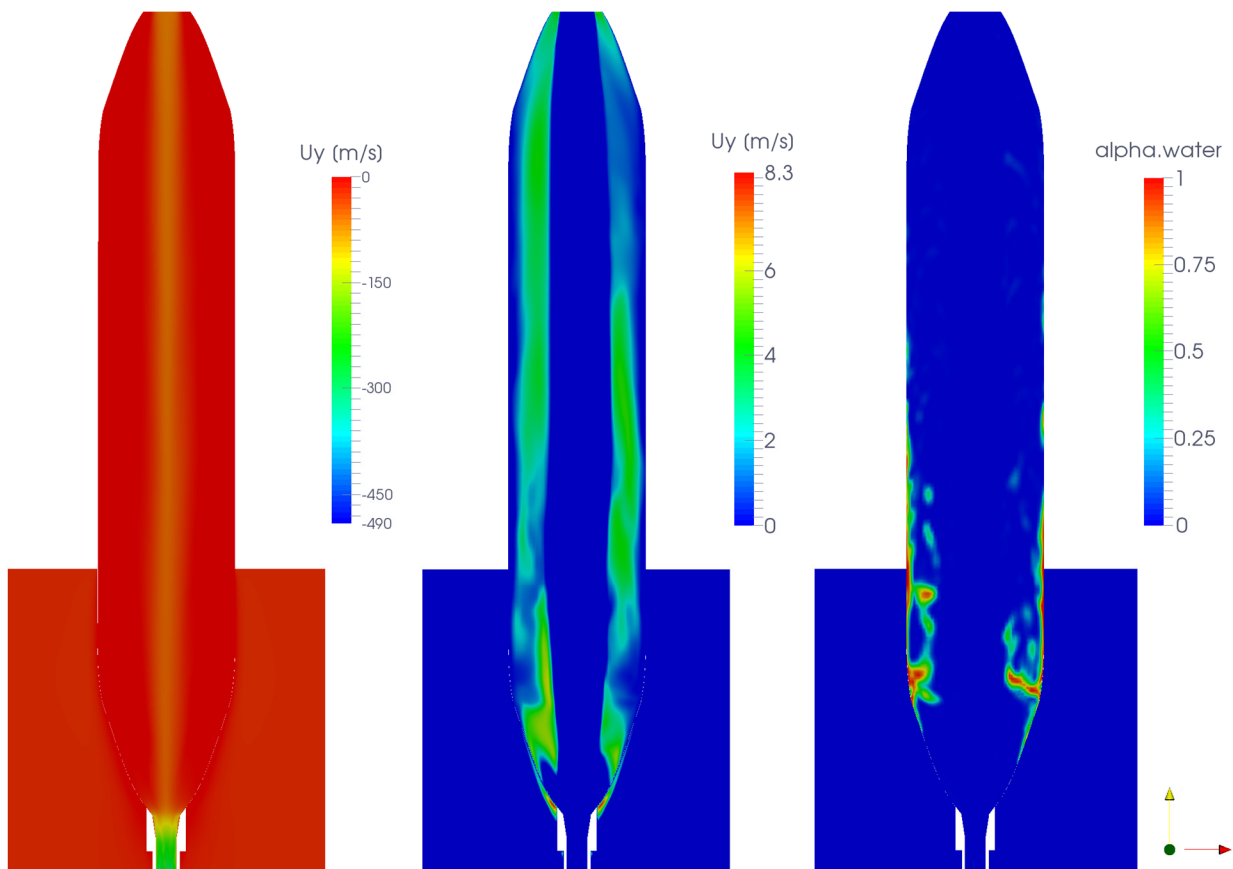


Figure 111: Backflow in the first chamber at nozzle 3, $t = 0,84 \text{ s}$

At both nozzles, due to the high velocity in the first chamber also a backflow appears on the walls of the chamber as shown in *Figure 111/2*. The backflow helps the remaining low amount of water to stay in the chamber in the form of a thick water film on the chamber wall. As the

outflow velocity at the nozzle becomes lower, the flow in the chamber will vary and the backflow will have a smaller impact. That results in the destabilization of the water film as in *Figure 111/3*. The remaining water amount in the chamber will also start to flow out. The effect can be seen also in the last time steps presented in *Figure 85* and in *91*. That means that the rocket is carrying around $0,15\text{ l}$ water almost without avail, which is a big additional mass. This effect can be recognized also in the functions in *Figure 112* and *Figure 113*. The increase of the mass flow can be also seen because of this reason at both nozzles. At the moment as the rest of the water amount flows out, the mass flow will rise again and in case off nozzle 4 it will reach the value of 1 kg/s . The effect in the accelerating force is not strong, because the outflow velocity is not so high any more, and the emerged momentum will stay small. This proves again, that the additional $\sim 0,15\text{ l}$ which stays in the first chamber is almost useless regarding the momentum. A closer view of the collected water amount in the first chamber can be seen in *Appendix C*.

Another important information is that at the single phase air outflow happens not every time at the actual nozzle geometry, because after the end of the multiphase outflow a little amount of water, a water film stays on the nozzle wall for a short time, making the outlet cross section smaller.

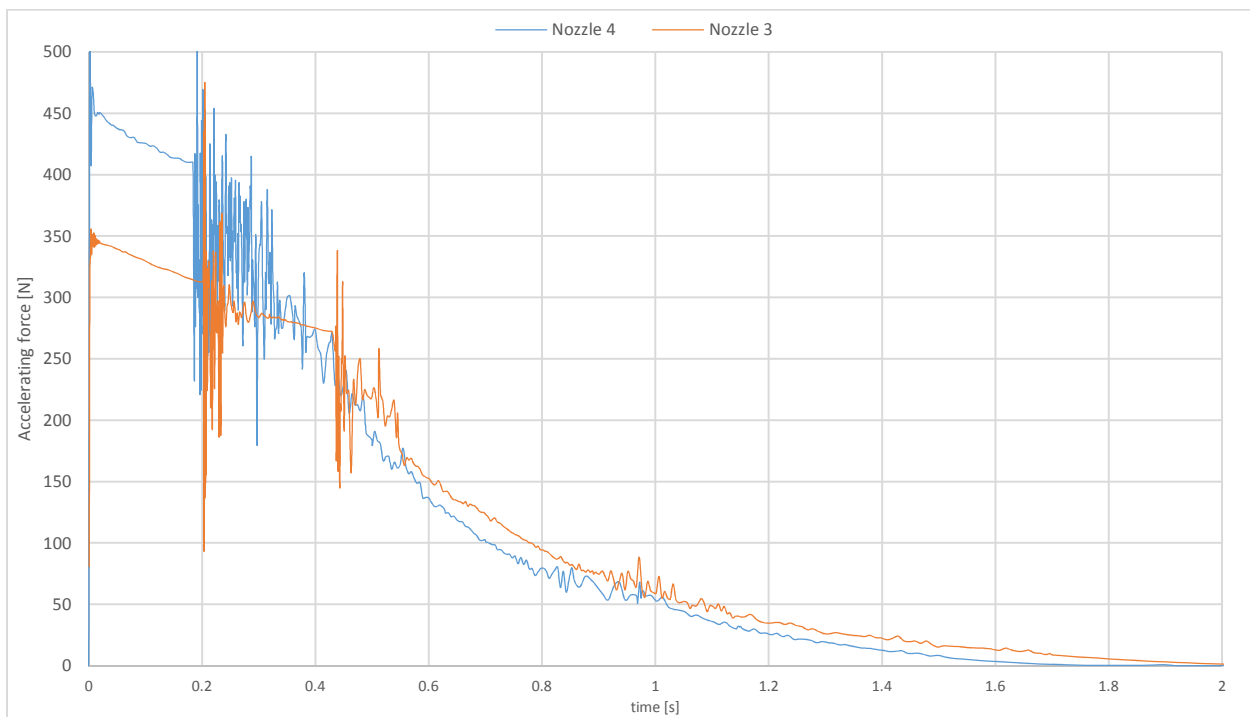


Figure 112: Comparison of the calculated total momentum at nozzle 4 and nozzle 3

The conclusion of the comparison of the two different water levels presented in *Figure 89, 90* is that the impact of the lower water level on the beginning of the cutting through effect and the multiphase outflow is insignificant. The air jet starting from the narrow chamber connection reaches the water level with no difference and has the same effect. Due to the lower water level the air jet will reach the water surface later but also it will be cut through much quicker.

The real role of the Laval nozzle starts only at the near pure air outflow. This happens approximately after $t = 0,545 \text{ s}$ for nozzle 3. At this moment the pressure in the rocket is $p_r = 12,2 \text{ bar}$, the numerical calculations delivered for this moment a rocket pressure of $p_r = 13,2 \text{ bar}$. The nozzle as seen in *Figure 94* and *95* is highly under-expanded and does not operate at the optimal point. That is easily recognizable on the shape of the jet, and the pressure difference at the nozzle exit. The details of the unexpanded jet, the created shock cell structure after the nozzle and its effect on the velocity field is illustrated in *Appendix C*.

If the air is expanding at the nozzle exit to a greater value as the ambient pressure then the jet shape will be bulging. In an under-expanded case the pressure difference at the nozzle will be a positive value. Near to the optimum operating point of the nozzle this difference will be smaller and in the optimum point zero. Therefore also the shape of the jet will be different, as shown in *Figure 95/2*. According to the simulation the optimum pressure difference for this nozzle is $p_r = 5,81 \text{ bar}$. Moving to lower pressures the nozzle will be again far from the optimum point and it will be over-expanded. In the case of nozzle 4 the gas has no chance to expand in the nozzle hence the pressure difference at the nozzle exit will be much higher, but the efficiency of the outflow much lower. The function of the force due to the time depending pressure difference at the nozzle exit is presented in *Figure 95*.

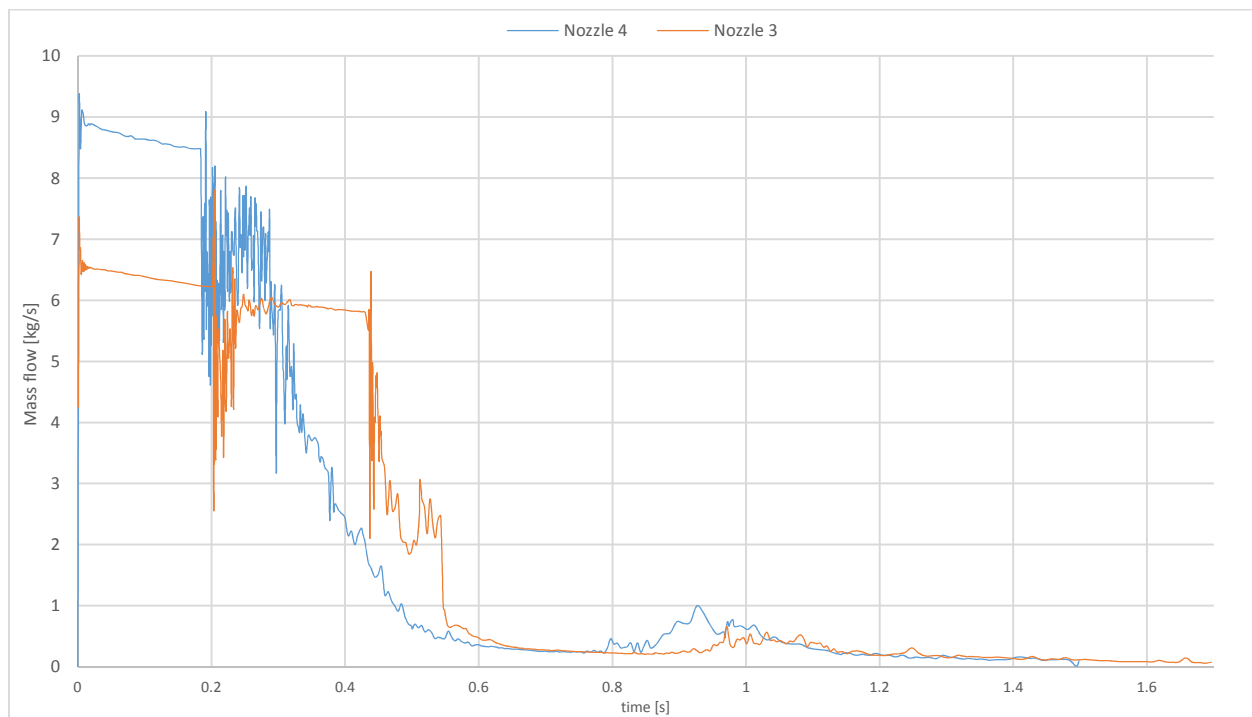


Figure 113: Comparison of the mass flow at nozzle 3 and nozzle 4

In comparison of nozzle performance for the outflow, the over-expanded nozzle is worse than the under-expanded nozzle because the nozzle's large exit area results in extra drag which derives from the negative pressure difference at the nozzle exit due to the unwished over expansion. That means that the generated momentum could be improved if the optimum point of the nozzle would be at lower pressure differences. Regardless of the pressure difference, the efficiency of the nozzle

would be slightly better by reshaping it in a longer nozzle, using a smaller beavel-angle or by using a bell shaped nozzle, because the flow would be almost entirely axial with negligible radial components. The improvement of the performance with a diffusor extension at nozzle 4 is doubtless.

IV. 7. Calculating the maximum altitude of the rocket, comparison of the nozzles

Now we have all the important functions which are describing the outflow for both nozzles. These functions are the total accelerating force, the mass flow and the total mass of the rocket presented in *Chapter 6.2.2*. By merging the results of the single and the two phase simulation we can also obtain the acceleration, velocity and altitude in the function of time by using the equations listed in the presented numerical calculation in *Chapter 6.1.1.3*. with the difference, that the mass flow and the total accelerating force – including the drag force, which can be calculated with the help of the drag coefficient – will be taken from the simulation. The results of the functions for both nozzles are listed in *Figure 114* and *115*. Due to the random two phase outflow also the function of the acceleration became chaotic.

As we can see in the functions, the difference between the two nozzles is not large. Using these initial conditions the better performance was achieved by a $\Delta h_{max} = 5,5 m$ advantage by nozzle 4 as it can be seen in *Figure 114, 115 and 116*. With the used initial conditions according to the simulation the maximum altitude of the rocket using nozzle 4 is $h_{max} = 158,9 m$ and using nozzle 3, $h_{max} = 153,4 m$. At nozzle 4 the outflow time is little shorter due to the larger cross section of the nozzle and therefore also the generated momentum respectively the acceleration is greater. Nozzle 3 has a smaller cross section, which results in a smaller (but longer) beginning accelerating force. The impact of the better performance (by using a diffusor extension) of nozzle 3 in the one phase air outflow is not enough to patch up the drawback against nozzle 4.

We have to take into account that regardless the used Laval nozzle, there exists an optimum for just the simple nozzle diameter to reach the best performance. The results shows that using these initial conditions, a simple nozzle with a diameter of $d = 15,5 mm$ stands much closer to the optimum as a simple nozzle diameter with $d = 12,9 mm$ with the additional diffusor, which improves the performance. That means that the optimum constant nozzle diameter at these initial settings is surely closer to nozzle 4 as to nozzle 3.

It could be also assumed, that the better performance is because of the different outflow process. In some moments due to the high pressure the air formed a diffusor shape in the water and therefor the transsonic air outflow showed up during the multiphase outflow also for nozzle 4. These kind of two phase outflow happened for a longer time in the case of nozzle 4. The strong accelerating force during the multiphase outflow can be well recognized at *Figure 115*. The outflow and the impact of the influential factors is very complex. For a detailed explanation of the differences the process has to be further analyzed.

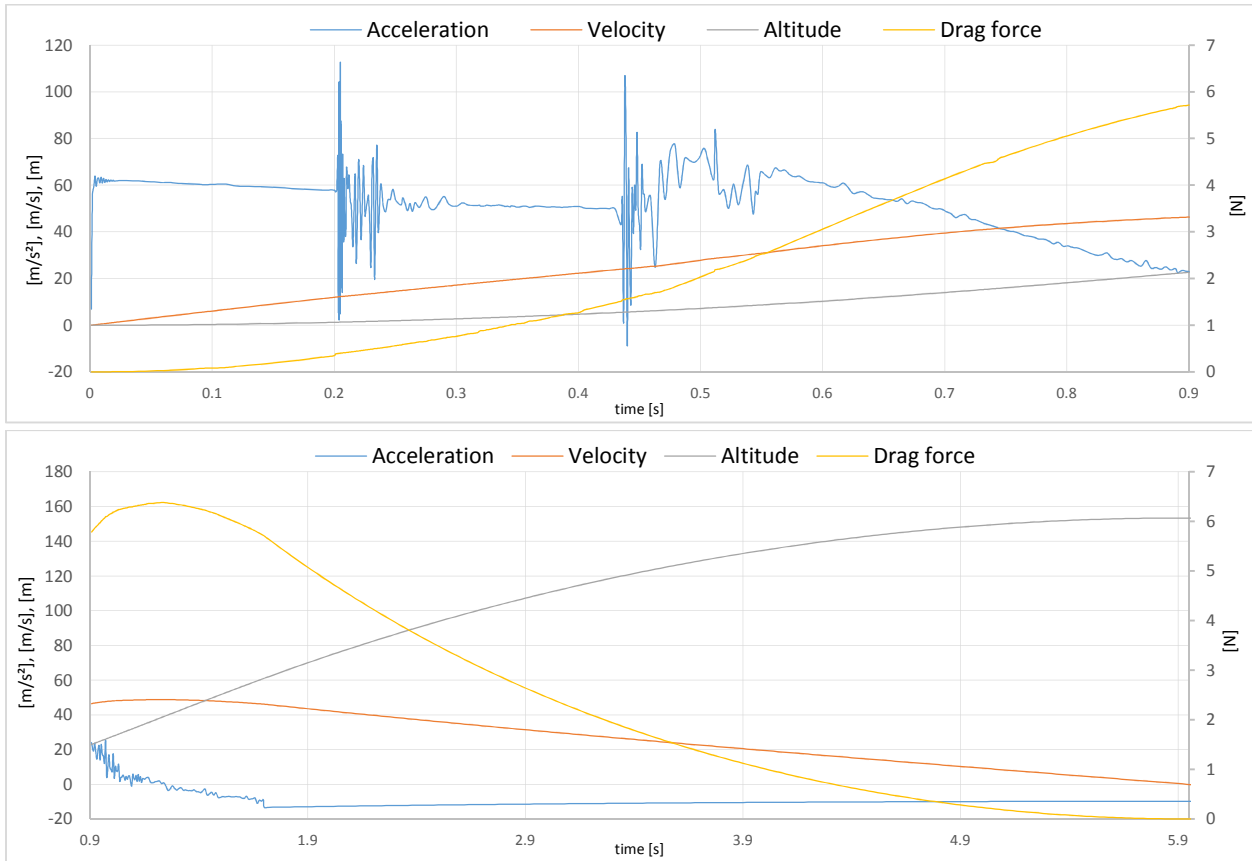


Figure 114: Flying of the rocket using nozzle 3, 3l

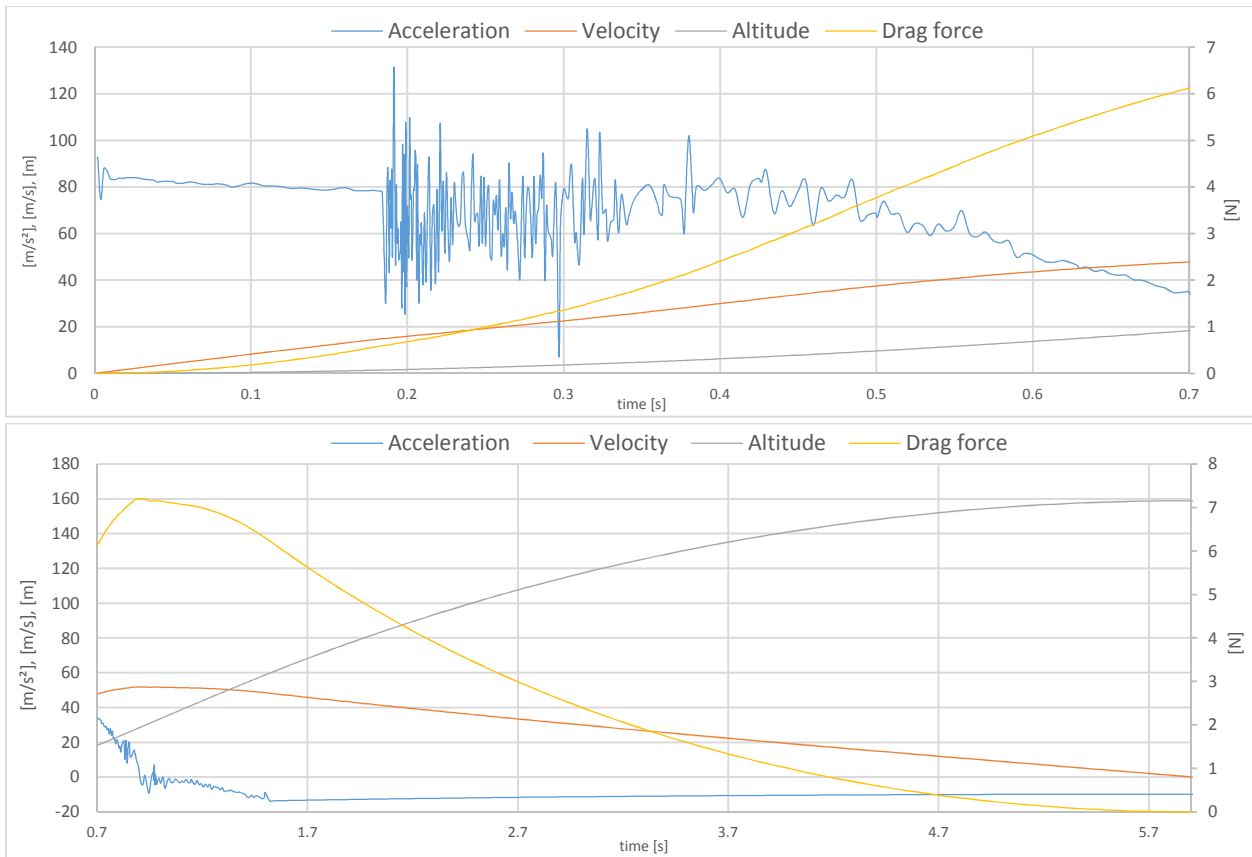


Figure 115: Flying of the rocket using nozzle 4

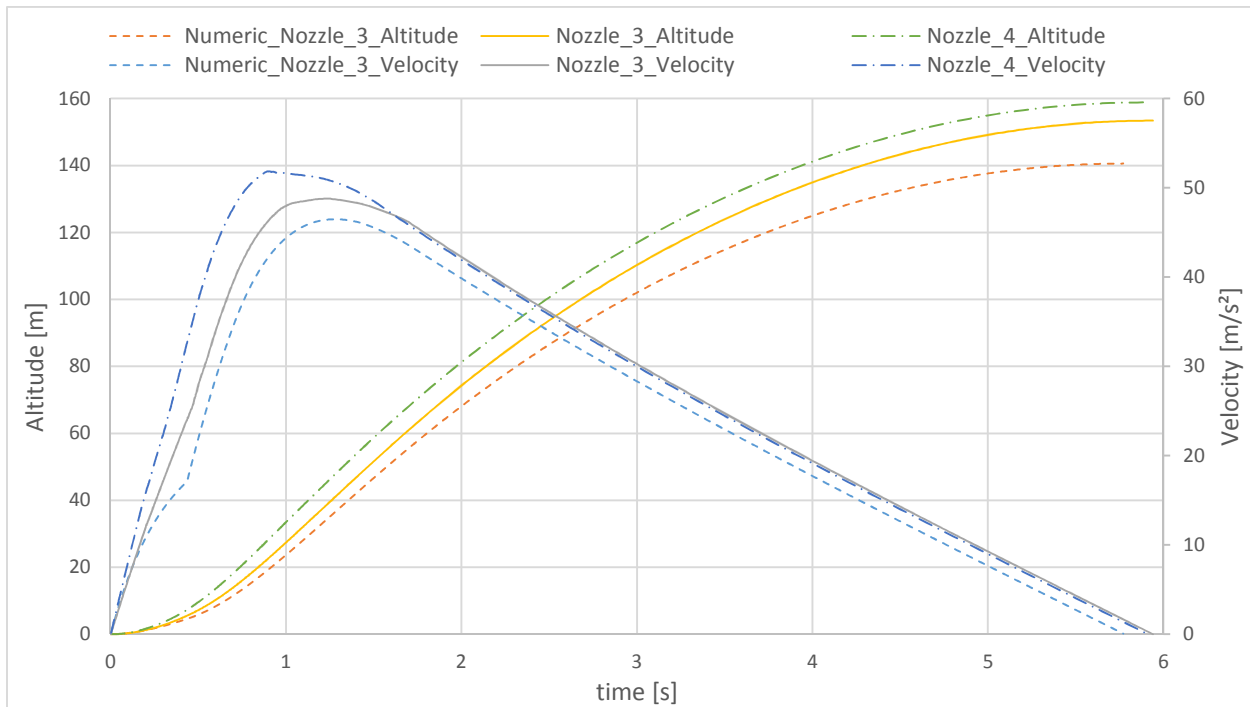


Figure 116: Comparison of the flights for nozzle 3, nozzle 4 and the numerical results

IV. 8. Future plans

The future steps include the finishing of the building of the presented rocket. The rocket will be equipped with the G-Wiz flight computer produced by Aerocon Systems Co [29]. In addition to many functions this device can measure and store the acceleration and altitude of the rocket with 500 Hz . That makes it possible to obtain the real functions of the altitude, velocity and acceleration. These results can be used for further investigation and validation of the simulation.

Another important objective is to find the optimum operating settings which lead to the maximum altitude of the rocket. One flight process takes much fewer time as the simulation. Therefore it has the advantage to retrieve all the functions of the rocket relatively quickly. Further comparison of the two solution can be seen in *Table 35*. Irrespectively of these details the finding of the optimum settings will be just a question of the number of the different measurements. Another way to see the behavior of the fluid in the first chamber and at the nozzle outlet is the recording of the outflow with a high speed camera. This solution would be advantageous if the chambers would be created from a transparent material, which is also a complex challenge regarding the safety and cost, if we consider the needs of a qualitative high speed camera recording, like the amount of light, the proper camera settings and the behavior of the jet.



Figure 117: Air-water rocket (previous model)

	<i>Plastic reinforced rocket</i>	<i>CFK reinforced rocket</i>	<i>CFD simulation</i>
<i>Settings of the initial conditions</i>	Safe until ~ 17 bar	Safe until ~ 22 bar	Wide range of pressure can be set.
<i>Reusability</i>	Safe reusable (creeping problems) deformation 15 – 20 times	Safe reusable much stiffer construction 20 << times	∞
<i>Cost of the virtual / real model</i>	Cheap solutions 100 -500 EUR	Expensive solutions 1500 – 2000 EUR	Negligible cost of the model creation
<i>Fabrication / preparation time</i>	2 week building time	4 week building time	Few days preparing time
<i>Measurement / calculation time</i>	~ 40 min	~ 40 min	~ 1000 h on 40 CPU + postprocessing time
<i>Cost of the measurement / simulation</i>	Negligible cost	Negligible cost	~ 1000 [h] on 40 CPU
<i>Quality of the results</i>	Video recordings	Video recordings Only the function of the altitude and the acceleration	Very detailed results
<i>Data size</i>	~ 500 Mb	~ 500 Mb	~ 1 Tb

Table 35: Comparison of the measurement and simulation

Learning from the results of the simulation the nozzle geometry is also an option what can be further optimized. It was proven in the thesis, that the numerical calculation is only useful for rough estimation due to the simplifications. The few calculated simulations delivered lot of new information but they were not enough to find the optimum nozzle geometry with the optimum settings. To find these settings, future measurements will be performed with the new rocket model. The following steps also include the further development of the rocket by creating a stronger and lighter rocket body. A previous created air – water rocket can be seen in *Figure 117*.

“May the winds be calm, may the skies be blue, and may all your rockets fly straight and true!”

Unknown source

V. Summary

The thesis considered two different cases of high speed multiphase flows. The basic goal of both jobs is to understand the details of the flow and find the weak spots of the systems. By finding and improving these factors the runoff of the process can be influenced in a positive direction.

The first case deals with the measurement of the atomization at a minimized 2:1 cold model blast furnace. The measurement would be at the actual furnace impossible due to the harsh environmental conditions. The advantage of the created model is not just the condition of the lower temperature but also the transparency. The plexiglas – used for the model creation – makes it possible to see the atomization directly. Due to this circumstance the measurement was performed with image analysis by recording the atomization with a high speed camera. In the later steps the recorded images were analyzed with the program ImageJ and the retrieved set of data was processed with Microsoft Excel to calculate the Sauter mean diameter of the performed atomization. Before the measurements the system was calibrated with sugar particles to control the accuracy of the method. As result we obtained the information that with smaller droplet diameters the accuracy of the measurement decreases dramatically. At the model “furnace” as model fluid paraffin oil, glycerol, ethanol and different solutions of water –glycerol were applied. Due to the before mentioned difficulty and in other cases the high viscosity of the fluid the originally planned measurement interval become much smaller. The measurement with paraffin oil were difficult, with ethanol and pure glycerol impossible. The measurements with water had the most positive results. Pure water used as model fluid is not the best choice because the modelled process will differ intently from the real, originally planned case. The glycerol – water mixtures provided the best matches with dimensionless computation data. This difference can be well perceptible at the values of the dimensionless numbers. The measurements accomplished in the proper interval delivered acceptable results. It was proved that imaging analysis is a suitable way to measure the Sauter mean diameter of an atomization but the method brings lot of difficulties and disturbing factors into the data processing especially at smaller droplet diameters and at higher viscosities. Therefore in this case either the quality of the recording must be improved or the method should be adapted or changed.

The second case discovered the details of a two phase high speed – partly supersonic – outflow at a pressurized air – water rocket nozzle. The purpose of the outflow is the generation of momentum, the acceleration of the rocket. Due to the high speed outflow the expelled gas delivers enough energy for the water that atomization occurs. The atomization is now just a side effect and the focus of the investigation is the calculation of this momentum, which will be done with the help of the program OpenFOAM. To prepare the simulation and to be able to roughly estimate the process analytical, numerical pre-calculations were performed. The simulation was split up into two separate parts. A simple single phase simulation for the „outer” flow around the rocket shell to calculate the drag coefficient of the rocket’s shape and the much more complex computation for the „inner” two phase flow. The inner flow describes the procedures in the pressure chambers of the rocket and also the two phase outflow at the nozzle. The finally simulated case was approached step by step starting with a simple model. After the proper preparation of the solver, the final geometry and mesh were constructed and by emerging the simulation results, the momentum of the rocket was calculated. Altogether three two phase simulations were performed. Two simulations with the same initial conditions but with different nozzle geometries – Laval and a simple nozzle – and a third case with the same Laval nozzle using a different initial condition.

With the performed computations we could see the behavior of the two phases water and air in the first chamber and also we could rate and compare the efficiencies of the used nozzles. As result we obtained that the simple nozzle performs better.

The simulation results showed that the overlapping of the two phases, outflow of water and air is longer than expected and the starting of the atomization is not the sign of the depletion of water. The high speed air jet in the rocket resulting from the narrow chamber connection cuts through the relatively high water level and this phenomenon changes the initially assumed model of outflow. That means that the nearly pure outflow of air starts with a lower pressure difference than expected which leads to another optimal nozzle shape. Summarized, the simulations delivered new and important information about the outflow process at the nozzle and also in the chamber. These new information raised also new questions, which can be answered only by further and deeper investigation of the process through measurements-, high speed video recording of rocket experiments and further CFD simulations.

VI. Literature and sources

- [1] Richter, T.: *Zerstäuben von Flüssigkeiten*. Expert-Verlag, 2004.
- [2] Ashgrinz, N.: *Handbook of atomization and sprays – Theory and Applications*, Springer, 2011.
- [3] Lin, S.P. ; Reitz, R.D.: *Drop and Spray Formation from a Liquid Jet*. In: *Annual Review of Fluid Mechanics* 30 (1998), S. 85-105
- [4] Wozniak, G.: *Zerstäubungstechnik - Prinzipien, Verfahren, Geräte*. Springer, 2003
- [5] *International Journal of Multiphase Flow, Fragmentation of falling liquid droplets in bag breakup mode*, 2012.
- [6] *Source of the external and internal nozzle figures:*
http://www.pnr.co.uk/docs/cat_atom/int_ext_mix.htm 24.06.2015.
- [7] Lefebvre, A. H.: *Atomization and Sprays*. Hemisphere Publishing Corporation, 1989.
- [8] *Figure of the schematic blast furnace:* www.hferrier.co.uk 20.02.2014.
- [9] Kirchbacher, F.: *Experimentelle Untersuchung von Sprühdüsen*. unveröffentlichte Bachelor-Arbeit, 2010, TU Wien, Institute for Chemical Engineering
- [10] Zauner, F.: *Experimentelle Analyse von industriellen Sprühdüsen*. Wien: Technische Universität, Institut für Verfahrenstechnik, Master-Arbeit, 2010.
- [11] Herwig, H.: *Strömungsmechanik*. Vieweg+Teubner, 2008
- [12] *ImageJ*, <http://imagej.nih.gov/ij/> 24.06.2015.
- [13] *Glycerine Producers Association, Physical Properties of Glycerine and Its Solution*, 1963.
- [14] *Dynamic viscosity of liquid water from 0°C to 100 °C* - <http://www.vaxasoftware.com>, 24.06.2015.
- [15] Willinger R. *Numerische Methoden für thermische Energiesysteme*, 2011, TU Wien, Institut für Energietechnik und Thermodynamik
- [16] Haddadi B., Nagy J., Jordan C., Harasek M. *Introduction to CFD, second edition*, 2014, TU Wien, Institute for Chemical Engineering
- [17] *OpenFOAM User Guide, Version 2.3.1*, 2014.
- [18] Faith A. Morrison. *Data correlation for Drag coefficient for Sphere*, Department of Chemical Engineering, Michigan Technological University, Houghton, MI 49931, 2013.
- [19] Schlichting, H.: *Boundary-layer theory, Seventh edition*. McGRAW-HILL Book Company, 1979.
- [20] *Source of the drag coefficient image:*
<http://www.aerospaceweb.org/question/aerodynamics/q0231.shtml> 24.06.2015.

- [21] *SolidWorks 2011* <http://www.solidworks.com/> 24.06.2015.
- [22] *Gambit* http://www.mne.psu.edu/cimbala/learning/fluent/gambit_introduction.htm 24.05.2015.
- [23] *Paraview* <http://www.paraview.org/> 24.05.2015.
- [24] *OpenRocket*, <http://openrocket.sourceforge.net/>, 24.06.2015.
- [25] *Cohesion and Adhesion in Liquids Surface Tension and Capillary Action, version 1.5, 2014, Table 1*
- [26] Lajos, T.: *Az áramlástan alapjai*, negyedik kiadás, 2008 (*English: The fundamentals of fluid mechanics*)
- [27] Környei, T.: *Termodinamika, Book of Budapest University of Technology*, 2007.
- [28] Hemida H. *OpenFOAM tutorial: Free surface tutorial using interFoam and rasInterFoam*, 2008,
http://www.tfd.chalmers.se/~hani/kurser/OS_CFD_2007/HassanHemida/Hassan_Hemida_VOF.pdf 24.06.2015.
- [29] https://www.apogeerockets.com/Electronics_Payloads 24.06.2015.

VII. Appendix A Recorded images with the HS camera

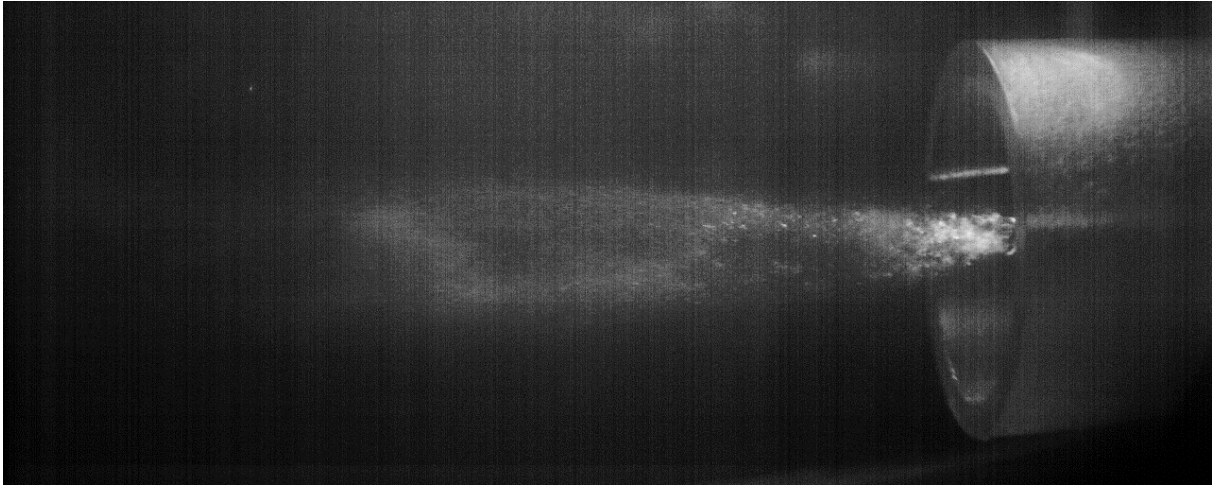


Figure 118: Atomization of ethanol (low viscosity) at the nozzle outlet



Figure 119: Water droplets after the atomization

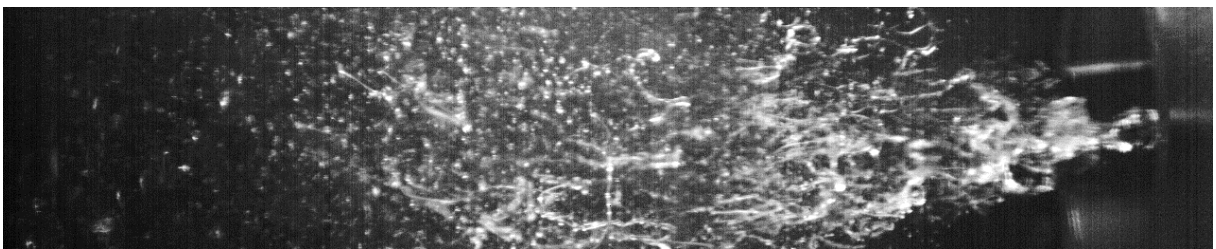


Figure 120: Atomization of paraffin oil at the nozzle

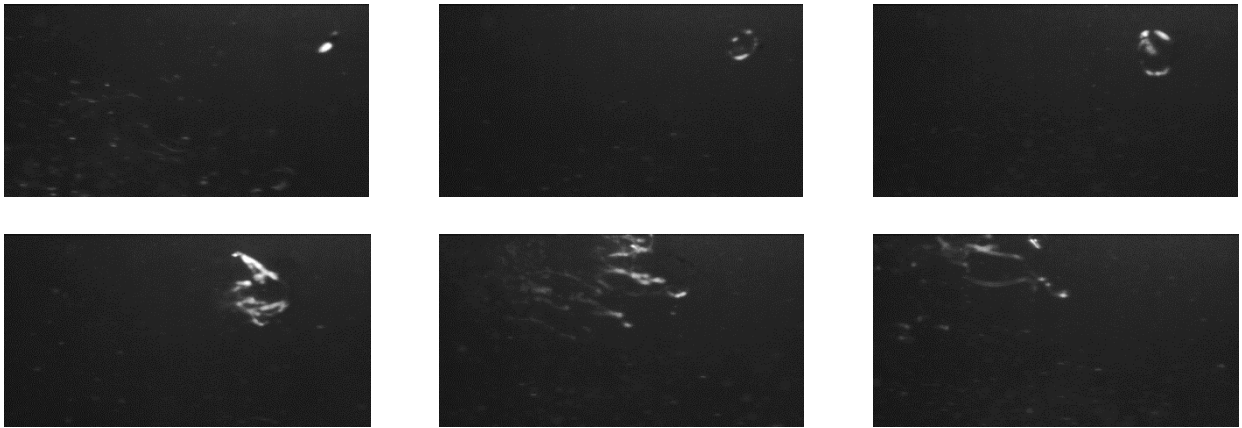


Figure 121: Atomization of a single paraffin oil droplet

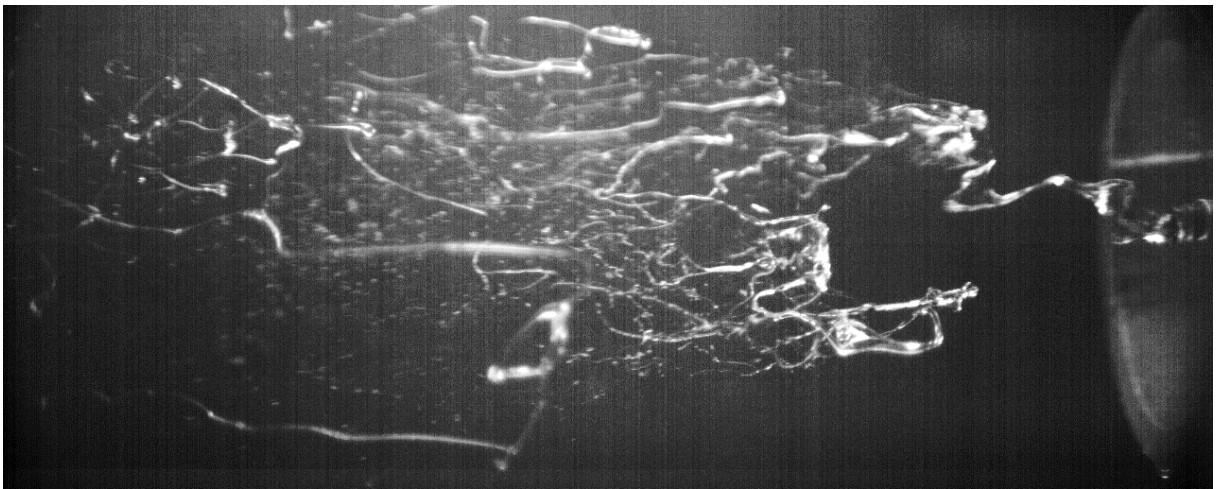


Figure 122: Atomization of pure glycerol (high viscosity) into filaments at the nozzle

VIII. Appendix B The used boundary conditions

Table 37 represents the boundary conditions for the first preparative simulations for the outer one phase flow to estimate the turbulent values for the different inlet velocities.

	<i>Unit</i>	<i>Int.Field</i>	<i>Inlet</i>	<i>Outlet</i>	<i>Outlet_end</i>
U	$[ms^{-1}]$	$(0\ u\ 0)$	fixedValue value $(0\ u\ 0)$	zeroGradient	zeroGradient
p	$[m^2s^{-2}]$	10^5	zeroGradient	fixedValue value 10^5	fixedValue value 10^5
$k/k - \varepsilon$	$[m^2s^{-2}]$	$0,375$	fixedValue value $0,375$	slip	zeroGradient
ε	$[m^2s^{-3}]$	$14,85$	fixedValue value $14,85$	slip	zeroGradient
$k/k - \omega$	$[m^2s^{-2}]$	$0,375$	fixedValue value $0,375$	slip	zeroGradient
ω	$[s^{-1}]$	100	fixedValue value 100	slip	zeroGradient

Table 36: Boundary conditions for the preparative one phase simulations for estimating k, ε and ω

For the final one phase simulation for determining the rocket's drag coefficient the boundary conditions in Table 38 were used. The setted values for k and ε are showed in Table 33.

	<i>Unit</i>	<i>Int.Field</i>	<i>Inlet</i>	<i>Outlet</i>	<i>Wall</i>	<i>No_slip_wall</i>
U	$[ms^{-1}]$	$(0\ u\ 0)$	fixedValue value $(0\ u\ 0)$	zeroGradient	fixedValue value $(0\ 0\ 0)$	zeroGradient
p	$[kgm^{-1}s^{-1}]$	10^5	zeroGradient	fixedValue value 10^5	zeroGradient	fixedValue value 10^5
T	$[K]$	293	fixedValue internalField	zeroGradient	zeroGradient	inletOutlet internalField
k	$[m^2s^{-2}]$	k	fixedValue value k	zeroGradient	kqRWallFunc. value $\sim 0,5$	slip
ε	$[m^2s^{-3}]$	ε	fixedValue value ε	zeroGradient	epsilonWallFunc. value ~ 4	slip
mut	$[kgm^{-1}s^{-1}]$	0	calculated value 0	calculated value 0	alphanWallFunc. value 0	calculated value 0
$alphan$	$[kgm^{-1}s^{-1}]$	0	calculated value 0	calculated value 0	mutWallFunc. value 0	calculated value 0

Table 37: Boundary conditions for determining the drag coefficient of the rocket

The boundary conditions of the computed two phase simulation are represented in the following *Table 38*. The values for the initial internal field are valid before running the command „setFields” which establishes the initial settings for the pressure and the water volume fraction in the pressure chamber. An additional important setting is the value of the surface tension of soapy water, which is $\sigma = 0,037 \text{ kg/s}^2$. The value was based on [25], *Table 1*.

	<i>Unit</i>	<i>Int.Field</i>	<i>Inlet</i>	<i>Outlet</i>	<i>Wall</i>	<i>Atmosphere</i>
U	$[\text{ms}^{-1}]$	(0 0 0)	polyFixedValue $\underline{U}(t) = \underline{v}_r(t)$	zeroGradient	fixedValue value (0 0 0)	pressureInlet OutletVelocity value (0 0 0)
p	$[\text{kgm}^{-1}\text{s}^{-1}]$	10^5	zeroGradient	totalPressure value 10^5	calculated value 0	totalPressure value 10^5
p_rgh	$[\text{kgm}^{-1}\text{s}^{-1}]$	10^5	zeroGradient	totalPressure value 10^5	calculated value 0	totalPressure value 10^5
T	[K]	300	fixedValue internalField	inletOutlet value 300	zeroGradient	inletOutlet value 300
k	$[\text{m}^2\text{s}^{-2}]$	0,1	fixedValue value 0,1	inletOutlet value 0,1	kqRWallFunc. value 0,1	inletOutlet value 0,1
nut	$[\text{m}^2\text{s}^{-1}]$	0	fixedValue value 0	calculated value 0	nutkWallFunc. value 0	calculated value 0
nuTilda	$[\text{m}^2\text{s}^{-1}]$	0	fixedValue value 0	inletOutlet value 0	zeroGradient	inletOutlet value 0
muSgs	$[\text{kgm}^{-1}\text{s}^{-1}]$	10^{-11}	zeroGradient	zeroGradient	zeroGradient	zeroGradient
alphaSgs	$[\text{kgm}^{-1}\text{s}^{-1}]$	10^{-11}	zeroGradient	zeroGradient	zeroGradient	zeroGradient
alpha.water	[1]	0	fixedValue value 0	zeroGradient	inletOutlet value 0	inletOutlet value 0

Table 38: Boundary conditions for the two phase simulation

```

forcesCoeffs
{
type forceCoeffs;
functionObjectLibs ( "libforces.so" ); // lib to load
outputControl timeStep;
outputInterval 1;
patches (wall) // Whole surface of the rocket
pName p;
UName U;
rhoInf 1.2;
CofR ( 0 0 0 );
liftDir ( 0 0 1 );
dragDir ( 0 -1 0 ); // Set the direction of the drag
pitchAxis ( 0 1 0 );
magUInf u; // Velocity of the flow
lRef 2.2; // Length of the rockett
Aref 0.00893; // Area of the largest cross section normal to the flow direction
}

```

Table 39: Settings in the controlDict file to calculate the drag coefficient in the program OpenFoam-2.3.0.

IX. Appendix C Further results of the simulations

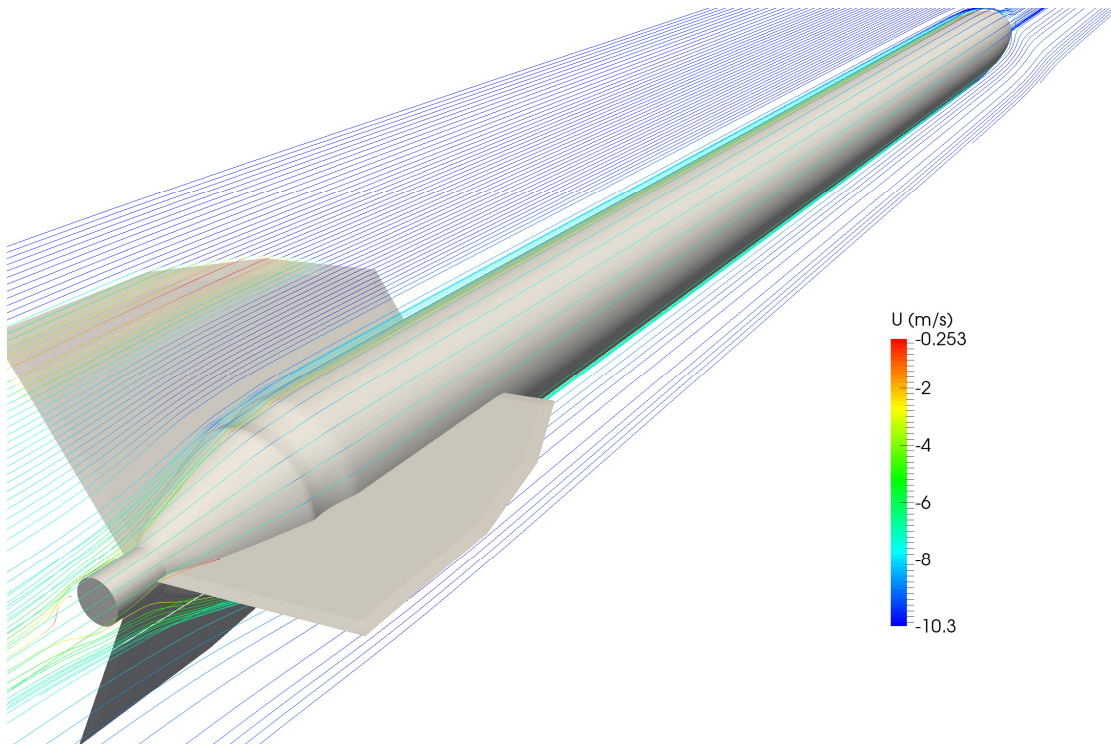


Figure 123: Stream lines around the rocket, steady state single phase simulation, $u_{y,inlet} = 10 \text{ m/s}$

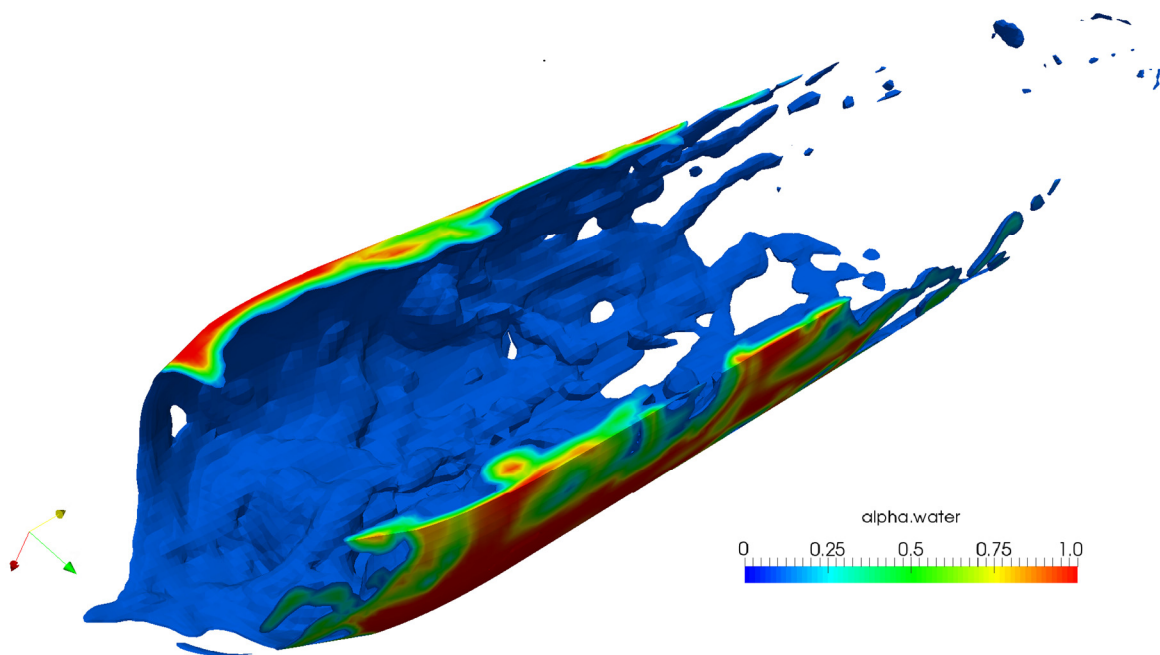


Figure 124: Water amount in the bottle, nozzle 3, 3l at $t = 0,55 \text{ s}$

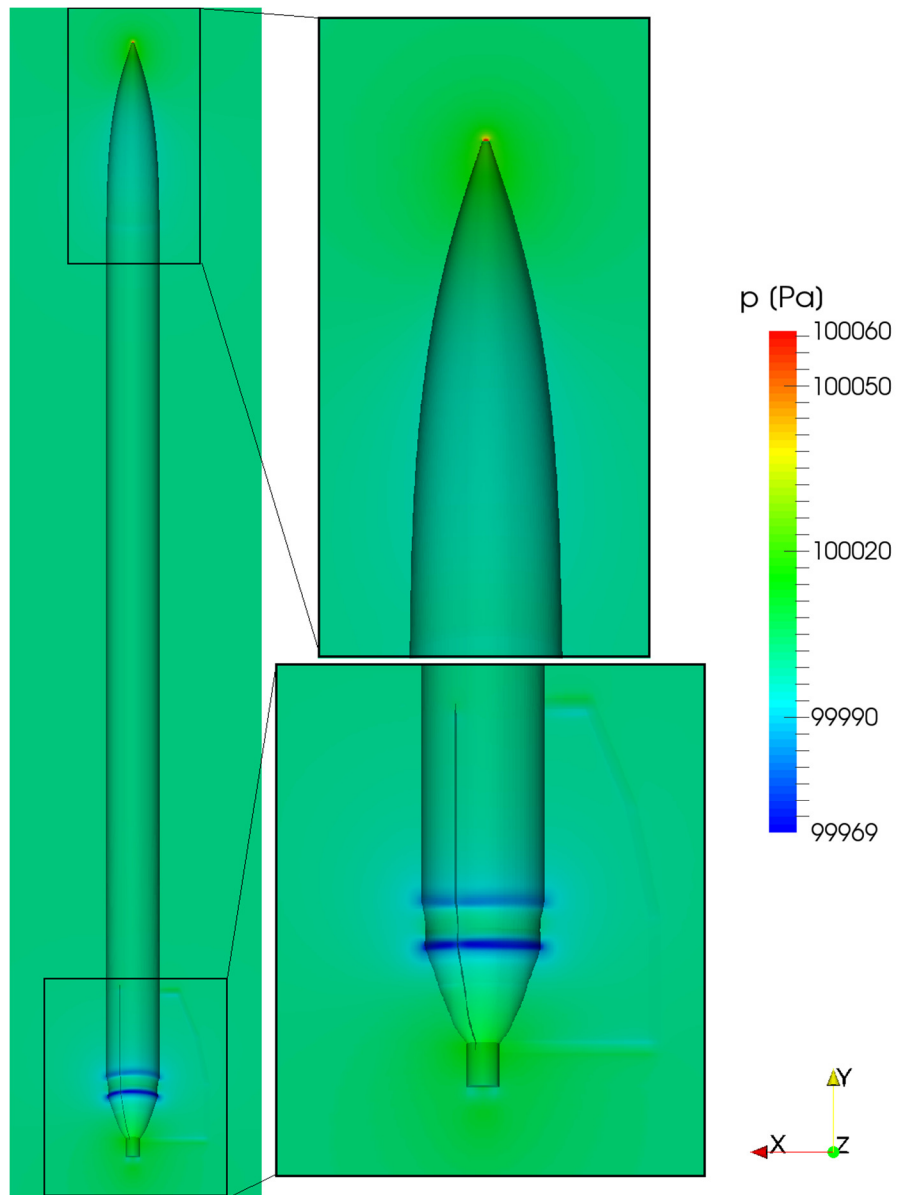


Figure 125: Pressure field around the rocket, steady state single phase simulation, $u_{y,inlet} = 10$ m/s

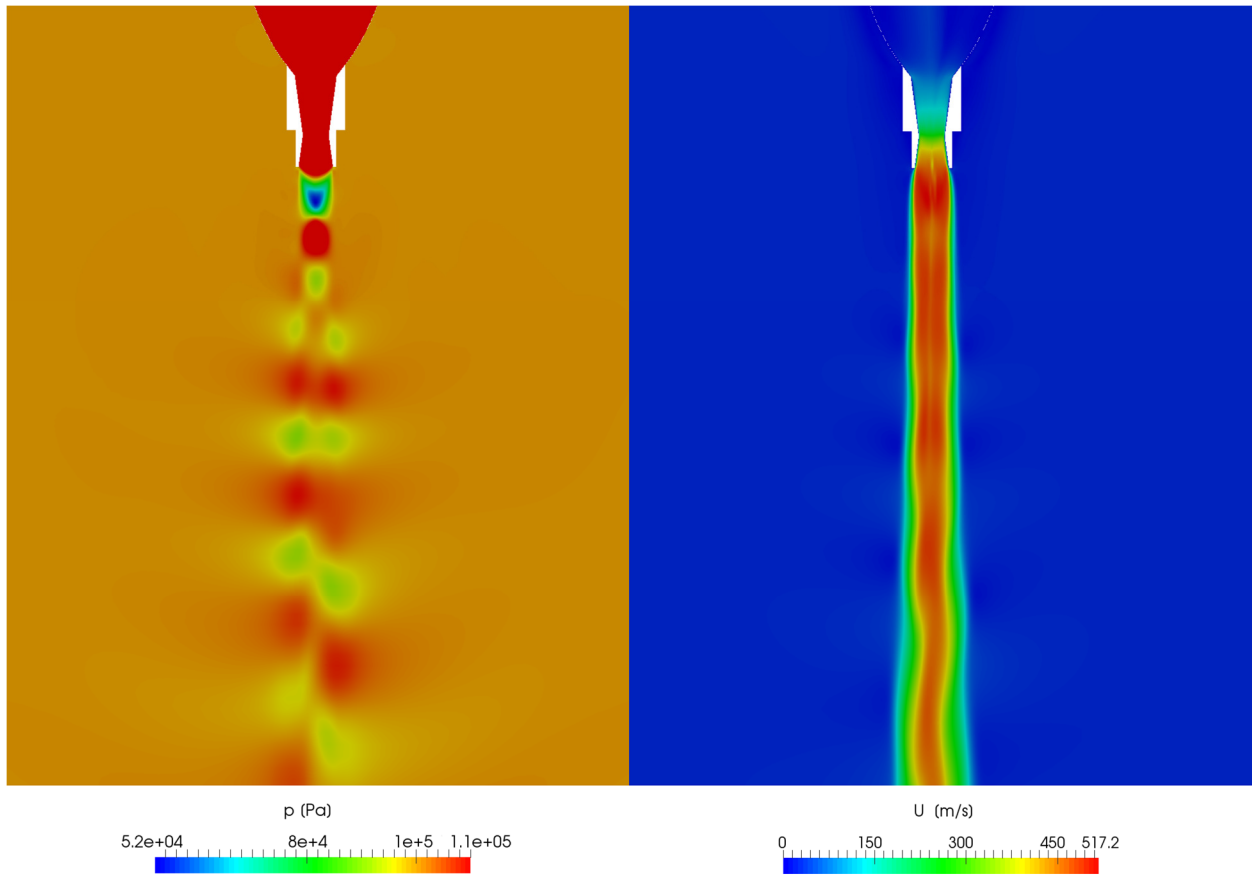


Figure 126: Shock cell structure and the resulting velocity field after the nozzle after the nozzle 3, 3 l
 $t = 0,667 \text{ s}$

X. Appendix D Further details of the rocket

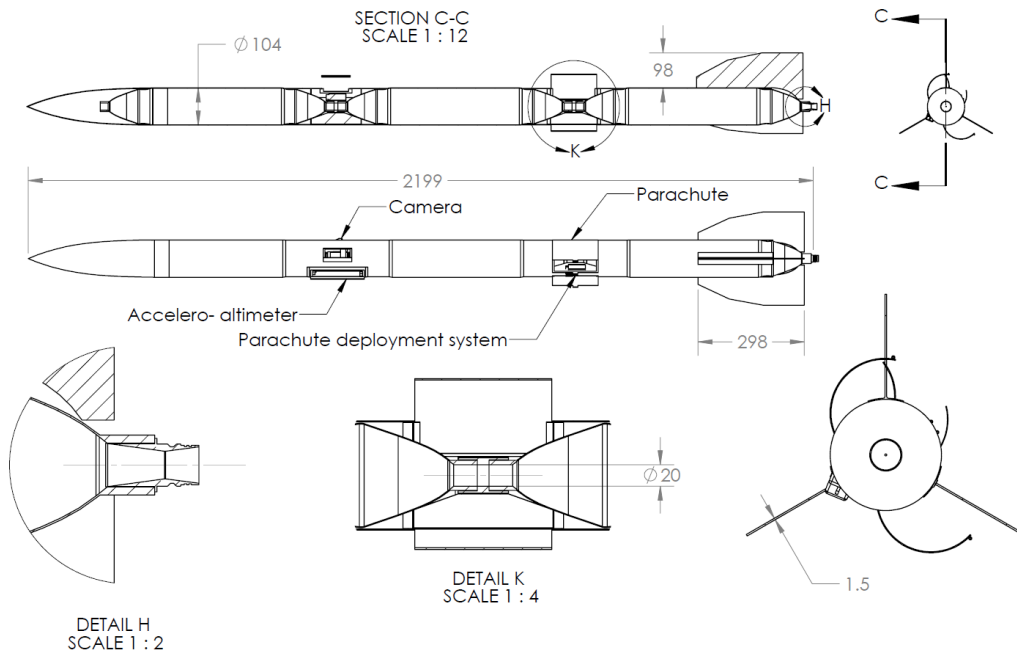


Figure 127: Details of the rocket geometry